The interplay between root growth and soil properties

Dissertation zur Erlangung des Doktorgrades der Naturwissenschaften (Dr. rer. nat.)

der

Naturwissenschaftlichen Fakultät III
Agrar- und Ernährungswissenschaften,
Geowissenschaften und Informatik

der Martin-Luther-Universität Halle-Wittenberg,

vorgelegt von

Herrn Maxime Phalempin

Geb. am 26.05.1991 in Namur (Belgien)

Gutachter :

Dr. Steffen Schlüter

Prof. Doris Vetterlein

Prof. Stephan Peth

Datum der Verteidigung: 04.07.2022

ABSTRACT

The overarching goal of this thesis is to improve the understanding of the interplay between root growth patterns and soil properties thanks to the use of X-ray computed tomography. Specifically, this work aims at characterizing how the absence of root hairs influences the root system architecture of *Zea mays* L. and to which extent this depends on soil texture (loam or sand). Another objective of this thesis is to characterize the influence of roots of *Zea mays* L. on the rhizosphere bulk density and to which extent this depends on the soil texture and the absence of root hairs. In parallel, a modeling exercise is undertaken to evaluate the effect of rhizosphere bulk density gradients on soil water uptake dynamics. Finally, this thesis aims at characterizing whether and under which circumstances roots of *Zea mays* L. ease their exploration of the soil by growing into existing biopores.

For the analysis of the root system architecture and how it is influenced by soil texture and the absence of root hairs, *Zea mays* root hair defective mutant (rth3) and the corresponding wild-type siblings were grown under well-watered conditions and the root system architecture was investigated using repeated X-ray CT scanning. For the analysis of rhizosphere bulk density gradients, more than 400 samples were extracted during laboratory and field experiments covering various combinations of soil texture, bulk density, structure heterogeneity, maize genotype and soil moisture. In order to address the question as to whether roots reuse biopores and under which circumstances, a soil column experiment which aimed at characterizing the degree of biopore recycling for two soil textures (sand and loam) and two bulk density treatments was carried out. In order to address these research questions, the development of a method for the segmentation of roots from 3D X-ray CT images was required.

With the help of X-ray CT, adaptations in root system architecture, root traits and/or rhizosphere properties in response to changes in soil texture and structure were identified. The absence of root hairs had no or little effect on the results. The difference in soil texture and structure caused (i) an adaptation of root diameter (i.e., roots growing in sand had a consistently bigger diameter than in loam), (ii) a modification of the growth angle of the roots (i.e., roots growing in loam had a greater propensity for growing towards and against the wall of the pots), (iii) alterations of root growth and root growth dynamics (i.e., root growth was greater in loam than in sand in the laboratory but smaller in the field experiment) and (iv) a change in root growth environment (under heterogeneous soil structure conditions such as the one encountered in the field, roots preferentially grew in existing pores whereas roots had to create their own pores in a homogeneous soil structure such as the one encountered in repacked soil columns). These findings highlight the ability of *Zea mays* L. to adapt to its soil environment.

Soil texture and structure did not only affect root growth patterns at the plant scale (cm-dm), but also affected how roots interact with the soil at the scale of individual root segments (μm-mm). Indeed, root growth influenced soil structure through a reorganization of soil particles in the vicinity of roots (< 1 mm from the root surface). Most prominently, the creation of a zone of increased porosity at the direct interface between the roots and the soil was observed (< 250 μm from the root surface). In loam and, depending on the antecedent soil structure, the soil past the zone of increased porosity (between 250 μm and 1 mm from the root surface) was either compacted (in homogeneous soil structure) or loose (in heterogeneous soil structure). In sand, roots could not plastically deform the rigid sand grains but rather pushed them away. Fine roots (< 200 μm in diameter) caused the rigid sand grains to align along their axis whereas big roots (> 350 μm in diameter) broke the fragile arrangement of grains and pushed them farther away than their own diameter. These findings highlight the ability of *Zea mays* L. roots to modify its growth environment and to which extent this depends on soil texture and structure.

In order to investigate the effect of the reorganization of soil particles induced by roots on root water uptake, a modeling study was undertaken. The experimental observations of rhizosphere bulk density gradients were used to derive soil hydraulic parameters in the vicinity of roots. Using a root water uptake model, the effect of rhizosphere bulk density gradients and mucilage concentration gradients were evaluated. During soil drying, a lower rhizosphere bulk density led to an earlier onset of water stress and to a reduced root water uptake that was sustained longer. The presence of mucilage led to a faster reduction of root water uptake. Root water uptake was rapidly reduced when both mucilage and rhizosphere bulk density gradients were considered.

Root growth also influenced soil structure through the creation of a biopore network, whose stability depended on the soil texture. In sand, many biopores collapsed due to the low cohesion between sand particles. The degree of biopore recycling in repacked loam was two orders of magnitude lower than the values previously reported in the literature. This difference was attributed to the low mechanical impedance, the good nutrient and aeration status in the repacked soil columns and to the inclusion of biopores of small diameter in the analysis. Root growth inside biopores was anecdotally observed. Visual analysis of the images showed that the propensity of roots to grow into biopores was higher when the angle at which roots and biopores touched was inferior to 45 degrees and when the root diameter was approximately equal to or inferior to the biopore diameter.

In summary, this thesis provides a broad analysis of root-soil interaction processes with the help of X-ray CT. Along with the pure scientific findings, this thesis presents new methodological approaches for the study of soil structure as well as root system architecture non-destructively.

ZUSAMMENFASSUNG

Das übergeordnete Ziel dieser Arbeit ist es, das Verständnis des Zusammenspiels zwischen Wurzelwachstumsmustern und Bodeneigenschaften durch den Einsatz der Röntgen-Computertomographie zu verbessern. Konkret soll in dieser Arbeit charakterisiert werden, wie das Fehlen von Wurzelhaaren die Architektur des Wurzelsystems von *Zea mays* L. beeinflusst und inwieweit dies von der Bodentextur (Lehm oder Sand) abhängt. Ein weiteres Ziel dieser Arbeit ist die Charakterisierung des Einflusses der Wurzeln von Zea mays L. auf die Lagerungsdichte der Rhizosphäre und inwieweit diese von der Bodentextur und dem Fehlen von Wurzelhaaren abhängt. Parallel dazu wird eine Modellierung vorgenommen, um die Auswirkung von Lagerungsdichtegradienten in der Rhizosphäre auf die Wasseraufnahmedynamik im Boden zu bewerten. Schließlich soll in dieser Arbeit charakterisiert werden, ob und unter welchen Umständen die Wurzeln von *Zea mays* L. den Boden leichter erschließen können, wenn Bioporen vorhanden sind.

Für die Analyse der Architektur des Wurzelsystems und wie diese durch die Bodentextur und das Fehlen von Wurzelhaaren beeinflusst wird, wurden *Zea mays* Wurzelhaardefekt-Mutanten (rth3) und der entsprechende Wildtyp unter gut bewässerten Bedingungen angebaut und die Architektur des Wurzelsystems mittels wiederholter Röntgen-CT-Scans untersucht. Für die Analyse der Lagerungsdichtegradienten in der Rhizosphäre wurden in Labor- und Feldexperimenten mehr als 400 Proben genommen, die verschiedene Kombinationen von Bodentextur, Lagerungsdichte, Strukturheterogenität, Maisgenotyp und Bodenfeuchtigkeit umfassten. Um der Frage nachzugehen, ob und unter welchen Umständen Wurzeln Bioporen wiederverwenden, wurde ein Bodensäulenexperiment durchgeführt, das darauf abzielte, den Grad des Bioporenrecyclings für zwei Bodentexturen (Sand und Lehm) und zwei Bodenlagerungsdichte zu charakterisieren. Zur Beantwortung der Forschungsfragen wurde eine Methode zur Segmentierung von Wurzeln aus 3D-Röntgen-CT-Bildern entwickelt.

Mit Hilfe der Röntgen-CT wurden Anpassungen der Architektur des Wurzelsystems, der Wurzelmerkmale und/oder der rhizosphärischen Eigenschaften als Reaktion auf Veränderungen der Bodentextur und -struktur identifiziert. Das Fehlen von Wurzelhaaren hatte keine oder nur geringe Auswirkungen auf die Ergebnisse. Der Unterschied in der Bodentextur und -struktur bewirkte (i) eine Anpassung des Wurzeldurchmessers (d. h., Wurzeln, die in Sand wuchsen, hatten durchweg einen größeren Durchmesser als in Lehm), (ii) eine Änderung des Wachstumswinkels der Wurzeln (d. h., Wurzeln, die in Lehm wuchsen, wuchsen eher in Richtung und gegen die Wand der Töpfe), (iii) Änderungen des Wurzelwachstums und der Dynamik des Wurzelwachstums (d. h., das Wurzelwachstum war im Labor in Lehm größer als in Sand,

im Feldversuch jedoch kleiner) und (iv) eine Veränderung der Umgebung für das Wurzelwachstum (unter Bedingungen mit heterogener Bodenstruktur, wie sie im Feld anzutreffen waren, wuchsen die Wurzeln bevorzugt in vorhandenen Poren, während die Wurzeln in einer homogenen Bodenstruktur, wie sie in den Bodensäulen anzutreffen waren, ihre eigenen Poren schaffen mussten). Diese Ergebnisse unterstreichen die Fähigkeit von *Zea mays* L., sich an seine Wachstumsumgebung anzupassen.

Bodentextur und -struktur beeinflussten nicht nur das Wurzelwachstum auf der Ebene der Pflanze (cm-dm), sondern auch die Interaktion der Wurzeln mit dem Boden auf der Ebene der einzelnen Wurzelsegmente (µm-mm). Tatsächlich beeinflusste das Wurzelwachstum die Bodenstruktur durch eine Umstrukturierung der Bodenpartikel in der Nähe der Wurzeln (< 1 mm von der Wurzeloberfläche). Am auffälligsten war die Entstehung einer Zone erhöhter Porosität an der direkten Schnittstelle zwischen den Wurzeln und dem Boden (< 250 µm von der Wurzeloberfläche). In Lehm und je nach vorheriger Bodenstruktur war der Boden hinter der Zone erhöhter Porosität (zwischen 250 µm und 1 mm von der Wurzeloberfläche) entweder verdichtet (bei homogener Bodenstruktur) oder locker (bei heterogener Bodenstruktur). Im Sand bewirkten feine Wurzeln (< 200 µm Durchmesser), dass sich die Sandkörner entlang der Wurzelachse ausrichteten, während grobe Wurzeln (> 350 µm Durchmesser die fragile Anordnung) der Körner durchbrachen. Diese Ergebnisse unterstreichen die große Fähigkeit der Wurzeln von *Zea mays* L., ihre Wachstumsumgebung zu verändern wobei diese Veränderung durch die Bodentextur und -struktur moduliert wird.

Um die Auswirkungen der durch die Wurzeln verursachten Umstrukturierung der Bodenpartikel auf die Wasseraufnahme der Wurzeln zu untersuchen, wurde eine Modellierungstudie durchgeführt. Die experimentellen Beobachtungen der Lagerungsdichtegradienten in der Rhizosphäre wurden zur Ableitung bodenhydraulischer Parameter in der Nähe der Wurzeln verwendet. Mit Hilfe eines Modells für die Wasseraufnahme durch die Wurzeln wurden die Auswirkungen der Lagerungsdichtegradienten in der Rhizosphäre und der Gradienten der Mucilagekonzentration bewertet. Während der Bodentrocknung führte eine geringere Lagerungsdichte der Rhizosphäre zu einem früheren Einsetzen von Wasserstress und zu einer verringerten Wasseraufnahme der Wurzeln, die länger anhält. Das Vorhandensein von Mucilage führte zu einer schnelleren Verringerung der Wasseraufnahme der Wurzeln. Die Wasseraufnahme der Wurzeln wurde rasch reduziert, wenn sowohl Mucilage als auch der Lagerungsdichtegradient der Rhizosphäre berücksichtigt wurden.

Das Wurzelwachstum beeinflusste auch die Bodenstruktur durch die Bildung eines Bioporen-Netzwerks, dessen Stabilität von der Bodentextur abhing. In Sand kollabierten viele Bioporen aufgrund der geringen Kohäsion zwischen den Sandpartikeln. Der Grad der Wiederverwendung von Bioporen in umgeschüttetem Lehm war um zwei Größenordnungen geringer als die in der Literatur angegebenen Werte. Dieser Unterschied wurde auf die niedrige mechanische Impedanz, den guten Nährstoff- und Belüftungszustand in den umgeschütteten Bodensäulen sowie auf die Einbeziehung von Bioporen mit kleinem Durchmesser in die Analyse zurückgeführt. Das Wurzelwachstum innerhalb der Bioporen wurde sporadisch beobachtet. Die visuelle Analyse der Bilder zeigte, dass die Neigung der Wurzeln, in die Bioporen hineinzuwachsen, größer war, wenn der Winkel, in dem sich Wurzeln und Bioporen trafen, weniger als 45 Grad betrug und wenn der Wurzeldurchmesser ungefähr dem Bioporendurchmesser entsprach oder kleiner war als dieser.

Zusammenfassend bietet diese Arbeit eine umfassende Analyse der Wurzel-Boden Interaktionsprozesse mit Hilfe der Röntgen-CT. Neben den rein wissenschaftlichen Erkenntnissen werden in dieser Arbeit neue methodenlogische Ansätze zur zerstörungsfreien Untersuchung der Bodenstruktur sowie der Architektur des Wurzelsystems vorgestellt.

CONTENTS

LIST OF FIGURES

LIST OF TABLES

ACRONYMS & ABBREVIATIONS

ADT **A**bsolute **D**ifference **T**ransform.

BD **B**ulk **D**ensity.

BLD **B**iopore **L**ength **D**ensity.

BRF **B**iopore **R**ecycling **F**raction.

CT **C**omputed **T**omography.

DAP **D**ays **A**fter **P**lanting.

DS **D**estructive **S**ampling.

EDT **E**uclidian **D**istance **T**ransform.

GV **G**ray **V**alue.

L **L**oam.

NCP **N**umber of **C**ontact **P**oints.

NLM **N**on-**L**ocal **M**eans.

RDH **R**oot **D**istance **H**istogram.

RLD **R**oot **L**ength **D**ensity.

ROI **R**egion **O**f **I**nterest.

RSA **R**oot **S**ystem **A**rchitecture.

RVF **R**hizosphere **V**olume **F**raction.

S **S**and.

US **U**ndisturbed **S**ampling.

WR **W**in**R**HIZO.

WT **W**ild-**T**ype.

CHAPTER *1*

INTRODUCTION

1.1 Scope of the thesis

1.1.1 Plants, one of the key actors in terrestrial ecosystems

Plants can be considered as one of the big winners of evolution and as one of the most complex living organisms of our terrestrial ecosystems. Over hundreds of millions of years, they have colonized every continent and have acquired very different shapes and sizes to adapt to their environment. At the global scale, they play a major role in the regulation of fluxes of heat, water, carbon and nutrients (Jasechko et al., 2013; Jobbágy & Jackson, 2004), which contributes to shaping the planet Earth as we know it today. The ability of plants to evolve and adapt to environmental conditions is, in part, conferred to them by their extremely adaptable underground organs: the **roots**.

As a result of their genetic heritage and their ability to respond to external stimuli, plant roots explore the soil volume in the quest for nutrients and water, thereby defining the spatial and temporal configuration of the root system, i.e., the **root system architecture** (RSA). The RSA of plants is very complex and is, for a given plant species, highly variable during its life cycle. On top of the internal genetic program associated to the development of the RSA, the RSA is also the result of the ability of the root system to exhibit some degree of plasticity, i.e., to favor root growth in sites where environmental conditions are favorable (Blaser et al., 2020; Fransen et al., 1998; Hodge, 2004). The expression of root plasticity depend strongly on the spatial distribution of soil properties, which are known to be very heterogeneous and anisotropic. Such soil properties can be physical (e.g., porosity, hydraulic conductivity, water content), chemical (e.g., pH, cation exchange capacity, organic matter content) or biological (e.g., the presence of pathogens or symbiotic fungi).

In a world where the scarcity of nutrients and water is continuously increasing, there is common view of plant physiologists and plant breeders that understanding the RSA response of crops to abiotic stresses and soil conditions may be the key to further increase yield without increasing land pressure (de Dorlodot et al., 2007; Lombardi et al., 2021). Since the RSA determines the extent of the region of the soil where water and nutrients can be taken up by the roots and utilized by the plant, breeding crops with an optimal root system architecture may constitute a solution to limit fertilizer input and increase water use efficiency, both of them may contribute to negating the effect of climate change (Uga, 2021; Wu et al., 2018). The study of the RSA of crops and its response to environmental factors is now more than ever a topic which deserves much attention by the scientific community.

In their toolbox for resource acquisition and adaptation to environmental conditions, plant roots possess a secret weapon: the **root hairs**. Roots hairs are cylindrical extensions of root epidermal cells, which develop 4 to 5 cm away from the root tip (Figure 1.1a). These tiny organs usually have a diameter between 5 to 20 µm and can extend from 0.1 up to 1.5 mm from the root surface (Figure 1.1b) (Gregory, 2008).
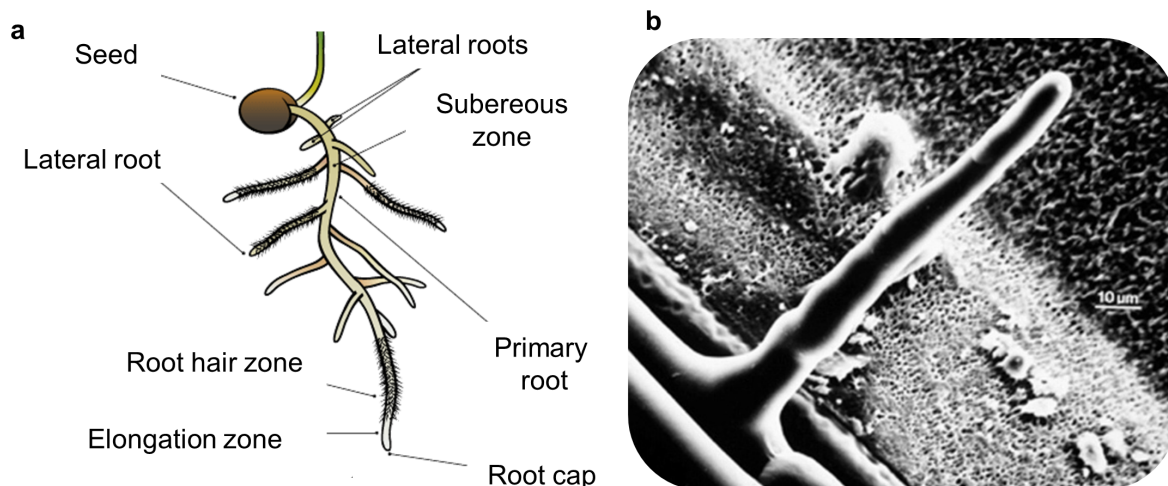
Figure 1.1: Schematic of the root system of an angiosperm where the location of the root hair zone on a root segment is depicted (subfigure a). Image modified from the portal "Formation en ligne de biologie végétale". Scanning electron micrograph of a root hair cell (subfigure b). Image from Grierson et al. (2014).

The development of root hairs, root hair density, activity and lifetime span has been shown to be a function of environmental conditions such as available phosphorus content in soil (T. Bates & Lynch, 1996; Z. Ma et al., 2001). Despite their relatively short lifetime span (i.e., 2 to 3 days according to Beck et al. (1989)), the roles of the root hairs for plant functions are numerous and diverse. Root hairs are thought to drastically increase the root surface area and effectively increase the root diameter (Grierson et al., 2014), thereby substantially contributing to the acquisition of soil nutrients, mainly of those of low mobility in soil and high demand in plants (Jungk, 2001). Moreover, it was shown that root hairs can help stimulating the establishment of synergistic interactions with micro-organisms (Fåhraeus, 1957), trigger the formation of the rhizosheath (Haling et al., 2014) and support the anchorage of the plant (Bailey et al., 2002; Bengough et al., 2016). Despite the important advancements in the field of research of root hairs and

their functions, little is known still about the influence of root hairs on the root system architecture and to which extent they influence the soil in their vicinity. A more detailed investigation of the function of root hairs is now possible utilizing root hair mutants, e.g., plant genotypes whose genes responsible for the initiation and/or elongation of root hairs have been knocked out. Such root hair mutants can be directly compared with their homologous root hairs bearing genotypes. In doing so, the question arises whether roots compensate the lack of hairs by investing energy in other root traits, e.g, an increased growth of fine roots to compensate for a reduced uptake ability.

1.1.2   A critical interface: the rhizosphere

The soil constitutes one of the most complex material on Earth. It is the result of the weathering of rocks and minerals, and can have diverse properties depending on the origin of the parent material, the climate and the vegetation under which it developed. Plant roots have developed an intimate relationship with the soil, which provides the roots with anchorage as well as a storage of water and nutrients required for plant growth. At the interface between the roots and the soil, a critical zone exists: the **rhizosphere**. The rhizosphere is the zone of soil in the vicinity of the roots, which is influenced by them and which has different properties than the soil farther away from the roots, i.e., the bulk soil (definition given by Hiltner (1904), see also Hartmann et al. (2008)).

Rhizosphere properties can differ from bulk soil in terms of physical properties, e.g., bulk density (Helliwell et al., 2017; Lucas et al., 2019), pore size (Koebernick et al., 2019), porosity (Bruand et al., 1996) and pore morphology (Whalley et al., 2005), all of which are know to alter water and gas regimes in soil. Differences in chemical properties such as pH (Bravin et al., 2009; Nye, 1981), redox state (Fischer et al., 1989; Rudolph-Mohr et al., 2017) and nutrient content (Gahoonia & Nielsen, 1991; Jungk, 2001; van Veelen et al., 2020) were also observed between the rhizosphere soil and the bulk soil. Soil biological parameters in the rhizosphere are also affected by the presence and activity of roots. This can be reflected in changes in enzymes activities (Razavi et al., 2016) as well as microbial community composition (Kandeler et al., 2002; Rüger et al., 2021).

Considering the interactions between all of the above-mentioned properties, the rhizosphere is regarded as one of the most complex component of terrestrial ecosystems and biogeochemical cycles (Hinsinger et al., 2009). In addition, since soil water and nutrients taken up by the plants have to traverse the rhizosphere before entering the root tissues, the rhizosphere is considered to be the critical interface which governs plant productivity and, consequently food, fuel and fiber production. Understanding and engineering rhizosphere properties may then well be the key to promoting sustainable agriculture and negating the effect of climate change (Ahkami et al., 2017; Ryan et al., 2009). Engineering rhizosphere properties may open new avenues for crop production management and contribute to limiting the input of mineral fertilization and increase the water use efficiency of crops (Ahmed et al., 2018).

1.1.3 X-ray CT: a game changer for root-soil interactions studies

The investigation of the RSA, the rhizosphere and root-soil interactions in general is hampered by the fragile and opaque nature of the soil. The technical difficulties associated with the extraction of an intact root system are manifold and, since analyzing the root system of a plant growing in soil leads to the disturbance of the soil matrix itself, the resulting RSA may be impacted by any measuring or sampling operations. Due to that, the investigation of the RSA is also cumbersome since a lot of biological replicates are required in order to increase the chance of capturing meaningfully and representatively the investigated phenomenon. As a result, the scientific knowledge on the processes occurring in soil and how these processes affect the RSA is somewhat fragmented (Mooney et al., 2012).

Since the beginning of the 90´s, the development of **X-ray computed tomography** (CT) technologies has paved new ways for the investigation of root-soil interactions processes and could be considered as a game changer. Thanks to its ability to see the internal structures of opaque objects in 3D with high resolution (i.e., down to the micrometer scale), X-ray CT has now diverse applications in various disciplines of geological sciences (Cnudde & Boone, 2013; Mees et al., 2003). For plant and soil scientists specifically, X-ray CT may constitute the "Holy Grail" as it enables to visualize root growth in soil non destructively (Figure 1.2).
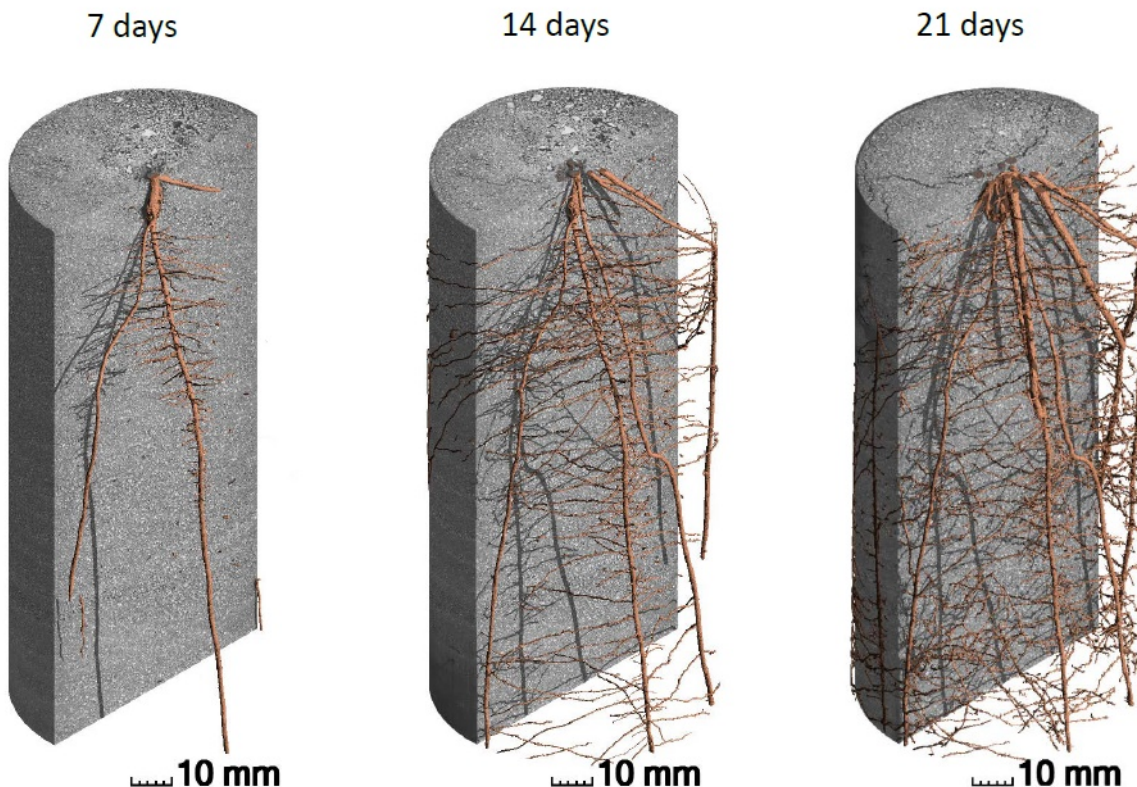
Figure 1.2: Root system architecture development of Zea mays L. in a repacked loamy soil over the course of 21 days of growth. The images were acquired with X-ray CT and segmented with the Rootine v.2 algorithm (Phalempin et al., 2021a).

The principles of X-ray CT images acquisition are based on the phenomenon of absorption and scattering of emitted rays. In short, X-ray beams are passed through the scanned sample and a fraction of the X-rays is either absorbed or scattered by its internal structures. The remaining X-rays transmitted to a panel detector, which comprises a layer of scintillating material, responsible for the conversion of X-rays into light. During the scanning of a sample, many shadow images (also called "projections") are acquired as the analyzed sample rotates on its stage. These projections are then digitally stacked together through a process called "reconstruction". The result is a graylevel image, in which the intensity of the gray values is directly related to the density and the attenuation coefficient of the material which constitutes the sample. In a typical X-ray CT image of a soil sample, pore voxels exhibit a low gray value whereas denser objects such as soil aggregates or sand grains appear brighter (Figure 1.3).
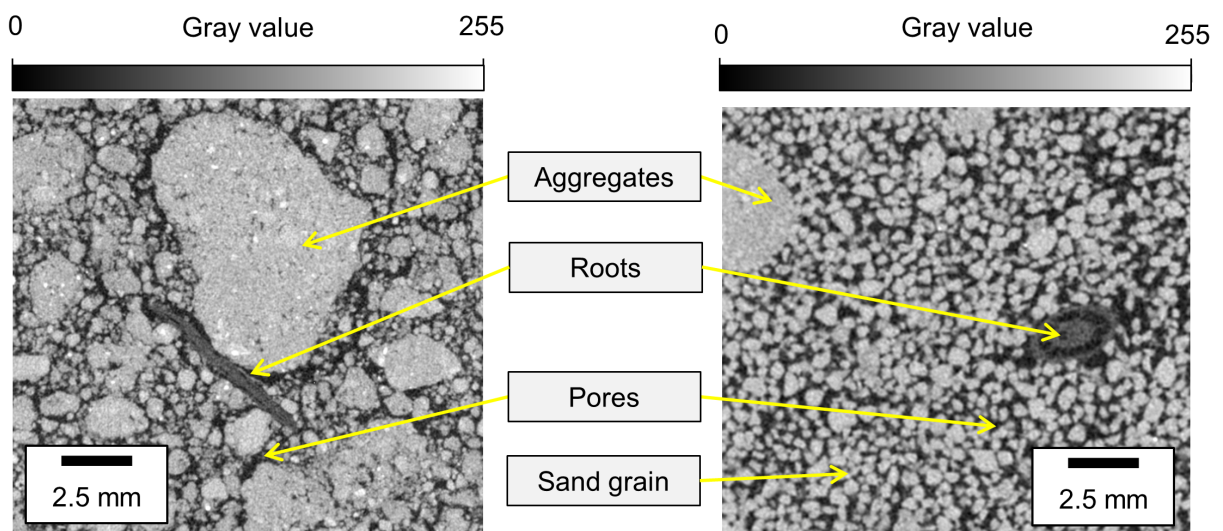
Figure 1.3: Two-dimensional cross sectional images acquired with X-ray CT for a loam (left) and a sand (right) substrate. The arrows point to typical features observed in soil samples scanned with X-ray CT, e.g., aggregates, sand grains, roots and pores. The image resolution is 25 µm for both images.

On many occasions, a prerequisite for the study of RSA, rhizopshere and/or root-soil interactions processes based on X-ray CT images is **root segmentation**. Root segmentation is the process during which all background voxels (e.g., aggregate and pore voxels) and root voxels are binarized. Root segmentation is often considered difficult as its success depends on the sufficient contrast in X-ray attenuation between soil particles, air filled pores, water filled pores, plant material and particulate organic matter (Mooney et al., 2012). On top of the difficulties associated with contrast, there is inherent trade-off between the size of the scanned sample and the image resolution. Practically, the bigger the sample size, the coarser the resolution. On figure 1.4, it is easy to notice the decrease in level of details of the image with a decreasing resolution and how this affects the ability to see roots. As a consequence, the trade-off between sample size and image resolution sometimes lead to a poor root recovery, i.e., roots cannot be detected when their diameter is smaller than the image resolution. In order to capture the complete root system during root segmentation, practicians are then forced

to analyze small samples or to constrain root growth in small pots. In turn, growing plants in small pots inherently introduce artifacts in the root system architecture as roots tend to grow towards the wall of the pot and are deflected downward upon hitting it (Figure 1.2).
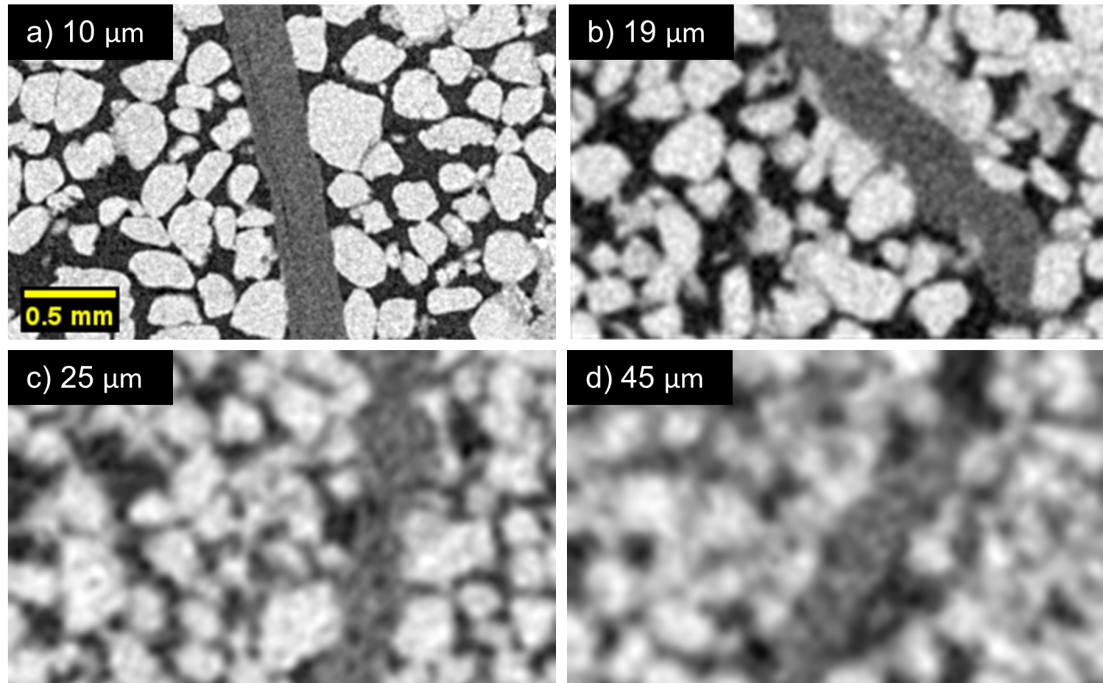
Figure 1.4: Relationship between the sample size and the image resolution for four samples extracted from a sandy soil scanned at a resolution of 10 µm (sample diameter of 16 mm, subfigure a), 19 µm (sample diameter of 30 mm, subfigure b), 25 µm (sample diameter of 50 mm, subfigure c) and 45 µm (sample diameter of 70 mm, subfigure d). The legend of subfigure a is valid for all other subfigures. Note the decrease in level of details of the image with a decreasing resolution and how this affects the ability to see the roots.

Despite the major advancements in the field, root segmentation is still viewed as one the most challenging computer vision problem in the discipline of plant sciences (Douarre et al., 2018). The associated challenges of root segmentation has made the development of algorithms an ever growing field. Since the last ten years, this development has brought about many segmentation algorithms, e.g., RooTrak (Mairhofer et al., 2012), Root1 (Flavel et al., 2017), SegRoot (T. Wang et al., 2019), Rootine (Gao, Schlüter et al., 2019), just to name of few. Every algorithm has its specific field of application and limitations. The increase in performance of root segmentation methods is a necessity to expand the knowledge on RSA response under different growth conditions.

1.2 Context and objectives

This thesis was carried out in the framework of the priority programme 2089 "Rhizosphere spatiotemporal organization — a key to rhizosphere functions" funded by the

German Research Foundation (project number 403801423). Having a special focus on imaging techniques (X-ray CT, among others), the main goal of this research project is to unravel the mechanisms influencing the rhizosphere spatiotemporal organization, at various scales. Specifically, the research project aims at assessing the impact of soil texture and the influence of root hairs on various parameters of the root system architecture and rhizopsphere properties. In that respect, the suggested guidelines include the systematic study of two *Zea mays* L. plant genotypes, i.e., a root hair defective (rth3) and its corresponding root hair bearing genotype (WT). The impact of the soil texture is investigated via the systematic use of two different substrates, i.e., a loam and a sand. To investigate various scales and differing conditions, laboratory as well as field experiments are carried out. For more information on the priority programme 2089, the reader is referred to the two introductory research articles by Vetterlein et al. (2020) and Vetterlein et al. (2021).

In line with the research program suggested by the priority program 2089, the overarching goal of this thesis is to improve the understanding of the interplay between root growth patterns and soil properties, at different spatial scales. This should be achieved by relying on X-ray CT as a central tool. In order to reach this overarching goal, the following specific research questions were considered:

1. What is the impact of the absence of root hairs on the root system architecture, and to which extent is this impact influenced by soil texture?

2. Does the soil in the vicinity of roots have different structural properties than the soil farther away? if yes, how is this influenced by soil texture and the presence of root hairs?

3. If differences in rhizosphere structure properties exists, what is the influence of these differences on the root water uptake dynamics? How is this influenced by the presence of mucilage concentration gradients, soil texture and soil bulk density?

4. To which extent do roots benefit from existing pores to ease their exploration of the soil? Specifically, under which conditions do roots reuse old root channels (i.e., biopores)? How is the reuse of biopores depending on soil texture and soil bulk density?

Prior to addressing these research questions, a methodological challenge had to be overcome. Indeed, an improved root segmentation algorithm had to be developed. The development of the new method was necessary in order to facilitate the analysis of the X-ray CT generated dataset and to increase the accuracy of the obtained results. The new segmentation method (or slightly modified versions of it) should be used as a central tool of this thesis.

1.3   Outline

This thesis is compiled in the form of a cumulative dissertation and is articulated in seven chapters. Besides the introduction (chapter 1) and the conclusion (chapter 7),

each chapter aims at providing answers to the previously enunciated research questions. These five chapters have been published (four out of five) or are submitted (one out of 5) in international and peer-reviewed journals. Only minor adaptations were made to the manuscripts in order to harmonize the style of writing throughout the thesis. The supplementary materials of each manuscript are provided in the appendix. A common list of references is also provided in the bibliography. The publications used in this thesis are listed below.

Chapter 2 Phalempin, M., Lippold, E., Vetterlein, D., Schlüter, S. An improved method for the segmentation of roots from X-ray computed tomography 3D images: Rootine v.2. Plant Methods 17, 39 (2021). doi: `https://doi.org/10.1186/s13007-021-00735-4`.

Chapter 3 Lippold, E., Phalempin, M., Schlüter, S., Vetterlein, D. Does the lack of root hairs alter root system architecture of Zea mays?. *Plant Soil*. doi : `https://doi.org/10.1007/s11104-021-05084-8`. Shared first authorship.

Chapter 4 Phalempin, M, Lippold, E, Vetterlein, D, Schlüter, S (2021). Soil texture and structure heterogeneity predominantly governs bulk density gradients around roots. Vadose Zone J. 1-17. doi : `https://doi.org/10.1002/vzj2.20147`.

Chapter 5 Landl M, Phalempin M, Schlüter S, Vetterlein D, Vanderborght J, Kroener E and Schnepf A (2021) Modeling the Impact of Rhizosphere Bulk Density and Mucilage Gradients on Root Water Uptake. Front. Agron. 3:622367. doi: `https://doi.org/10.3389/fagro.2021.622367`. Shared first authorship.

Chapter 6 Phalempin M, Landl M, Wu G-M, Schnepf A, Vetterlein D, Schlüter S. (submitted to Soil & Tillage Research on the 23.10.2021). Maize root-induced biopores do not influence root growth of subsequently grown maize plants in well aerated, fertilized and repacked soil columns.

To conclude this introductory chapter, short and concise summaries of each chapter are shown in figure 1.5 in order to provide the reader with a synoptic view of the content of this thesis. After the present introduction, the chapter 2 focuses on the description of the newly developed root segmentation algorithm. Chapter 3 then addresses the influence of root hairs and soil texture on RSA. These two chapters deal with the analysis of whole column X-ray CT scans such as the one shown in figure 1.2. For the subsequent chapters, a change of scale is considered and a finer resolution is achieved thanks to the analysis of smaller subsamples, extracted either from the field experiment or from columns such as the ones considered in chapter 3. Chapter 4 has a focus on rhizosphere soil structure properties. Based on the results described in chapter 4, a modeling exercise is carried out in chapter 5 in order to evaluate the effect of considering rhizosphere soil structure properties on the dynamics of root water uptake. Finally, chapter 6 aims at evaluating whether roots reuse old root channels, thereby benefiting from antecedent soil structure to ease their ingression into the soil.

	Chapter 2	Chapter 3	Chapter 4	Chapter 5	Chapter 6
Objective	Develop of a root segmentation method with a higher accuracy than Rootine v.1.	Understand the impact of root hairs and soil texture on the root system architecture of *Zea mays* L.	Characterize bulk density gradients around roots and the influence of soil heterogeneity.	Evaluate the effects of bulk density and mucilage concentration gradients on soil water dynamics.	Quantify the degree of biopores recycling and how it is affected by soil bulk density and texture.
Method	• Segmentation was done on a dataset of *Zea mays* L., in a scenario with a high or a low soil heterogeneity and signal to noise ratio. • Results of Rootine v.1 and the new method were compared with WinRhizo.	• "Wild-type" *Zea mays* L. and its corresponding hairless mutant "rth3" were grown in repacked loam and sand under fertilized and well watered conditions. • X-ray CT scanning was performed to study RSA over time.	• More than 400 samples were extracted in field and laboratory experiments in which soil structure, texture, plant genotype, soil water status varied greatly. • Samples were scanned with X-ray CT.	• Pedotransfer functions were used to derive soil hydraulic properties as a function of the distance from the root surface. • Set-up of a 1D root water uptake model and simulation of a drying experiment.	• A novel method based on the repeated X-ray CT scanning of soil samples and co-registration of the images was developed. • Biopore recycling was studied *in silico* with the root growth model "CPlantBox"
Key results	• In a worse case scenario, the new method recovered 44% more roots than v.1 and enabled to better match the diameter distribution. • More than half of the added root was attributed to a new step of false negatives recovery.	• Root diameter was bigger in sand than in loam. • Root growth was higher in loam than in sand. • Shoot growth was lower in loam than in sand. • Compensation for the lack of root hairs was not found.	• In repacked loam, roots induced compaction of the deformable loam aggregates • In structured loam, roots grew in existing pores. • In sand, fine roots aligned rigid grains along their axis. Big roots pushed away the grains further than their own diameter.	• The interfacial gap between the root and the soil had a stronger effect on water uptake than the root-induced compaction • Rhizosphere bulk density and mucilage gradients led a smaller transpiration rate of 5 to 8 %, as compared to a control treatment.	• *In silico* and *in vivo*, roots were piercing through the biopores rather than growing into them. • Biopores were collapsing in sand, whereas they were stable in loam. • Roots degraded quicker in loam as compared to sand.
Conclusion	Rootine v.2 facilitates higher root segmentation accuracy and comprises less parameters than its preceding version.	The RSA of *Zea mays* L. is affected more by substrate than by root hairs.	Soil texture and structure predominantly governs bulk density gradients around roots.	Gradients in rhizosphere bulk density and mucilage concentration sustain transpiration at a lower level.	Maize roots do not grow into biopores in repacked, well aerated and fertilized soil with low mechanical impedance

Figure 1.5: Synoptic view of the content of this thesis.

CHAPTER *2*

AN IMPROVED METHOD FOR ROOT SEGMENTATION OF X-RAY CT 3D IMAGES

X-ray computed tomography is acknowledged as a powerful tool for the study of root system architecture of plants growing in soil. In this paper, we improved the original root segmentation algorithm "Rootine" and present its succeeding version "Rootine v.2". In addition to gray value information, Rootine algorithms are based on shape detection of cylindrical roots. Both algorithms are macros for the ImageJ software and are freely available to the public. New features in Rootine v.2 are (i) a pot wall detection and removal step to avoid segmentation artifacts for roots growing along the pot wall, (ii) a calculation of the root average gray value based on a histogram analysis, (iii) an automatic calculation of thresholds for hysteresis thresholding of the tubeness image to reduce the number of parameters and (iv) a false negatives recovery based on shape criteria to increase root recovery. We compare the segmentation results of Rootine v.1 and Rootine v.2 with the results of root washing and subsequent analysis with WinRHIZO. We use a benchmark dataset of maize roots (*Zea mays* L. cv. B73) grown in repacked soil for two scenarios with differing soil heterogeneity and image quality. We demonstrate that Rootine v.2 outperforms its preceding version in terms of root recovery and enables to match better the root diameter distribution data obtained with root washing. Despite a longer processing time, Rootine v.2 comprises less user-defined parameters and shows an overall greater usability. The proposed method facilitates higher root detection accuracy and has the potential for improving high-throughput root phenotyping procedures based on X-ray computed tomography data analysis.

2.1   Introduction

X-ray computed tomography (CT) is acknowledged as a powerful tool for the study of root system architecture of plants growing in soil. However, the study of the root system architecture is only possible after performing root segmentation, i.e., the binarization of the grayscale data into root voxels and background voxels. Root segmentation is often regarded as a tedious and difficult task as its success depends on several factors such as the image resolution, the signal-to-noise ratio during image acquisition and the gray value (GV) contrast between the roots and all other surrounding features in soil (Mooney et al., 2012).

In the past years, many methods have been developed to segment and visualize roots in tomograms acquired with X-ray CT (Blaser et al., 2020, 2018; Flavel et al., 2017, 2012; Gao, Schlüter et al., 2019; Gerth et al., 2021; Koebernick et al., 2014; Kuka et al., 2013; Maenhout et al., 2019; Mairhofer et al., 2012; Mooney et al., 2012; Pfeifer et al., 2015; Soltaninejad et al., 2020; Tabb et al., 2018; Teramoto et al., 2020; Xiong et al., 2020). Some algorithms rely on simple thresholding methods (Kuka et al., 2013). With these methods, the roots are segmented based on a histogram analysis and a GV criterion. These methods usually fail at segmenting roots properly because of the overlapping GV of roots, water, organic matter and the soil matrix. The GV at the edges of roots, water, organic matter and soil matrix also show gradual changes of intensity spanning several voxels rather than a crisp intensity step (Schlüter et al., 2014). This effect, known as the "partial volume effect", is also responsible for poor segmentation results when using simple thresholding methods. More advanced thresholding methods rely on the use of adaptive local thresholding values (also referred to as "Region growing"), which use an additional connectivity criterion to binarize the root and background voxels (Blaser et al., 2018).

For both the simple and the adaptive thresholding methods, there is an inherent trade-off to be made by the user. If the GV range assigned to roots bounded by two thresholds is too broad, over-segmentation may occur (i.e., segmented root edges extend into the surrounding features and appear frayed) and the false positives need to be removed through user-interaction, which is a subjective, tedious and time-consuming task. Inversely, if the GV range is too narrow, an important loss of roots may occur which biases the root system architecture analysis of the scanned sample. To tackle the issue of overlapping GV of roots and other materials, root tracking methods such as the "RooTrak" algorithm have been developed (Mairhofer et al., 2012). With this method, the volumetric data is viewed as a sequence of X-Y cross-sectional images aligned along the Z axis. As the 3D stack is explored, root cross sections appear to move in the image and such "movements" can be used to reconstruct the root system. Methods relying on deep-learning algorithms and multi-scaled based approaches have also recently been applied for the segmentation of roots in X-ray CT images. Promising applications of deep learning for the segmentation of roots from X-ray CT data were recently demonstrated by Soltaninejad et al. (2020).

Gao, Schlüter et al. (2019) proposed a new algorithm to segment root systems growing in soil by exploiting a typical morphological characteristic of the roots, i.e., their cylindrical shape. This approach was first introduced for vessel detection in medical imaging (Frangi et al., 1998). The vessel enhancement filter was later adopted to segment roots in 3D Magnetic Resonance Imaging data (Schulz et al., 2013). The rationale

of this method is that the cylindrical shape of roots is unique among all materials and features found in soil. The shape-based semi-automated algorithm is named "Rootine" (Gao, Schlüter et al., 2019) and has shown to outperform the "Root1" (Flavel et al., 2017) and "Region growing" (Blaser et al., 2018) methods in terms of root recovery and segmentation accuracy. This demonstrated promising future applications of the algorithm for high-throughput root phenotyping based on X-ray CT data analysis. However, the Rootine algorithm relies on a substantial number of parameters to be calibrated by the user. Moreover, Rootine suffers from the fact that some of the parameters and their effects are difficult to identify and to interpret by a non-experienced user.

In this paper, we aim at developing an improved method for the segmentation of roots from 3D X-ray CT images that overcomes the aforementioned drawbacks of Rootine. The objectives of this work are then to develop a new Rootine version (i.e., "Rootine v.2") for which the segmentation accuracy and the user friendliness are increased. Specific objectives are to propose a second version in which (i) the root recovery is higher, (ii) the segmented root diameters are better captured, (iii) segmentation artifacts are reduced, (iv) the number of tunable parameters is reduced and (v) the parameters are related to root properties (i.e., their GV, shape and connectivity).

The ability of the new segmentation algorithm to fulfill these criteria is evaluated by systematic comparison with the former algorithm Rootine (which will be referred to as "Rootine v.1") and the results obtained by conventional, destructive root sampling and analysis of the washed-off roots with the software WinRHIZO. In addition, a comparison between both algorithms is made by considering aspects such as the runtime and the overall usability of the algorithms. In that respect, the benchmark dataset of the "worse case" scenario presented in Gao, Schlüter et al. (2019) is used. This benchmark dataset was chosen to test Rootine v.2 as it presents several challenges to overcome, namely a high soil heterogeneity, a poor quality of the images (i.e., a low number of projections during image acquisition) and a rather low image resolution as compared to the diameter of the roots to segment. The two first challenges contributed to a deterioration of the signal-to-noise ratio whereas the third exacerbates the partial volume effect at the edges of the fine roots. In the study of Gao, Schlüter et al. (2019), these challenges led to a rather low root recovery of Rootine v.1 (i.e., 29 %) in comparison with conventional root sampling. These challenges combined make the benchmark dataset of Gao, Schlüter et al. (2019) a perfect candidate for further testing and improvements of root segmentation algorithms.

In order to show that the improvements in segmentation quality are not solely due to an overfitting of Rootine v.2 for this particular dataset, we also demonstrate the performance of the new version on the so called "best case" scenario dataset of Gao, Schlüter et al. (2019). In this "best case" scenario, the soil and the scan settings were chosen in order to create low soil heterogeneity and a high signal-to-noise ratio. Those two aspects contributed to a robust estimation of root length (i.e., 99 % of recovery) in comparison with root washing and analysis with WinRHIZO. Finally, a 3D visual comparison of the results obtained with Rootine v.2, Rootine v.1, Root1 and the region growing method available in VG Studio Max 2.1 is provided for a small test cube image of the worse case scenario.

2.2   Material and Methods

2.2.1   Plant growth conditions and destructive sampling

Maize plants (*Zea mays* L. cv. B73) were grown in repacked soil sieved down to 2 mm particle size. The plants were grown in a climate chamber for 21 days in cylindrical containers of 7 cm inner diameter and 23 cm height. Six plants were analyzed for each scenario. One day after X-ray CT scanning, the plants were harvested and the pots were cut in several layers of 4 cm. The roots in those layers were washed off with deionized water and stored in a 50% ethanol solution prior to analysis. In order to assess root length density (RLD) for each layer, root samples were scanned with a flatbed scanner (EPSON perfection V700) and the obtained images were analyzed with WinRHIZO Pro (Version 2019a, Regent Instruments, Canada). In total, twelve layers were investigated for each scenario (i.e., two per growing pot, one at the top and one at the bottom). For detailed information on the plant growth conditions and the destructive root sampling method, the reader is referred to Gao, Schlüter et al. (2019).

2.2.2   Workflow of Rootine v.2

The workflow of Rootine v.2 is synoptically shown in figure 2.1 where the novelties of the algorithm are highlighted in blue and the steps and/or parameters that were modified from the original Rootine v.1 are shown in purple.

Image acquisition   3D X-ray CT images were acquired and reconstructed into an 8-bit grayscale 3D tomogram having a voxel size of 45 µm. The 8-bit conversion allows saving space without considerable loss of information. During the 8-bit conversion, contrast was optimized using a percentile stretching method, i.e., 0.2 % of the darkest and brightest voxels are set to 0 and 255, respectively. A linear stretching is applied for all GV between 0 and 255. Considering the geometry of the panel detector of the X-ray CT device (X-TEK XTH 225, Nikon Metrology), pots were scanned at two depth intervals (i.e., a bottom and top depth) making sure that an overlapping region was present. For more information regarding the image acquisition procedure, the reader is here again referred to Gao, Schlüter et al. (2019).

Preprocessing   Before concatenation of the bottom and the top images, the overlapping regions in both scans are removed using the "Slice remover" function available in the free software ImageJ (Schindelin et al., 2012). After concatenation, the obtained image comprises 3000 voxels in the Z dimension, 1750 voxels in the X and Y dimension and has a size of approximately 8.6 GB. The vertical extent of the stack is 13.5 cm. At the boundary of the two stitched images in the concatenated stack, a GV discontinuity is present due to an illumination drift caused by the X-ray CT hardware (see figure S2 by Gao, Schlüter et al. (2019)). This GV discontinuity is corrected for using the "Attenuation correction" plugin (Biot et al., 2008) in ImageJ. This correction applies a linear transformation of GV to each slice of the stack in order to make the average and standard deviation of the background constant and equal to that of a reference slice throughout the stack (Biot et al., 2008). Note that this GV discontinuity is specific
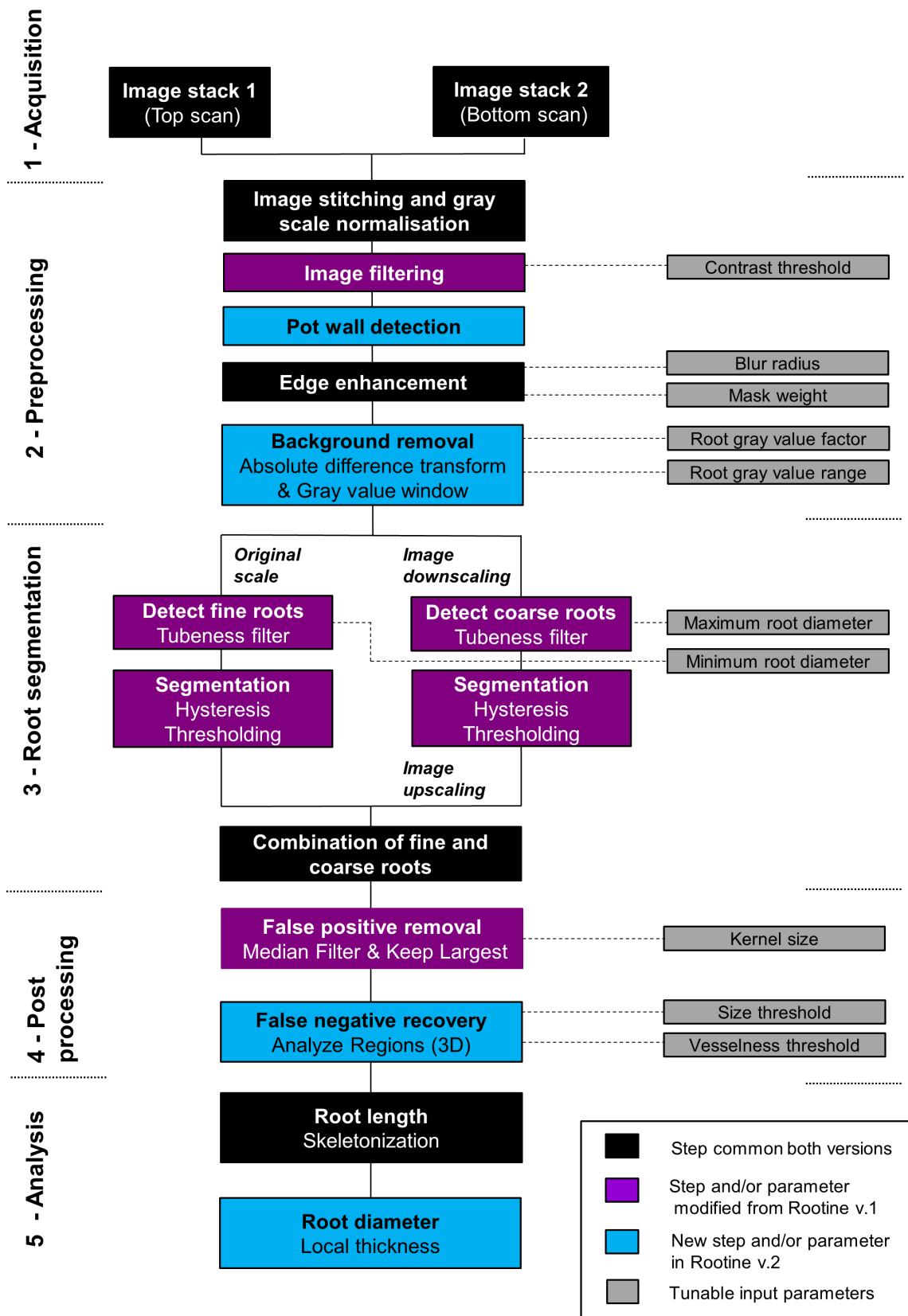
Figure 2.1: *Synoptic view of the Rootine v.2 workflow including the comparison with Rootine v.1.*

to the X-ray CT hardware used in the benchmark dataset of Gao, Schlüter et al. (2019) and that this step might not be necessary with other set-ups.

Once the GV discontinuity of the stitched stack is corrected for, a filtering step is performed with a "3D Non-local Means (NLM)" filter (Tristán-Vega et al., 2012). This filtering step is performed with a plugin available in the ITK library (McCormick et al., 2014). This filter was chosen as it is fast (Tristán-Vega et al., 2012) and can easily be incorporated in the workflow thanks to its standalone application. Note that in contrast to Gao, Schlüter et al. (2019) (see figure S3 by Gao, Schlüter et al. (2019)), we converted the images to 16-bit and added a constant GV offset of 50000 to avoid the change of contrast inherent to the use of this filter. The change in contrast is an outcome of the Rician noise model implemented in this filter (Tristán-Vega et al., 2012) as it was originally implemented for Magnetic Resonance Imaging. Avoiding the non-linear contrast enhancement for the low attenuation materials makes the results directly comparable to other softwares implementing a 3D NLM filter (e.g., Avizo™). The strength of filtering is determined by the parameter "Contrast threshold" (t_{con}) which needs to be given by the user as an input parameter. It is adjusted to the standard deviation of the image noise assessed by histogram analysis. Similarly to Gao, Schlüter et al. (2019), the remaining parameters of the 3D NLM filter were set to default. The result of the 3D NLM filtering can be assessed by comparing the original grayscale data (Figure 2.2a) and the filtered image (Figure 2.2b) for a subvolume of the worse case scenario.
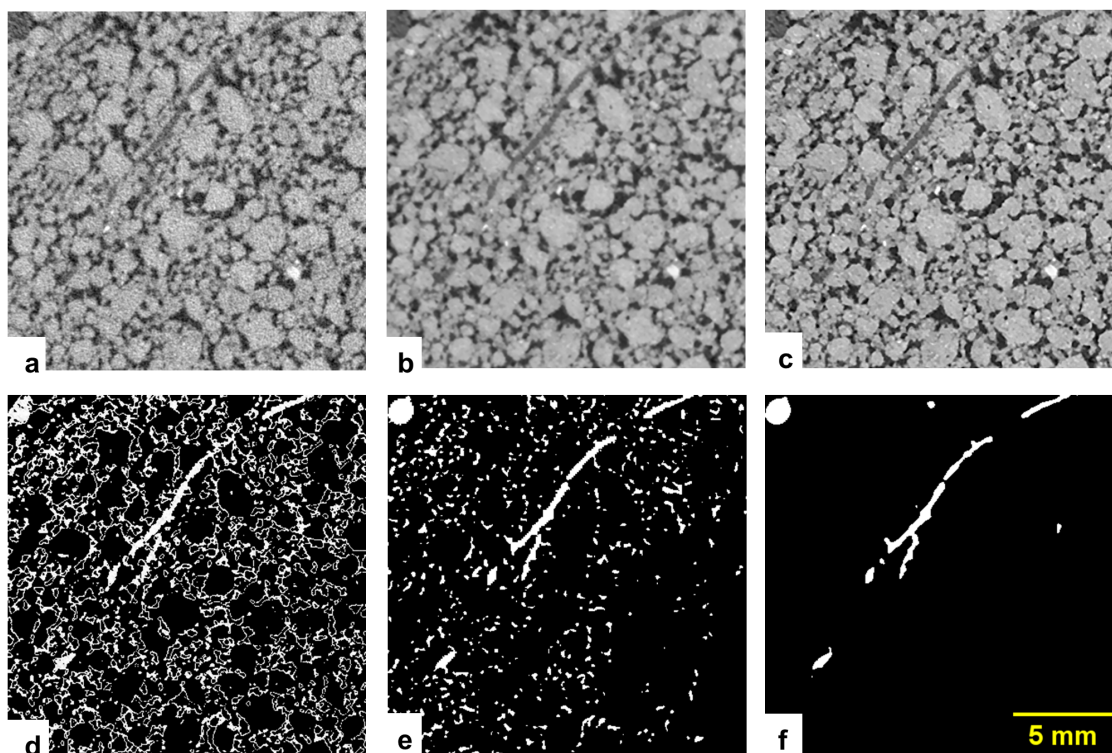
Figure 2.2: Results of the steps of Rootine v.2 for a subvolume of the worse case scenario. (a) The original grayscale image; (b) The obtained image after denoising with the 3D NLM filter; (c) The obtained image after performing edge enhancement of subfigure b; (d) Resulting image after background removal with ADT on subfigure c; (e) Results of the root segmentation applied on subfigure d before applying postprocessing steps; (f) Segmented roots after applying the postprocessing steps on subfigure e.

Rootine v.2 features a new pot wall detection step. This step serves two purposes. The first purpose is to create a mask which excludes the pot wall from the data to segment. The second purpose is to use the characteristic GV of the pot wall to generate a peak in the histogram. The generated peak is used later on for the calculation of the average root GV during a background removal step. In order to create a mask which excludes the pot wall, the coordinates of a circular region of interest (ROI) bounded within the pot wall limit need to be defined manually at three Z slices of the stack, i.e., at the first, the middle and the last slices. Those three sets of coordinates need to be given as input. The coordinates of the bounded ROI for all Z slices are then linearly interpolated from the given X-Y coordinates of the bounded ROI at the three Z slices. This allows creating a 3D mask, i.e., a mask whose boundaries in the X and Y dimensions move as the stack is explored in the Z dimension. Creating a 3D mask is necessary to cope with pots being tilted during the X-ray CT scanning. Note that, at the resolution used in the benchmark datasets and considering the pot height, a certain tilt of the pots is always present. For tilted pots, a 2D mask would result either in masking the roots growing along the pot wall or in the inclusion of the pot wall in the data to segment. With the 3D mask, a logical "AND" operation is used on the filtered image in order to remove the pot wall from the data to segment.

Once the bounded ROI is calculated for all Z slices, an extended ROI is created by simple extension of the bounded ROI by 50 voxels (Figure 2.3a). The extended ROI serves the purpose of including the pot wall in the histogram analysis of the stack so that a characteristic peak is generated. After extracting the histogram of the extended ROI, a function searches for the maxima in the lowest part (i.e., from 0 to 128) and in the highest part (i.e., from 128 to 255) of the histogram. This function then retrieves the GV of those maxima, i.e., P1 and P2 which correspond to the average GV of the pot wall and of the soil matrix, respectively (Figure 2.3b). Those two values are used further down in the workflow during the background removal step.

An edge enhancement step is then applied with the "Unsharp Mask" filter in ImageJ. "Unsharp Mask" filters enhance the local contrast between root edges, the surrounding soil matrix and pores (Sheppard et al., 2004). The degree of edge enhancement is controlled by two input parameters. "Blur radius" is the standard deviation of the blur radius of the Gaussian filter kernel and "Mask weight" determines the strength of the filtering. The result of the edge enhancement step can be assessed by comparing the image filtered with 3D NLM (Figure 2.2b) and the image after "Unsharp Mask" (Figure 2.2c).

A new feature of the Rootine v.2 algorithm is to apply a background removal step. During the background removal, every voxel whose GV deviates too much from the average root GV ($\bar{v}_r$) is masked out. This operation is performed in a three steps procedure. During the first step, a calculation of the root average GV is carried out using the previously identified characteristic peaks of the pot wall and the soil matrix. Assuming that a shift of P1 and P2 would result in similar shift of $\bar{v}_r$, $\bar{v}_r$ can be calculated for every image of the dataset using equation 2.1,

$$\bar{v}_r = f_r(P2 - P1) + P1 \tag{2.1}$$

where $\bar{v}_r$ is the root average GV, f_r is the root GV factor which has to be determined a priori on a representative test image and P1 and P2 are the characteristic peaks of the pot wall and the soil matrix, respectively. The first step allows coping with differ-
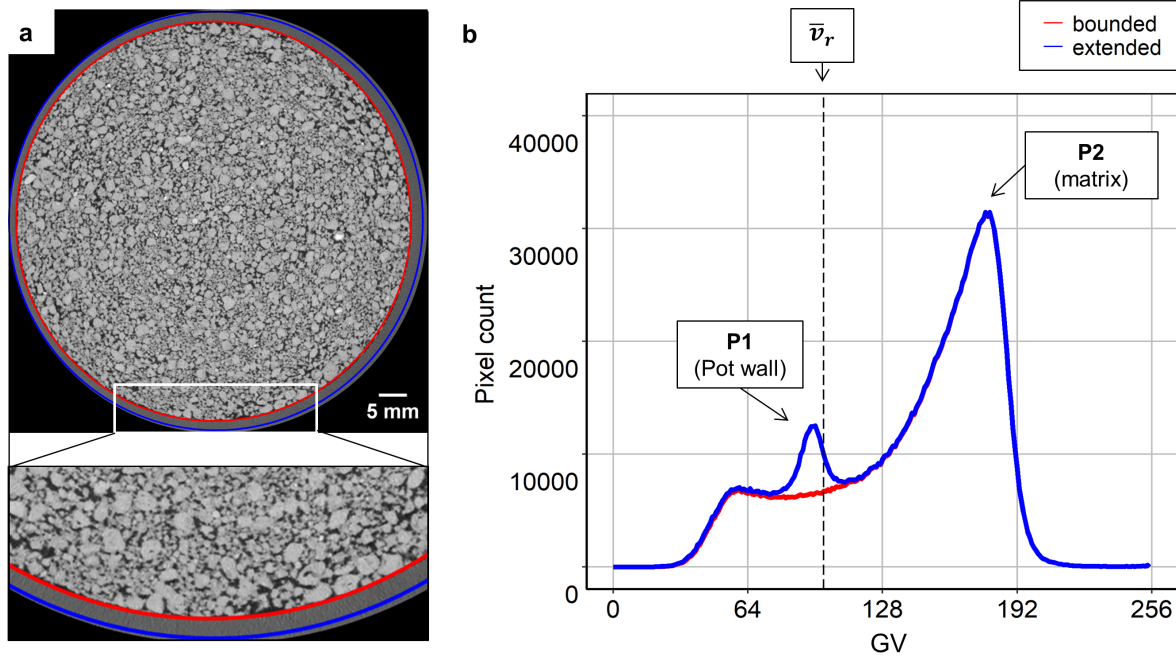
Figure 2.3: Mask creation and calculation of the average root GV based on characteristic peaks. Subfigure a depicts the drawing of a circular ROI bounded within the pot wall (red circle) on a 2D section of the worse case scenario. The bounded ROI serves the purpose of creating a mask. By extension of the bounded ROI by 50 pixels, an extended ROI is created (blue line); (b) Histogram of the bounded and extended ROI illustrated in subfigure a. The extended ROI serves the purpose of creating a peak in the histogram which is used to calculate the average root GV.

ently contrasted images in the dataset. Differences in image contrast are due to the percentile stretching method used during the 8-bit conversion when reconstructing the tomograms. Once $\bar{v}_r$ is calculated, a second step named "Absolute Difference Transform" (ADT) is applied. The rationale of this step is to brighten the GV of the roots and darken all background voxels, including pores and soil matrix, as both materials have a GV different than $\bar{v}_r$. For every voxel, this is done by computing

$$v_{ADT} = 255 - |v_f - \bar{v}_r| \tag{2.2}$$

where v_{ADT} is the voxel GV after the ADT and v_f is the voxel GV prior ADT. The background is then masked out by thresholding the image with a threshold value (t_{ADT}) calculated with

$$t_{ADT} = 255 - \frac{R_r}{2} \tag{2.3}$$

where R_r is the root GV range centered around $\bar{v}_r$. R_r has to be determined a priori on a representative test image and has to be given as input parameter. The image obtained after background removal serves as the input image for the subsequent root segmentation step. This three-step procedure replaces the simple pore masking step in Rootine v.1. The result of the background removal step can be assessed by comparing the image after edge enhancement (Figure 2.2c) and the image after background removal (Figure 2.2d).

Root segmentation   A specificity of the Rootine algorithms is to segment roots by exploiting one of their inherent characteristics, i.e., their cylindrical shape. To do so, the "Tubeness filter" available in ImageJ is used. In brief, the tubeness filter performs a smoothing of the image and produces an image in which the GV are directly related to how similar an object is to a cylinder. Generally, a scaled approach is adopted, i.e., the same image is filtered with Gaussian filters of different strength determined by their σ values, segmented and then combined. For low σ values, the roots of small diameters evoke high GV after tubeness filtering whereas the bigger roots either appear hollow or display low GV after tubeness filtering. Increasing the σ values of the tubeness filter then results in the opposite effect, i.e., the roots of greater diameter appear brighter whereas the roots of smaller diameter vanish. The obtained series of images are then segmented using the "3D Hysteresis thresholding" method available in the 3D ImageJ Suite (Ollion et al., 2013) and then combined to reconstitute the full root system. Hysteresis thresholding is a segmentation method requiring two thresholds. With an upper threshold (t_{hys}^{high}), seed regions definitively belonging to roots are determined. The upper threshold is less relevant for segmentation accuracy and can be set a priori. From the upper threshold, a region growing process connects all voxels brighter than a lower threshold (t_{hys}^{low}). This region growing process improves edge continuity in gradient images (Canny, 1986) and the class assignment of partial volume voxels (Schlüter et al., 2010), thereby reducing the presence of false positives.

In this work, we introduce a new method to estimate the lower threshold applied during hysteresis thresholding. This estimation is based on the measurement of root diameters present in the image to segment. The link between the lower threshold applied during hysteresis thresholding and the root diameters was made by analyzing carefully the results of the tubeness filter for increasing σ values applied on the same image of a hypothetical root (Figure 2.4a). This was achieved with the following sequence of operations. First, a root having a diameter d_r was created by drawing a white cylinder on a black background. Then, this root image was filtered with tubeness of increasing σ values. Note that the absolute value of the tubeness intensity depends on the gradient magnitude and hence the level of smoothing. Therefore, the tubeness filter results were normalized, i.e., the highest GV after filtering is set to 255 during conversion from 32-bit to 8-bit. In order to generalize the obtained results, we introduce the normalized smoothing strength q which is equal to

$$q = \frac{\sigma}{d_r} \tag{2.4}$$

where σ is the smoothing strength of the tubeness filter and d_r is the root diameter. Both parameters are expressed in number of voxels. For each q value, a GV transect along the root diameter axis is plotted (Figure 2.4b). It is shown that, for low q values, the filtered root appears hollow and the GV transect has symmetrical peaks on both sides of the root diametrical axis and a minimum exactly at the root diametrical axis. For q values greater than 0.125, the transects have a concave parabolic shape with their symmetrical axis centered on the root diametrical axis. For a given q value, the GV at the intersection of the parabola and the original root outline (i.e., the vertical blue dashed lines in figure 2.4a and 2.4b) corresponds to the optimal lower threshold (t_{hys}^{opt}) to use during hysteresis thresholding in order to precisely capture the original root diameter. To formalize the calculation of t_{hys}^{opt}, we retrieved t_{hys}^{opt} (i.e., the colored dots in

figure 2.4b) for all *q* values and fitted a regression model (Figure 2.4c) which describes best the relationship between those two parameters (i.e., highest possible R^2 values). We then calculated t_{hys}^{opt} for *q* = 0.5 using the model regression (i.e., t_{hys}^{opt} = 79, see the dashed line on figure 2.4c). With the optimal lower threshold calculated and with a measurement of the diameter of the root to segment, the sigma value of the tubeness filter can be estimated (Equation 2.5). It is important to note that, in case of image rescaling, the resolution factor (f_s) needs to be accounted for in the measurement of d_r. Thus, equation 2.4 is recast to:

$$\sigma_i = q d_{r,i} f_s \qquad (2.5)$$

where σ_i is the smoothing strength of the tubeness filter to use to properly segment a root of a certain diameter $d_{r,i}$, *q* is the normalized smoothing strength and f_s is the resolution factor. For the segmentation of fine roots, the images were segmented at the original resolution (i.e., f_s =1) whereas the bigger roots were segmented with an input image downscaled by a factor of 2 (i.e., f_s =0.5) in order to reduce processing time without considerable loss of information. To determine values for $d_{r,i}$ a priori, an increment approach was adopted to account for the continuous distribution of root diameters (Figure 2.5). This approach requires three parameters, namely the minimum root diameter ($d_{r,min}$), the root diameter increment ($d_{r,inc}$) and the maximum root diameter ($d_{r,max}$). All three parameters are expressed in number of voxels. The minimum and maximum root diameters were determined by measuring the diameter of the finest and biggest root in the image with the "Measure" tool available in ImageJ. The root diameter increment parameter refers to the increment at which roots of increasing diameters are detected. Here, a root diameter increment value equal to 4 voxels was set, which yields an incremented σ value of 1 at the coarse resolution according to equation 2.5. With these three parameters, an incremented calculation estimates the appropriate sigma values of tubeness for each resolution and scale considered and root diameters targeted. After filtering with tubeness and subsequent segmentation with hysteresis thresholding, the results were combined into one image with a logical "MAX" operation, i.e., a voxel is assigned to the root class if it is assigned to roots in at least one resolution or scale. This updated approach replaces the fixed scales and manually defined t_{hys}^{low} for each scale in Rootine v.1. The result of the root segmentation step is shown in figure 2.2e.

Postprocessing   The postprocessing steps aim at removing artifacts which were created in the course of segmentation. Such artifacts may include for instance segmented particulate organic matter or isolated pores whose GV are in the same range as the one of the roots. First, a 3D Median filter available in ImageJ is applied on the segmented images in order to smoothen the root surfaces. The degree of filtering is determined by the kernel size of the filter which needs to be given as an input parameter. On one hand, this filtering operation is favorable as it trims some over-segmentation voxels extending from the roots into the surroundings. On the other hand, this trimming also causes some fine root segments to be disconnected from the root system. After 3D Median filtering, the unconnected objects are removed using a connectivity criterion. This operation is performed with the "Keep Largest" function available in the "MorpholibJ" plugin library (Legland et al., 2016). Prior to "Keep Largest", an extra set of slices is added at the top of the stack to ensure the connectivity of all root segments from top to bottom. This is necessary when the seed from which all roots emerge is not part of the
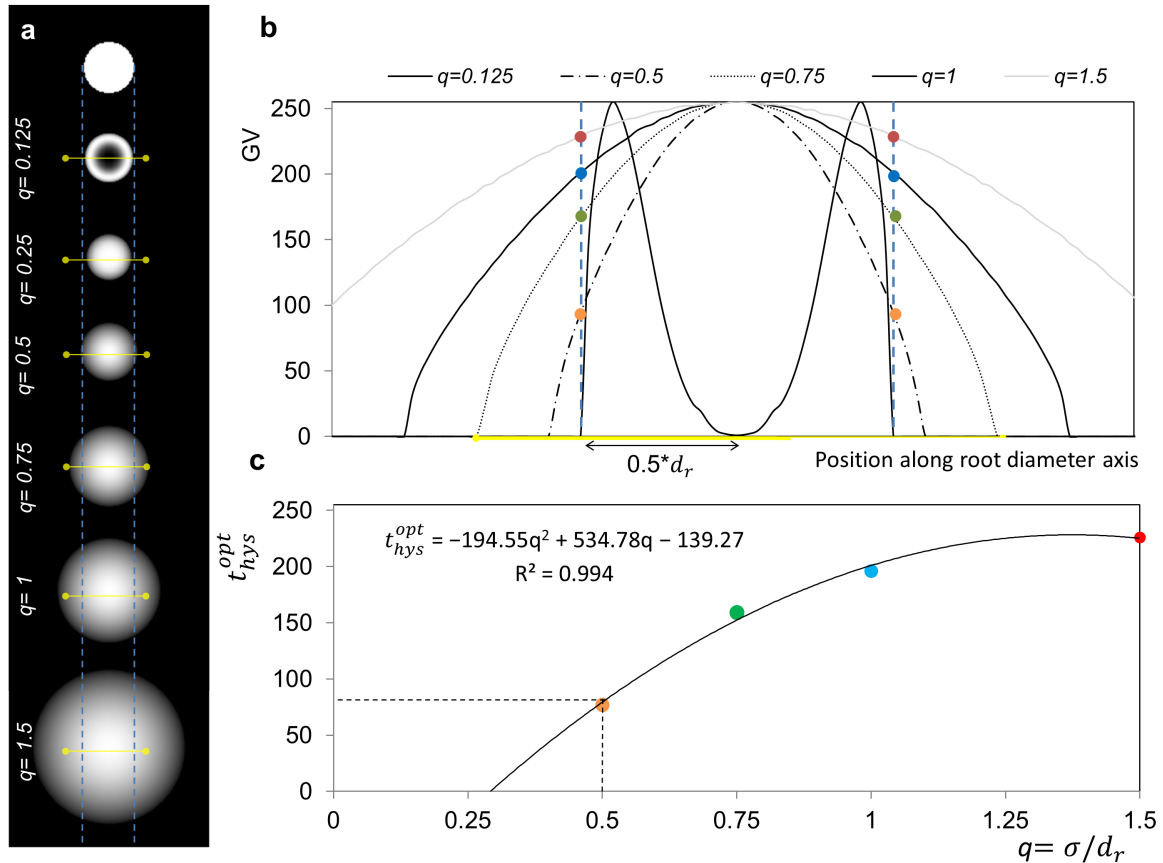
Figure 2.4: Estimation of σ values of the tubeness filters and the optimal lower thresholds of hysteresis thresholding. (a) Results of the tubeness filter on a hypothetical root of a diameter d_r obtained for different q values. The dashed blue lines show the original root outline whereas the solid yellow lines show the position of the transects used to plot the GV along the root diameter axis; (b) Plot of GV along the root diameter axis for some of the q values shown in subfigure a. The colored dots at the intersection between the root outline and the GV parabola correspond to t_{hys}^{opt} for a given q value; (c) Line of best fit imposed on the couple of points q and t_{hys}^{opt}. In this study, we calculated t_{hys}^{opt} corresponding to q = 0.5 using the model regression. The calculated value is indicated by the dashed line (i.e., t_{hys}^{opt}=79)

image. In the case of *Zea mays* L., adding this step is essential as it allows keeping the brace and crown roots which do not directly emerge from the seed but always enter the ROI from the top.

A new feature of Rootine v.2 is to implement a "false negatives" recovery step. This step labels and evaluates every object unconnected to the root system and test whether it fulfills shape criteria which evoke the typical shape of roots. Those unconnected objects are either segmented clusters of pores and/or segmented particulate organic matter (i.e., false positives) or root segments which were disconnected due to the trimming effect of the previously applied 3D Median filter (i.e., false negatives). Here, we evaluate every unconnected object based on two criteria, i.e., its "Vesselness" and its size. To evaluate the vesselness, a simplified formulation of the vesselness function proposed by Frangi et al. (1998) was adopted and a "vesselness score" of individual objects was derived. This is based on the analysis of the length of the semi-axes of fitting ellipsoids to binary objects instead of evaluating the Hessian matrix (i.e., the sec-

	Minimum root diameter	Root diameter increment = 4 voxels					Maximum root diameter
d_r [voxels]	4	8	12	16	20	24	**28**
d_r [µm]	180	360	540	720	900	1080	1260
σ	2	4	6	8	10	12	14
f_s	1	0.5	0.5	0.5	0.5	0.5	0.5

Detect fine roots   Detect coarse roots

Figure 2.5: Approach for the detection of roots of increasing diameters at the original and the coarse resolutions.

ond derivative of GV) of each voxel. The semi-axes of the fitting ellipsoids are denoted as λ_1, λ_2 and λ_3. By convention and in order to make abstraction of the local orientation of the considered object in the 3D space, we pose $\lambda_1 \leq \lambda_2 \leq \lambda_3$. For every object, the following geometrical ratios were computed.

$$R_b = \frac{\lambda_1}{\sqrt{\lambda_2 \lambda_3}} \tag{2.6}$$

$$R_a = \frac{\lambda_2}{\lambda_3} \tag{2.7}$$

The first ratio accounts for the deviation from a blob-like structure. For a blob-like object (i.e., $\lambda_1 \approx \lambda_2 \approx \lambda_3$), R_b will attain high values whereas it will have low values for elongated objects (i.e., $\lambda_1 \approx \lambda_2 << \lambda_3$). The second ratio is essential for distinguishing between plate-like and cylinder-like structures. For a plate-like object (i.e., $\lambda_1 << \lambda_2 \approx \lambda_3$), R_a will reach its maximum whereas it will be low for elongated objects. Based on the defined ratios, we evaluate how similar an object is to a cylinder by deriving its vesselness score (ν) according to equation 2.8.

$$\nu = exp(-R_b^2)exp(-R_a^2) \tag{2.8}$$

The vesselness score can have values ranging from 0.13 for a perfect sphere to $\approx$ 1 for an infinitely long cylinder. The relationship between the length of the semi-axes of the fitting ellipsoids, the calculated geometrical ratios and some properties of the vesselness score are illustrated in figure 2.6 for simple geometrical objects, i.e., a sphere, a plate and a cylinder. In addition to the vesselness criterion, a size criterion is used in order to exclude small objects which originate mostly from the noise level in the image and may by chance fulfill the vesselness criterion. The size criterion is given by a single value being equal to the greatest length of the semi-axes of the fitting ellipsoid, i.e., λ_3. In practice, evaluating the unconnected objects is performed in three steps. All steps rely on operations available in the "MorpholibJ" plugin library. Firstly, a label

is assigned to every unconnected object via the "Connected Components Labeling" function. Secondly, for every unconnected object, the length of the semi-axes λ_1, λ_2 and λ_3 of the fitting ellipsoids are computed with the "Analyze Regions 3D" function. Thirdly, the vesselness score is calculated and assigned to each label using the "Assign Measure to Label" function. An object is then considered a false negative only if the following conditions are met:

$$\nu_i > t_v \quad and \quad \lambda_{3}, i > t_s \tag{2.9}$$

where ν_i and $\lambda_{3,i}$ are the vesselness and the size score of the object i and t_v and t_s are the vesselness and the size threshold, respectively. The vesselness and the size threshold are input parameters which need to be given and calibrated by the user. After differentiating the false positives from the false negatives, the false negatives are added to the connected root system whereas the false positives are discarded. Figure 2.7 illustrates this new approach of the postprocessing scheme implemented in Rootine v.2. The effect of the post processing steps is shown in the difference between figure 2.2e and 2.2f.

Sphere

$\lambda_{3 = }\lambda_{2 = }\lambda_1$

$Rb = Ra = 1$

$\nu = 0.13$

Plate

$\lambda_{3 = }\lambda_2$

$\lambda_3 \gg \lambda_1$

$Rb \ll Ra$

$\lim_{\lambda_2 \to \lambda_3} \nu(\lambda_2) \approx 0.36$

Cylinder

$\lambda_{1 = }\lambda_2$

$\lambda_3 \gg \lambda_1$

$Ra \ll Rb$

$\lim_{\lambda_3 \to \infty} \nu(\lambda_3) \approx 1$
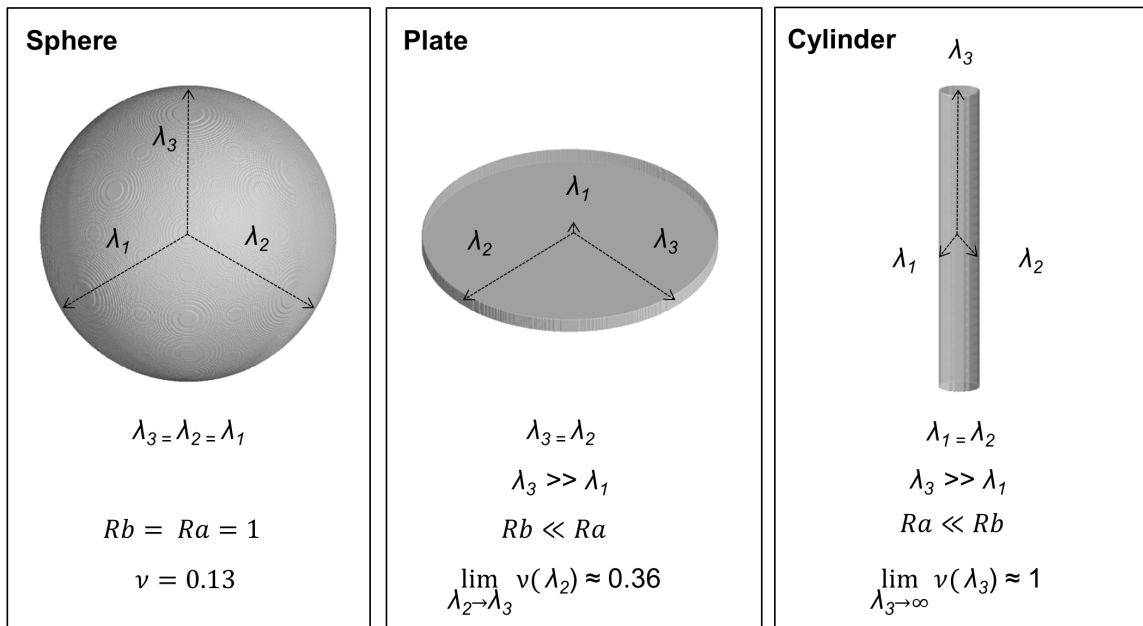
Figure 2.6: Vesselness score, R_b and R_a values for a sphere, a plate and a cylinder.

Quantification and analysis   Following postprocessing, the images can be analyzed and quantified in terms of root length and diameter. The quantification of root length from X-ray CT data has to be preceded by a step of skeletonization which conducts a medial axis transform of the segmented root image. This results in an image where all roots are reduced to a one voxel wide object which makes the calculations of root length more reliable and faster. This is achieved by sequentially applying the "Skeletonize (2D/3D)" and "Analyze Skeleton (2D/3D)" methods available in the BoneJ plugin library (Doube et al., 2010). The root recovery is assessed by plotting the root length calculated after skeletonization of the segmented root system and the root length analyzed with WinRHIZO (WR). By imposing a line of best fit to the relationship between
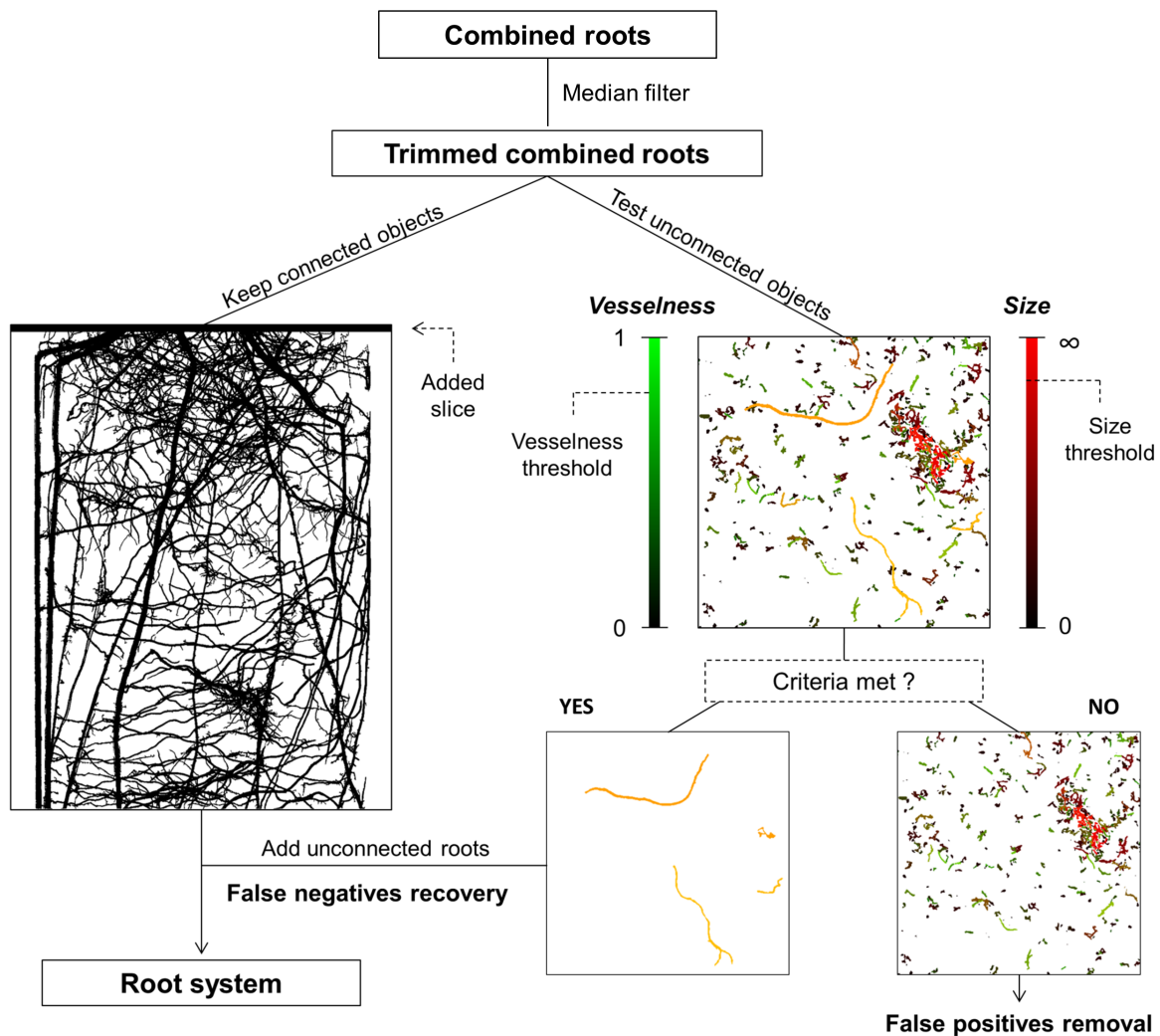
Figure 2.7: *Illustration of the postprocessing steps implemented in Rootine v.2. First, a 3D Median filter is applied on the results of the root segmentation step. Then, all connected objects are kept by applying the "Keep Largest" function. In order to ensure full connectivity of the roots at the top of the stack, a slice is added at the top (left-hand side of the figure). The remaining unconnected objects are subjected to a test evaluating their shape, i.e., their "vesselness" and size. This is illustrated here by showing a Z-Projection of a 400x400x400 image from the best case scenario dataset (right-hand side of the figure). The green scale bar indicates the vesselness score whereas the red scale bar indicates the size score. The intensity of the yellow color depicts the combination of these two scores. If the score of an object exceeds both the vesselness and size threshold, it is considered as a false negative and will subsequently be added to the connected root system. If not, it will be considered as a false positive and will be discarded.*

both root lengths (CT and WR), the root recovery and the error consistency (i.e., the slope and the coefficient of determination of the line of best fit, respectively) can be evaluated. The quantification of the root diameter distribution is performed with the "Local Thickness" plugin available in BoneJ. This method assigns to every root voxel a value corresponding to the diameter of the largest sphere which locally fits into the root. The results of the local thickness images are intersected with the skeleton images with

a logical "AND" operation. The resulting images are skeletonized root systems where each medial axis voxel contains the local root diameter information. This intersection is performed in order to avoid that big roots contribute to more voxels than smaller roots in the histogram. The histogram of the obtained images is then computed to retrieve the root length corresponding to every diameter class. Note that, even though roots were destructively sampled at two different layers for six replicates, the results are shown here by pooling all replicates and all layers together for each scenario. For both the root length and the root diameter distribution, the root length is normalized by dividing by the volume of the soil layer and the results are expressed in terms of RLD.

Summary of the workflow and its parameters   This section concludes the description of the workflow of Rootine v.2. Figure 2.1 and table 2.1 provide an overview of the steps of the workflow and the tunable parameters involved to obtain a segmented root system from an input grayscale data acquired with X-ray CT. Table 2.1 also lists the effect and the sensitivity of the parameters on the segmentation accuracy. Note that the effect and sensitivity of the parameters have been assessed visually thanks to the acquired user-experience during the calibration of the method for our specific dataset. The mention of the sensitivity of the parameters has the sole purpose of giving general advice to potential users during the calibration of Rootine v.2 for their specific dataset.

2.3   Results

In the worse case scenario, Rootine v.2 outperformed its preceding version by an increase of the root recovery up to 73 % of the total root length, against 29% for Rootine v.1 (Figure 2.8a). The coefficient of determination is roughly equal for both algorithms (i.e., R^2 = 0.76 and 0.79 for Rootine v.1 and v.2, respectively). A 2D Maximum Z-Projection of a selected sample (circled in black in figure 2.8a) shows that the over-segmentation is low (Figure 2.8b). Detected roots appear relatively smooth and there are barely any root voxels extending into their surroundings. In the 2D Maximum Z-Projection, some root segments are disconnected from the root system. Those segments are the ones added by the false negatives recovery step during postprocessing. Figure 2.8b also shows that the gain in root length with Rootine v.2 is mainly contributed by additional fine roots (operationally defined as roots having a diameter $\leq$ 180 μm). The increased fine root recovery is also reflected in the root diameter distribution (Figure 2.9a). On top of a higher root recovery of the fine roots, Rootine v.2 also better captured the root diameter of the big roots (operationally defined as roots having a diameter $\geq$ 900 μm) as compared to its preceding version. This can be seen on figure 2.9a where Rootine v.2 agrees better with WR data for the diameter classes larger than 900 μm as compared to Rootine v.1. The second peak (corresponding to the primary roots) only underestimates WR values by 4 voxels for Rootine v.2, whereas this second peak is completely absent for Rootine v.1. The better agreement of the root diameter distribution with Rootine v.2 can also be assessed visually by superimposing the segmented images of both algorithms and by directly comparing them with the grayscale X-ray CT data (Figure 2.9b). The visual comparison of the results obtained with the region growing method, the Root1 algorithm, Rootine v.1 and Rootine v.2 for a

Table 2.1: Rootine v.2 parameters, their values, their effects and their sensitivity on the segmentation accuracy.

Step	Parameter	Value		Effect	Sensitivity
		Worse case	Best case		
Image filtering	Contrast threshold (t_{con})	60	60	Controls the degree of smoothening (i.e., noise removal of the input image).	Medium
Edge enhancement	Blur Radius	1	0.9	Controls the sharpening of the image.	High
	Mask Weight	0.7	0.8		High
Background removal	Root gray value factor (f_r)	0.1	0.18	Sets the average gray value of the roots.	Very high
	Root gray value range (R_r)	65	70	Controls the root gray value window centered around the average root gray value.	Very high
Detect fine roots	Minimum root diameter (d_{min})	4	4	Controls the root recovery of the fine roots.	High
Detect coarse roots	Maximum root diameter (d_{max})	28	28	Controls the accuracy of the root diameter outline of the biggest root.	Medium
False positives removal	Kernel size of median filter	3	2	Controls the degree of smoothening of the roots and trimming of over-segmented voxels.	High
False negatives recovery	Size threshold (t_s)	25	25	Controls the quality of the false negatives recovered.	High
	Vesselness threshold (t_v)	0.85	0.9		High

subvolume of the worse case scenario shows that Rootine v.2 outperformed other root segmentation state of the art methods as well (Figure 2.10).
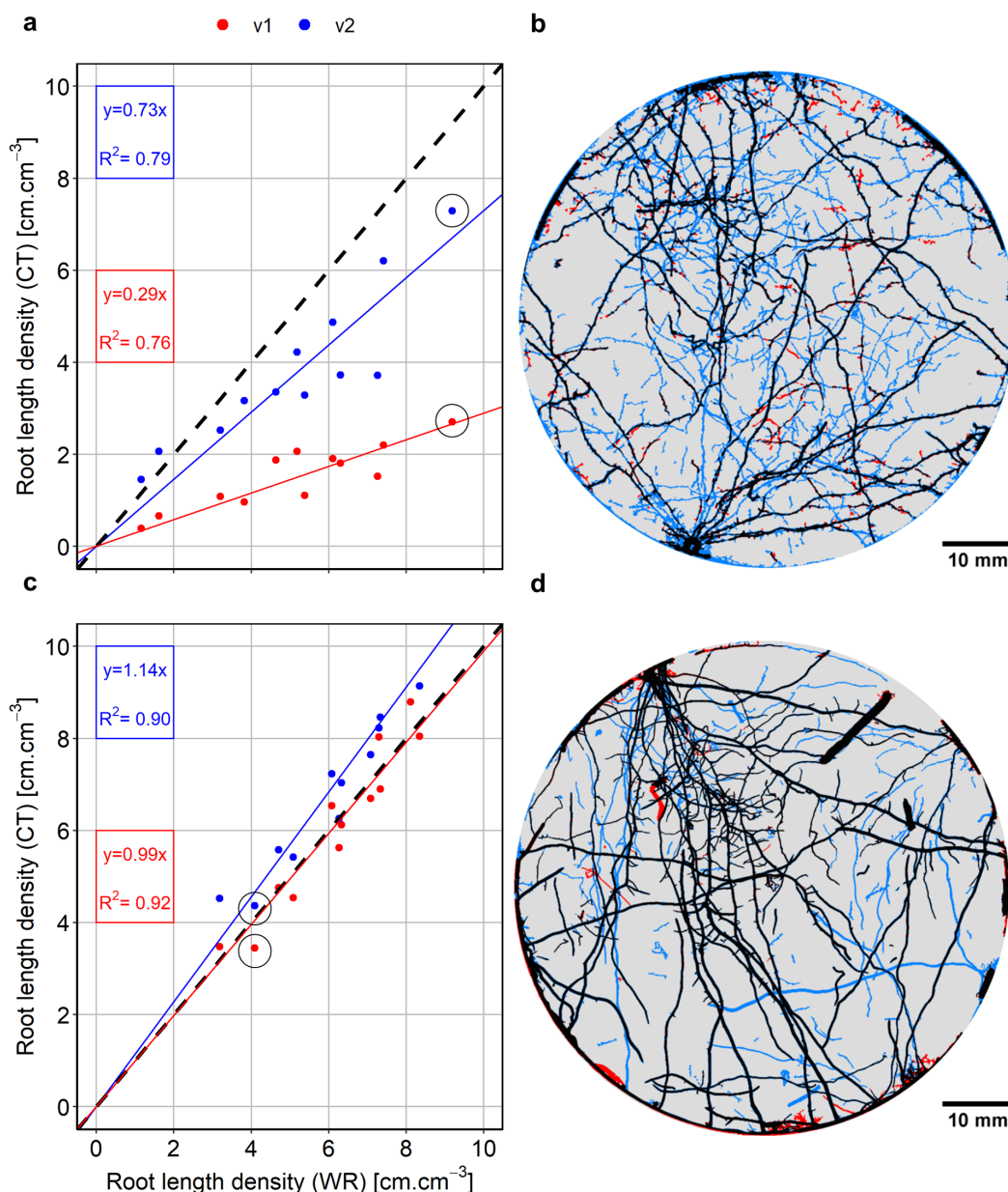
Figure 2.8: Root recovery of Rootine v.2 for the worse and best case scenario.(a&c) Comparison with the former Rootine v.1 and the RLD determined with destructive sampling and scanning of washed-off roots (WinRHIZO) for the worse case and the best case scenario, respectively. The dashed line indicates the 1:1 line. (b&d) Visual comparison of the segmented root systems obtained with Rootine v.1 and Rootine v.2 for the corresponding sample circled in black on subfigures a and c for the worse case and the best case scenario, respectively. Roots detected by both algorithms are depicted in black, the ones only detected by Rootine v.2 are shown in blue, whereas roots only detected by Rootine v.1 are shown in red.

In the best case scenario, the root recovery of Rootine v.2 amounts to 114 % of the total root length against 99 % for Rootine v.1 (Figure 2.8c). Again, the coefficient of determination is roughly equal for both versions (i.e., $R^2 = 0.92$ and 0.90 for Rootine v.1 and v.2, respectively). Similarly to the worse case scenario, a 2D Maximum Z-Projection of the segmented roots of a selected sample (Figure 2.8b) offers a
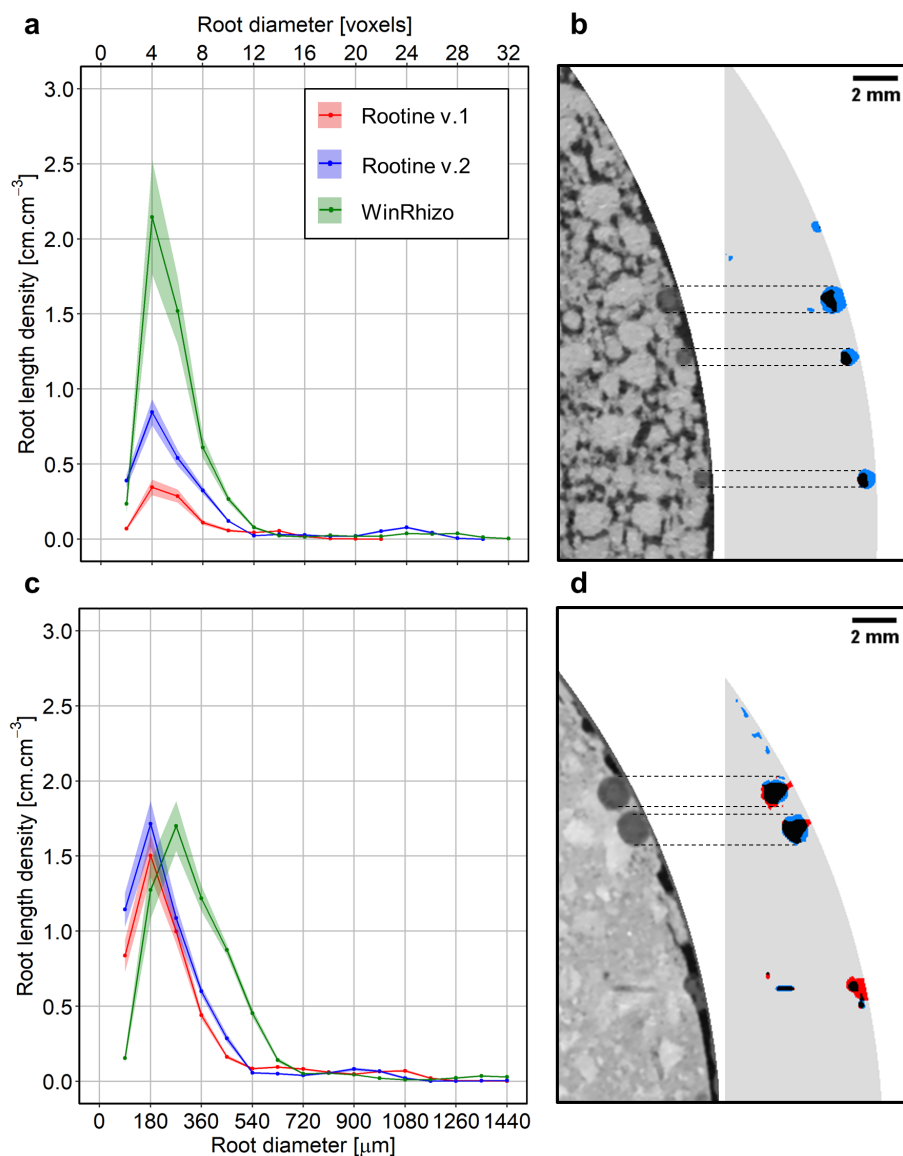
Figure 2.9: Root diameter distribution and root outline segmentation accuracy for the worse and best case scenario.(a&c) RLD distribution as a function of root diameter for Rootine v.1 and v.2 and the destructive sampling data obtained by scanning washed-off roots (WinRHIZO) for the worse case and the best case scenario, respectively. The semitransparent ribbon denotes the standard error of the measurements (n=12). (b&d) Visual comparison of the segmented root diameter outlines for both Rootine v.1 and Rootine v.2 supported by the original X-ray CT grayscale data for the worse case and the best case scenario, respectively. Roots detected by both algorithms are depicted in black, the ones only detected by Rootine v.2 are shown in blue, whereas roots only detected by Rootine v.1 are shown in red. Dashed horizontal black lines highlight the fact that Rootine v.2 better captures root diameter in comparison with Rootine v.1.

visual comparison of the segmentation results of both versions. Here again, the over-segmentation is low as roots appear smooth and devoid of any over-segmented voxels at their boundaries. The increase in root recovery is also mostly contributed by the addition of fine roots. The agreement of the root diameter distribution is equally good for both versions (Figure 2.9c).
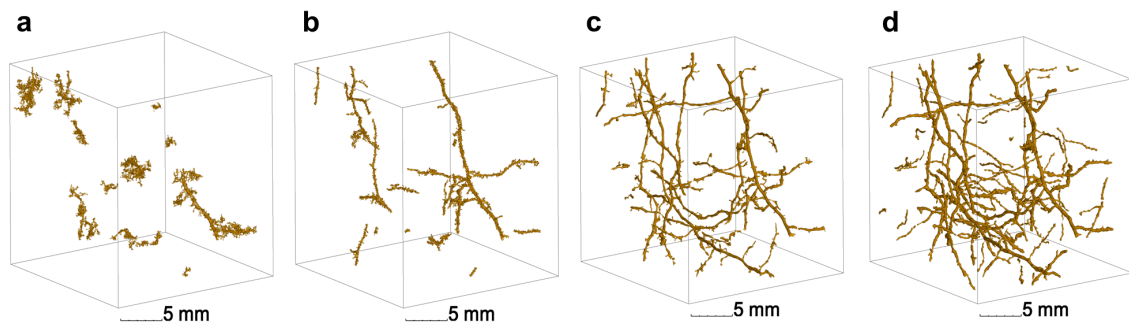
Figure 2.10: Results obtained with Region growing (subfigure a), Root1 (subfigure b), Rootine v.1. (subfigure c) and Rootine v.2 (subfigure d) for a subvolume from the worse case scenario.

2.4   Discussions

2.4.1   Segmentation accuracy

In the worse case scenario, most of the roots that were missed by Rootine v.1 and v.2 belonged to the category of the fine roots. This was expected considering that one of the main challenges of the benchmark dataset is a low image resolution as compared to the small diameter of the fine maize roots. Indeed, the analysis of the cumulative frequency of root diameter of the WR data revealed that the fine roots comprised roughly 45 % of the total root length. Fine roots pose a tremendous challenge due to the presence of partial volume voxels at the boundary of the roots and their surroundings. This challenge is even bigger when the contrast between the roots and their surroundings is low, which was true for the worse case scenario. We attempted to capture more fine roots at the original resolution by reducing the minimum root diameter to two voxels (i.e., resulting in a smoothing strength of $\sigma = 1$). However, this resulted in too much over-segmentation. Still, Rootine v.2 was able to capture twice as much of the fine roots as compared to Rootine v.1 in the worse case scenario. This can be attributed to the background removal step during preprocessing and to the false negatives recovery step during postprocessing. The background removal prevented the presence of false positives even when segmenting the images at the original resolution. In contrast, the soil heterogeneity and the low signal-to-noise ratio of the worse case scenario forced Gao, Schlüter et al. (2019) to downscale the images by a factor of 2 prior root segmentation. The authors argued that segmenting the images at the original resolution resulted in too much over-segmentation. By applying an adequate background removal operation, Rootine v.2 was able to avoid over-segmentation while improving the recovery of fine roots considerably. On top of an adequate background removal, the ADT step increases the GV intensities of the roots prior tubeness filtering, which is favorable for their subsequent detection. The false negatives recovery step also contributed to a fair amount of the root recovery. By computing the RLD before and after this step, this contribution can be evaluated. On average, it amounted to 25.5 % ($\pm$ 1.9 % standard error, n=12) of the total RLD. So the false negatives recovery step explained more than half of the gain in root recovery between Rootine v.1 and v.2.

In the best case scenario, the RLD inferred from X-ray CT was higher than the one measured with WR. This is an indication of the presence of false positives and/or

over-segmentation at the boundaries of root voxels. We rule out the latter since the visual inspection of the images showed virtually no root voxels extending into their surroundings. The overestimation of root length with Rootine v.2 could be due to the false negatives recovery step during which some actual false "positives" were considered as being false "negatives" and added back to the root system. For the best case scenario, the contribution of this step to the total RLD was lower than for the worse case scenario and amounted to 12.5 % ($\pm$ 0.8 % standard error, n=12). The overestimation of the root recovery could also be due to the uncertainties associated with the root washing procedure and further analysis with WR. The Z-Projection shown in figure 2.8d is one of the samples whose X-ray CT RLD data point exceeded the RLD data measured with WR (i.e., the sample circled in black above the 1:1 line in figure 2.8c). When taking a closer look at figure 2.8d, it is obvious that the increase in root recovery is partly due to the addition of real roots. During root washing, a soil sample is placed on a sieve, the soil is then washed off with water and the roots remaining on the sieve (here having a 1 mm mesh size) are picked with a tweezer and stored in ethanol prior to analysis. Some fine roots can easily go unnoticed on the sieve due to their size. The fact that the overestimation of WR data by Rootine v.2 occurs specifically for the fine roots is an indication supporting this argument. On top of the root washing, errors in WR data might be induced by an uneven distribution of the roots on the tray during scanning. An uneven distribution of the roots might cause two fine roots located very close to each other to be detected as one root with a larger diameter instead. During the analysis with the WinRHIZO software, a noise threshold value has to be set to exclude small dirt particles from the root length calculation. A high noise threshold value leads to smooth root surfaces but also results in the loss of fine roots. An improper setting of this parameter may then also induce errors. We rule out the effect of storing roots in ethanol on the WR results as this procedure has proved to be valid to conserve root samples without considerable influence on the measurements of root length (i.e., $< 1\%$ of underestimation) and diameter (i.e., 5 % of underestimation) (Logsdon & Reneau, 1988). Both the potential loss of roots during washing and the underestimated detection of fine roots by WinRHIZO could explain the overestimation of the root recovery in the best case scenario. Note that if the RLD data characterized with WR is underestimated, it is likely that the root recovery in the worse case scenario is overestimated.

The segmentation accuracy was evaluated based on quantitative aspects such as the root recovery and the comparison of root diameter distribution. Additionally, segmentation accuracy was also evaluated visually based on qualitative aspects, i.e., how accurately the root diameter outlines were segmented. With Rootine v.1, the primary roots often showed irregular shapes. With Rootine v.2, primary roots were segmented with a higher accuracy and showed a prominent circular shape when viewed in a 2D X-Y cross section. This can be seen in figure 2.9b and 2.9d. This increase in accuracy can most likely be ascribed to the fact that more scales were considered during the tubeness filtering at the coarse resolution with Rootine v.2. However, this difference in capturing the root diameter outlines was not big enough to be reflected in the root diameter distribution in the best case scenario. By visually comparing the results of Rootine v.1 and v.2, it was also noticeable that the latest version showed less false positives and less segmentation artifacts. Such segmentation artifacts include for instance the over-segmentation of roots growing along the plastic wall of the pot. Rootine v.1 did not

feature a pot wall detection and removal step. Since the root average GV is close to the one of the pot wall (see the corresponding GV of $\bar{v}_r$ and P1 in figure 2.3b), it was often observed on the results of Rootine v.1 that segmented root were extending into the plastic wall. This was particularly true in the best case scenario. With Rootine v.2, the pot removal step prevented that from happening.

2.4.2 Number of tunable parameters

One of the objectives of this work was to develop an algorithm for which the number of tunable parameters is reduced. Note that we consider as "tunable" the parameters which require adjustments and calibration when applied to other datasets (i.e., experiments with different plants, scan settings and/or soil heterogeneity).

In Rootine v.1, we identified twelve tunable parameters in total, namely five for the preprocessing, six for the root segmentation and one for the postprocessing. For the preprocessing, one parameter was used for filtering the original grayscale image (i.e., the contrast threshold of the 3D NLM filter), two for edge enhancement (i.e., the blur radius and the mask weight of the Unsharp mask filter) and two for masking the pores by single thresholding (pores were masked with different thresholds at the original and at the coarse resolution). For the root segmentation step at the original resolution, one σ value and the corresponding t_{hys}^{low} for hysteresis thresholding method were used. For the root segmentation step at the coarse resolution, three σ values were used. The obtained results of the tubeness filtering were then merged and one t_{hys}^{low} for the hysteresis thresholding method was used to segment the results of the coarse root detection (this amounts to four parameters). The upper threshold for hysteresis thresholding (t_{hys}^{high}) was kept constant and high enough for every tubeness filtering scale and is thus considered non-tunable. For the postprocessing, Rootine v.1 relied on one parameter, i.e., the kernel size of the 3D Median filter.

In Rootine v.2, the pore masking thresholds were replaced by the root GV factor (f_r) and the root GV range (R_r) . The parameters of the 3D NLM filter and the Unsharp mask filtering are also used in the new version. With the introduction of the automatic calculation of the σ values and t_{hys}^{opt} and keeping t_{hys}^{high} high enough and constant for every tubeness filtering scale, the number of parameters required for the root segmentation was reduced to two (i.e., $d_{r,min}$, $d_{r,max}$). As they have been set once for the new root segmentation approach, we consider the parameters q, f_s and $d_{r,inc}$ as "quasi-fixed" and therefore non-tunable. For the postprocessing, a smoothening step of the root outline was performed with the "3D Median" filtering step requiring one parameter (i.e., the kernel size). The false negatives recovery step added two parameters, i.e., the vesselness (t_v) and the size (t_s) thresholds. In total, the number of tunable parameters in Rootine v.2 was reduced to ten, i.e., five for the preprocessing of the image, two for the root segmentation and three for the postprocessing. It is worth noting that more parameters are required to use the full functionalities of Rootine v.2, i.e., the coordinates of the ROI mask. Those coordinates need to be directly evaluated on the image and are not considered to influence the segmentation results if appropriate values are given. The comparison between the tunable parameters used in Rootine v.1 and Rootine v.2 for every image processing step is shown in table 2.2.

Table 2.2: Tunable parameters used in Rootine v.1 and v.2.

Parameters	
Rootine v.1	**Rootine v.2**
Image filtering	
Contrast threshold (t_{con})	
Edge enhancement	
Blur Radius	
Mask Weight	
Pore masking	**Background removal**
Pore threshold at the original resolution	Root gray value factor (f_r)
Pore threshold at the coarse resolution	Root gray value range (R_r)
Detect fine roots	
Sigma value ($\sigma\,1$)	Minimum root diameter (d_{min})
Low threshold for hysteresis thresholding (t_{hys}^{low})	
Detect coarse roots	
Sigma value 2 ($\sigma\,2$)	Maximum root diameter (d_{max})
Sigma value 3 ($\sigma\,3$)	
Sigma value 4 ($\sigma\,4$)	
Low threshold for hysteresis thresholding (t_{hys}^{low})	
False positives removal	
Kernel size of median filter	Kernel size of median filter
	False negatives recovery
	Size threshold (t_s)
	Vesselness threshold (t_v)

2.4.3 Runtime and overall usability of Rootine v.1 and v.2

Besides the segmentation accuracy and the number of parameters, the assessment of the performance of a segmentation algorithm also has to take into account the time it takes to process the images. This is important for application in high-throughput root phenotyping based on X-ray CT data analysis. To process a stack having a dimension of 1750x1750x3000 voxels (in X, Y and Z dimension, size $\approx$ 8.6 GB), it took Rootine v.1 3.8 hours to complete the preprocessing, the segmentation and the post-processing steps. In comparison, Rootine v.2 took 6.8 hours to complete the same steps. The second version is 1.8 times slower than the first version for the analyzed image size. This is mainly due to the consideration of more scales during tubeness filtering at the coarse resolution. For both algorithms, the evaluation of the runtime was performed on a workstation having 64 Intel® Xeon® Gold 6142 cores running at 2.60 GHz each. To this date, filtering with the tubeness filter represents the bottleneck of the workflow. This is related to the fact that the tubeness filter is only implemented in a single threaded fashion in the ImageJ software. There should be no fundamental constraint that would restrict its parallelization and Rootine (regardless of the versions) would benefit a lot from it. Note that there exists a multithreaded implementation of the tubeness plugin which was developed in the context of ImageJ Ops (Tinevez, 2018). We have however not tested it. It is worth noting that both algorithms can be run in a

user interaction-free mode (i.e., from the command line) once the parameters are adjusted. This provides an advantage and, in our opinion, reduces the necessity of having a fast algorithm as the macro can run in the background and/or overnight. When it comes to root system architecture studies, a longer runtime can be well accepted as long as the root recovery is substantially increased. Despite the longer time required to segment the images, we are confident that the increase of the overall usability of Rootine v.2 can save the user some time for the adjustments of the parameters. Indeed, Rootine v.2 features input parameters which are linked to root physiological properties such as their GV and their diameter. These tunable parameters are easy to adjust as they can be directly assessed visually on a test image.

2.5 Conclusion

Rootine v.2 has been developed for improved root segmentation accuracy in X-ray CT data. It exploits intrinsic properties of root systems such as the connectivity of root branches and the cylindrical shape of roots to distinguish roots from the background. It was demonstrated that Rootine v.2 outperforms its precursor version as well as other state-of-the-art root segmentation methods in terms of root recovery. The gain in root recovery could be mainly ascribed to the absolute difference transform of the grayscale data prior to shape detection with a series of tubeness filters and to a false negatives recovery step. The other major advancements of Rootine v.2 are (i) a pot wall detection and removal step, (ii) a calculation of the root average gray value based on a histogram analysis and (iii) an automatic calculation of thresholds for hysteresis thresholding of the tubeness image. Moreover, the analysis of the root diameter distribution is readily integrated in the new version. The total number of tunable parameters for the entire workflow was reduced from twelve to ten. Rootine v.2, in comparison to Rootine v.1, functions less in a "black box" fashion as its parameters can be more easily interpreted and are easier to adjust. The proposed method has the potential of improving high-throughput root phenotyping procedures based on X-ray CT data analysis. Similarly to its preceding version, Rootine v.2 is a macro for the image processing software ImageJ and is made freely available to the public.

CHAPTER *3*

IMPACT OF ROOT HAIRS ON THE ROOT SYSTEM ARCHITECTURE OF *ZEA MAYS*

Root hairs initiation is one root trait among many which enables plants to adapt to environmental conditions. How different traits are coordinated and whether some are mutually exclusive is currently poorly understood. Comparing a root hair defective mutant with its corresponding wild-type, we explored if and how the mutant exhibited root growth adaptation strategies and how dependent this was on substrate. *Zea mays* root hair defective mutant (rth3) and the corresponding wild-type siblings were grown under well-watered conditions on two substrates with contrasting texture and hence nutrient mobility. Root system architecture was investigated over time using repeated X-ray computed tomography. There was no plastic adaptation of root system architecture to the lack of root hairs, which resulted in lower uptake of nutrients especially in the substrate with high sorption capacity. The function of the root hairs for anchoring did not result in different root length density profiles between genotypes. Both maize genotypes showed a marked response to substrate. This was well reflected in the spatiotemporal development of rhizosphere volume fraction but especially in the highly significant response of root diameter to substrate, irrespective of genotype. The most salient root plasticity trait was root diameter in response to substrate. Coping mechanisms for lacking root hairs were limited to a shift in root-shoot ratio in loam. Further experiments are required, to elucidate whether observed differences can be explained by mechanical properties beyond mechanical impedance, root or microbiome ethylene production or differences in diffusion processes within the root or the rhizosphere.

3.1 Introduction

Root hairs are important for nutrient uptake, in particular for those with low mobility like phosphorus (P) (T. Bates & Lynch, 2001; Jungk, 2001). In addition, root hairs are thought to be important for anchorage during establishment and root tip penetration into the soil (Bengough et al., 2016; Haling, Brown et al., 2013). Their role for water uptake is discussed controversially (Carminati et al., 2017; Marin et al., 2020). Root hair formation as an anatomical feature is just one root trait among many which enables plants to adapt to environmental conditions such as low nutrient availability, limited water supply or unfavorable physical conditions (J. E. Schmidt & Gaudin, 2017). Other plastic root morphological traits include changes in root diameter (diameter distribution, specific root length) or an overall change in root distribution in space. In summary, alterations in root system architecture enable an extremely flexible response to soil physical factors and limited or heterogeneous distribution of resources in time and space (Hodge, 2006; Morris et al., 2017). Furthermore, physiological traits can be altered, like activities of nutrient transporters and water channels, release of specific root exudates, and investment in mycorrhizal symbioses (Hodge, 2006; Pierret et al., 2007; J. E. Schmidt & Gaudin, 2017; Z. Wen et al., 2019). Such alterations would be reflected in higher normalized uptake rates (J. E. Schmidt & Gaudin, 2017). As all these root traits come at different carbon costs for establishment and maintenance, the extent to which they are exploited is potentially reflected in the root:shoot ratio (Klamer et al., 2019; Lynch et al., 2005). How the different traits are coordinated and whether some are mutually exclusive is currently poorly understood (Z. Wen et al., 2019). The relative importance of root traits is probably modulated by the soil and its physical and chemical properties. On the one hand nutrient availability depends on the sorption capacity and the forms of binding for the nutrients in question, for instance phosphorus (Y. Wang & Lambers, 2020). On the other hand texture related properties such as mechanical impedance, macroporosity, water holding capacity and aeration strongly impact root system architecture (Bengough et al., 2011; Lucas et al., 2019) and specifically root hair length (Hoffmann & Jungk, 1995). Hairs favor contact in low strength soils, and improve penetration of high strength soils, hence their relevance for P uptake is expected to depend on soil physical conditions (Haling, Brown et al., 2013). To address the plasticity of root traits in response to the lack of hairs under different soil physical conditions we compared a root hair defective mutant to the corresponding wild-type in two substrates. Specifically, we investigated the following hypotheses:

- Under nutrient limited conditions, the lack of root hairs will be compensated by an increased investment in root growth in general and more specifically in the growth of fine roots to maintain sufficient root surface area;

- The role of root hairs for anchorage will cause an adaptation in root system architecture, more specifically soil depth exploration with time, which could partly mask their expected response to low nutrient availability;

- The differences between wild-type and mutant will be larger in a substrate with a high sorption capacity, i.e., low mobility of the limiting nutrients, as this increases the need for enhanced soil exploration;

- Substrate itself will alter root system architecture, irrespective of genotype and nutrient supply, due to differences in mechanical properties and aeration.

In this study, *Zea mays* root hair defective mutant (rth3) and the corresponding wild-type siblings (WT) were grown for three weeks under well-watered conditions on two substrates with contrasting texture and hence nutrient mobility; loam and sand. Root system architecture was investigated non-invasively by repeated X-ray computed tomography (CT) scanning. This enabled not only to derive spatial distribution of roots over time, but likewise to address the changes in root demography and hence the spatial distribution of 'active' roots. The latter is important, since we assumed that roots and in particular root hairs are only functional in uptake for a few days (Jungk, 2001; Vetterlein & Doussan, 2016). The potential and limitations of X-ray CT as a non-invasive tool to study root system architecture in 4D is explored in detail. From this data we were able to observe changes over time and to derive rhizosphere volume fractions, which are traits which cannot be derived with destructive sampling. We also used conventional destructive root sampling to provide independent validations for root lengths and root diameters.

3.2   Material and Methods

3.2.1   Experimental design

The main experiment was set up as a two factorial, randomized design with six replicates. The term replicates here refers to individual soil columns. Factor one was substrate with two levels (loam (L), sand (S)). Factor two was *Zea mays* genotype with two levels comprising B73 wild-type (WT), and a root hair defective mutant (rth3). The experiment was set up in duplicate; one set consisting of six columns for each of the four treatments (L _WT, L _rth3, S _WT, S _rth3) was used for X-ray CT scanning. The other set, likewise with six columns per treatment, served as a control to check whether the X-ray dose associated with CT scanning had an impact on the parameters of interest (Control).

3.2.2   Genotypes

For the experiments, the Zea mays root hair defective mutant rth3 and the corresponding wild-type siblings were selected (T.-J. Wen & Schnable, 1994). The monogenic mutant rth3 is transposon induced and shows normal root hair initiation but disturbed elongation. The mutant shows no aberrant shoot phenotype, but grain yield in field experiments is reduced by 19 to 42% compared to the wild-type (Hochholdinger et al., 2008). The mutated gene encodes a GPI-anchored COBRA-like cell wall protein RTH3 that is involved in the organization of the synthesized cellulose (Weber et al., 2018). The rth3 mutant used in these experiments are genetically highly homozygous because they have been backcrossed to the inbred line B73 for more than eight generations.

3.2.3 Substrates, sieving and packing

The loam substrate was obtained from the upper 50 cm of a haplic Phaeozem soil profile, dried to 10% gravimetric water content and then sieved to <1 mm. The sand substrate constitutes a mix of 83.3% quartz sand (WF 33, Quarzwerke Weferlingen, Germany) and 16.7% of the sieved loam. Details on chemical and physical properties are provided by Vetterlein et al. (2021). A brief summary is provided in table 3.1.

Columns were packed carefully in order to avoid particle sorting and hence the presence of layers. This was achieved by placing a coarse sieve (4 mm of mesh size) above a column during filling which was continuously moved laterally. The loam treatment was packed to a bulk density (BD) of 1.26 g cm^{-3}, while the sand treatment was packed to a bulk density of 1.47 g cm^{-3}. Filling the columns to the target bulk density was achieved by "tapping" the entire column on a flat surface.

3.2.4 Soil column design

Individual soil columns consisted of an acrylic glass tube (25 cm height, 7 cm inner diameter). A nylon mesh (30 μm mesh size) was placed at the bottom of the column in order to retain the soil. The columns were filled up to 23 cm height with the substrates (Figure 3.1). With such a set-up, the volume available for plant growth was 885 cm^3.

3.2.5 Soil fertilization

Nitrogen (N), Phosphorus (P), Potassium (K), and Magnesium (Mg) were added at a dose twice as high in sand as compared to loam. Calcium (Ca) as well as micronutrients were only applied to sand (Table 3.2). This substrate-specific fertilization was carried out to account for the initial substrate specific differences in nutrient availability. The aim was to achieve a phosphorus level per shoot dry weight which was below adequate supply for the WT genotype (< 3.5 mg g^{-1} according to Bergmann (1986)) in order for root hairs to play a role in P acquisition under P limiting conditions. The fertilization dose used in this experiment was tested in pre-trials in order to achieve similar plant growth for WT, but still low plant P status (Vetterlein et al., 2021).

3.2.6 Plant growth conditions

Maize seeds were surface sterilized for 5 min in 10% hydrogen peroxide and placed at a depth of 1 cm. The soil surface was covered with quartz gravel to reduce evaporation. Columns were carefully watered from top and bottom to an average volumetric water content of 22% for loam and 18% for sand. Fluctuation of water content was low as watering intervals were shortened as plant transpiration increased. Growth chamber was set to 22°C during the day and 18°C at night with a 12 hour light-period, 350 μM m^{-2} s^{-1} photosynthetically active radiation and a constant relative humidity at 65%. Growth duration was 21 days, i.e., harvest was conducted on day 22 after planting.

Table 3.1: Physico-chemical properties of the loam and sand.

Soil	BD [g cm^{-3}]	pH (CaCl$_2$)	CaCO$_3$ [g kg^{-1}]	Sand [%]	Silt [%]	Clay [%]	CEC [mmol$_c$ kg^{-1}]	Corg [%]	Nt [%]	P plant available [mg kg^{-1}]	K plant available [mg kg^{-1}]	Fe$_{ox}$ [g kg^{-1}]
Loam	1.26	6.21	<1	33.2	47.7	19.1	76.1	0.84	0.084	33.41	26.57	1.32
Sand	1.47	6.25	<1	88.6	8.1	3.3	13.0	0.14	0.014	5.67	5.44	0.2

Table 3.2: Fertilizer application [mg$_{nutrient}$ kg^{-1}] to the loam and sand.

Nutrient	N	P	K	Mg	Ca	Mn	Zn	Cu	B	Fe
Chemical	NH$_4$NO$_3$	CaHPO$_4$	K$_2$SO$_4$	MgCl$_2$ x 6H$_2$O	CaSO$_4$ x 2H$_2$O	MnSO$_4$ x H$_2$O	Zn(NO$_3$)$_2$ x 4H$_2$O	CuSO$_4$ x 5H$_2$O	H$_3$BO$_3$	Fe-EDTA
Loam	50	40	50	25						
Sand	100	80	100	50	100	3.25	0.79	0.5	0.17	3.25

3.2.7 Shoot biomass sampling and nutrient analysis

At day 22 after planting, shoots were cut and dried at 65°C for 72 hours. After the determination of shoot dry weight the material was ground down to fine powder. Carbon and nitrogen were analyzed by combustion with a CNS analyser (vario EL cube, Elementar, Germany). P, K, Ca were determined by inductively coupled plasma-optical emission spectroscopy (ARCOS, Spectro AMETEC, Germany) after pressure digestion with nitric acid and hydrogen peroxide in a microwave (Mars 6, CEM Corporation, USA). Shoot nutrient content was obtained by multiplying the measured tissue concentration and the shoot dry weight. In order to compare the uptake of a nutrient with high mobility to one with low mobility without confounding impact of plant growth, the Ca:P ratio in the shoot biomass was assessed for each replicate.

3.2.8 Sampling of roots, WinRHIZO and root hair length measurement

After the shoot was cut, the soil was pushed out of the acrylic column using a custom made subsampling device (UGT GmbH, Germany) and then sliced into seven layers. The second, fourth and sixth layer were used for undisturbed subsampling (US), i.e., for investigation of spatial gradients, gene expression, microbiome analyses, which are presented elsewhere (Ganther et al., 2021, 2020; Vetterlein et al., 2021). The remaining layers were used for destructive sampling (DS). These layers were put on a 0.63 mm sieve and roots were washed off carefully with deionized water. Roots were stored in 50% alcohol solution (i.e., diluted Rotisol®). Subsequently, roots were scanned at 720 dpi with a 35 µm resolution using a flatbed scanner (EPSON perfection V700). Root traits were analyzed using the software WinRHIZO 2019 (Regent Instruments, Canada). The length of the root hairs was measured under a microscope on 1 cm long root segments of lateral roots 1 cm after the first emerging hairs above the root tip. Three segments per column were analyzed.

3.2.9 Mycorrhizal colonization

After scanning with WinRHIZO the degree of mycorrhizal colonization was determined. For the depth 6.1-9 cm (WR2) ten fine root (diameter < 1 mm) segments per column were selected for staining with ink (4001 Pelikan®) after clearing roots in KOH (10%) (Vierheilig et al., 1998). For each column, 100 fields of view were evaluated under the microscope. Following McGonigle et al. (1990), the presence of arbuscules, hyphae and vesicles was scored separately.

3.2.10 X-ray CT scanning

X-ray CT was performed with an industrial computed tomograph (X-TEK XTH 225, Nikon Metrology) operated at 160 kV and 296 µA. A total of 2748 projections with an exposure time of 500 ms each were acquired during a full rotation of a column. Samples were placed 18.2 cm away from the X-ray source during image acquisition. A 0.5 mm thick copper filter was used between the source and the column in order to reduce beam artifacts. A lead shield with a window (2.5*2.5 cm) was also placed

between source and the column to minimize photons scatter outside the field of view, i.e., to the plant shoot and in the soil outside the field of view. With this set-up, the dose per scan measured with a radiophotoluminescence dosimeter in the center of the column amounted to 1.2 Gy (Lippold, Kleinau et al., 2021). The obtained images were reconstructed into a 3D tomogram having voxel side length of 45 μm and an 8-bit grayscale via a filtered back projection algorithm with the CT Pro 3D software (Nikon metrology). During the 8-bit conversion, the grayscale range was normalized with a percentile stretching method which sets the darkest and brightest 0.2% voxels to 0 and 255, respectively.

X-ray CT scanning was performed at 7, 14 and 21 days after planting (DAP) during night time to not interfere with plant photosynthesis. Columns were scanned at two depth intervals making sure that an overlapping region was present. Each depth interval scan took 23 min to complete. The bottom and top scans were then stitched together so that the analyzed region had a vertical extent of -1.27 to -14.77 cm from the soil surface (Figure 3.1).
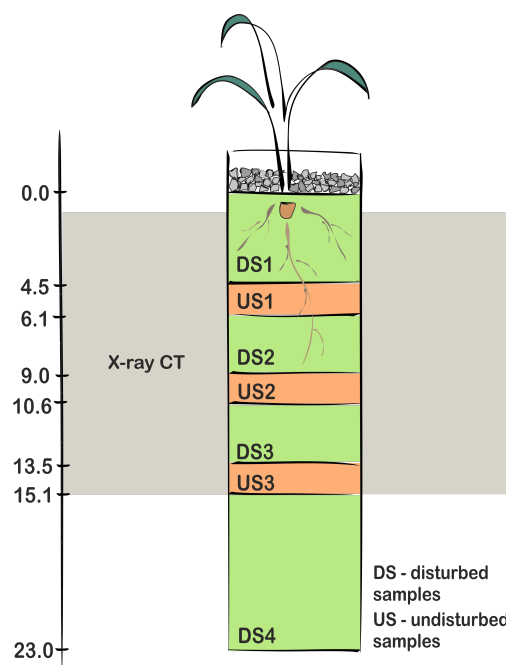
Figure 3.1: *Sketch of a soil column indicating X-ray CT-scanned depth (gray, 1.0-15.1 cm), depth for destructive sampling (DS) (light green, DS1 0-4.5 cm, DS2 6.1-9.0 cm, DS3 10.6-13.5 cm, DS4 15.1-23.0 cm) as well as layers for undisturbed sampling (US) providing higher resolution scans and material for microbiome and gene expression analyses addressed in Ganther et al. (2021, 2020) (orange; US1 4.5-6.1 cm, US2 9.0-10.6 cm, US3 13.5-15.1 cm).*

3.2.11   Root segmentation

Root segmentation of each column scan was performed with the algorithm Rootine v.2 (see chapter 2). Rootine v.2 is a free macro for the image processing software ImageJ (Schindelin et al., 2012). It combines a series of pre- and postprocessing filters with a shape based detection of cylindrical roots at various scales.

In order to assess the recovery of roots during segmentation, a comparison was made with the results from destructive sampling. The investigated layers were located at the depth of 6.1-9.0 cm and 10.6-13.5 cm for DS2 and DS3 respectively (Figure 3.1). The obtained root length measurements were compared to the ones obtained with X-ray CT for the soil depths investigated with both methods. The root recovery and the error consistency (i.e., respectively the slope and the coefficient of determination of the line of best fit) were assessed by pooling genotypes and depths together.

3.2.12 X-ray CT derived analysis

The properties of the root systems obtained with X-ray CT data were systematically investigated in a depth-dependent fashion. To perform such analysis, the methods described below were applied sequentially after splitting the full 3D stacks in 20 depth intervals, yielding an equidistant spacing of 6.75 mm in the Z direction.

Root length density   The quantification of RLD was performed after a step of skeletonization with the "Analyse Skeleton" plugin available in the BoneJ plugin suite (Doube et al., 2010). The skeletonization step conducts a medial axis transformation of the segmented root system, thereby reducing every root to a 1 pixel wide object. The RLD was then calculated by dividing the obtained root length by the analyzed volume in the considered soil layer. With simple arithmetic operations on the RLD results obtained at different scanning events, the fraction of young roots (i.e., roots younger than 7 days old) was calculated for 14 and 21 DAP.

Mean root diameter   The quantification of the root diameter distribution was performed directly on the segmented root systems with the "Local Thickness" method available in the BoneJ plugin. This method assigns to every root voxel a value corresponding to the diameter of the largest sphere that fits into the root and contains it. In order to avoid that big roots contribute to more voxels than smaller roots in the obtained histogram, the results of this method were intersected with the skeletonized images. The resulting images are skeletonized root systems, for which each medial axis voxel contains the local root diameter information. The histograms of the obtained images were then computed to retrieve the root length corresponding to all root diameter classes. Additionally, and in a more condensed fashion, the mean of the frequency distribution (here referred to as the mean root diameter) was assessed by computing the first central moment of the histogram.

Mean root distance   The quantification of the euclidian distances to root in soil was performed by applying a so-called "Euclidian Distance Transform" on the segmented root systems. This method assigns to every soil voxel a value corresponding to its distance to the closest root in a 3D volume. Retrieving the root distance histogram (RDH) (i.e., the histogram of the results obtained from the euclidian distance transformation) provides additional information with regard to how roots explore the available soil volume over time (Schlüter et al., 2018). In a similar fashion as for the mean root diameter, the mean of the frequency distribution (referred to as the mean root distance) was assessed by computing the first central moment of the RDH.

Rhizosphere volume fraction   The rhizosphere volume fraction (RVF) is here defined as the rhizosphere volume divided by the total soil volume analyzed. The rhizosphere volume was computed by integrating the RDH over all distances smaller than a given rhizosphere extent. The rhizosphere extent was taken from literature and considered equal for both soil textures. The value of 1.8 mm was deduced from the figure 4 of Hendriks et al. (1981) who measured the concentration profile of the isotopically exchangeable soil phosphate at the surface of 5 days old maize root segments grown in a sandy soil.

3.2.13   Statistics

The software R version 3.53 (R Core Team, 2017) and the libraries lme4 (D. Bates et al., 2015), car (Fox & Weisberg, 2019), multcomp (Hothorn et al., 2008), ggplot2 (Wickham, 2009) and emmeans (Searle et al., 1980) were used for the statistical analyses. Two-factorial ANOVAs for the fixed factors substrate, genotype and their interaction were conducted in conjunction with Tukey's HSD tests. A log-transformation was used prior to statistical analyses if normal Q-Q plots and Shapiro test indicated that the normal distribution criterion was not met. Significant differences between treatments are displayed with small letters for $p < 0.05$. When relevant, mean values and standard errors around the mean of six replicates are provided.

3.3   Results

3.3.1   Shoot and root growth, P acquisition

Plant P tissue concentration was low in both substrates, i.e., in loam 2.4 mg g^{-1} for rth3 and 2.6 mg g^{-1} for WT, in sand 2.7 mg g^{-1} for rth3 and WT). Achieving low plant P tissue concentrations was intended so that root hairs could play a role in P acquisition under P limited conditions. Overall, there was a significant impact of substrate on shoot and root growth, with a shift in root:shoot ratio (Figure 3.2a, b, c). Lack of root hairs resulted in a reduction of shoot and root growth. These effects were larger for shoots than for roots, the latter being reflected in a shift in root:shoot ratio towards the roots for rth3 (Figure 3.2c). Growth reduction (shoot and root) was larger for loam than for sand and the differences between genotypes were even more obvious for plant P content (Figure 3.2d). There was no significant difference between the genotypes with respect to P uptake per unit root surface, albeit there was a tendency for lower uptake for rth3 as compared to WT for loam (Figure 3.2e). Likewise the Ca:P ratio showed higher values for rth3 as compared to WT for loam. However, no difference between genotypes was found for sand (Figure 3.2f). A higher investment in root growth to compensate for the lack of absorbing surface provided by root hairs was not found in absolute terms (Figure 3.2b) but in relative terms, at least for loam (Figure 3.2c). The X-ray dose associated with X-ray CT scanning had no significant impact on shoot or root growth with the scan settings and scanning frequency chosen (Figure AF1). The results presented refer to the six scanned replicates per treatment.
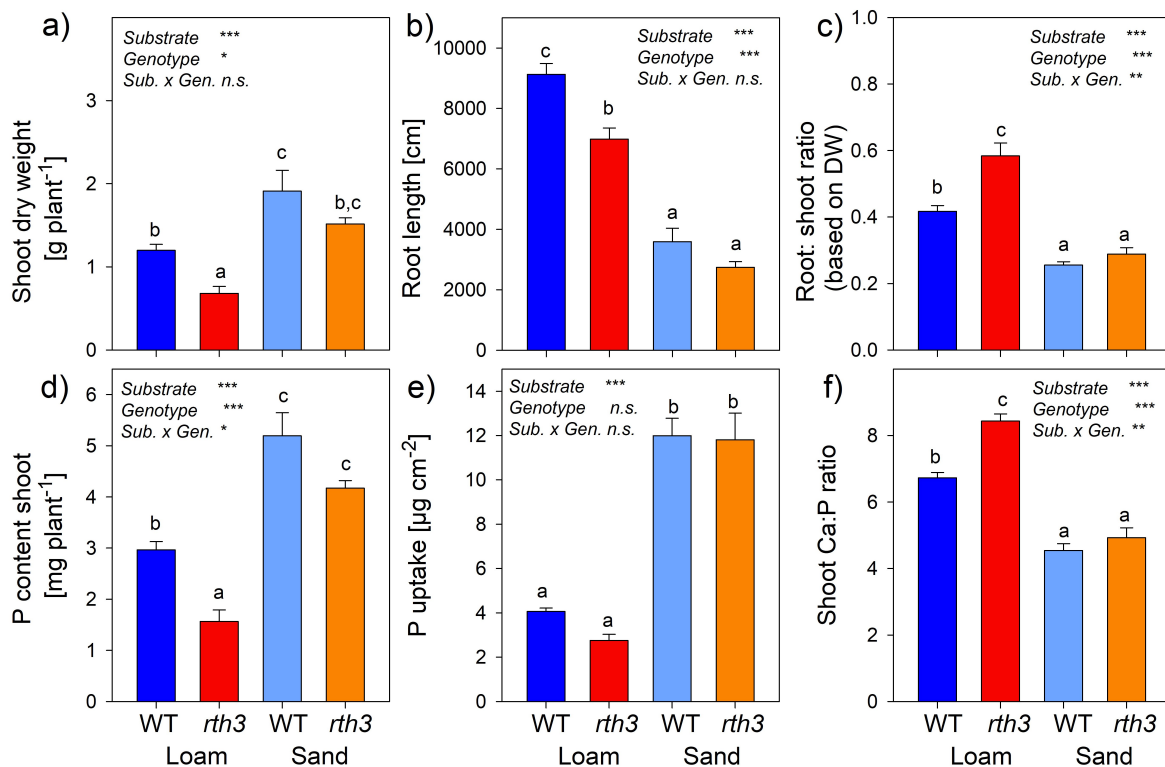
Figure 3.2: Impact of substrate (loam, sand) and maize genotype (wild-type - WT, root hair defective mutant rth3 – rth3) on (a) shoot dry weight, (b) root length, (c) root:shoot ratio, (d) shoot P content, (e) P uptake per unit root surface and (f) the stoichiometric ratio of the mobile element Ca over the immobile nutrient P in the shoot 22 days after planting.

3.3.2 Root system architecture in 4D

Time resolved X-ray CT scanning and superposition of scans from different time points provided insight into the 3D architecture of the root system and its temporal development including qualitative information on root diameters (Figure 3.3). Comparison with the sketch of maize root development clearly shows that, with X-ray CT, the primary roots and seminal roots including their laterals can be identified (pink colour – 7 days). The roots captured additionally at day 14 (green) mainly represent the crown roots and their laterals, while those captured at day 21 represent the brace roots (blue). It should be noted that this simple assignment between scanning events and root type is only valid for the main root axis and differs in detail for the lateral roots. Note that the recovery of roots with X-ray CT was different for the loam and sand and that this difference should be kept in mind for the interpretation of the X-ray CT acquired results. The recovery of roots was equal to 99% (R^2 = 0.84; n = 24) for the sand treatment whereas it amounted to 71% (R^2 = 0.61; n = 19) for the loam treatment (Figure AF2).

3.3.3 Root length density

Root length density profiles (Figure 3.4 and AF3) showed significant differences between substrates for most depth intervals at 14 DAP and the lower ones at 21 DAP.
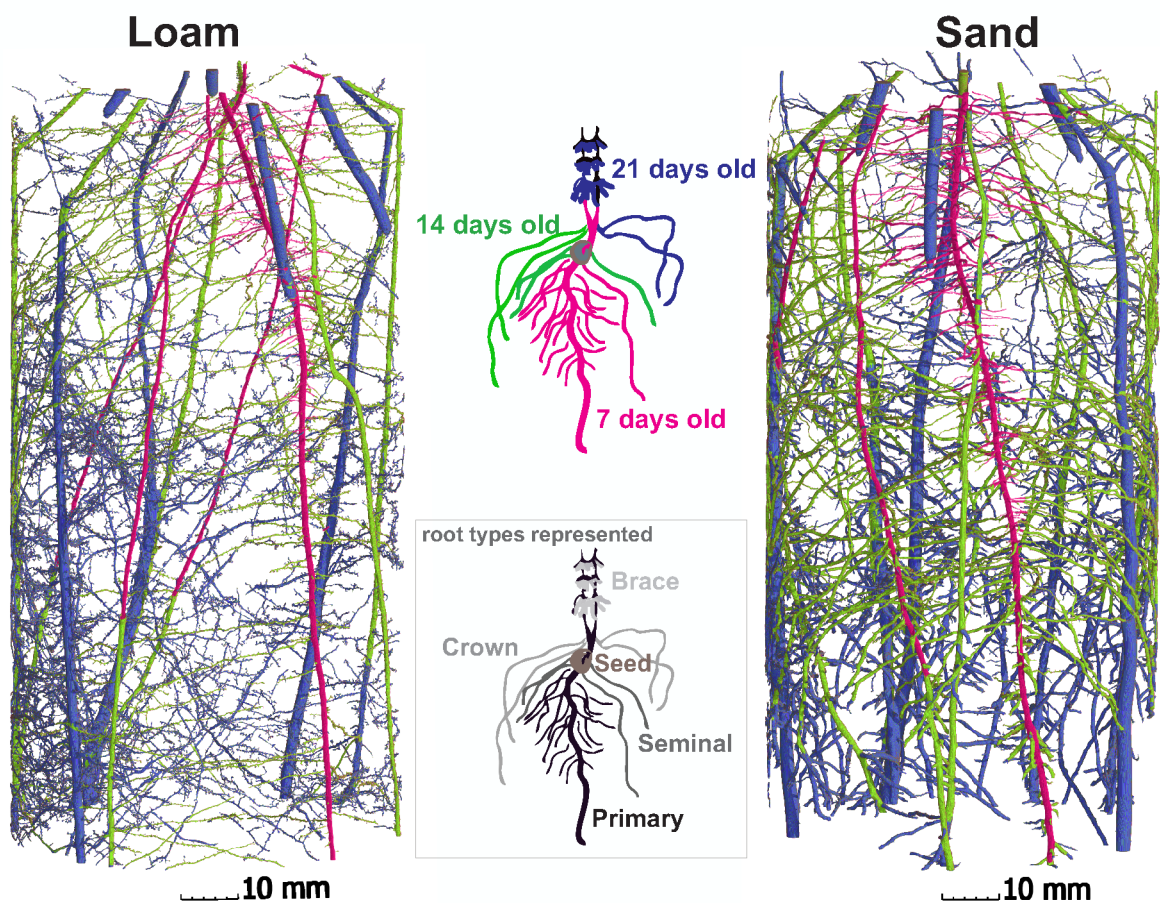
Figure 3.3: Root system architecture (from -1.27 to -14.77 cm depth) derived from X-ray CT scanning at 7, 14 and 21 days after planting (pink = 7 DAP; green = roots grown between 7 and 14 DAP; blue = root grown between 14 and 21 DAP). A representative example for WT (root length of the sample closest to the mean of the six biological replicates per treatment) is shown in both substrates. The sketch in black and gray illustrates the different root types of maize which can be found.

Genotype only had a significant impact on depth exploration at 7 DAP, when overall RLD was still very low. For 21 DAP significant impact of genotype in the upper depth intervals is related to desiccation induced artifact described below. Hence, only the differences found for the lower depth intervals will be discussed further. The strong increase in root length density in the lower part of the columns observed for loam towards the end of the experiment was mostly outside the scanned region. This was quantified by destructive sampling and analysis with WinRHIZO at harvest (Figure AF3). It should be noted that, due to lower recovery of roots in loam than in sand, the root length densities for the loam treatments were underestimated relative to the sand treatments for X-ray CT derived data (Figure AF2, AF3). This was especially true for L _WT on day 21 with the highest proportion of roots <100 μm (Figure AF4).

Depth profiles of differences in RLD between two consecutive scans (Figure 3.5) show that the share of young roots (i.e., <7 days old) in the scanned region is significantly higher for sand than for loam at 14 DAP in most of the lower depth intervals. For loam, plants started to explore deeper unscanned soil layers earlier. At 21 DAP how-

ever, this is reversed, i.e., plants in loam showed significantly higher fraction of young roots in the scanned region.
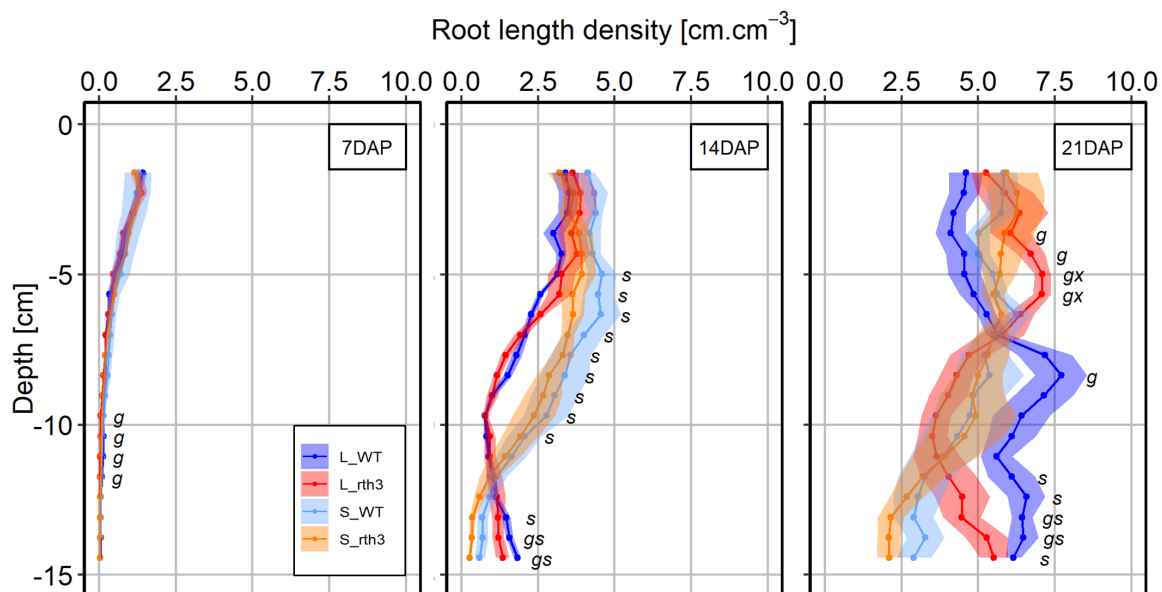
Figure 3.4: Change of root length density with depth for 7, 14 and 21 days after planting for two maize genotypes (wild type - WT, root hair defective mutant rth3 – rth3) grown in loam (L) and sand (S). Data are derived from X-ray CT scanning. The semi transparent ribbons areas represent the standard error around the mean of the measurements (n=6). Two-factorial ANOVA in conjunction with Tukey's HSD tests were conducted for each depth interval. Significant effect of factor is denoted by s for substrate, g for genotype and x for interaction, for $p > 0.05$ no letter is displayed.

3.3.4 Root diameter distribution

Root diameter information is available from X-ray CT for all three scanning events (7, 14, 21 DAP) (Figure 3.6) and from destructive sampling after harvest (22 DAP) (Figure AF4). The comparison of root diameter distributions in selected depth layers shows a good agreement between the two measuring approaches (data not shown). The root diameter distribution from X-ray CT is summarized with mean root diameter profiles to simplify the comparison between treatments (Figure 3.6). Mean root diameter is consistently and, for 14 and 21 DAP also significantly, smaller for plants grown in loam as compared to those grown in sand, irrespective of soil depth or method used for the analysis of root diameter. For loam, a significantly larger share of roots falls into diameter classes < 200 µm (Figure AF4). Differences in root diameter between genotypes are not as obvious; however, for DAP 21 a significant impact of genotype is observed with coarser roots seen for rth3 especially in sand in X-ray CT based data. For destructive sampling a similar tendency is seen. Mean root diameter based on destructive sampling was 360 µm for WT and 390 µm for rth3 in sand, and 230 µm for WT and 240 µm for rth3 in loam, respectively.
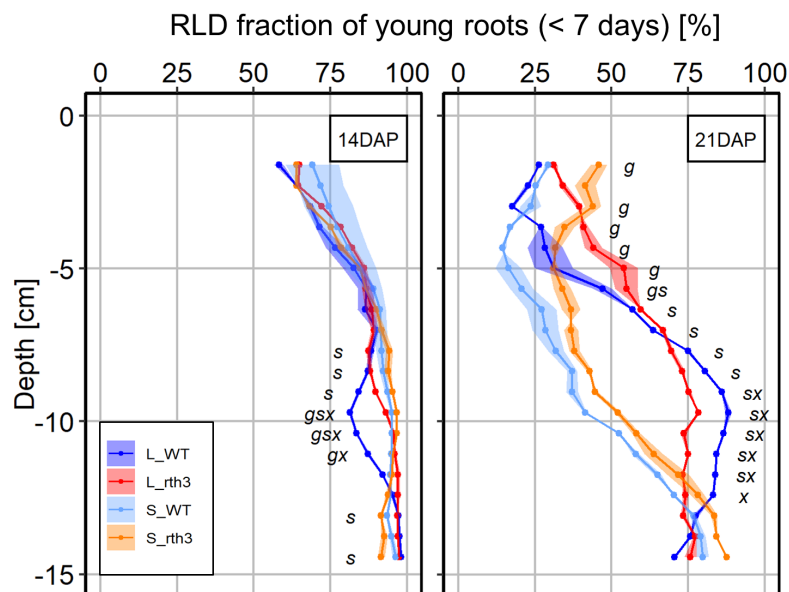
Figure 3.5: Depth distribution of roots younger than 7 days at 14 days and 21 days after planting for two maize genotypes (wild-type - WT, root hair defective mutant rth3 – rth3) grown in loam (L) and sand (S). Data are derived by simple arithmetic operations on the dataset shown in figure 3.4. The semi transparent ribbons areas represent the standard error around the mean of the measurements (n=6). Two-factorial ANOVA in conjunction with Tukey's HSD tests were conducted for each depth interval. Significant effect of factor is denoted by s for substrate, g for genotype and x for interaction, for p > 0.05 no letter is displayed.

3.3.5   Root distance maps

The exploration of the soil by roots can be visualized with root distance maps (Figure 3.7a) and quantified with root distance histograms (Figure 3.7b). The mean root distance in soil is derived from the RDH and differentiated according to soil depth. In general, the mean root distance reflects the root length density rather well (Figure 3.4). That is, an increase in root length density results in a higher frequency of short root distances making large distances less frequent (Figure 3.7b) and hence reducing mean root distance (Figure 3.8). Seven days after planting the root network is poorly developed at the bottom of the field of view and comprises only the primary root and a few seminal roots without laterals, which causes a marked increase of mean root distance with depth. At this early stage the same root length densities in sand and loam evoke different mean root distances across the entire column. This is due to two out of six replicates which had no laterals yet along the primary root at this time point for the treatment S _WT (Figure AF6). Their absence has a huge impact on mean root distance in a sparsely populated soil (7 DAP) that is not reflected to the same degree in RLD. In addition, sand and loam treatments might differ in the spatial arrangement of seminal roots. The seminal roots and the primary root seem to be more clustered in one semicircle of the column wall in loam as compared to more equidistant radial positions in sand (Figure 3.9). At 14 DAP the root length density was higher in sand for almost the entire field of view except for the very bottom (below -12 cm). This difference in RLD was also reflected in the corresponding depth distribution of mean root distance, i.e., shorter mean root distance with a higher RLD and vice versa. At 21 DAP the field
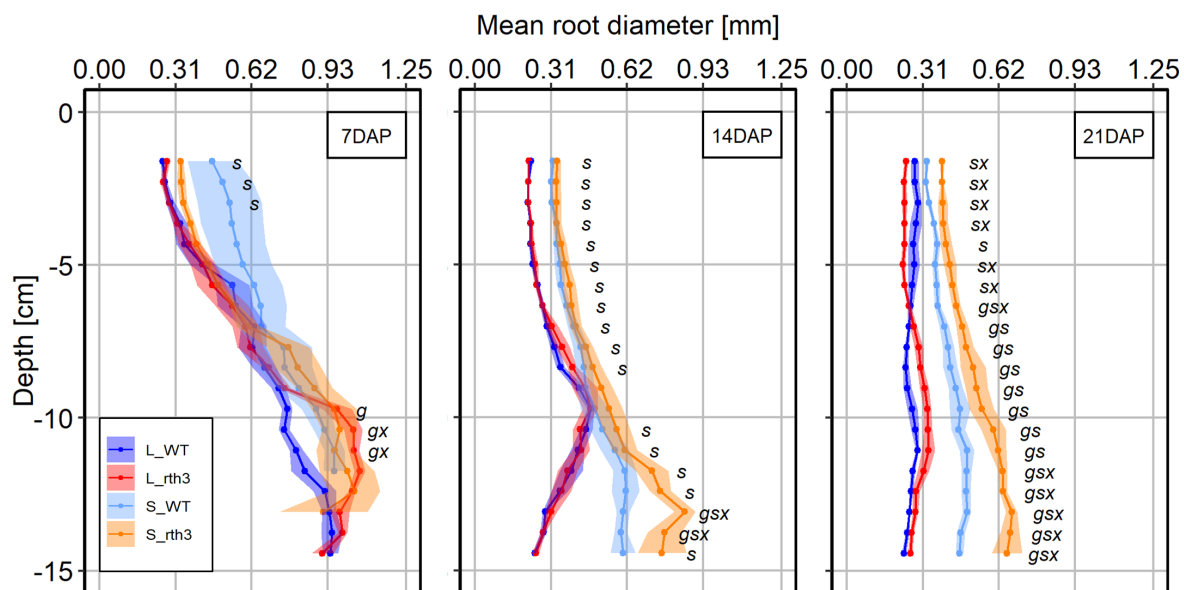
Figure 3.6: *Change of mean root diameter with depth for 7, 14 and 21 days after planting for two maize genotypes (wild-type— WT, root hair defective mutant rth3–rth3) grown in loam (L) and sand (S). Data are derived from X-ray CT scanning. The semi transparent ribbons areas represent the standard error around the mean of the measurements (n=6). Two-factorial ANOVA in conjunction with Tukey's HSD tests were conducted for each depth interval. Significant effect of factor is denoted by s for substrate, g for genotype and x for interaction, for p > 0.05 no letter is displayed.*

of view is already densely populated with roots in both substrates. There seems to be a universal limit of $\approx$ 3 mm below which the mean root distances cannot fall despite different RLD in the range of 4 to 8 cm cm^{-3}. For all scanning events differences in mean root distance between genotypes are absent in both substrates, except for the lowest depth intervals at 7 DAP.

3.3.6 Rhizosphere volume fraction

We recall that the hypothetical rhizosphere volume fractions (Figure 3.9) are directly derived from the root distance histograms by determining the frequency of soil voxels with root distances inferior to 1.8 mm, which we considered to be a typical rhizosphere extent for P. For root hairs of the maize wild-type, we measured the mean root hair length and the retained average value was 0.24 mm with no significant difference between substrates but a tendency towards longer root hairs in sand. For the WT treatment, the root hair effect on the rhizosphere extent was taken into account by simply adding the measured root hair length of 0.24 mm to the rhizosphere extent of 1.8 mm. Again, the vertical distributions of rhizosphere volume fractions reflect root length density profiles for all time points very well. The only deviation from this congruence is a much higher RVF in the top 5 cm at 21 DAP in sand despite similar RLD values in that depth. This increase in RVF was not exclusively due to the larger root diameter in sand, as this would have led to more soil voxels in the direct vicinity of the root interface in the entire scanned region and not just the top. The insets at 21 DAP (Figure 3.9) show
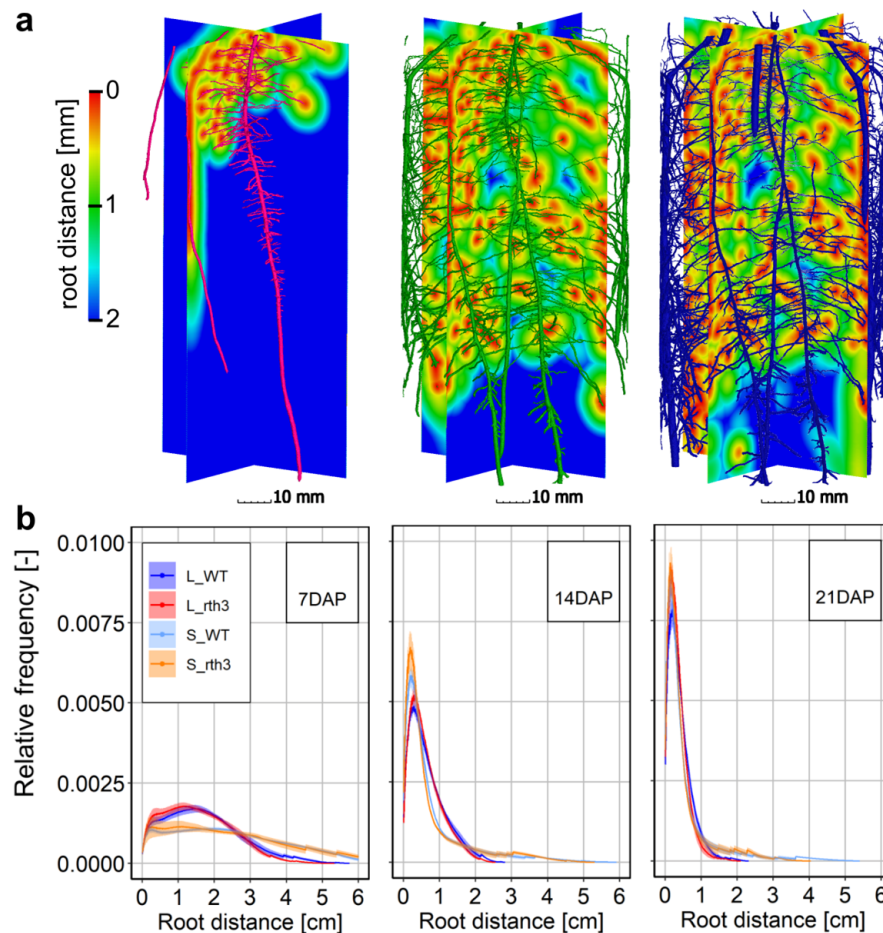
Figure 3.7: *(a) Root distance maps determined 7, 14 and 21 DAP for the S_WT sample depicted in figure 3. b) The root distance histograms are shifted towards shorter distance with increasing root length density over time.*

vastly different RVF (orange) for one loam (a) and one sand (b) column with identical RLD. Roots in loam had a preference for growing along the wall, supposedly in cracks that formed due to desiccation. The rhizosphere of roots growing along the wall was truncated to a semi-circle and contributed less to the RVF. Despite explicitly accounting for hair length, genotype had no significant effect on RVF.

3.4 Discussions

For the discussion part of our work, we will attempt to answer our original hypotheses stated in the introduction.

Is the lack of root hairs compensated by an increased investment in root growth in general and more specifically in the growth of fine roots?

Despite employing two complementary root system architecture measurements (X-ray CT, destructive sampling), we did not observe an increase in fine root growth as a compensation for the lack of roots hairs. This is surprising, as the mutant exhibited a plastic response in root growth with respect to substrate. This finding is in contrast to
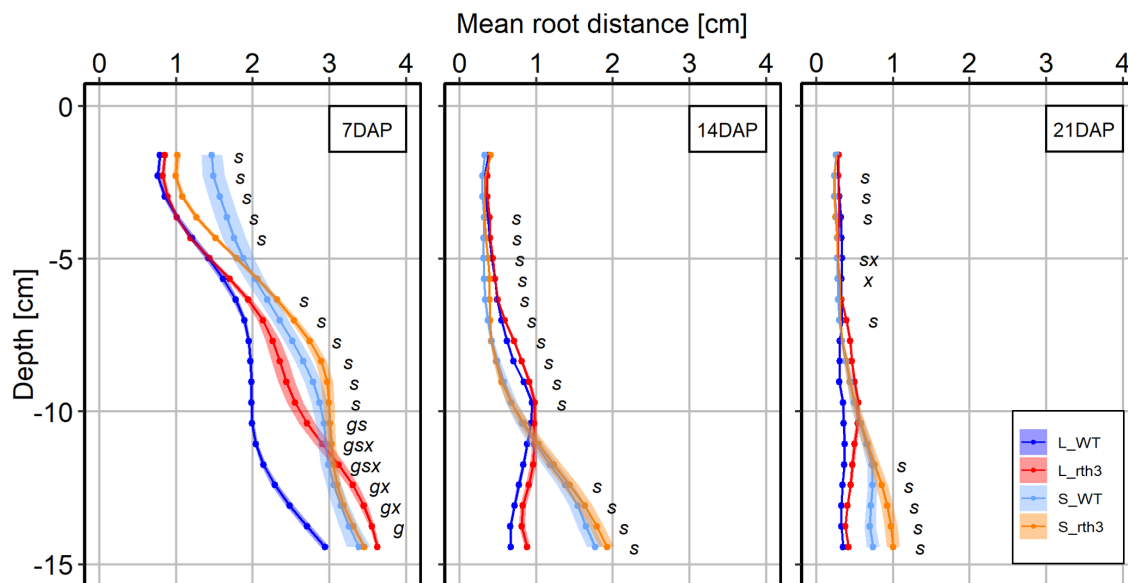
Figure 3.8: *Depth profile of mean root distance for 7, 14 and 21 days after planting for two maize genotypes (wild-type - WT, root hair defective mutant rth3 – rth3) grown in loam (L) and sand (S). The semi transparent ribbons areas represent the standard error around the mean of the measurements (n=6). Two-factorial ANOVA in conjunction with Tukey's HSD tests were conducted for each depth interval. Significant effect of factor is denoted by s for substrate, g for genotype and x for interaction, for p > 0.05 no letter is displayed.*

the one by Klamer et al. (2019) who compared *Zea mays* WT to the root hair defective mutant rth2. They reported a shift towards finer roots for the mutant. However, in order to detect this shift, they had to compile data across treatments differing vastly in P and water supply. Their plants were growing in subsoil material and were non-mycorrhizal, while the plants in the present experiment showed first signs of mycorrhizal colonization (Table AT1) despite the early growth stage. A more intense infection with mycorrhizal fungi as a compensation for the lack of hairs was suggested by Li et al. (2014) for barley and confirmed by Kumar et al. (2019) for maize, but only for later growth stages.

The type of mutation is another potential explanation for the differences in compensation mechanism observed by Klamer et al. (2019) and the present experiment. In mutant rth3 the mutated gene encodes a GPI-anchored COBRA like cell wall protein involved in the organization of the synthesized cellulose (Hochholdinger et al., 2008). For the rth2 gene, the mechanism is not yet identified. In general, a significantly higher investment in root growth by the root hair defective mutant as it is reported in literature (Dodd & Diatloff, 2016; Klamer et al., 2019) is also found in the present study, although only in relative but not in absolute terms and only for loam, i.e., the substrate with lower P mobility. The shift in root:shoot ratio was not sufficient to compensate for the lack of hairs as total P uptake was significantly lower for rth3 as compared to WT in loam. With respect to physiological plasticity our results are inconsistent. While without morphological and physiological compensation lower uptake rates per unit root are expected, we found no significant differences in normalized P uptake between the genotypes, with only a tendency towards lower values for rth3 in the substrate with the lower P mobility. In general, much lower P uptake rates per unit root surface were found for loam as compared to sand, despite the low plant P status in loam (leaf tissue P concentration

Rhizosphere volume fraction [%]
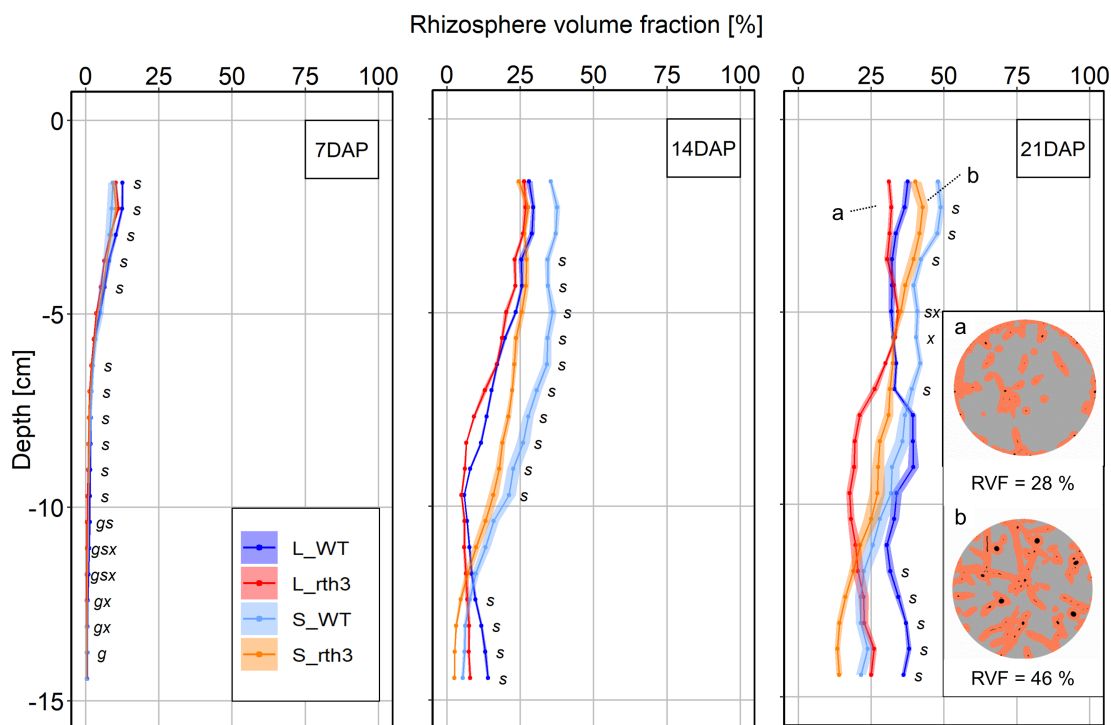
Figure 3.9: Depth profile of rhizosphere volume fraction for 7, 14 and 21 days after planting for two maize genotypes (wild-type - WT, root hair defective mutant rth3 – rth3) grown in loam (L) and sand (S). Rhizosphere volume fraction is determined assuming a typical rhizosphere extent of < 1.8 mm for P depletion reported by Hendriks et al. (1981) for 5 days old root segments. For the wild-type 0.24 mm were added to account for hair length. The semi transparent ribbons areas represent the standard error around the mean of the measurements (n=6). Two-factorial ANOVA in conjunction with Tukey's HSD tests were conducted for each depth interval. Significant effect of factor is denoted by s for substrate, g for genotype and x for interaction, for p > 0.05 no letter is displayed.

of 2.4 mg g^{-1} for rth3 and 2.6 mg g^{-1} for WT), which is expected to trigger expression of high affinity P transporters. This is in line with relative root gene expression data for the same experimental set-up, reported by Ganther et al. (2021). They did not find gene functions relating to phosphate uptake to be differentially expressed between WT and rth3. It is still possible that the activity of the transporters is regulated at the protein level, since apart from transcriptional regulation, post-translational modifications of phosphate transporters are widespread (Vetterlein & Tarkka, 2018).

For soil based systems, uptake rate per unit root is strongly influenced by diffusion and root-soil contact. Haling, Brown et al. (2013) found significantly lower P uptake rates per unit root length for the root hair defective mutant of barley compared to the wild-type, for high but more so for low P soils. Root hairs were relevant for maintaining contact in loose soils and for improved penetration in dense soils. The importance of hairs for P uptake in particular under conditions of restricted P transport is confirmed by observations in hydroponics, i.e., systems with no major limitations for transport. N. Suzuki et al. (2003) found in hydroponic systems no differences in P uptake rates per unit root dry weight between rice genotypes differing in root hair development, irre-

spective of P supply. The differences between substrates observed here are related to their differences in P diffusion.

> *Is the role of root hairs for anchorage causing an adaptation in root system architecture? – How does this relate to soil exploration?*

Bengough et al. (2016) have demonstrated the importance of root hairs for anchorage using the same maize genotypes as in the present study. Peak anchorage forces were up to five times greater for the wild-type compared to the root hair defective mutant. As a consequence, wild-type primary roots penetrated deeper into the soil during a given time interval as compared to the mutant. The difference was five fold at low bulk density and decreased continuously with increasing bulk density/mechanical impedance. At the bulk density and water content (Figure AF5) investigated in the present experiment, penetration resistance in both substrates was below 0.2 MPa (Rosskopf et al., 2021) (see also figure AF13). This value is one order of magnitude below the critical value for root elongation rate of 2 MPa suggested by Bengough et al. (2011). With two exceptions no differences were observed in depth exploration between the two genotypes within the same substrate. At 7 DAP, wild-type showed significantly higher values in the lower depth intervals, which is in line with the postulated role of hairs for anchorage, however in absolute values these differences were very small. A distinct exception occurred for the last time point in loam most likely due to a technical artifact. During the last four days of growth, plant water consumption for wild-type in loam was so high, that short-term desiccation of top soil occurred between the watering events. This likely caused root shrinkage, which in turn reduced recovery with X-ray CT. The study of Bengough et al. (2016) focused on the very early growth stage, i.e., 3 days after germination with just the primary root (1 to 3 cm long) at the start of the experiment and a duration of the experiment of maximum 48 hours. At later growth stages, it can be expected that lateral root formation as well as seminal roots partly take over the function of anchorage from the hairs (Bailey et al., 2002). In our experiment, lateral roots on the primary root were abundant at 7 days after planting (Figure AF6).

Root distance histograms were derived from X-ray CT data to quantify soil exploration in more detail, as they simultaneously take into account the actual 3D geometry, differences in length and diameter (Schlüter et al., 2018). Root distance histograms or the mean root distance derived from these data (Figure 3.7, 3.8) are a very sensitive measure in particular at early growth stages when soil exploration is poor. This is indicated by the strong impact of delayed lateral root formation in two out of six replicates being reflected in mean root distance but not in RLD. While the measure nicely reflects the progressive exploration of the soil columns from top to bottom and over time with distinct differences between substrates, no significant differences between genotypes were observed. At later growth stages, when root length densities were higher a limit in mean root distance of 3 mm was attained. Such a limit of approximately 3 mm was also reported by Lucas et al. (2019) for root-induced biopores in undisturbed field samples. This suggests that an investment in more root growth may not pay off in terms of better soil exploration but only increase competition between roots for the same resources. However, whether that is really the case would be better assessed with nutrient specific rhizosphere volume fractions, which are more sensitive to growth patterns at high RLD.

For the RVF, for which the measured root hair length (0.24 mm) was explicitly added to the assumed extent of the P depletion zone (1.8 mm derived from Hendriks et al. (1981)) for the wild-type, no significant effect of genotype was detected at 14 and 21 days after planting at all depths. The RVF reached 25 to 50% at day 21 (Figure 3.9), indicating that a large fraction was already explored for P at this early stage. Note that these results are hypothetical and depend on the assumed extension of rhizosphere. More accurate RVF estimates would require spatially resolved information about radial depletion patterns of plant available P on multiple, intact rhizosphere sections to capture them representatively.

It should be noted that the measured root hair length of 0.24 mm is rather short as compared to literature data. Frequently higher values in the range of 0.7 to 0.9 mm are reported for maize (Hendriks et al., 1981; Weber et al., 2018). In general root hair lengths can vary with soil P status and bulk density (Haling, Brown et al., 2013; Jungk, 2001); there was a tendency towards longer root hairs in sandy substrate. Increasing hair length in our calculation of RVF would result in higher values (Figure AF7). This increase is linear for realistic root hair lengths. The relative importance of root diameter over root hair length for RVF would increase as the extension assumed for the rhizosphere process in question decreases. Root length density is the dominant factor that governs differences in RVF. However, genotype (i.e., added hair length) and substrate had an additional impact (Figure AF8). For the latter one cannot disentangle the preferential growth along the wall in loam (fewer neighboring soil voxels for roots at the wall) from the differences in root diameter (increasing the number of neighboring soil voxels with circumference) between loam and sand. These results are valid irrespective of the exact value for the hypothetical spatial extent of P depletion, i.e., for the only variable that could not be measured in our study.

Is the difference between wild-type and mutant larger in a substrate with a high sorption capacity, i.e., low mobility of the limiting nutrients?

Nutrient mobility is expected to be lower in loam as compared to sand considering that loam has a higher number of sorption sites due to its higher content of Fe-oxides, clay and organic matter (Vetterlein et al., 2021). Interpretation of biomass nutrient concentration *per se* is confounded by dilution through growth. Interpretation of shoot nutrient uptake is confounded by differences in shoot size and hence nutrient requirement. To evaluate differences in mobility we therefore used not only P uptake itself, but in addition the stoichiometric ratio of Ca (having a high mobility in soils) over P (having a low mobility in soils) (Ågren & Weih, 2012). For our substrates Ca:P ratio was well suited to show the differences between genotypes for loam. Differences between genotypes were significant for most of the measured growth and uptake parameters in loam, but not in sand. This is in line with our hypothesis and the observation of others (Haling, Brown et al., 2013; N. Suzuki et al., 2003), i.e., roots hairs only matter if transport to the root surface is limiting the uptake.

Why do we see a high plasticity with respect to substrate, but only small compensation for the lack of root hairs?

While differences between genotypes in root traits were small in loam or absent in sand for most time points and soil depths, they were very prominent between substrates, irrespective of genotype. This is all the more remarkable as X-ray CT measurements systematically underestimated the root length (in particular fine roots) in loam.

Differences between substrates were observed for root diameter, for depth distribution of RLD, share of young roots and the associated measurements such as mean root distance and RVF. While some literature suggests that intensive fine root development can increase P uptake (Lynch, 2011; Richardson et al., 2009), this is only true if P is non-uniformly distributed, e.g., greater in topsoil than in the subsoil. In uniform low P, it is more common that exploratory behavior is favored, with increased branching only occurring when a patch of greater P is encountered. As reviewed by Mollier und Pellerin (1999), a shift in root:shoot ratio is found in most studies, but results regarding root length or more specific root traits are inconsistent. In their own study with maize, they observed only a transient promotion of root growth 4 days after P starvation, which was related to carbon partitioning between shoot and root. Despite these findings, there is an agreement that local increase in P supply promotes lateral root formation in a P deficient system (Gao, Blaser et al., 2019). In the current experiment, we rule out P supply as a reason for shift in root traits between substrates. Indeed, P supply was homogenous and no differences between genotypes in loam were detected, despite their difference in P uptake. Roots in loam showed a shift to smaller root diameter classes (Figure AF4) and smaller mean root diameters across all depth intervals and both genotypes (Figure 3.6). Differences in root diameters were detected early on and were very consistent at later time points. Changes were observed in all diameter classes. Careful inspection of segmented images (Figure 3.3) indicated that all root types were affected, i.e., it was not only due to a shift in the share of main axis (primary, seminal, crown, and brace roots) and lateral roots. It should be noted, that for 21 DAP an additional differentiation in root diameter between genotypes was observed. Especially in sand coarser roots were detected for rth3 compared to the wild-type.

The most frequent cause for shifts in root diameter reported in literature is alterations in soil compaction, bulk density and mechanical impedance, which are tightly linked with changes in soil water content and gas diffusion (Bengough et al., 2006, 2011; Clark et al., 2003; Colombi & Walter, 2016; Correa et al., 2019). Root diameter increase by up to 2-fold in case of mechanical impedance has been reported, as a result of cortical cells expanding radially due to microfibril reorientation in the primary cell wall (Bengough et al., 2011). Causal relationship is straight forward, if increasing bulk densities within the same soil/substrate are investigated (Haling, Brown et al., 2013; Tracy et al., 2012). An increase in root diameter upon compaction was also observed for our loam in a parallel experiment (Table AT2). When comparing different substrates causal relationships are more difficult to unravel. Kirby und Bengough (2002) have nicely shown for the comparison of a sandy loam and a clay loam that penetration resistance alone is not sufficient to predict root thickening. They demonstrated that local values of axial and shear stresses experienced by the root near its tip may be as important as penetration resistance in constraining root growth. Ethylene is often associated with the morphological response of roots to mechanical impedance (Clark et al., 2003; Dreyer & Edelmann, 2018). Increased levels of ethylene have been observed to induce increase in root diameter even for unimpeded roots (Baluška et al., 1993). An induced expression of genes related to phytohormone signalling was detected only in sand by Ganther et al. (2021) in an experimental set-up like the one used here. Ethylene, but also gibberellic acid and jasmonate were affected, which indicates that processes related to development and growth are altered by the substrate. Further studies are required to evaluate whether observed differences can be explained by

mechanical properties beyond mechanical impedance (Kirby & Bengough, 2002), root (B. Ma et al., 2013; Pandey et al., 2021) or microbiome ethylene production (Y. Zhang et al., 2020) or differences in diffusion processes within the root or in the rhizosphere (Hartman, 2020). Anoxia as a trigger for ethylene production is ruled out for our system, at least not beyond occasional microsites. At the volumetric water content used in this experiment (22 % in loam, 18% in sand), air filled pore volume is well above 10% even at the bottom of the sand columns (Vetterlein et al., 2021).

Increase in root diameter in sand as compared to loam did not result in an increased investment in root growth in general. Root:shoot ratio was lower in sand. This suggests that plant demands in terms of water and nutrients could be covered with a less intensive soil exploration. As differences in P uptake did not occur in sand it is difficult to assess whether compensation for the lack of root hairs did not occur in sand because there was no need for it or because fine root growth was hindered by other factors in this substrate. Unfortunately, no support for either possibility can be derived from the data of Klamer et al. (2019) as they have evaluated changes in diameter across all treatments including two textures.

System limitations – relevance for field conditions

It should be noted that despite major advances in root segmentation in the past years (Phalempin et al., 2021a; Soltaninejad et al., 2020), we still face the trade-off between image resolution and sample size resulting in fine roots being partly missed out. In the present case, this afflicts the differences between sand and loam as the share of fine roots was larger in loam. Smaller column diameter associated with a higher scanning resolution would have overcome this problem, but would have restricted our experiment to even shorter growth period. One could argue that already in the present set-up results after 14 days are less confounded by the limited volume than the ones obtained 21 days after planting. This is also reflected in the higher standard errors observed for the later time point. Shorter growth duration would make it even more difficult to account for interaction of roots with the microbiome, in particular the mycorrhizal symbiosis, which is only starting to interact within the given time (Vetterlein & Tarkka, 2018). Moreover, we emphasize the limitation of pot trials for the study of exploration strategies. The limited soil volume of pot trials may induce feedback loops which would not be observed in the field at the same time point. Comparison of present data with those from the field with the same treatments (Vetterlein et al., 2021) will not only show whether the findings are consistent but in particular how much we can learn under controlled conditions about the behavior in the field.

3.5   Conclusion

Adaptations in root system architecture in response to lacking root hairs were investigated with a comprehensive experimental set-up that combined nutrient uptake analysis, destructive root sampling and X-ray CT scanning. This allowed monitoring various root system architecture metrics over time. The CT derived metrics enabled the quantification of soil exploration and the integration of the effect of various root traits, i.e., root diameter, 3D-distribution, depth distribution, hair length. Experimental conditions were well suited to confirm the general consensus on root hairs being of

particular relevance for uptake of low mobility nutrients such as P, especially in soils with a high sorption capacity. Root hair defective mutants showed low plasticity of root traits related to limited P availability, despite their general ability to express high root plasticity. The function of the root hairs for anchoring did not result in different depth profiles of the root length density. We suggest that, in more developed root systems, as in our experiment, part of the anchoring function can be taken over by lateral roots. Both maize genotypes showed a marked response to substrates differing in soil texture mainly reflected in mean root diameter. Increase in root diameter is typically induced by higher penetration resistance. However, penetration resistance was low at the given water content in both substrates. Further experiments are required to elucidate whether observed differences can be explained by mechanical properties beyond mechanical impedance, root or microbiome ethylene production or differences in diffusion processes within the root or in the rhizosphere. A more systematic literature review including studies comparing textures at different levels of nutrient supply is needed. Results from field studies comparing different substrates under the same environmental conditions can also help to unravel the mechanisms involved.

CHAPTER *4*

SOIL BULK DENSITY IN THE VICINITY OF ROOTS

Rhizosphere soil is known to differ from the bulk soil due to numerous physicochemical processes induced by root growth. The spatial extent and magnitude of the influence of roots on the surrounding soil is still debated controversially. To date, most studies focused on a limited number of soil types and plant species and were carried out under homogeneous soil structure conditions (i.e., finely sieved and repacked soil). With the help of X-ray CT, we present the results of an image processing workflow, which enabled to analyze soil structure around roots of maize plants under different degrees of soil structure heterogeneity. We analyzed more than 400 samples extracted during laboratory and field experiments covering various combinations of texture, bulk density, packing heterogeneity, maize genotype and soil moisture. We show that soil texture and structure heterogeneity predominantly governs the magnitude of bulk density alteration around roots. In homogeneous soil structure, roots had to create their own pores by pushing away soil particles, which confirms previous findings. Under more heterogeneous conditions, we found that roots predominantly grew in existing pores without inducing compaction. The influence of root hairs, root length density, plant growth stages had no or little impact on the results. The effect of root diameter was more pronounced in sand than in loam. Fine roots caused sand grains to align along their axis whereas big roots broke the fragile arrangement of grains. Our findings have implications for water and solute transport dynamics at the root-soil interface, which may affect plant productivity.

4.1 Introduction

Characterizing soil properties at the root-soil interface is key to a better understanding of environmental processes and to the promotion of sustainable agriculture. Indeed, this interface mediates water and nutrient uptake as well as root exudates distribution and diffusion. The zone of the soil in the vicinity of roots which is influenced by them is termed the "rhizosphere" whereas the zone which is not impacted by the roots is referred to as the "bulk soil". The rhizosphere soil is known to differ from the bulk soil due to the numerous physical, chemical and biological processes induced by root growth (Hinsinger et al., 2009; Rugova et al., 2017; Vetterlein et al., 2020; Whalley et al., 2005). Such processes include particle rearrangement, which may lead to soil compression or loosening (i.e., to an increase or decrease of local bulk density), both of which are known to alter water regimes and gas exchanges in the soil (Menon et al., 2015; Pla et al., 2017). The earliest evidences of the influence of soil particle rearrangement by roots suggested a compaction effect, as assessed visually with microscopy (Barley, 1954; Bruand et al., 1996). More recently, the advent of X-ray computed tomography (CT) has offered the possibility to investigate the rhizosphere with unprecedented accuracy and non-destructively. In the last decade, this motivated researchers to determine rhizosphere soil properties for different soil types and plant species. To date, however, the literature is still controversial regarding the magnitude and spatial extent of the influence of roots on the surrounding soil. Some studies reported root-induced soil compaction (Aravena et al., 2011; Vollsnes et al., 2010) whereas some studies observed a zone of looser soil around the roots (Burr-Hersey et al., 2020; Helliwell et al., 2017). Some other studies reported both, i.e., a zone of higher porosity at the direct root-soil interface followed by a zone of lower porosity farther away (Helliwell et al., 2019; Koebernick et al., 2019, 2017; Lucas et al., 2019). Moreover, most of these studies have been carried out in laboratory conditions with repacked and finely sieved soil. There is currently a lack of knowledge as to how the results acquired under laboratory conditions can be transferred to field conditions where the soil heterogeneity is greater.

On one hand, root-induced soil compaction can be attributed to the fact that the volume that roots occupy in soil has to be accommodated by an equal loss of the pore space volume. Dexter (1987) was the first to mathematically describe root-induced compaction when considering the radial expansion of roots in soil. On the other hand, an increase of macroporosity in the rhizosphere was attributed to fluctuations in water content due to root water uptake and/or to wetting and drying cycles, which were shown to be responsible for crack formations (R. Ma et al., 2015), especially in clayey soil (Yoshida & Hallett, 2008). Increase of porosity in the vicinity of roots was also attributed to the phenomenon of root shrinkage occurring during soil desiccation (Carminati et al., 2009). Another mechanism, which can potentially explain the macroporosity increase at the root-soil interface is the packing of soil particles at the root surface (Koebernick et al., 2019). The influence of packing of convex particles around a larger rigid surface is known to generate a zone of higher porosity at the interface between the particles and the rigid surface. This phenomenon is known as the "surface wall effect" and it has been studied both experimentally and mathematically for randomly packed beds of spheres in cylindrical containers (Guo et al., 2017; Mueller, 2010; Reimann et al., 2017; M. Suzuki et al., 2008).

The initiation of root hairs is one root trait among many, which enables plants to adapt to environmental conditions. Root hairs provide a significant advantage for plant growth, particularly under conditions which restricts root elongation (e.g., in compacted soils) (Haling, Brown et al., 2013). The role of root hairs in root tip anchorage was suggested by Stolzy und Barley (1968) and later experimentally demonstrated by Bengough et al. (2016) for very young primary roots of maize plants still lacking laterals. The advantage in anchorage provided by root hairs may suggest that, by penetrating soils having a higher mechanical resistance, roots of a hair-bearing plant genotype may compact the soil more because of their greater ability to push away soil particles or to ingress denser soil aggregates instead of being deflected by them. Root hairs are also known to influence the rhizosphere soil by promoting soil aggregation (Moreno-Espíndola et al., 2007). Root hairs enable higher transpiration rates under drying conditions (Carminati et al., 2017), which would, in turn, increase the likelihood of crack formation and thereby increase macroporosity. The effect that root hairs may exert on soil particles is still debated controversially. Using X-ray CT scanning, Koebernick et al. (2017) found that a barley genotype with root hairs had a significantly greater soil pore volume fraction at the root–soil interface, as compared to the root hair defective mutant. However, no differences in pore structure were found for the same genotypes investigated in a subsequent experiment in which the sieving procedure was modified (Koebernick et al., 2019).

Based on the literature, it seems that the extent to which the soil around roots differs from the bulk soil might be the result of interacting factors such as soil type, plants species (Helliwell et al., 2019) and the presence of root hairs (Koebernick et al., 2017). In an attempt to reconcile contrary views on the subject, Lucas et al. (2019) introduced a new conceptual model, which suggests that the initial soil structure, i.e., the availability of pores big enough for roots to grow into, is the governing factor to predict root-induced soil compaction.

In this work, we present an extensive study of bulk density (BD) distribution extending from the root surface to the bulk soil using X-ray CT. Specifically, we investigated the following hypothesis:

- Changes in soil structure around roots depend on the particle size (i.e., the texture) and the spatial arrangement of soil particles (i.e., the structure). Following up on the work of Lucas et al. (2019), we hypothesize that root-induced compaction, if observed, will be greater in a structurally homogenous environment (i.e., finely sieved and repacked soil) as compared to a heterogeneous environment (coarsely sieved and structured soil);

- Modification of soil structure induced by root growth depends on root diameter. In line with the mathematical background provided by Dexter (1987), we hypothesize that root-induced compaction, if observed, will be greater for big roots than for fine roots due to the increased volume of big roots;

- The presence of root hairs has an influence on the modification of soil structure induced by root growth. Bearing the experimental results of Bengough et al. (2016) in mind, we hypothesize that root-induced compaction, if observed, will be greater for roots with root hairs as compared to roots without root hairs due to the role of root hairs in providing anchorage.

In order to address these hypotheses, we compiled data from several laboratory and field experiments. Specifically, we characterized bulk density distribution extending from the root surface into the bulk soil for two *Zea mays* genotypes (i.e., one root hair-bearing genotype and one root hair defective mutant) grown in two different soil textures (i.e., loam and sand), in experiments in which the soil sieving, packing procedure and bulk density differed. Thanks to the sampling at different plant growth stages and to the different plant growth conditions in the field and in the laboratory, additional insights are provided regarding the influence that the age of the rhizosphere, its desiccation history and the root length density has on rhizosphere soil structural properties. With the help of X-ray CT, we present here the results of an image processing workflow, which enabled to analyze bulk density in the vicinity of roots for more than 400 samples.

4.2 Material and Methods

4.2.1 Genotypes

In order to determine the influence of root hairs on rhizosphere soil structural properties, the *Zea mays* genotype root hair defective mutant (rth3) and the corresponding B73 wild-type (WT) were selected for the growth experiments. The mutant rth3 shows normal root hair initiation but disturbed elongation. It shows no aberrant shoot phenotype but grain yield is reduced by 19 to 42% as compared to the wild-type (Hochholdinger et al., 2008).

4.2.2 Soil material

The substrate loam (L) was obtained from the upper 50 cm of a haplic Phaeozem soil profile. The substrate sand (S) constitutes a mix of 83 % quartz sand (WF 33, Quarzwerke Weferlingen, Germany) and 17 % of the loam. Details on chemical and physical properties are provided elsewhere (Vetterlein et al., 2021). The loam and sand substrates were the same for all experiments carried out in this study. However, soil structure differences across experiments arose due to differences in sieving and packing procedures.

4.2.3 Experimental set-up and sample preparation

4.2.3.1 Field experiment

The field experiment was established in Bad Lauchstädt, Germany (51°22′0′′ N, 11°49′60′′E). In order to ensure homogeneity in terms of soil structure at the start of the experiment, 24 individual rectangular pits (11*3.1 m) were excavated to a depth of 1 m. The pits were filled with a 25 cm thick gravel layer and a 75 cm thick layer of the loam or sand packed to a BD of 1.36 and 1.5 g cm^{-3}, respectively. The loam was sieved using a heavy duty double deck vibrating screen (Keestrack Combo; 3.2 m^2 area per deck) having a mesh aperture of 20 mm. After sieving, the loam was gradually placed in layers of 15 cm by a wheel loader (Volvo EW140C), evened out with the wheel loader bucket and compacted with a vibrating plate (weight 70 kg with a pressure of 80 kPa at

reduced speed). For the sand plots, a similar procedure was employed but no vibrating plate was used. Treatments were established in twelve replicates for each soil type. Out of the twelve plots of one soil type, six were planted with the WT genotype, the other six with the rth3 genotype. More information regarding the field plot set-up and the plant growth conditions in the field experiment is provided by Vetterlein et al. (2021). In the field experiment, two approaches were chosen to obtain the samples. Figure 4.1 provides an overview of the experimental design of the two sampling approaches in the field. Table 4.1 summarizes the difference between the two approaches in terms of sieving and packing procedure.
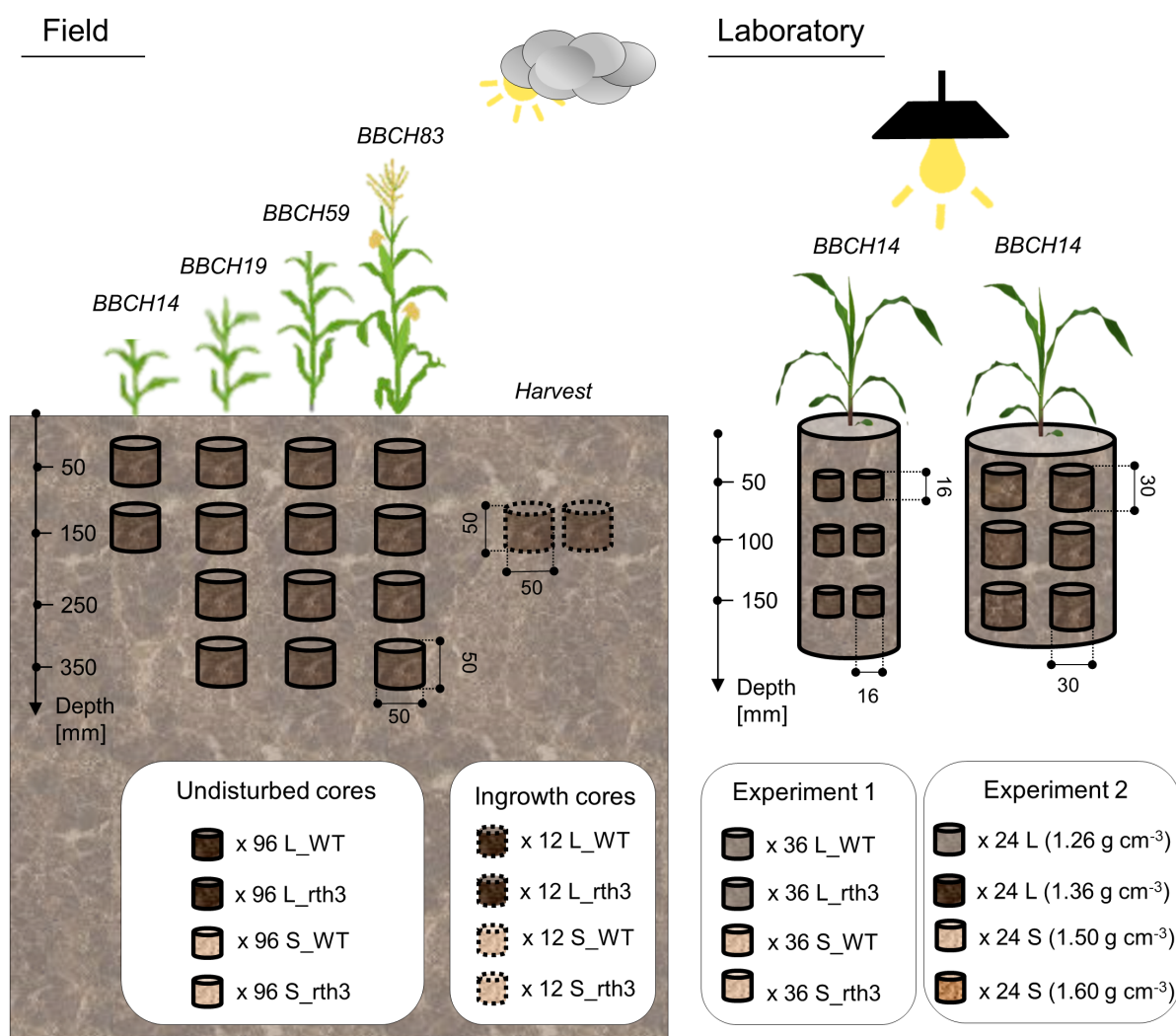
Figure 4.1: Overview of the experiments conducted in the field and in the laboratory where the number of samples extracted is specified for each treatment. The drawing is not to scale. Dimensions are expressed in millimeters. The letters "L" and "S" refers to loam and sand, respectively whereas the acronyms "WT" and "rth3" refer to the wild-type and root hair defective mutant, respectively. Note that the number of samples refers to the total number of samples extracted and not to the number of samples analyzed for the characterization of rhizosphere soil properties (i.e., samples with no roots were excluded).

The first approach entailed the sampling of undisturbed cores at different plant growth stages during the growing season. The cores were extracted with aluminum

cylinders of 5 cm in height and diameter. The sampling campaigns were carried out at different growth stages, i.e., BBCH14, BBCH19, BBCH59 and BBCH83, in accordance with the German coding of phenological growth stages of maize (Bleiholder et al., 2001). At BBCH14, the sampled depth intervals were 2.5-7.5 and 12.5-17.5 cm considering the shallow rooting depth of the plants at this early growth stage. For the later growth stages, cores were taken at the depth intervals 2.5-7.5, 12.5-17.5, 22.5-27.5 and 32.5-37.5 cm in the same pit in between the maize rows. Once the cores were extracted, they were stored at 4°C in sealed plastic bags in order to avoid desiccation prior to CT scanning. In total, 384 undisturbed cores were extracted from the field. The first approach investigated the effect of soil structure heterogeneity, plant growth stages and soil moisture conditions on rhizosphere soil structure properties. It aimed at capturing field conditions as well as possible.

The second approach entailed placing ingrowth cores underneath the growing plants and leaving them during the entire growing season in order to allow the roots to populate the cores. The cores were packed in plastic cylinders of 5 cm in height and diameter. The wall, the top and bottom of the cylinders were perforated with a drill of 2 mm in diameter so that roots could enter the cores from all sides. The loam in the ingrowth cores was filled in the laboratory with soil sieved down to 2 mm, i.e., it is more homogenous than in the undisturbed cores. The sand originated from the sieved material used to fill the plots in the first field experiment (i.e., sieved down to 20 mm) and was not further sieved down as all sand grains that make up the typical granular structure would have passed the 2 mm sieve anyway. The bulk density to which the ingrowth cores were packed was the same as in the field plots. The soil was gradually filled by layers of 1 cm and gently consolidated at each filling step. Once packed, the cores were buried in field plots and two cores per plot were placed next to each other at 15 cm depth right underneath a plant shortly after germination. The location was accessed laterally through an excavated tunnel so that the topsoil in the field plot was not disturbed. In total, 48 ingrowth cores were buried in the field plots. At harvest, they were extracted and stored at 4°C in sealed plastic bags in order to avoid desiccation prior to X-ray CT scanning. The motivation behind the establishment of the second approach was to create a different growing environment for roots by combining a finer sieving (for loam) and a more uniform packing of the soil as compared to the undisturbed cores and to still capture field conditions.

4.2.3.2 Laboratory experiments

The laboratory experiments were conducted with soil columns in a climate chamber. The climate chamber was set to 22°C during the day and 18°C at night with a 12 hours light-period, 350 µM m^{-2} s^{-1} of photosynthetically active radiation and a constant relative humidity at 65%. Harvest was conducted on day 22 after planting. In the laboratory, this growth duration corresponded to the BBCH14 plant growth stage (i.e., four leaves unfolded). Water content was tested in trial experiments in order to ensure appropriate soil moisture conditions for plant growth and to avoid water logging in the bottom part of the sand columns. The retained average volumetric water content values were 22% and 18% for loam and sand, respectively. At the end of the growing period, subsamples were taken using a custom made subsampling device (UGT GmbH, Germany). In the laboratory, two experiments were conducted. For both exper-

iments, six subsamples per column were extracted (two per depth at -5, -10 and -15 cm). Differences between the two experiments arose from differences in treatments, sample size and soil packing procedure (Table 4.1). Figure 4.1 provides an overview of the experimental design of the two experiments conducted in the laboratory. The motivation behind the establishment of the laboratory experiments was to compare rhizosphere soil structure under well-watered conditions with field conditions for which fluctuating water content as well as drought stress occurs.

Table 4.1: Bulk density (BD), sieving and filling methods for the combination of soil textures and plant genotypes in the experiments conducted.

Experiment	Soil texture	Plant genotype	BD [g cm^{-3}]	Sieve aperture [mm]	Filling method
Laboratory experiment 1	Loam	WT	1.26	1	Pouring and settling
		rth3			
	Sand	WT	1.47		
		rth3			
Laboratory experiment 2	Loam	WT	1.26	1	Filling by layers and gently consolidating after each layer
			1.36		
	Sand		1.5		
			1.6		
Undisturbed cores in the field	Loam	WT	1.36	20	Filling by layers and compacting
		rth3			
	Sand	WT	1.5		Filling by layers
		rth3			
Ingrowth cores in the field	Loam	WT	1.36	2	Filling by layers and gently consolidating after each layer
		rth3			
	Sand	WT	1.5	20	
		rth3			

For the first experiment, plants were grown in the laboratory in the same fashion as in Lippold, Phalempin et al. (2021) (see section 3.2.6). In brief, columns (25 cm height, 7 cm inner diameter) were packed carefully in order to avoid particle sorting and hence the presence of layers. The soil was sieved down to 1 mm and poured into the columns up to a height of 23 cm. The loam columns were packed to a BD of 1.26 g cm^{-3}, while the sand columns were packed to a BD of 1.47 g cm^{-3}. Filling the columns to the target bulk density was achieved by repeatedly and delicately tapping the column on a flat surface to provoke particle settlement and slight compaction. The subsamples extracted at the end of the growing period consisted of aluminum cylinders of 1.6 cm in height and diameter. Six columns of each combination of soil texture (i.e., loam and sand) and plant genotype (i.e., WT and rth3) were sampled. This sampling procedure yielded a total of 144 subsamples, which were stored at 4°C in sealed plastic containers prior to X-ray CT scanning. The first laboratory experiment aimed at evaluating the effect of texture and root hairs on rhizosphere soil structure properties.

For the second experiment, plants were grown in the laboratory in the same fashion as in the first experiment in terms of growth duration and conditions. However,

subsample size, column size and soil packing methodology differed. The packing procedure was changed from pouring the soil into the columns at once to gradually placing layers of soil and by gently consolidating the soil at each filling step. In the second experiment, only the WT genotype was used but the columns were packed to a different bulk density in order to investigate the effect of different degrees of soil compaction. The columns (20 cm height, 10 cm inner diameter) were filled up to 18 cm in ten layers step. For the low bulk density treatment, four columns per soil texture were packed to 1.26 and 1.5 g cm^{-3} for the loam and the sand, respectively. For the high bulk density treatment, four columns per soil texture were packed to 1.36 and 1.6 g cm^{-3} for the loam and the sand, respectively. At the end of the growing period, six subsamples of 3 cm in diameter and height were extracted per column. This sampling procedure yielded a total of 96 subsamples to analyze, which were stored at 4°C in sealed plastic bags prior to X-ray CT scanning. The second laboratory experiment aimed at evaluating the effect of texture and bulk density on rhizosphere soil structure properties.

4.2.4 X-ray CT scanning

X-ray CT scanning was performed with an industrial CT scanner (X-TEK XTH 225, Nikon Metrology) having an Elmer-Perkin 1620 detector panel (1750 × 2000 pixels). The obtained images were reconstructed into a 3D tomogram having an 8-bit grayscale via a filtered back projection algorithm with the CT Pro 3D software (Nikon metrology). The conversion to 8-bit allowed saving space without losing considerable information. During the 8-bit conversion, the grayscale range was normalized with a percentile stretching method. This method sets the darkest and brightest 0.2% voxels to 0 and 255, respectively, and performs a linear stretching in between. Considering the different size of the samples analyzed in this study, the image resolution, beam energy, beam current, number of projections and exposure time for each projection were adjusted for all experiments (Table 4.2).

4.2.5 Root segmentation and diameter differentiation

Root segmentation was performed with a modified version of the root segmentation algorithm "Rootine v.2" (see chapter 2). Rootine v.2 is a free macro available for the free image analysis software ImageJ (Schindelin et al., 2012). In addition to gray value information, Rootine v.2 is based on the shape detection of cylindrical roots. Some of the key steps of Rootine v.2 and modifications of the original version for this study (when applicable) are briefly described below.

After X-ray CT scanning, all images were visually analyzed and samples devoid of roots were not considered for analysis. For the remaining samples, circular region of interests (ROI) were defined. The circular ROI were created in order to exclude the wall from the analyzed region. Subsequently, the size of the circular ROI was reduced by 10 % in order to exclude regions where potential soil structure disturbance due to sampling was present.

After defining the ROI, the images were subjected to preprocessing steps. First, the images were filtered with a 3D non local means filter (Tristán-Vega et al., 2012) available in the ITK library (McCormick et al., 2014), except for the samples having a resolution of 10 μm for which the 2D non local means filter available in ImageJ was

Table 4.2: Core diameter, image resolution, beam energy and current, number of projections, exposure time for each projection and time required per sample for all samples analyzed in the experiments conducted.

	Unit	Subsamples (Experiment 1)	Subsamples (Experiment 2)	Undisturbed cores	Ingrowth cores
Core diameter	mm	16	30	50	50
Image resolution	µm	10	19	25	25
Beam energy	kV	115	130	140	140
Beam current	µA	85	150	200	200
Number of projections		2748	2500	2400	2400
Exposure	ms	1000	700	500	500
Duration of scan per sample	min	46	29	20	20

used. After filtering, a step of edge enhancement was performed with the "Unsharp Mask" filter available in ImageJ. Then, a background removal step was applied via an "absolute difference transform" whose rationale and technical aspects are described in chapter 2 (Equation 2.2). The obtained images served as input for the root segmentation *per se*.

Rootine v.2 is tailored for the segmentation of roots in whole column scans where the image resolution is close to the smallest root diameter to segment. For whole column scans, the distribution of root diameters is continuous within a range that is plant species-dependent. For the samples used in this study, the distribution of root diameters is not continuous but rather discrete, considering that roots of different types and orders can be present within a sample and vary substantially amongst all samples in a dataset. To cope with this discreteness, Rootine v.2 was modified in order to perform a "root diameter targeted approach" instead of using a "root diameter incremented approach", as implemented in the original version of Rootine v.2. With the new approach, every image was visually analyzed and the diameter of the roots in the image was measured using the "Measure" tool available in ImageJ. The sigma values of the tubeness filter implemented in ImageJ were then calculated based on the measured root diameters according to the formalizing steps described in chapter 2 (Equation 2.5). The results of the tubeness filter were segmented using the "3D Hysteresis Thresholding" operation (Ollion et al., 2013) available in ImageJ.

After root segmentation, the obtained images were subjected to post-processing steps. First, a 3D median filter available in ImageJ was applied in order to smoothen the root surface. In the original version of Rootine v.2, small isolated objects are discarded by using a connectivity criterion of the root branches from top to bottom, which is tailor-made for whole column scans. For the samples as used in this study, roots can

enter the ROI from all sides. In order to cope with this, Rootine v.2 was modified and the connectivity criterion was replaced by a size exclusion criterion in order to get rid of every object whose size fell under a user-defined threshold. The size exclusion step was performed with the "Size Opening (2D/3D)" plugin available in the "MorphoLibJ" plugin suite (Legland et al., 2016). The size exclusion threshold was adapted for every dataset since the number of voxels comprising a false positive depends on the image resolution. With the obtained images, the root length was calculated after a step of skeletonization with the "Skeletonize (2D/3D)" plugin available in the BoneJ plugin (Doube et al., 2010).

Additional image processing steps were applied on the segmented root images in order to analyze rhizosphere soil structure properties for different root diameter classes. To differentiate root diameter classes, the root diameter was first computed with the "Local Thickness" plugin available in ImageJ. This plugin relies on the "Maximum Inscribing Sphere" method and assigns to every root voxel a value corresponding to the diameter of the largest sphere which locally fits into the root. The results were then segmented with threshold values corresponding to the defined diameter classes. Two diameter classes were defined, one class with roots having a diameter smaller than 200 µm and one class with roots having a diameter superior to 350 µm.

4.2.6 Pore segmentation, pore and grain size distribution analysis

Pore segmentation was performed with a simple thresholding method. This resulted in images where two distinct phases were segmented (i.e., one phase for the pore space and one phase for the soil matrix). The threshold detection methods and the preprocessing steps were adapted in order to obtain the best results possible for each dataset. The accuracy of the pore segmentation was evaluated visually by comparing the original grayscale data and the outline of the segmented pores. For the samples having a resolution inferior or equal to 19 µm, the original grayscale images were subjected to edge enhancement with the "Unsharp Mask" filter available in ImageJ. This step enhances the local contrast between the matrix and the pores (Schlüter et al., 2014) and improved the pore segmentation results. The "Otsu" method (Otsu, 1979) in ImageJ was then used to determine an adequate threshold for each image. For the samples having a resolution of 25 µm, the images were filtered with a 3D non local means filter and the filtered image served as input for the pore segmentation. The threshold values were determined with the fuzzy c-means clustering method (Jawahar et al., 1997) using Quantim v.4 (www.quantim.ufz.de). After segmenting the pores, the analysis of pore and grain size distribution was conducted on the binary pore and grain images with the "Local Thickness" plugin available in ImageJ.

4.2.7 Characterization of rhizosphere soil properties

The characterization of the rhizosphere soil structure properties was performed by assuming that changes in gray values (GV) are a suitable proxy for changes in bulk density. This rationale is based on the intrinsic properties of the X-ray attenuation, i.e., a feature of low density (e.g., an air-filled pore) exhibits a low X-ray attenuation and is hence assigned a low gray value after reconstruction of the tomogram. In contrast, an object of high density (e.g., a soil aggregate) exhibits a high X-ray attenuation and is

therefore assigned a high gray value after reconstruction (Figure 1.3). In addition, we consider gray value as a proxy for bulk density as more reliable than porosity because gray values contain information on sub resolution features and analyzing gray values does not require the choice of thresholding values for pore segmentation.

The characterization of the rhizosphere soil structure properties was performed in a similar fashion as in Lucas et al. (2019). This characterization relies on the computation of the so-called "Euclidian Distance Transform" (EDT). The EDT was computed on the binary root system images with the dedicated "Exact Euclidian Distance Transform (3D)" method available in ImageJ. The result of this operation is an image in which every soil voxel is assigned a value corresponding to its distance to the closest root in a 3D volume (see figure 3.7). The EDT result is then combined with the original grayscale image into a composite image. This combination yields an image in which every voxel contains the grayscale information in one channel and the distance to the closest root information in another channel. On the composite image, a loop in the X and Y dimensions is then initiated for all Z slices and the information of both channels is retrieved simultaneously (more details on this workflow are given in figure 5.2 in chapter 5). This results in an output file in which the average GV for each distance class from the root i (GV_i) is stored. Additionally, the number of voxels (N_i) used for the calculation of GV_i is available for each distance class. The distance class interval is a multiple of the image resolution and is therefore different across datasets.

The EDT was computed separately for the two root diameter classes considered. In order to exclude the influence that roots from one root diameter class have on the other root diameter class, the EDT images were masked with the dilated root images of the other root diameter class (e.g., to analyze the class < 200 μm, the roots having a diameter > 350 μm were dilated and served as a mask for the EDT image of the root diameter class < 200 μm). The root images were dilated such that the EDT mask extended at least up to 500 μm from the root surfaces. This masking step is important when analyzing the rhizosphere properties of a lateral root belonging to the class < 200 μm which emerge from a root belonging to the class > 350 μm. In such instance and if no masking was done, the influence of the lateral root on the soil in its vicinity would be confounded by the influence of the root belonging to the class > 350 μm at the point of emergence of the lateral.

4.2.8 Data and statistical analysis

In order to analyze the output data described above, the following data processing steps were applied. First, the first statistical moment of the gray value distribution was calculated using the number of voxels as the number of observations for each root distance class i (Equation 4.1).

$$GV_{im} = \frac{\sum_i^n GV_i N_i}{\sum_i^n N_i} \tag{4.1}$$

where GV_{im} is the mean GV of an image, GV_i and N_i are the average GV and the number of voxels counted for each distance class i from the root, respectively, i is the distance class from the root and n is the number of root distance classes (i.e., n=256 with an 8-bit resolution). With GV_{im}, a normalization step was carried out (Equation 4.2).

$$dev_i = 100(\frac{GV_i}{GV_{im}} - 1) \qquad\qquad (4.2)$$

where dev$_i$ is expressed in percent and is the deviation from GV_{im} for each root distance class i. This normalization step is necessary because the image contrast can differ due to the percentile stretching method used during reconstruction and conversion to 8-bit. Applying a normalization step eases the comparison between two images having different contrast (i.e., having different GV_{im}). Negatives values of dev$_i$ indicate zones of lower bulk density whereas positives values indicate zones of higher bulk density, as compared to the mean bulk density of the sample. The bulk soil is defined as the zone of the soil where the deviation from the mean GV is equal to 0. Note that, since a decrease or increase of GV$_i$ necessarily means a decrease or increase of dev$_i$, the words "gray value", "deviation from the mean GV" will be used interchangeably throughout the rest of this chapter. The deviation from the mean GV for each treatment was obtained by calculating the weighted average of dev$_i$ of each sample within a treatment using the number of voxels N$_i$ as weighting factors. An example of the output data and of the data analysis steps is shown in the supplementary information (Figure AF9). Data analysis was carried out in R Studio 3.53 (R Core Team, 2017) using the multcomp (Hothorn et al., 2008), car (Fox & Weisberg, 2019), plyr (Wickham, 2011) and ggplot2 (Wickham, 2009) libraries.

4.3   Results

The different packing and sieving procedures induced visual differences in initial soil structure (Figure 4.2). For loam, the most noticeable differences can be seen when comparing the samples extracted in the field for which the soil was prepared with large-scale machinery as compared to the samples for which the soil was prepared in small volumes in the laboratory. For the undisturbed cores extracted in the loam plots, aggregates of sizes up to 20 mm were observed and the spatial arrangement of those aggregates generated an increased heterogeneity of the pore space (i.e., creating bigger and more irregular pores). Noticeable differences are also visible when comparing loam and sand across all experiments. For loam, the structure is predominantly caused by the presence of aggregates, a fine textured phase containing sub-resolution pores (i.e., pores which cannot be resolved because they are smaller than the image resolution) and the pore space. For the undisturbed and ingrowth cores in sand, the only heterogeneity consists of occasional loam aggregates in an otherwise homogeneous sand matrix composed of rigid quartz grains without internal pores. For the subsamples from column experiments with sand, the embedded loam aggregates were much smaller due to the fine sieving down to 1 mm.

The sampling at different growth stages, under different growth conditions and at several depths led to very different root length density (RLD) values in the analyzed samples (Figure AF10). Due to the constrained volume available for root growth in the laboratory experiments, RLD was, on average, much greater for the samples extracted in the laboratory as compared to the samples extracted in the field. In the laboratory, the loam treatments exhibited more growth than the sand treatment whereas this was the opposite in the field. For loam in general and for the wild-type genotype growing
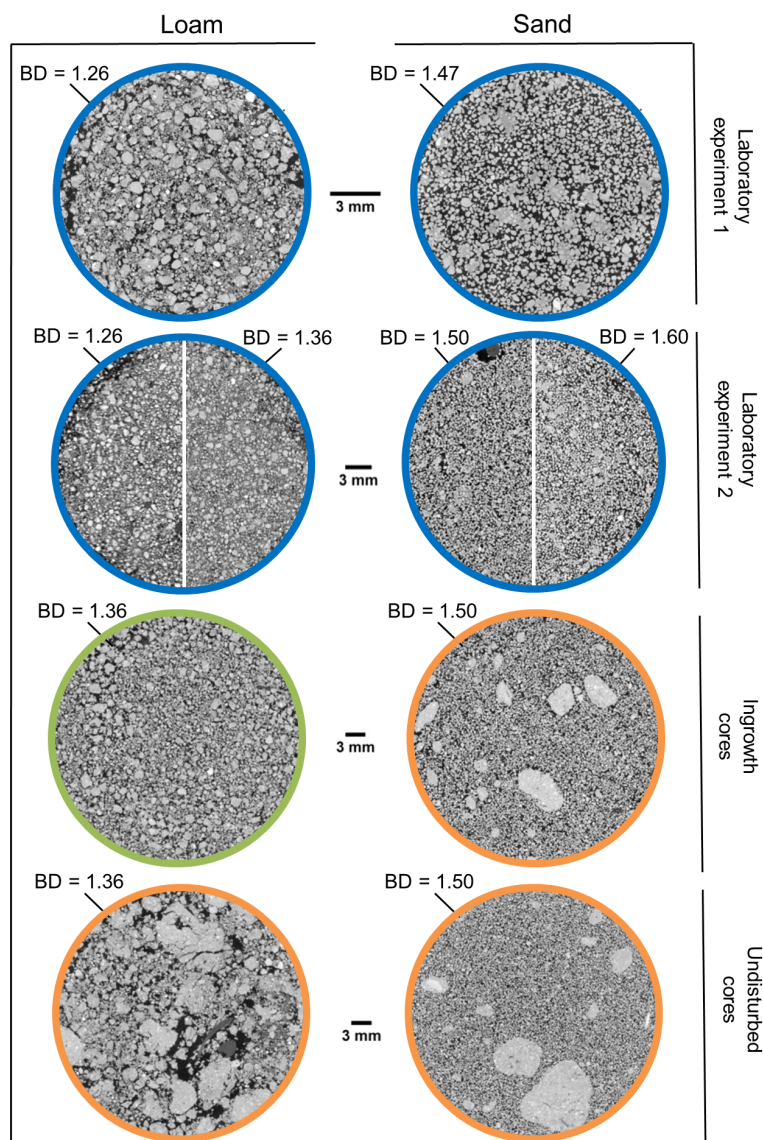
Figure 4.2: Two-dimensional cross sections of X-ray CT images highlighting the differences in soil structure observed for the experiments carried out in the field and in the laboratory and for the two soil textures investigated. Differences in sample size and scanning resolution are denoted by the scale bar. The circles around the images denotes the mesh aperture of the sieve (blue=1 mm, green=2 mm, orange=20 mm). Bulk density of the sample is annotated at the top of each image. Note the increase of structure heterogeneity from top to bottom for the loam samples. For sand, the only heterogeneity consists of occasional loam aggregates in an otherwise homogeneous sand matrix composed of rigid quartz grains without internal pores.

in loam in particular, drought symptoms were observed before BBCH 59 was reached. For the sand treatments in the field, drought stress was not as severe as plants were smaller at this stage (data not shown). In those laboratory and field experiments in which the influence of root hairs was investigated, there was no genotype effect as root growth was not statistically different between WT and rth3 in both soil textures. In the laboratory experiment in which the effect of soil compaction was investigated, the initial bulk density had no significant effect on root growth for both sand and loam (Figure AF10c).

For all experiments, genotypes, root diameter classes and soil textures, the deviation from the mean GV close to the root surface (i.e., < 100 µm) was very negative (Figure 4.3).
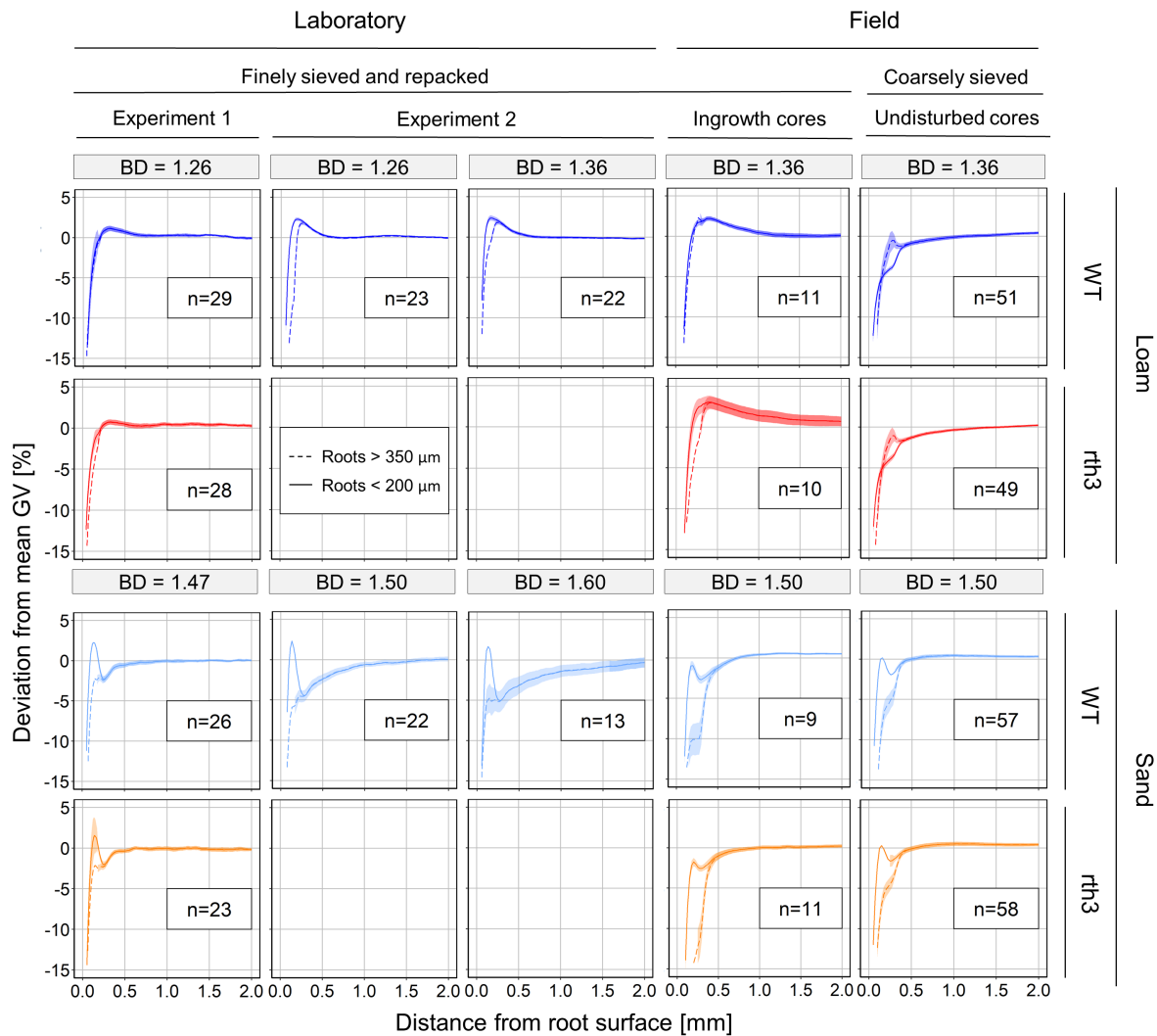
Figure 4.3: Deviation from the mean GV as a function of the distance from the root surface. Root diameter class inferior to 200 µm is depicted with a solid line whereas the root diameter class superior to 350 µm is indicated by a dashed line. The semitransparent ribbon denotes the standard error. The number of samples and bulk density for each treatment is given with n and BD, respectively. The mentions "WT" and "rth3" refers to the wild-type and root hair defective mutant maize genotypes, respectively.

The very negative deviation from the mean GV close to the root surface indicates the presence of a zone of lower bulk density close to the roots as compared to the bulk soil. The extent of this zone varied slightly across experiments but rarely exceeded 0.5 mm except for the loam samples with the greatest soil structure heterogeneity (i.e., the undisturbed cores extracted from the field). The biggest differences in the deviation from the mean GV mainly arose between soil textures and experiments. The most obvious difference between the sand and the loam treatment is noticeable for fine roots. For the root diameter class < 200 µm of the sand treatments, the presence of an

overshoot past the mean GV was observed at a distance of approximately 0.2 mm from the root surface. Past the overshoot, an abrupt decrease of GV below the mean GV was observed and another minimum was attained. Past this minimum, the deviation from the mean GV gradually increased again towards zero. Interestingly, this damped oscillation was typical for the root diameter class < 200 µm and was observed in most of the sand samples. For the root diameter class > 350 µm in sand, the presence of the overshoot was absent and only a decline of gray values towards the root surface was observed. For the loam treatments, the only difference between the root diameter classes is that the gray value distribution from the bulk soil towards the root surface was steeper for the root diameter class > 350 µm for the undisturbed cores. Analyzing BBCH stages separately revealed that this difference in loam is mainly contributed by the diameter class > 350 µm of BBCH19 (Figure AF11).

For the loam treatments, the biggest difference arose across experiments rather than across genotypes or root diameters. For the samples prepared with finely sieved soil in small volumes and which had a more homogeneous soil structure, an overshoot past the mean GV was observed directly after the zone of lower bulk density close to the root surface. This overshoot suggests a zone of soil compaction at a distance from the root surface ranging from 0.25 to 1 mm. The peak deviation from the mean GV is in the range of 1 to approximately 2.5%. In the experiment where the effect of bulk density was investigated, the deviation from the mean GV for the low and high bulk density treatment is very similar in terms of peak deviation and extent from the root surface. For the undisturbed cores, the gray value overshoot is absent and only a zone of lower bulk density is observed up to a distance 1 mm. Comparing treatments within a given experiment revealed almost no differences between the WT and rth3 genotypes for both soil textures.

4.4   Discussions

4.4.1   Influence of soil texture and structure

The main and first hypothesis of our work was that changes in soil structure in the vicinity of roots depend on the soil texture and antecedent structure. Salient differences were observed between sand and loam, which is why the results obtained for both soil textures are treated distinctively in the discussion part.

For loam, two distinct patterns emerged when analyzing the results of the samples having an antecedent homogeneous soil structure as compared to the samples for which the soil structure heterogeneity was greater. In a homogeneous soil structure, no or few pre-existing pores were present because of the fine sieving and careful packing in the laboratory (Figure 4.2). Under these circumstances, the zone of lower bulk density close to the roots was short. The presence of this zone is well in-line with previous studies using high resolution X-ray CT under similar homogeneous soil conditions (i.e., finely sieved and repacked soil) (Burr-Hersey et al., 2020; Helliwell et al., 2017, 2019; Koebernick et al., 2019; Lucas et al., 2019). The zone of lower bulk density close to the roots extended up to 0.5 mm from the root surface which is also in the range of values reported in the literature. In the study of Helliwell et al. (2017), the decrease in bulk density close to the root surface in a clayey soil was attributed to

the formation of micro-cracks due to plant water uptake. In our study, the laboratory experiments were conducted under well-watered conditions. A visual assessment of the images from these datasets revealed virtually no cracks formed radially around the roots. We therefore exclude soil swelling and shrinking as potential factors causing a decrease in bulk density close to the root surface. This decrease in bulk density at the root surface is more likely the result of the surface wall effect, as already suggested by Koebernick et al. (2019) and Lucas et al. (2019). Past the zone of lower bulk density, a zone of compaction was observed. This zone of compaction can be attributed to the fact that roots predominantly had to push away soil particles when no existing pores were present. This is supported by the visual analysis of the soil in the vicinity of a primary root for which a typical compacted zone was observed (Figure 4.4). The extent and the peak deviation from the mean GV in the zone of compaction is well in accordance with the values that Helliwell et al. (2019) and Lucas et al. (2019) reported at approximately similar initial bulk densities and soil textures. In the experiment where the effect of initial bulk density was investigated, there was no difference in the extent and magnitude of the root-induced compaction between the high and the low bulk density treatment.
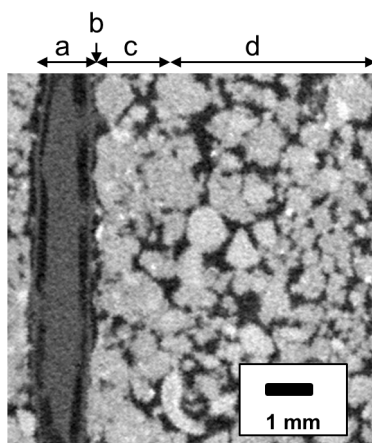
Figure 4.4: Two-dimensional plane of root growing in finely sieved and repacked loam for a sample scanned at a resolution of 25 µm. The arrows on top of the figure delineate the following zones. (a) the primary root. (b) the root-soil interface. Note the imperfect contact between the root and the loam particles which is responsible for the decline of gray value very close to the root. (c) The zone of compaction induced by the root pushing away soil particles. (d) the bulk soil.

In an attempt to understand which factors influenced root-induced soil compaction in loam under homogenous soil structure conditions, correlations were established between the peak deviation from the mean GV (dev_{peak}, see figure AF9c) and the root length density and the mean root diameter within a sample, the mean porosity and the mean pore size of the bulk soil (Figure AF12). The coefficients of correlation calculated were low for all four properties (i.e., $R^2 \leq 0.18$) which suggested that none of these properties was robust enough to explain root-induced soil compaction in finely sieved and repacked loam.

In a more heterogeneous soil structure, the zone of lower bulk density close to the roots extended twice as far and there was no zone of compaction farther away. The

difference with the bulk density distribution in finely sieved and repacked soil can be explained in part by the presence of existing pores for roots to grow into in a more heterogeneous soil structure. This is supported by a local analysis of bulk density distribution in dense or loose areas which were identified according their pore size distribution analyzed for three undisturbed cores (Figure 4.5). Based on figure 4.5, it seems that the propensity of roots to induce soil compaction depends on the initial local soil structure that roots encounter, i.e., a decline of gray value towards the root surface was mainly observed when the structure in which roots grew was initially loose and where pores big enough for roots to grow into were present. With that in mind, the absence of a zone of compaction for the undisturbed cores extracted in the loam field plots could be attributed to the high local pore space heterogeneity induced by the coarse sieving and packing procedure. Under these conditions, roots predominantly penetrated existing pores without inducing compaction. Note that our observations consolidate the findings of Lucas et al. (2019) who suggested that the initial soil structure is an important factor for predicting root-induced compaction.

Another potential factor explaining the decrease in bulk density close to the root surface is root shrinkage as a consequence of soil desiccation. In the field, drought stress increased over the whole growing season and dry conditions could have led to root shrinkage, especially for the wild-type genotype growing in loam. In this treatment, plants showed the largest shoot biomass early on and were hence affected by severe drought earlier than other treatments. Permanent wilting point was reached at BBCH59 (13.6 % volumetric water content, corresponding to a matric potential of approximately -30000 cm). A more detailed look at the bulk density distribution obtained for the undisturbed cores extracted at different growth stages revealed differences, in particular for the roots > 350 μm diameter (Figure AF11). Very likely, roots were partly desiccated and shrunken at BBCH59 and to a lesser extent at BBCH83. Shrunken roots and/or partially degraded roots would induce an offset in the distance from the root surface whose effect could be confounded with the surface wall effect. Also, this distance offset would mean, that the rather constant position of the GV peak at 0.2 to 0.3 mm from the root surface is smeared across a larger distance range, when samples with and without drought stress are lumped together, thus potentially removing the GV overshoot altogether. This phenomenon cannot be ruled out for the ingrowth cores in the field.

For sand, the results across experiments and genotypes are very similar. A possible explanation for this similarity is that sand was originally very consistent in terms of granulometry and that homogeneous structure conditions were guaranteed despite the different sieving and packing procedures. A careful inspection of figure 4.2 supports this statement. The results obtained for the low and high bulk density treatments are very similar as well. This suggests that there is no impact of initial bulk density on the results, at the bulk density investigated in this study. The main differences in sand are noticeable for the different diameter classes and these differences will be treated in the dedicated section down below.

4.4.2 Influence of root diameter

The second hypothesis of our work was that root-induced compaction, if observed, will be greater for big roots than for fine roots due to the greater volume of

Figure 4.5: Local analysis of the deviation from the mean GV as a function of the distance from the root surface and the pore size distribution in zones denser (red line) or looser (blue line) than the whole sample (black line) for three loam undisturbed cores extracted in the field. The horizontal red and blue dashed lines represent the deviation from the mean GV of the dense and loose zones, as compared to the mean GV of the whole sample.

big roots. Here again, differences were observed between sand and loam and the results obtained for both soil textures are treated separately down below. Before discussing the effect of root diameter for each soil texture, it is worth noting that there were great differences in root diameter distribution for plants growing in loam and in sand. Indeed, plants growing in sand had systematically a larger share of big roots and bigger roots, on average, as compared to plants growing in loam (Figure AF17). This observation was true, both in the field and in the laboratory experiments.

In loam, there was no or only small effects of root diameter on root-induced soil compaction under homogeneous conditions (Figure 4.3 and AF12b). That is in contradiction with the results obtained by Lucas et al. (2019) and the model of soil compression around roots suggested by Dexter (1987). A possible explanation for this is that the difference in root diameter for the two classes investigated (i.e., < 200 and > 350 µm) might not have been large enough to cause a detectable difference in compaction. Broadening the range of root diameter classes could have helped to capture those differences but would have resulted in having too few roots in the upper diameter class to construct reliable statistical analysis.

For sand, root diameter had a much greater effect on rhizosphere soil structure properties. This effect manifested itself by the presence of a damped oscillation for the root diameter class < 200 µm, which was absent for the root diameter class > 350 µm. To understand these differences, a local analysis targeting roots of different diameter was carried out (Figure 4.6).
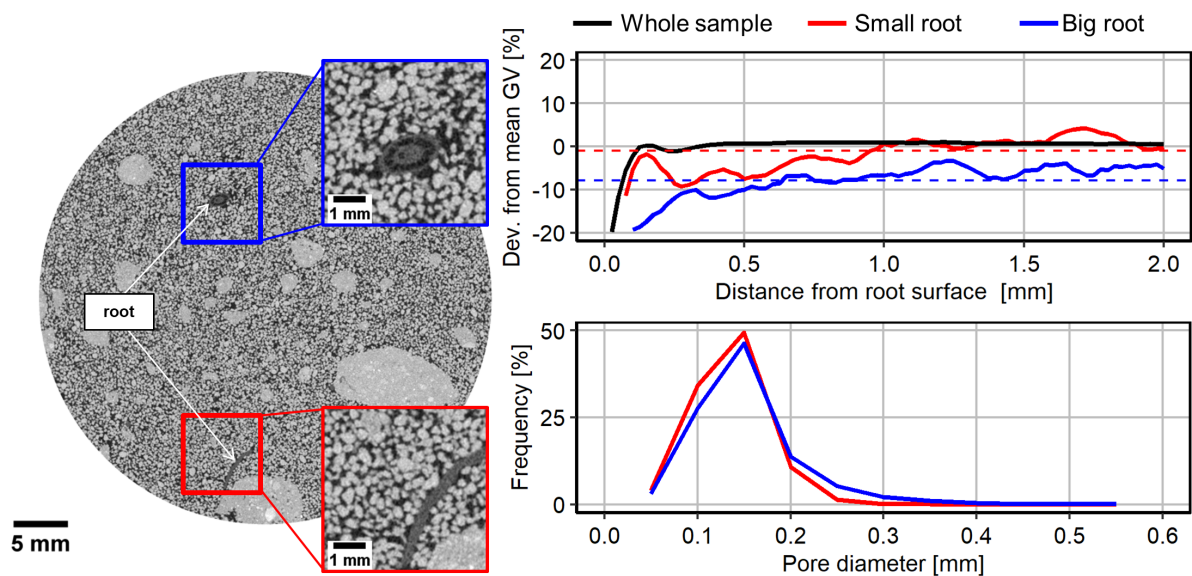
Figure 4.6: *Local analysis of the deviation from the mean GV as a function of the distance from the root surface and the pore size distribution around a small root (red line) or a big root (blue line), in comparison with the whole sample (black line) for one undisturbed core extracted in the sand field plots. The horizontal red and blue dashed lines represent the deviation from the mean GV of the zone around the big and the small root, respectively, as compared to the mean GV of the whole sample.*

By visual evaluation only, it is noticeable that the big root created bigger pores in its surroundings, whose presence evoked a longer tailing of the pore diameter frequency distribution. In contrast, the small root caused the sand grains to align along

the root surface. In order to understand the nature of the alignment of sand grains, an analysis of a sample scanned at the highest resolution (i.e., 10 µm) was carried out. By analyzing a zone around a small root for this sample (Figure 4.7), it appears that the gray value distribution has the shape of an oscillatory function. This observation is well in line with the model established by M. Suzuki et al. (2008) who first mathematically described this damped oscillatory function of void distribution as a function of the distance from the wall in particle packed bed reactors. On this oscillatory function, several zones can be delineated. The closest zone to the root (i.e., zone a-b) shows a substantial drop of gray values that we now confidently attribute to the surface wall effect (M. Suzuki et al., 2008). At the point b, the gray value reaches a maximum which we can now attribute to the center of grains aligned at the root surface. From point b to c, the gray value decreases again because of the interstitial porosity between sand grains. This oscillatory pattern is then repeated from point d to c, d to e and so forth but is damped as the distance from the root surface increases and the grain packing becomes more randomized. By conducting an analysis of the sand grain diameter, we found that the periodicity of this oscillatory function is approximately equal to the median sand grain diameter $\bar{d}$ (i.e., $\bar{d} \simeq$ distance a to b). Mueller (2010) highlighted that this oscillatory behavior is observed when particles are regularly shaped and have similar sizes. In our study, almost all sand grains had a size comprised between 100 and 250 µm, which is a fairly narrow size range (Figure 4.7). The absence of the oscillatory pattern for the root diameter class > 350 µm could be explained by the fact that big roots do not only force particles to align by rotating and tilting but push them farther away than their own diameter.
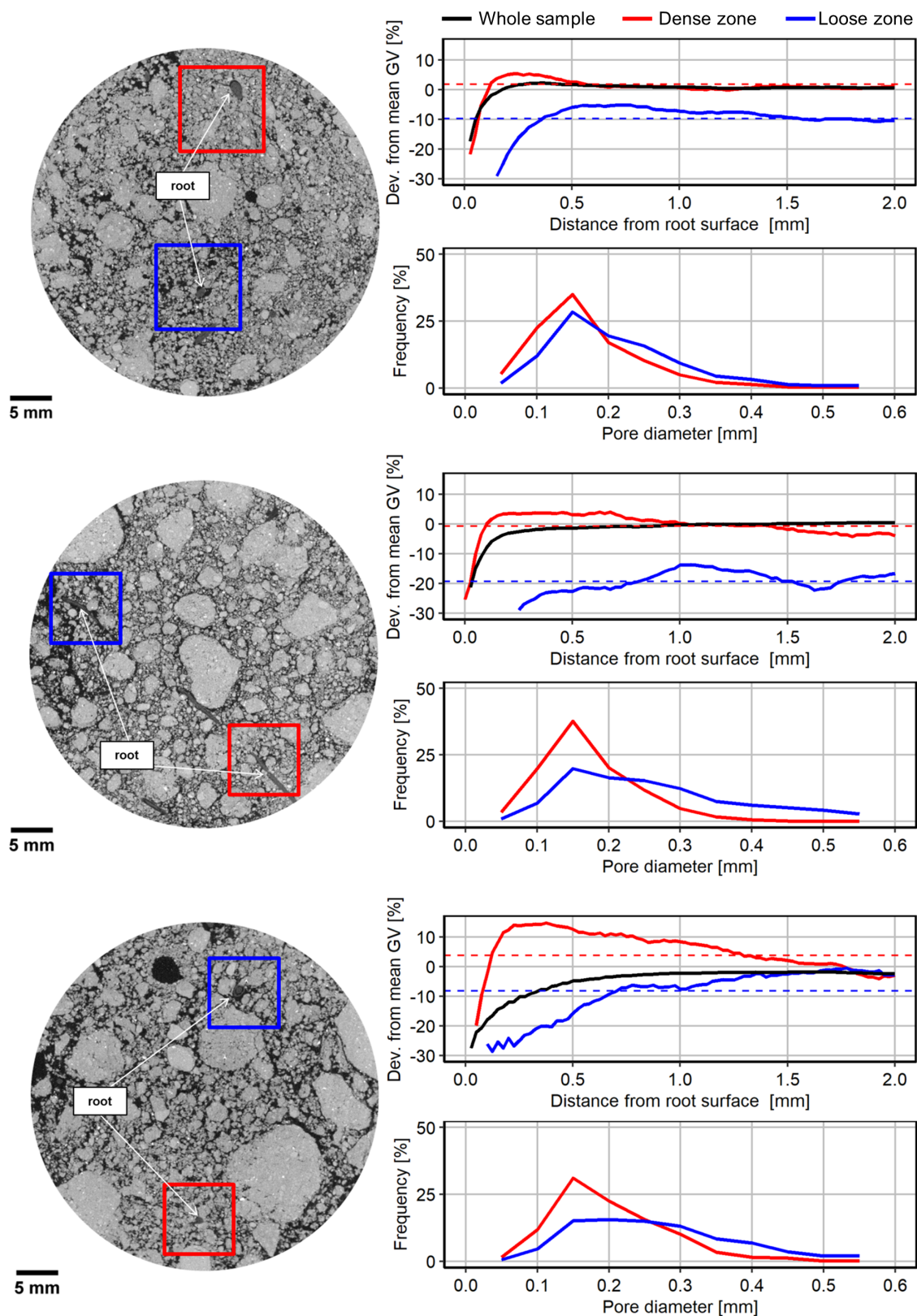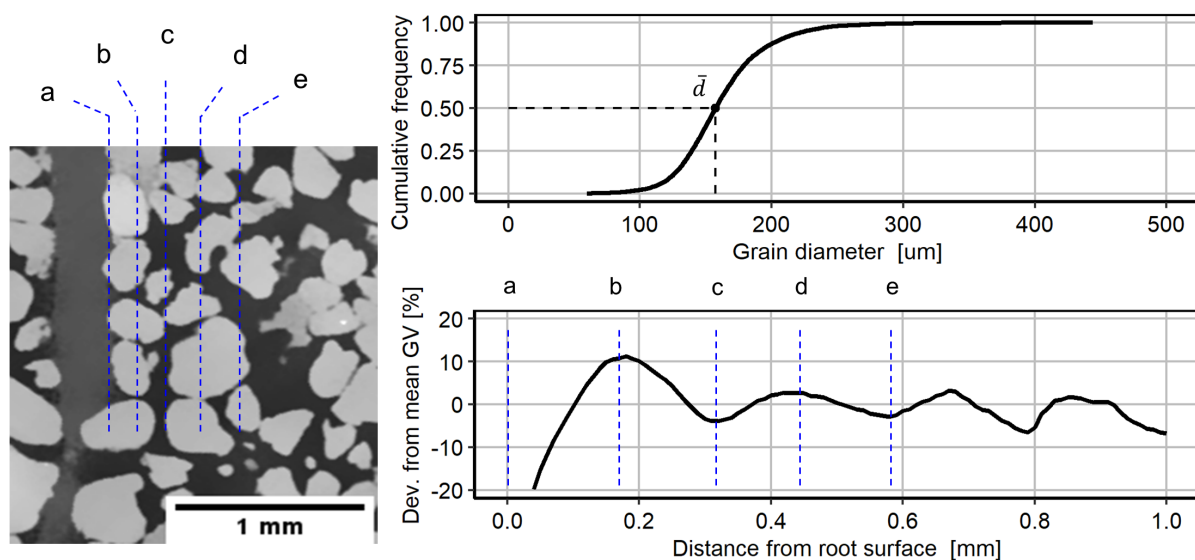

Figure 4.7: Local analysis of the deviation from the mean GV as a function of the distance from the root surface for one sand subsample scanned at a resolution of 10 µm. The gray value distribution has the shape of a damped oscillatory function, whose periodicity is approximately equal to the median grain diameter.

4.4.3   Influence of root hairs

The third hypothesis of our work was that roots with root hairs would induce a greater soil compaction than roots without root hairs because of the anchorage provided by the hairs. Contrary to our hypothesis, the presence of root hairs did not influence bulk density distribution in the vicinity of the roots. Our results are supported by the findings of Koebernick et al. (2019) who also found no differences in rhizosphere soil structure properties between a root hair bearing and a root hair defective barley genotype. Bengough et al. (2016) suggested that the role of root hairs in providing anchorage was mitigated when BD was equal to 1.3 g cm^{-3} or higher. However, BD lower than 1.3 g cm^{-3} were investigated in the laboratory. Therefore, root hair influence was expected to be observed in those two experiments. The absence of the effect of root hairs could be explained by two factors, i.e., the root hair length and the age of the plant. A microscopic examination of root segments was carried out and we found that the mean root hair length was 0.24 mm with no significant difference between loam and sand (Lippold, Phalempin et al., 2021). Frequently, higher values in the range of 0.7 to 0.9 mm are reported for maize. Shorter root hairs decrease the ability to anchor the growing root tip in soil if an insufficient length of each root hair is secured within the rhizosphere soil pores (Bengough et al., 2016). In our study, the ability of the root hairs to provide anchorage might have been lessened by their relatively short size. Bengough et al. (2016) studied the role of root hairs using the same maize genotypes as in the present study. However, the authors studied juvenile plants for which laterals were absent. In our study with older plants, we speculate that lateral and seminal roots took over the role of the root hairs in providing anchorage which might also have lessened their importance (Bailey et al., 2002).

4.4.4   Relevance for rhizosphere research

Our findings have implications for water and solute transport dynamics at the root-soil interface. Under heterogeneous conditions such as the one investigated in the field, the root-soil contact and the volume of soil in the vicinity of roots was less as compared to under homogeneous soil structure as the one investigated in the laboratory. Under water limited conditions, heterogeneous soil structure might result in patchy water uptake, i.e., root water uptake is favored in dense local zones where the root-soil contact is greater than in loose zones. To investigate such structure related heterogeneities in root function, more dedicated experiments comparing different structures are required.

To the best of our knowledge, only few studies have considered the differences in soil structure properties in the vicinity of roots when trying to model water flow in the rhizosphere. Aravena et al. (2014) showed that root-induced soil compaction led to an increase in water flow towards the root in a very loose soil (i.e., 1 g cm^{-3}). Landl et al. (2021) showed that the lower bulk density around the roots, as observed in our study, had the effect of reducing water flow to the roots. By modeling the coupled effect of rhizosphere bulk density and mucilage concentration gradients in the rhizosphere at the single root segment scale, they showed that transpiration levels were kept lower during longer times and that this could be regarded as beneficial since it would prevent fast dehydration (see chapter 5). Modeling approaches of water flow should orient

towards integrating explicitly the rhizosphere soil structure and to evaluate its effect on soil water dynamics at the plant scale (Landl et al., 2021). Rhizosphere soil structure properties, and how it differs from bulk soil properties, should also be considered for the interpretation of chemical imaging data, the study of diffusive processes such as mucilage exudation and the assessment of the suitability of the rhizosphere as a habitat for microorganisms.

4.5 Conclusion

With the help of X-ray computed tomography, we presented the results of an image processing workflow, which enabled to analyze the bulk density changes in the vicinity of roots for more than 400 samples extracted during laboratory and field experiments. Our study consolidated previous knowledge regarding the conditions under which a zone of denser or looser soil is observed in the vicinity of roots. In homogeneous soil structure such as in finely sieved and repacked soil, roots had to create their own pores by pushing away particles. Under these conditions, the presence of a zone of lower bulk density close to the root surface was attributed to the surface wall effect and this zone was followed by a zone of compaction farther away. In more heterogeneous conditions such as in field experiments, the zone of lower bulk density close to the root surface was attributed to the fact that roots predominantly grew in existing pores, thereby reducing the root-soil contact and thus the ability of roots to compact their surroundings. The effect of root diameter was found more pronounced in sand than in loam. In sand, fine roots (< 200 µm in diameter) caused sand grains to align along their axis whereas bigger roots (> 350 µm in diameter) broke the fragile arrangement of sand grains. In contrast to rigid sand particles, loamy aggregates could also be deformed plastically, leading to different patterns of bulk density changes. We thereby showed that soil texture and structure heterogeneity predominantly governs bulk density distribution around roots and that other factors such as the presence of root hairs or root length density had no or little impact on the results. Our findings have implications for water and solute transport dynamics at the root-soil interface as well for the interpretation of chemical imaging data, the study of diffusive processes from the root to the soil and the assessment of the suitability of the rhizosphere as a habitat for microorganisms.

CHAPTER *5*

IMPACT OF BULK DENSITY AND MUCILAGE ON ROOT WATER UPTAKE

In models of water flow in soil and roots, differences in the soil hydraulic properties of the rhizosphere and the bulk soil are usually neglected. There is, however, strong experimental evidence that rhizosphere and bulk soil hydraulic properties differ significantly from each other due to various root-soil interaction processes. Two processes, which can also influence each other, are rhizosphere loosening or compaction and mucilage deposition. In this work, we identified realistic gradients in rhizosphere bulk density and mucilage concentration using X-ray CT imaging and related them to soil hydraulic parameters for two different soil textures and soil bulk densities. Using a 1D-single-root model, we then evaluated both the individual and combined effects of these gradients on soil water dynamics using scenario simulations. We showed that during soil drying, a lower rhizosphere bulk density leads to an earlier onset of water stress and to a reduced root water uptake that is sustained longer. The presence of mucilage led to a faster reduction of root water uptake. This is due to the stronger effect of mucilage viscosity on hydraulic conductivity compared to the mucilage- induced increase in water retention. Root water uptake was rapidly reduced when both mucilage and rhizosphere bulk density gradients were considered. The intensity of the effect of gradients in rhizosphere bulk density and mucilage concentration depended strongly on the interplay between initial soil hydraulic conditions, soil textures and soil bulk densities. Both gradients in rhizosphere bulk density and mucilage concentration appear as a measure to sustain transpiration at a lower level and to avoid fast dehydration.

5.1 Introduction

The rhizosphere is defined as the small soil volume around the roots, whose physical, chemical and biological properties are influenced by the plant roots (Hinsinger et al., 2009). The properties of the rhizosphere soil are therefore significantly different to the properties of the bulk soil farther away from the roots. When a root penetrates the soil, it alters the arrangement of soil particles and therefore the local compaction of the rhizosphere (Dexter, 1987; Koebernick et al., 2019) (see also figure 4.3). Growing roots furthermore release the organic compound mucilage that was shown to affect the water retention characteristics of the rhizosphere (Ahmed et al., 2014; Moradi et al., 2011). Both the local compaction of the rhizosphere as well as root mucilage deposition can thus be expected to have a significant impact on the water transport from the soil to the roots and therefore also on root water uptake (Whalley et al., 2005).

Recently, a lot of work has been published on the dynamic development of soil structure in the rhizosphere using non-invasive X-ray CT imaging. Several studies have found lower bulk densities in the immediate vicinity of the roots than farther away in the bulk soil for different plant types, soil textures and soil moisture contents (Helliwell et al., 2017, 2019; Koebernick et al., 2019; Lucas et al., 2019). It is assumed that the low point in bulk density in the immediate vicinity of the root is caused by the incomplete packing of the larger, incompressible mineral particles, which are displaced by the growing root (Koebernick et al., 2019). Furthermore, root shrinking due to soil drying, which causes a loss of contact between root and soil, may also play a role (Carminati et al., 2013; Koebernick et al., 2018). Helliwell et al. (2019); Koebernick et al. (2019); Lucas et al. (2019) observed that this low point in bulk density close to the root was partly followed by a peak value before the density of the bulk soil was reached. Other studies predominantly observed a compaction of the rhizosphere close to the root (Aravena et al., 2011, 2014; Bruand et al., 1996; Koebernick et al., 2017; Vollsnes et al., 2010). Rhizosphere compaction can be justified by the fact that the volume occupied by a root must be compensated by a loss of the same volume of pore space of the surrounding soil (Dexter, 1987; Lucas et al., 2019). Lucas et al. (2019) found that rhizosphere compaction only developed at medium levels of soil bulk density and that its occurrence depends on the soil texture and on the particle size to which the soil was sieved. If the soil was too loose, the roots found their way through existing pores. If the soil was too dense, the roots could not overcome the mechanical stress and resorted to pre-existing pores.

Variations in bulk density have a direct impact on soil hydraulic parameters and can therefore be expected to affect soil water dynamics and root water uptake (Aravena et al., 2011, 2014; Daly et al., 2015; Koebernick et al., 2019). Daly et al. (2015); Koebernick et al. (2019) investigated the structure of rhizosphere and bulk soil using X-ray CT imaging and related the changes in observed porosity to changes in soil hydraulic properties using the Young-Laplace equation and a homogenization method that allows deriving Darcy's law from Stoke's equations for fluid flow. However, the limited imaging resolution restricted the separation of the CT images into pore and solid phase and only allowed the description of the influence of the rhizosphere soil structure on the wet end of the water release characteristics (i.e., above -800 cm pressure head). Using X-ray CT imaging, Aravena et al. (2011) and Aravena et al. (2014) showed that in low-density soils, the compaction of the rhizosphere can increase the unsaturated hydraulic

conductivity of the soil and thus the root water uptake due to an increased contact area between adjacent soil aggregates.

In recent years, many studies have shown the importance of root mucilage deposition for the water dynamics in the rhizosphere (Ahmed et al., 2014; Carminati et al., 2010; Carminati, Zarebanadkouki et al., 2016; Ghezzehei & Albalasmeh, 2015). It is a well-known phenomenon that mucilage increases the water retention due to its high water-holding capacity. The increased water content at a given pressure head then results in a higher unsaturated hydraulic conductivity (van Genuchten, 1980). However, mucilage also increases the water viscosity, and thereby decreases the unsaturated hydraulic conductivity at a given pressure head. Depending on the relative importance of the increase in water retention and in viscosity, hydraulic conductivity can either increase or decrease due to the impact of mucilage at a given pressure head (Carminati, Zarebanadkouki et al., 2016; Moradi et al., 2011).

The actual extent of the impact of mucilage on soil water dynamics depends on its spatial distribution around the roots (Holz, Leue et al., 2018). Due to the difficulty of imaging mucilage in soil non-invasively and quantitatively, knowledge about the spatial distribution of mucilage is very limited. Most modeling studies have therefore assumed constant mucilage concentrations in the rhizosphere (Carminati, Kroener et al., 2016; Schwartz et al., 2016) or linearly decreasing concentrations from the root surface to the bulk soil (Kroener et al., 2016). The radial extent of the rhizosphere affected by mucilage was assumed to be between 1 and 2 mm (Kroener et al., 2016; Schwartz et al., 2016). Recent studies, however, have shown that the radial gradients of mucilage distribution around a root are relatively steep and that the extent of the rhizosphere affected by mucilage was only about 0.6 mm (Holz, Leue et al., 2018; Zickenrott et al., 2016). Furthermore, it is known that mucilage is secreted at the root tips and that its distribution varies along the root axis (Holz, Zarebanadkouki et al., 2018; van Veelen et al., 2018). This has not been taken into account in previous modeling studies.

The aim of this modeling study was to assess how the individual and combined effects of variations in rhizosphere bulk density and mucilage concentration affect soil water dynamics and root water uptake in two soils with different hydraulic properties, namely loam and sand. These soils were furthermore compacted to two different bulk density levels. Variations in rhizosphere bulk density were measured experimentally using X-ray CT and were assumed to affect soil hydraulic parameters according to the empirical relations derived by Assouline (2006a, 2006b). The distribution of mucilage in the rhizosphere of a growing root was predicted by solving the diffusion-reaction equation in a moving reference frame (Kim & Silk, 1999) using appropriate model input parameter values from the literature. The impact of mucilage concentration on soil hydraulic parameters was evaluated via the model proposed by Kroener et al. (2014), that was parameterized with optimized values from the literature. Using a 1D rhizosphere model, we then simulated a drying scenario to evaluate the individual and combined effects of rhizosphere bulk density and mucilage concentration on soil water dynamics and root water uptake. The workflow of the study is illustrated schematically in figure 5.1.
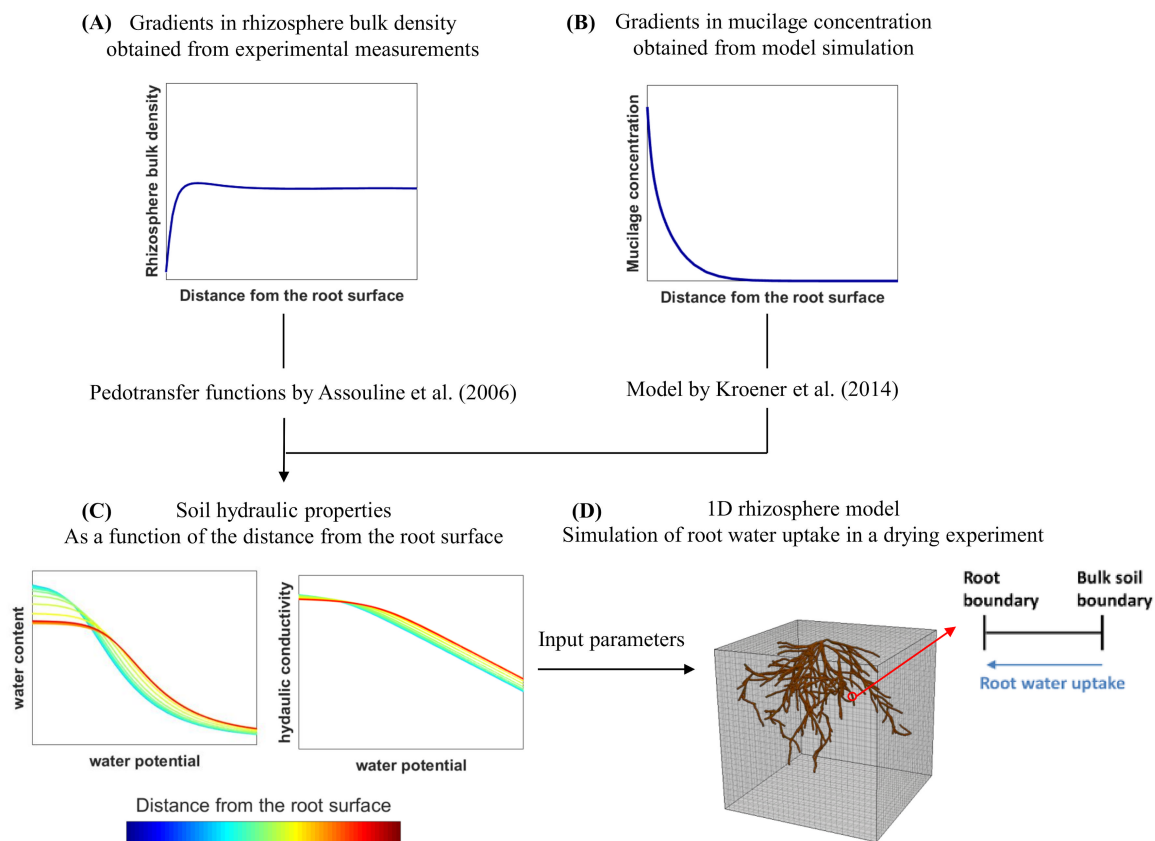
Figure 5.1: *Illustration of the workflow of the present study: Gradients in rhizosphere bulk density (A) were obtained from experimental measurements with X-ray CT and related to soil hydraulic properties using the pedotransfer functions by Assouline (2006a, 2006b). Gradients in mucilage concentration (B) were obtained from model simulation and related to soil hydraulic properties using the model by Kroener et al. (2014). The obtained soil hydraulic properties (C) were then used as input parameters in a 1D-rhizosphere model (D) to evaluate the effects of rhizosphere bulk density and mucilage gradients on root water uptake in a drying experiment*

5.2 Material and Methods

5.2.1 Analysis of the rhizosphere bulk density

5.2.1.1 Experimental set-up and X-ray CT imaging

The bulk density changes in the rhizosphere were investigated for two soils with differing textures, i.e., a loam and a sand that were compacted at two different bulk density levels (low and high). The loam was compacted to 1.26 and 1.36 g cm^{-3} whereas the sand was packed at 1.5 and 1.6 g cm^{-3}, respectively. The loam was obtained from the upper 50 cm of a haplic Phaeozem soil profile, dried to 0.1 g g^{-1} gravimetric water content and then sieved down to <1 mm. The sand constitutes a mix of 83.3% quartz sand (WF 33, Quarzwerke Weferlingen, Germany) and 16.7% of the sieved loam. Details on chemical and physical properties are provided by Vetterlein et al. (2021).

Maize plants were grown in cylindrical containers of 18 cm height and 10 cm diameter over a period of 22 days in a climate chamber (Vötsch Industrietechnik GmbH).

The columns were carefully watered from the top and from the bottom to an average volumetric water content of 0.22 cm^3 cm^{-3} and 0.18 cm^3 cm^{-3} for loam and sand, respectively. The climate chamber was set to 22 °C during the day and to 18°C at night with a 12 hours light period, 350 μMm^{-2}s^{-1} photosynthetically active radiation and a constant relative humidity of 65 %. After 22 days of growth, the plants were harvested and undisturbed cylindrical soil samples (3 cm in height and diameter) were taken at 5, 10 and 15 cm depth from the soil surface.

X-ray computed tomography was performed with an industrial μCT scanner (X-TEK XTH 225, Nikon Metrology) operated at 130 kV and 150 μA. A total of 2500 projections with an exposure time of 708 ms each were acquired during a full rotation of a sample. The obtained images were reconstructed into a 3D tomogram having a voxel size of 19 μm and an 8-bit grayscale via a filtered back projection algorithm with the CT Pro 3D software (Nikon metrology). After X-ray CT imaging, the images were visualized and the samples devoid of roots were not considered for further analysis. For the loam, 24 samples were analyzed per bulk density level. For the sand, 23 and 13 samples were analyzed for the low and high bulk density, respectively.

5.2.1.2   Analysis of bulk density variation around the roots

The variation in rhizosphere bulk density around the roots was obtained from the X-ray CT images of the scanned samples. First, root segmentation of each sample was performed with a modified version of the segmentation algorithm Rootine v.2 (Phalempin et al., 2021a) in order to distinguish root voxels from background voxels. After root segmentation, we computed the so-called 'Root distance maps' on the segmented root system image using the 'Euclidian Distance Transform (3D)' plugin available in ImageJ (Schindelin et al., 2012). This resulted in images in which every soil voxel is assigned a value equal to its distance to the closest root in a 3D volume. The resulting images were then merged with the original gray scale data into one composite image. In this composite image, each voxel contains the root distance information in one channel and the gray value information in another channel. By looping over all x, y and z coordinates and retrieving the value of each channel, we obtained the average gray value as a function of the distance from the root surface. The average gray value profile was thereafter normalized by division by the mean gray value of the image (Equation 4.2). Finally, the deviation from the mean gray value was used to derive rhizosphere bulk density properties for each sample and treatment. The rationale of the employed method is that gray value changes can be used as proxy for changes in soil bulk density that also considers sub-resolution differences, as already suggested by Lucas et al. (2019). The workflow used in this study to analyze the variation in rhizosphere bulk density around the roots is shown in figure 5.2 for one small illustrative image of the loam low bulk density dataset.

5.2.2   Analysis of mucilage concentration in the rhizosphere

The impact of mucilage on soil hydraulic parameters depends on the spatial distribution of mucilage in the soil. The spatial distribution of mucilage is a function of numerous factors such as mucilage deposition rate, root radius and root growth rate and it is extremely hard to measure those factors directly (Holz, Zarebanadkouki et al.,
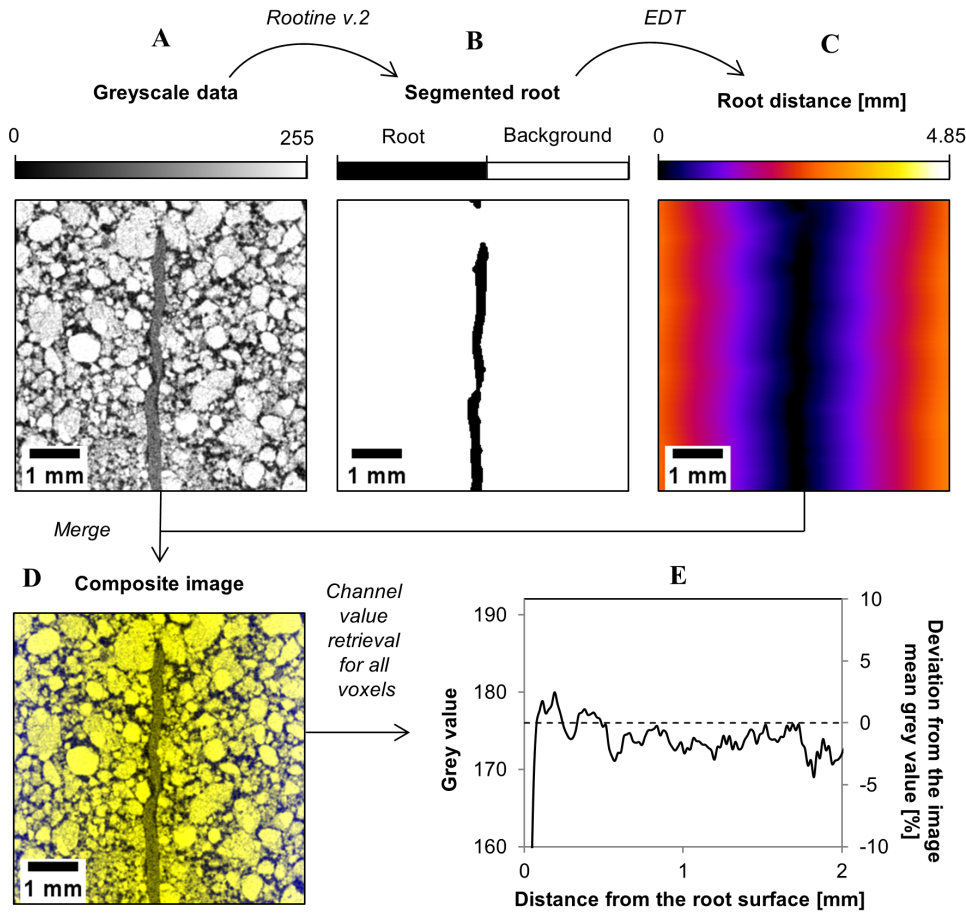
Figure 5.2: Workflow used to analyze the variation in rhizosphere bulk density around the roots. After root segmentation of the gray scale data (A), a root distance map is computed on the segmented root system (B). This root distance map (C) is then merged with the gray scale data into a composite image (D). This composite image is analyzed and the value of each of its channel is retrieved. This allows plotting the deviation from the mean gray value as a function of the distance from the root surface (E), which is further used to characterize the rhizosphere bulk density by simple scaling of the bulk soil bulk density

2018). We therefore set up a 2D axi-symmetric simulation model in COMSOL Multiphysics to predict the mucilage concentration profile around a root. We applied the diffusion-reaction equation in a moving reference frame so that the origin was always at the moving root tip. The root elongation was then implemented in analogy to the advection term (Kim & Silk, 1999):

$$\theta \frac{\partial}{\partial t} C = \frac{1}{r} \frac{\partial}{\partial r} (r D(\theta) \frac{\partial C}{\partial r}) + (D(\theta) \frac{\partial^2 C}{\partial r^2}) - (\theta v \frac{\partial C}{\partial z}) - KC\theta \qquad (5.1)$$

with the boundary condition,

$$D(\theta) \frac{\partial C}{\partial r} = -E \quad at \quad r = r_0 \quad and \quad z = [0, h_{tip}], \qquad (5.2)$$

where θ is the volumetric water content (cm^3 cm^{-3}), C is the concentration of mucilage (g g^{-1} dry soil), t is the time (d), r is the radial distance from the root axis (cm), z

is the distance from the root tip (cm), v is the root elongation rate (cm d^{-1}), K is the decomposition rate of mucilage at which fresh mucilage is decomposed to mucilage derivatives (d^{-1}), h$_{tip}$ (cm) is the zone behind the root tip where deposition occurs, E (µgd^{-1} per root tip) is the deposition rate, and D(θ) is the effective diffusion coefficient of mucilage in soil (cm^2 s^{-1}). The effective diffusion coefficient strongly depends on water content θ, i.e., with decreasing water contents the liquid phase becomes more and more tortuous and disconnected, which reduces effective diffusion. Several models (Bresler, 1973; Millington & Quirk, 1961; Papendick & Campbell, 1981) exist to estimate D(θ). Most of these models have been developed and tested for spreading of low molecular weight solutes. Mucilage also contains polymers of high-molecular weight, which may cause even more complex molecular transport dynamics within the soil pore space. Here, we chose the widely used empirical Millington und Quirk (1961) model to calculate D(θ) as

$$D(\theta) = D_0 \frac{\theta^{10/3}}{\phi^2} \qquad (5.3)$$

where D$_0$ is the diffusion coefficient of mucilage in pure water (cm^{2}s^{-1}) and ϕ is the soil porosity (-). This model was tested against experimental datasets in various studies (Chou et al., 2012; Moldrup et al., 2000; Partridge et al., 1999). Considering that

$$\phi = 1 - \frac{\rho_r}{\rho_s} \qquad (5.4)$$

where ρ_r is the soil bulk density in the rhizosphere and ρ_s is the soil particle density (set to ρ_s=2.65 g cm^{-3}), we scaled the porosity with the measured rhizosphere bulk density gradients. Processes such as root water uptake, compaction and mucilage deposition change the soil water content locally. For reasons of simplicity, however, the radial spreading of mucilage around the root (Equation 5.1 and 5.2) was computed using a constant soil water content of θ=0.4 cm^3 cm^{-3}. We chose two different mucilage deposition rates E (low and high) in the range of values found in literature (Chaboud, 1983; Zickenrott et al., 2016). All remaining model parameters were taken from our own measurements and from the literature and are listed in table 5.1. At the top and the side boundaries of the domain, we assumed a zero gradient. The bottom boundary was set to zero flux.

According to Nguyen et al. (2008) and Mary et al. (1993), the decomposition half-life of the organic compounds of mucilage may vary between 3 and 11 days. Carminati (2013), however, have shown experimentally that mucilage-like substances have an impact on the water content in the rhizosphere of roots that were as old as 2-3 weeks. The reason may be that microbes do not only degrade mucilage, but also produce gel-like substances called bacterial exopolysaccharides (Carminati & Vetterlein, 2012), which have similar physical properties as mucilage (Or et al., 2007). We therefore concluded that not only fresh mucilage, but also its derivatives alter soil hydraulic properties and further assumed that all of the degraded mucilage was converted to mucilage derivatives. Due to a lack of experimental data, we supposed that mucilage derivatives have the same impact on soil hydraulic properties as fresh mucilage. Albalasmeh und Ghezzehei (2014) suggested that dry mucilage is tightly bound to soil particles and no longer diffuses freely into the soil. This theory is supported by experimental findings by Carminati et al. (2010), who showed that the thickness of the rhizosphere of lupine

roots did not significantly change within one week of observation using neutron radiography. We therefore assumed that the mucilage derivatives are irreversibly bound to the soil particles and can no longer move by diffusive transport. Based on these assumptions, the radial profile of the concentration of mucilage derivatives at a distance sufficiently far away from the root tip does not change anymore with time. Furthermore, hydrodynamic dispersion of mucilage was neglected, which we justified with the rather slow water fluxes.

Table 5.1: Parameter values for the computation of the mucilage concentration profile around a single maize root.

Parameter	Symbol	Value	Unit	Source
Root elongation rate	v	0.9	mm d^{-1}	Materechera et al. (1991)
Root radius	r	0.1	mm	Our measurement
Liquid diffusion coefficient of mucilage	D_0	4e^{-8}	cm^2 s^{-1}	Watt et al. (2006)
Porosity	ϕ	variable	-	Our measurement
Mucilage deposition rate	E	12 (low) 24 (high)	μg d^{-1} per root tip	Chaboud (1983)
Decomposition rate of mucilage	k	0.22	d^{-1}	Nguyen et al. (2008)
Root length behind the tip from which the mucilage is deposited	h$_{tip}$	2	mm	Iijima et al. (2003)

5.2.3 Analysis of the effect of rhizosphere bulk density and mucilage concentration on soil hydraulic parameters

5.2.3.1 The effect of rhizosphere bulk density on soil hydraulic parameters

The pore space in aggregated soils can be classified into textural and structural pore space (Leij et al., 2002). Textural pore space, which is determined by the distribution of soil primary particles, is relatively stable. Structural pore space, which is defined by the position and orientation of aggregates relative to one another, however, can easily be modified when exposed to external forces (Leij et al., 2002; Or & Ghezzehei, 2002; Or et al., 2000). Following these considerations, we assume that all observed changes in rhizosphere bulk density are caused by modifications of the structural pore space. We used the pedotransfer functions by Assouline (2006a), Assouline (2006b) and Carman (1997) to relate the changes in rhizosphere bulk density to changes in soil hydraulic parameters. Assouline (2006a, 2006b) calibrated and validated the relationships between soil hydraulic parameters and soil bulk density at various compaction levels between 0.68 and 1.59 g cm^{-3}. The rhizosphere bulk density levels used in our study cover a range between 0.9 and 1.6 g cm^{-3} and are thus within this range.

5.2.3.2   The effect of mucilage concentration on soil hydraulic parameters

The high water adsorption capacity of mucilage leads to an increase in the water content of the rhizosphere for a given matric potential and thereby affects the water retention in the rhizosphere (Carminati et al., 2010). To simulate the effect of mucilage concentration on soil water retention, we used the model by Kroener et al. (2014)

$$h_m(\theta_m) = h(\theta) - \omega_0 c_w^\beta \tag{5.5}$$

where $h_m(\theta_m)$ and h(θ) are the pressure heads with and without the impact of mucilage, θ_m and θ are the volumetric water contents with and without the impact of mucilage and ω_0 and β are fitting parameters that describe how c_w, the gravimetric mucilage concentration in water (g g^{-1}), affects the overall water retention behavior. c_w is thereby defined as

$$c_w = \frac{C \rho_r}{\theta_m \rho_w} \tag{5.6}$$

where C is the local gravimetric concentration of mucilage in the soil (g g^{-1}), ρ_r is the local rhizosphere bulk density (g cm^{-3}) and ρ_w is the density of water (1 g cm^{-3}). Kroener et al. (2018) investigated the influence of soil texture on the mucilage-related increase in water content at a given water potential. They found that mucilage concentrations of 1 and 8 (mg g^{-1} dry soil) increase the water content by 0.5 and 6.6 % in coarse and fine sand and by 11.2 and 12.5 % in silty soil at a water potential of -500 cm. We assumed that the silty soil corresponds approximately to our loam. With the help of the simplex method (Nelder & Mead, 1965) and our soil hydraulic parameter sets, we then optimized the fitting parameters ω_0 and β so that the findings of Kroener et al. (2018) were approximated as accurately as possible. We obtained ω_0=10^{10} and β=4.1 for loam and ω_0=6.9^6 and β=2.99 for sand. These values are in good agreement with the parameters used in other studies (Carminati, Kroener et al., 2016; Kroener et al., 2016; Schwartz et al., 2016). ω_0 can vary by some orders of magnitude because the fitted parameter ω_0 is extremely sensitive to slight changes of the value of the fitted exponent β.

Due to its high viscosity, mucilage decreases the soil hydraulic conductivity. We approximated this decrease by the relation given by Ahmed et al. (2014):

$$K_m = \frac{\mu_w}{\mu(c_w)} K \tag{5.7}$$

where K_m and K (Equation 5.11) are the unsaturated hydraulic conductivities in soil with and without mucilage and μ_w and $\mu(c_w)$ are the viscosities of water (μ_w = 1 mPa s^{-1}) and mucilage, respectively. The latter is given as

$$\mu(c_w) = \mu_w(1 + v c_w^d) \tag{5.8}$$

where v=566 and d=1.4 are unitless fitting parameters given by Ahmed et al. (2014).

5.2.4   Analysis of bulk soil hydraulic parameters

We measured the soil water retention and soil hydraulic conductivity curves for both soils loam and sand at the low bulk density levels (ρ = 1.26 and 1.5 g cm^{-3} for

loam and sand, respectively) with the HYPROP system (METER Group AG). Five 250 cm^3 metal cylinder replicates were analyzed for each soil texture. We then used the HYPROP-FIT software (Pertassek et al., 2015) to fit soil hydraulic parameters to these curves, which are used in the closed-form equations established by Mualem (1976) and van Genuchten (1980):

$$\theta(h) = \theta_r + \frac{\theta_s - \theta_r}{\left(1 + (\alpha h)^n\right)^{1 - \frac{1}{n}}} \qquad (5.9)$$

$$Se = \frac{1}{\left(1 + (\alpha h)^n\right)^{1 - \frac{1}{n}}} \qquad (5.10)$$

$$K(Se) = K_{sat} Se^l (1 - (1 - Se^{\frac{n}{n-1}}))^2 \qquad (5.11)$$

where h is the absolute value of the pressure head (cm), θ_s and θ_s are saturated and residual water content, respectively, α is the inverse of the air entry suction (cm^{-1}), n is a shape parameter (-), Se is the water saturation (-), l is the tortuosity (-) and K and K_{sat} are unsaturated and saturated hydraulic conductivities (cm d^{-1}), respectively. According to Mualem (1976), we assumed l=0.5. Note that we have kept θ_s separated from the soil porosity ϕ, considering that θ_s may be smaller than ϕ due to air entrapment in the soil. All soil hydraulic parameters are given in table 5.2.

Table 5.2: Bulk soil hydraulic parameters for loam and sand at the low bulk density level.

Soil type	ρ g cm^3	θ_s cm^{3}cm^{-3}	θ_r cm^{3}cm^{-3}	α cm^{-1}	n -	l -	K_{sat} cm d^{-1}
Loam	1.26	0.494	0.041	0.0256	1.49	0.5	145
Sand	1.5	0.414	0.03	0.038	2	0.5	1864

5.2.4.1 One-dimensional rhizosphere model

To evaluate the impact of changes in water retention and hydraulic conductivity due to variations in rhizosphere bulk density and mucilage concentration on soil water dynamics and root water uptake, we set up a 1D rhizosphere model in COMSOL Multiphysics, which is schematically illustrated in figure 5.3. This 1D model represents a radial cut through a soil cylinder surrounding a single root and thus contains a root and a bulk soil boundary. We prescribed the xylem water potential h_x and computed the radial flux J_r at the root boundary as

$$J_r = k_r(h - h_x) \qquad (5.12)$$

where k_r (d^{-1}) is the radial root hydraulic conductivity and h (cm) is the soil water potential at the root surface. The xylem water potential h_x applied by the plant was set to h_x = -15000 cm during the day and h_x = 0 cm during night (Cai et al., 2018). To allow a smooth transition in pressure between day and night, we considered daily sinusoidal

variations (Doussan et al., 2003). At the bulk soil boundary, we set a no-flux condition. The Richards equation was then solved in radial coordinates as

$$\frac{\partial \theta}{\partial t} = \frac{1}{r}\frac{\partial}{\partial r}(rk(\theta)\frac{\partial h}{\partial r} = 0 \tag{5.13}$$

where r (cm) is the radial distance to the root surface. Assuming that the root is located vertically within the soil domain, gravity was neglected.
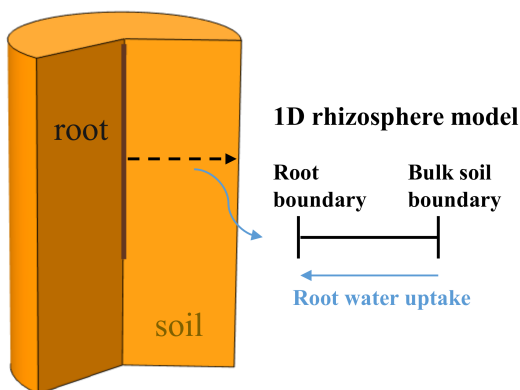
Figure 5.3: Schematic illustration of the 1D rhizosphere model

5.2.4.2   Scenario description

We considered six different scenarios. In the control scenario, no impact of variations in rhizosphere bulk density or mucilage was considered. In the rhizosphere bulk density scenario, we only took into account variations due to gradients in rhizosphere bulk density. In the mucilage high scenario, we considered the impact of high mucilage deposition. In the mucilage low scenario, we took into account the influence of low mucilage deposition. In the rhizosphere bulk density and mucilage high respectively mucilage low scenarios, variations due to both rhizosphere bulk density and high respectively low mucilage depositions were considered. An overview with the respective symbols is given in table 5.3.

Table 5.3: Overview of simulation scenarios.

Name	Symbol
Control	c
Rhizosphere bulk density	rbd
Mucilage high	mh
Mucilage low	ml
Rhizosphere bulk density and mucilage high	rbd + mh
Rhizosphere bulk density and mucilage low	rbd + ml

5.2.4.3 Simulation set-up

We set up a virtual drying experiment. The root radius was set to 0.1 mm, which corresponds approximately to the median maize root radius found in the X-ray CT experiment. According to Gardner (1960), the maximum distance that water has to travel from any point in a soil domain to the nearest root is less than or equal to half the mean distance between neighboring roots, which is calculated as

$$HMD = (\pi RLD)^{-\frac{1}{2}} \tag{5.14}$$

where RLD is the root length density (cm cm^{-3}) and HMD is the half the mean distance (cm). An assumed root length density of RLD=0.5 cm cm^{-3} leads to HMD=0.8 cm, which was the radial extent of our soil domain. We used a radial root hydraulic conductivity of K_{rad} = 1.9e^{-4} d^{-1} (Meunier et al., 2018) and two different initial pressure heads h_{ini} = -10 cm, a value that could be typically assumed directly after watering, and h_{ini} = -100 cm, a value that is close to field capacity. All parameters are listed in table 5.4. To catch all small-scale variations in soil hydraulic properties due to variations in rhizosphere bulk density and mucilage concentration, we discretized the soil domain into 1D elements of 1e^{-3} mm side length. We used adaptive time stepping with a relative tolerance of 0.0001 s convergence criteria. The simulations were run over 15 days.

Table 5.4: Simulation set-up of the virtual drying experiment.

Parameter	Description	Value	Unit
r_0	Root radius	0.1	mm
r_1	Radial expansion of soil domain	8	mm
K_{rad}	Root radial hydraulic conductivity	1.9e^{-4}	d^{-1}
h_x	Xylem water potential	-1.5e^4	cm
h_{ini}	Initial pressure head	-10	cm

5.3 Results

5.3.1 Gradients in rhizosphere bulk density

Figure 5.4 shows the rhizosphere bulk density as a function of distance from the root surface for both soil textures and soil bulk densities. Rhizosphere bulk density in the immediate vicinity of roots was lower than in the bulk soil for both loam and sand. Farther away from the root surface, a minor soil compaction could be observed for loam. The shape of the rhizosphere bulk density variation is reminiscent of an oscillatory wave, which is caused by particle re-alignment when the root penetrates the soil (Koebernick et al., 2019; M. Suzuki et al., 2008). The low bulk density at the root-soil interface may also be caused by gap formation due to root shrinkage (Carminati et al., 2013; Koebernick et al., 2018).
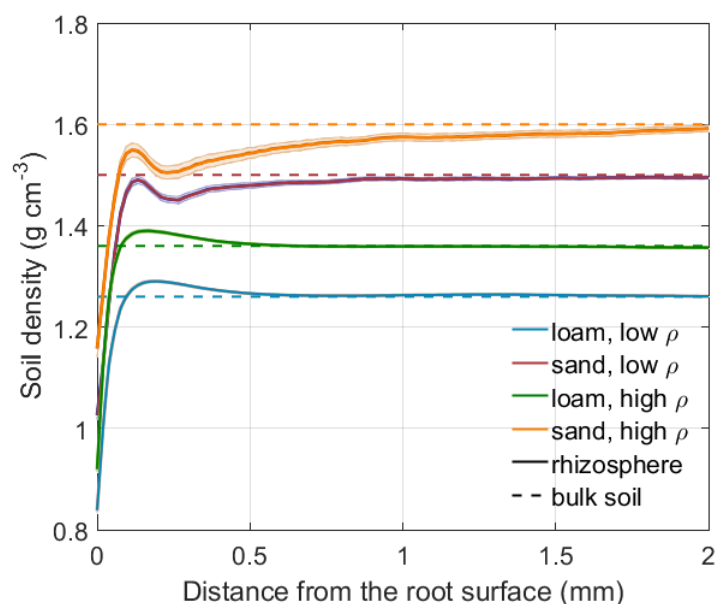
Figure 5.4: Rhizosphere bulk density as a function of the distance from the root surface for both soil textures and bulk densities. The semi transparent ribbons denote the standard error of the measurement around the mean for 24 (loam, low and high density), 23 (sand, low bulk density) and 13 (sand, high bulk density) samples. The dashed lines represents the bulk soil density for each soil texture and bulk density level.

5.3.2   Gradients in mucilage concentration

Figure 5.5A shows the concentration profiles of fresh mucilage and mucilage derivatives for the example of low density loam in soil with uniform rhizosphere bulk density simulated with a low and a high mucilage deposition rate (Table 5.1). For further model simulation of the impact of mucilage on root water uptake, we used the radial concentration profiles of mucilage derivatives at a distance sufficiently far away from the root tip since they can be considered as constant in time. For both low and high mucilage deposition rates, we computed radial mucilage concentration profiles for both soil textures and soil bulk density levels as well as with and without rhizosphere bulk density gradients (Figure 5.5B, C). The radial mucilage concentration profiles differed slightly for the different soil textures and more significantly in consideration of the radial gradients in rhizosphere bulk density. The low rhizosphere bulk density in the immediate vicinity of the root led to a larger mucilage concentration (mg mucilage g^{-1} dry soil) within a distance of 0-0.1 mm from the root surface.

5.3.3   Effect of gradients in rhizosphere bulk density and mucilage concentration on the soil hydraulic parameters

From each of the radial rhizosphere bulk density respective mucilage concentration profiles shown in figure 5.4 and 5.5B, C, we took 500 values at a distance of 0-10mm from the root surface. The 500 points were drawn in logarithmically spaced distances (many points near the root and fewer points further away), because both rhizosphere bulk density and mucilage concentrations near the root change strongly
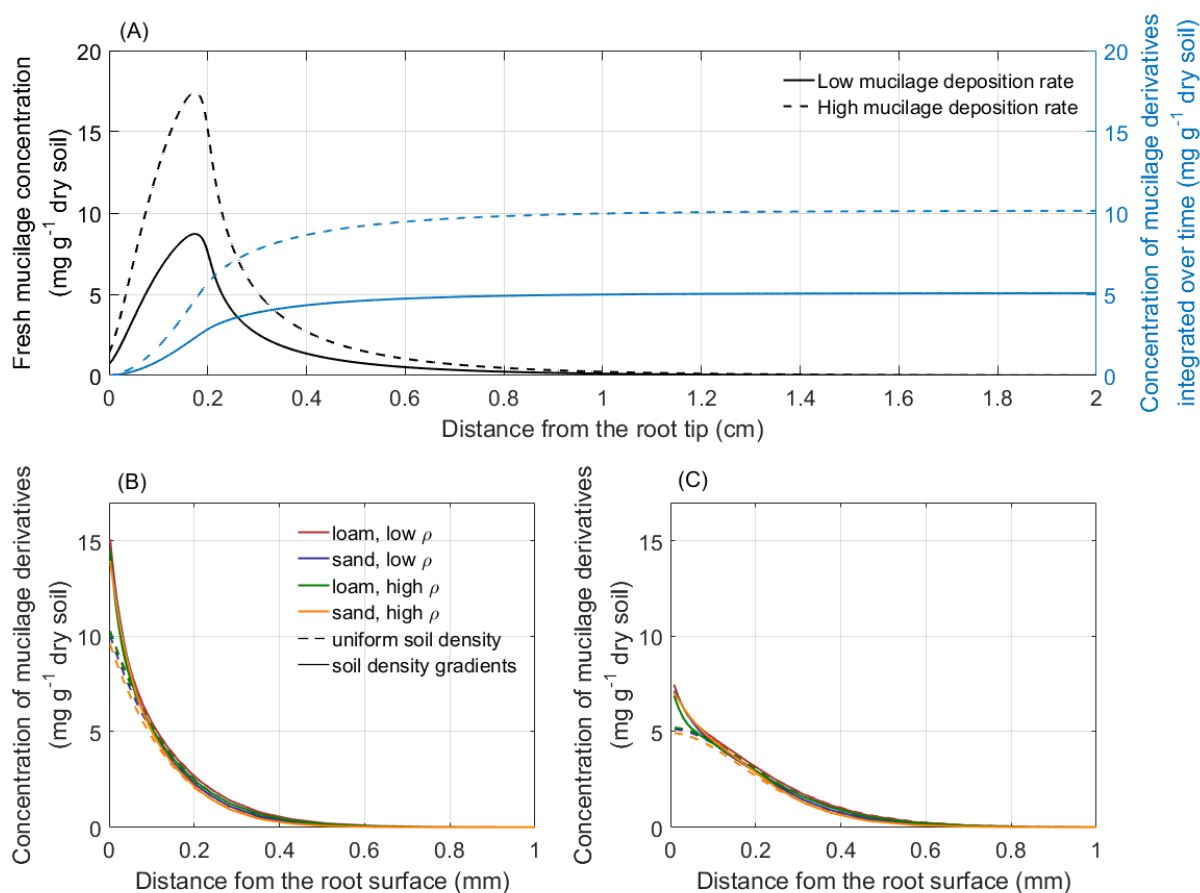
Figure 5.5: Concentration profiles of fresh mucilage and mucilage derivatives after a simulation time of 30 days: along the root axis for the example of low bulk density loam with uniform rhizosphere bulk density simulated with a low and a high mucilage deposition rate (A); radial concentration profile of mucilage derivatives sufficiently far away from the root tip for the high (B) and the low (C) mucilage deposition rate around a single maize root in loam and sand for both bulk densities with and without the consideration of radial gradients in rhizosphere bulk density.

over small distances in the radial profiles. For each of the 500 rhizosphere bulk density values, we computed the soil hydraulic parameters. For each of the 500 mucilage concentration values, we computed soil water retention curves and estimated the corresponding soil hydraulic parameters.

Figure 5.6 shows the deviations in soil hydraulic parameters relative to the bulk soil values (Table 5.2) due to variations in rhizosphere bulk density for both loam and sand and low and high levels of soil bulk density. A decrease in rhizosphere bulk density led to an increase in saturated volumetric water content θ_s due to an increase in the fraction of large pores (Figure 5.6A, (Assouline, 2006a), Equation 5.5). The residual water content θ_r in the rhizosphere slightly decreased due to the decrease in specific soil particle surface when rhizosphere bulk density decreased (Figure 5.6B, (Assouline, 2006a), Equation 5.6). The inverse of the air entry suction α increased with a decrease in rhizosphere bulk density due to an earlier air entry point caused by the higher fractions of large pores (Figure 5.6C, (Assouline, 2006a) converted from

Brooks and Corey). Changes of the van Genuchten shape parameter n depend on the development of the pore size distribution: If the variance of the distribution of pore radii increases more than the mean pore radius, a decreased shape parameter n is to be expected. If the opposite is the case, the shape parameter n increases (Stange & Horn, 2005). We assumed that both the variance and the mean size of the pore radii increase uniformly and n therefore remained constant (Figure 5.6D). According to the Kozeny-Carman relation (Carman, 1997), the saturated soil hydraulic conductivity K_{sat} increases when rhizosphere bulk density decreases due to the increased volume of large pores (Figure 5.6E). Variations in rhizosphere bulk density give information about the total change in the volume of voids, but not about the volume distribution of voids, i.e., the tortuosity or the aggregate connectivity (Assouline, 2006a). We therefore kept the tortuosity parameter constant at l=0.5.

Figure 5.6: Relative changes in the van Genuchten parameters θ_s (A), θ_r (B), α (C), n (D) and K_{sat} (E) due to variations in rhizosphere bulk density for loam and sand and for low and high soil bulk density levels.

Figure 5.7 shows the deviations in soil hydraulic parameters relative to the bulk soil values (Table 5.2) due to variations in mucilage concentration (low and high concentrations according to the radial concentration profiles in figure 5.5B, C) for both loam and sand and for both low and high levels of soil bulk density. Mucilage has no impact on the saturated water content θ_s and on the residual water content θ_r since it does not influence the pore size distribution (Figure 5.7A, B). Due to the high water adsorption capacity of mucilage, it is generally assumed that the inverse of the air entry suction α decreases with increasing mucilage concentration. With our parameterization, however, α remained constant, which is in line with findings by Kroener et al. (2018) for coarse and medium textured soils (Figure 5.7C). The shape parameter n also decreased due to the high water adsorption capacity of mucilage, since for a given decrease in pressure head the water content decreases less than in soil without mucilage. It must be noted that this decrease in n was stronger in sand than in loam (Figure 5.7D). Considering that mucilage increases the viscosity, the saturated hydraulic conductivity decreased (Figure 5.7E). To date, it is not clear how mucilage affects soil pore tortuosity (Haupenthal et al., 2021). We therefore kept the tortuosity parameter constant at l=0.5.

Subsequently, we combined the effects of variations in rhizosphere bulk density and mucilage concentration on soil hydraulic parameters assuming superposition. The effects of both gradients in rhizosphere bulk density and mucilage concentration on soil hydraulic parameters are shown in figure 5.8. While the saturation and residual water content θ_s and θ_r are only influenced by rhizosphere bulk density, the shape
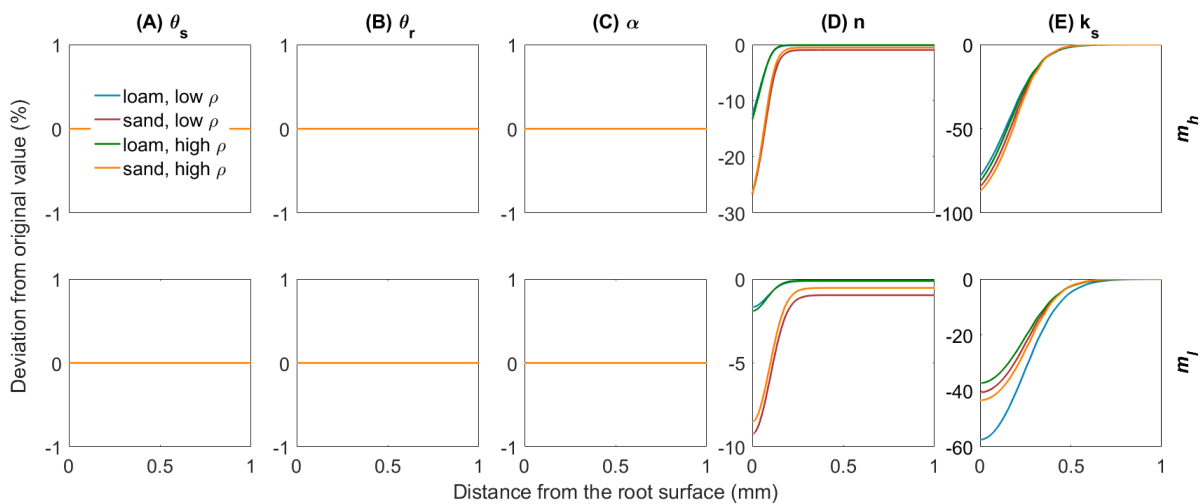
Figure 5.7: Relative changes in the van Genuchten parameters θ_s (A), θ_r (B), α (C), n (D) and K_{sat} (E) due to variations in mucilage concentration for loam and sand, for low and high soil bulk density and for low and high mucilage deposition rates.

parameter n depends only on the mucilage concentration (Figure 5.8A, B, and D). The inverse of the air entry suction α as well as the saturated soil hydraulic conductivity K_{sat} are a function of both the rhizosphere bulk density and the mucilage concentration (Figure 5.8C, E). In our parameterization, mucilage had only a very small influence on α. Therefore, α increases in the rhizosphere due to the earlier air inflow caused by the higher fractions of large pores. Both rhizosphere bulk density and mucilage have a strong impact on K_{sat}. In the immediate vicinity of the root, the impact of rhizosphere bulk density is stronger and K_{sat} therefore increases, whereas at a distance of about 0.1 to 0.4 mm, mucilage formation is more important and K_{sat} decreases.
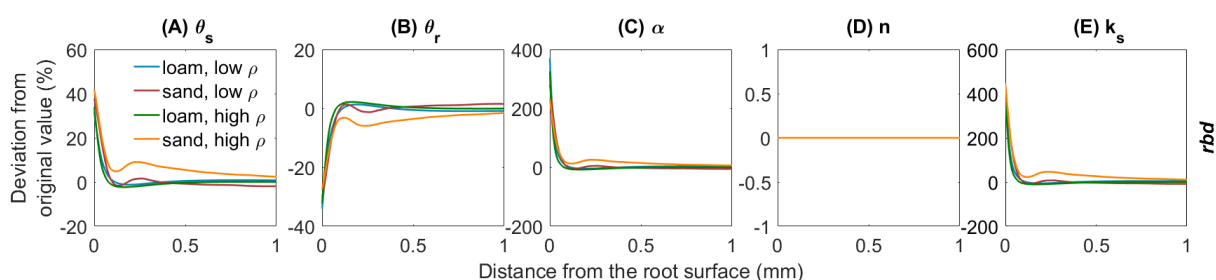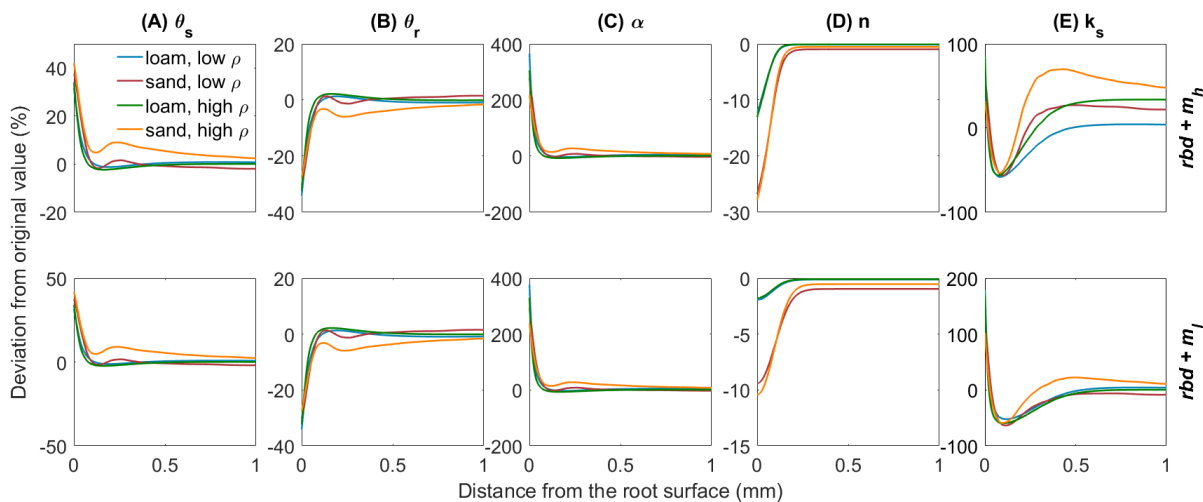

Figure 5.8: Relative changes in the van Genuchten parameters θ_s (A), θ_r (B), α (C), n (D) and K_{sat} (E) due to variations in rhizosphere bulk density and mucilage concentration for loam and sand, for low and high soil bulk density levels and for low and high mucilage deposition rates.

5.3.4 Effect of gradients in rhizosphere bulk density and mucilage concentration on the soil water retention and soil hydraulic conductivity curves

Using the previously computed soil hydraulic parameters, we computed soil water retention and soil hydraulic conductivity curves as a function of rhizosphere bulk density and mucilage concentration gradients for both loam and sand and for both low and high soil bulk density (Figure 5.9 and 5.10). Reduced rhizosphere bulk density resulted in increased water content when the soil was wet and in decreased water content when the soil was dry. Similarly, soil hydraulic conductivity increased at pressure heads close to zero and decreased when the pressure head became more negative. Mucilage increased the water retention, especially in case of very negative pressure heads. For the low mucilage concentration, the increase in water retention was only very small and more pronounced in sand than in loam. While the hydraulic conductivity increased due to the higher retention of mucilage, it was simultaneously reduced due to the higher viscosity of mucilage. In loam, both high and low concentrations of mucilage led to a general decrease in the soil hydraulic conductivity. For low mucilage concentrations, the same was true in sand. However, high mucilage concentrations in sand led to increased hydraulic conductivity in dry soil. The simultaneous consideration of mucilage deposition and gradients in rhizosphere bulk density led to a higher mucilage concentration in the rhizosphere (Figure 5.5B, C), which in turn affected water retention and hydraulic conductivity. For the high mucilage concentration, the combined effect of mucilage and rhizosphere bulk density led to a general increase of retention in the whole saturation range. This was true for both loam and sand as well as low and high soil bulk density. For the low mucilage concentration, the combined effect of mucilage and rhizosphere bulk density led to a general increase of water retention in the wet range. In the dry range of loam, water retention was increased close to the root, but decreased farther away. In the dry range of sand, it was generally decreased. The combined effect of mucilage and rhizosphere bulk density led to a general decrease in the soil hydraulic conductivity at pressure heads of less than approximately -10 cm. In general, rhizosphere bulk density had a stronger influence when saturation was high ($h\geq$-10 cm), while the effect of mucilage concentration was higher in the negative range of pressure heads.

5.3.5 Scenario simulations

At the beginning of the simulation period, the pressure head was uniform. Due to the differences in soil hydraulic parameters, however, water content and soil hydraulic conductivity distribution in the rhizosphere varied for the different soil textures, soil bulk density levels, initial conditions and scenarios (Figure 5.11 and 5.12). For the subsequent drying experiment, the initial conditions are important since they determine the amount of water that is available in the soil domain.

At an initial pressure head of -10 cm, the low rhizosphere bulk density in the immediate vicinity of the root led to an increase in water content at the root boundary in loam for both bulk densities and the high density sand (Figure 5.11(I A, C, D)) and to a decrease for the low-density sand (Figure 5.11(I B)). At an initial pressure head of -100 cm, the low rhizosphere bulk density close to the root led to a decrease in soil water
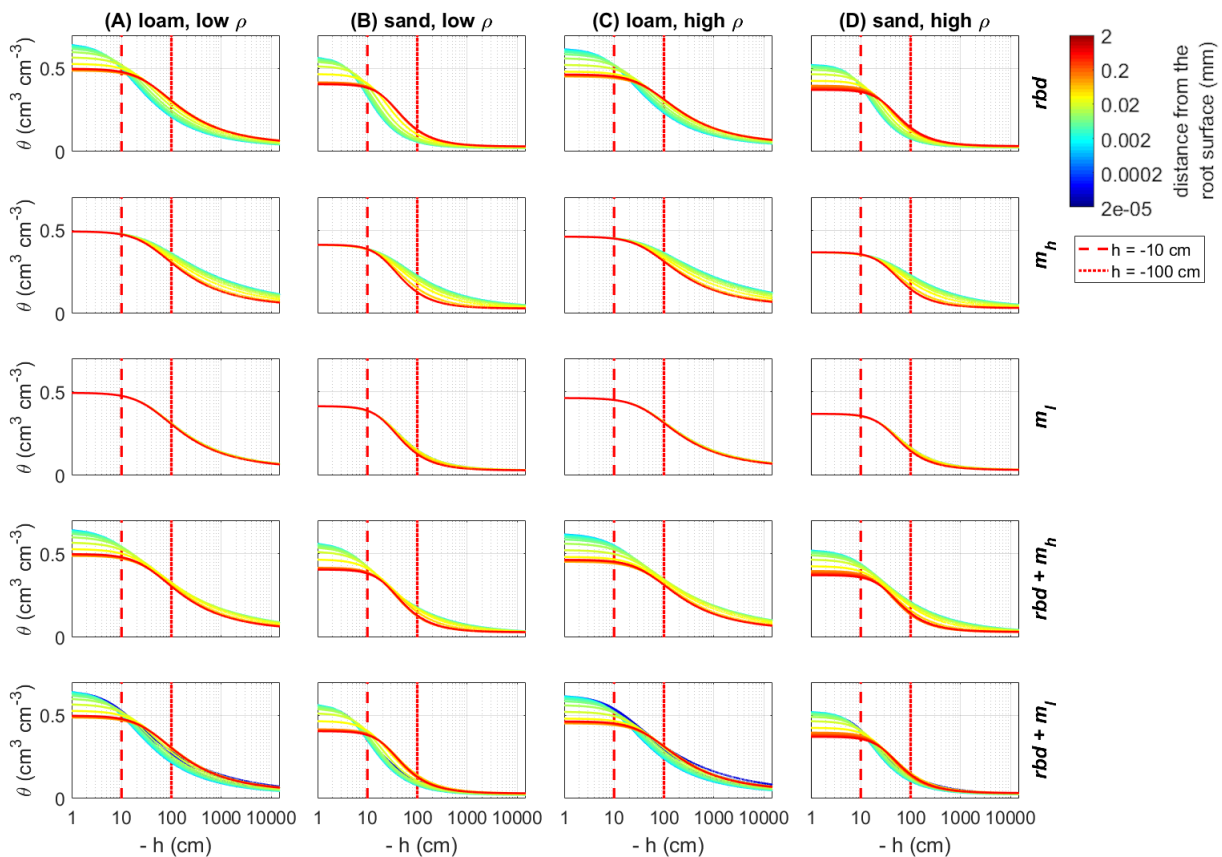
Figure 5.9: Changes in the soil water retention curves due to gradients in rhizosphere bulk density and/or mucilage concentration for loam and sand and low and high soil bulk density, the vertical red lines indicate the initial pressure heads used in the simulation h_{ini} = -10 cm and h_{ini} = -100 cm.

content for both soil textures and bulk densities (Figure 5.12 (I)). These differences as well as the irregular course of the water content curve can be explained by the differences in the inflection points of the water retention curves for the different soil textures and bulk densities (Figure 5.9 (*rbd*)). At an initial pressure head of -10 cm, mucilage did not have a significant impact on soil water content, since its effect on retention starts at lower pressure heads (Figure 5.9 (*mh, ml*) and 5.11 (I)). At an initial pressure head of -100 cm, the effect of mucilage is already visible through a higher water content at the root surface (Figure 5.9 (*mh, ml*) and 5.12 (I)).

At an initial pressure head of -10 cm, the gradients in rhizosphere bulk density led to an increase in hydraulic conductivity in the immediate vicinity of the root in high-density loam and sand (Figure 5.11 (II C, D)), and to a decrease in low-density loam and sand (Figure 5.11 (II A, B)). At an initial pressure head of -100 cm, the gradients in rhizosphere bulk density led to a decrease in hydraulic conductivity at the root surface for both soil textures and bulk densities (Figure 5.12 (I)). At both initial pressure heads as well as for both soil textures and bulk densities, mucilage led to a decrease in hydraulic conductivity in the immediate vicinity of the root due to the impact of viscosity (Figure 5.11 (II) and 5.12 (II)).

Figure 5.13 and 5.14 show for the two initial pressure heads, soil textures, soil bulk densities, and for all scenarios the net transpiration rate, the cumulative transpira-
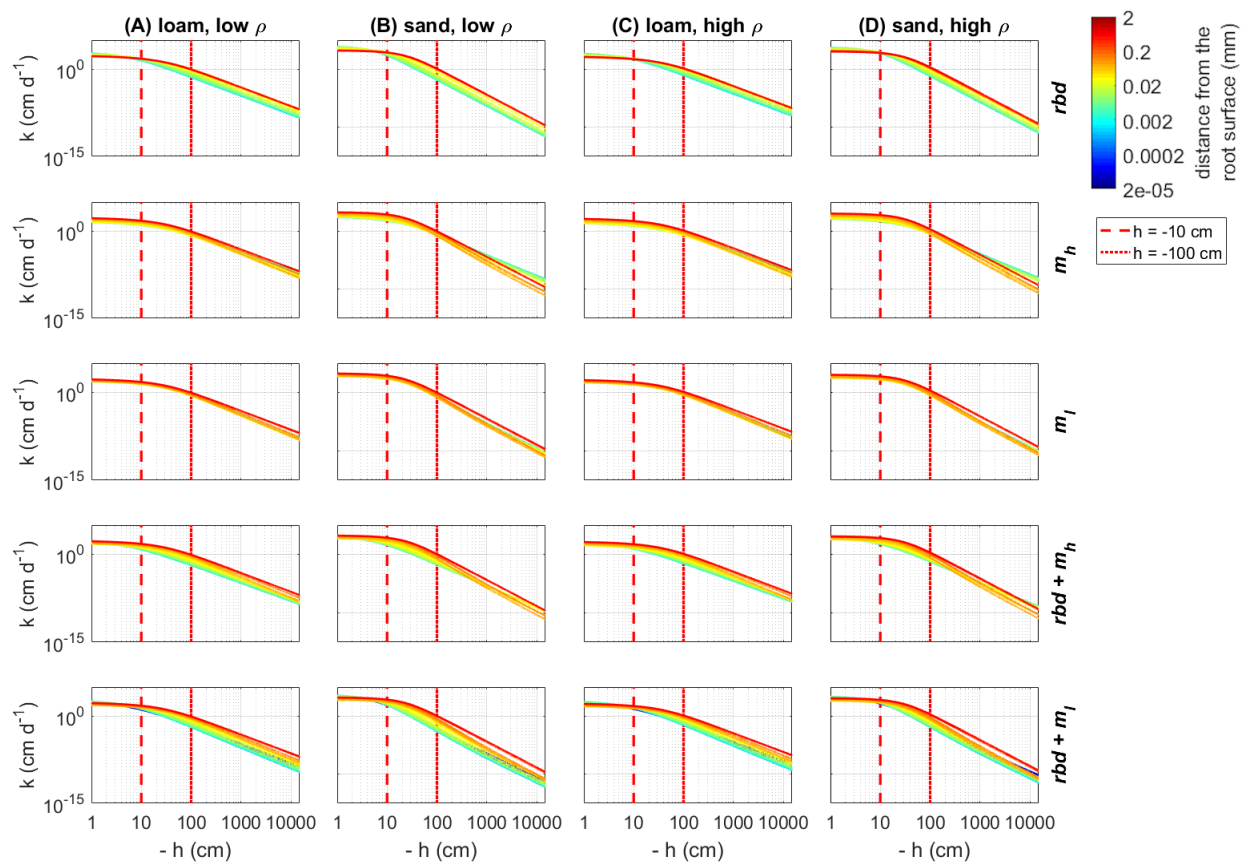
Figure 5.10: Changes in the hydraulic conductivity curves due to gradients in rhizosphere bulk density and/or mucilage concentration for loam and sand and low and high soil bulk density, the vertical red lines indicate the initial pressure heads used in the simulation h_{ini} = -10 cm and h_{ini} = -100 cm.

tion rate as well as the cumulative transpiration of the scenarios with rhizosphere bulk density and/or mucilage gradients relative to the control scenario. Due to the huge gradients in pressure head as well as in soil hydraulic conductivity in the rhizosphere, the simulation scenarios with low-density sand, including rhizosphere bulk density variation and low mucilage concentration (Figure 5.13 B (*rbd + ml*) and 5.14 B (*rbd + ml*)) did not converge and were therefore omitted.

Compared to the control scenario, the rhizosphere bulk density gradient led to an earlier water stress onset and a higher reduction in the transpiration rate by 2 to 4 % for both initial pressure heads, soil textures and bulk densities (Figure 5.13 and 5.14). This can be explained by the lower soil hydraulic conductivity at the root surface due to the drop in rhizosphere bulk density, which limited the water transport towards the root (Figure 5.10 (rbd)). Over time, however, the cumulative transpiration in the rhizosphere bulk density scenarios approached that of the control scenario (Figure 5.13 (III) and 5.14 (III)). Due to the initially large amount of available water in the scenarios with loam and high-density sand at an initial pressure head of -10 cm (Figure 5.13 (III A, C, D)), the cumulative transpiration in the rhizosphere bulk density scenarios was even higher than in the control scenario at the end of the simulation.
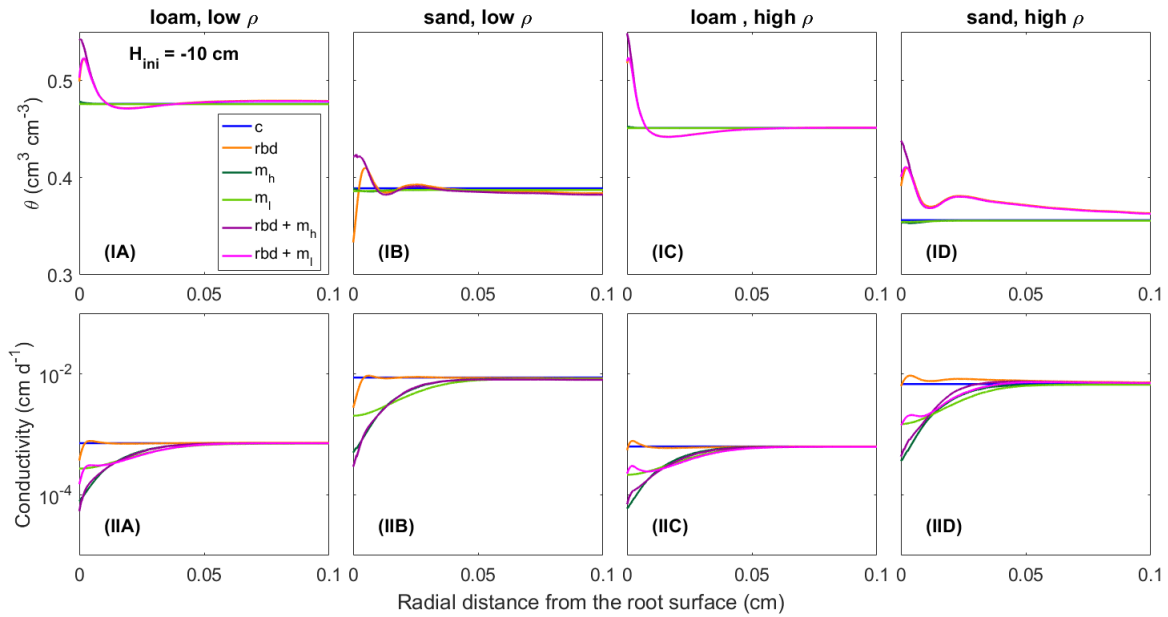
Figure 5.11: Radial gradients of water content (θ) (I) and soil hydraulic conductivity (II) at the start of the simulation period for loam and sand, for low and high soil bulk density (A, B, C, D), for the different scenarios (Table 5.3) and an initial pressure head of h_{ini} = -10 cm.
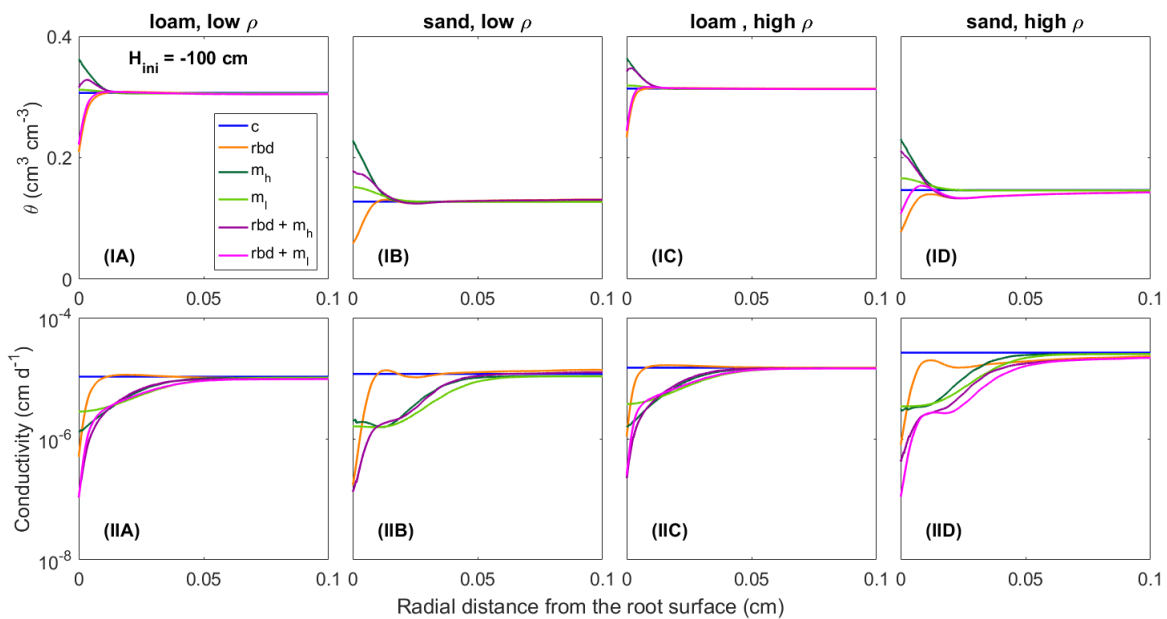
Figure 5.12: Radial gradients of water content (θ) (I) and soil hydraulic conductivity (II) at the start of the simulation period for loam and sand, for low and high soil bulk density (A, B, C, D), for the different scenarios (Table 5.3) and an initial pressure head of h_{ini} = -100 cm.

The presence of mucilage also led to an earlier water stress onset and a higher reduction in the transpiration rate by 2 to 4 % compared to the control scenario for both soil textures and bulk densities (Figure 5.13 and 5.14). The reason is again the lower soil hydraulic conductivity close to the root surface, which limited water transport (Figure 5.10 (*mh*, *ml*)). Interestingly, in the scenarios with sand, at pressure heads < -500 cm the soil hydraulic conductivity directly at the root surface was actually higher
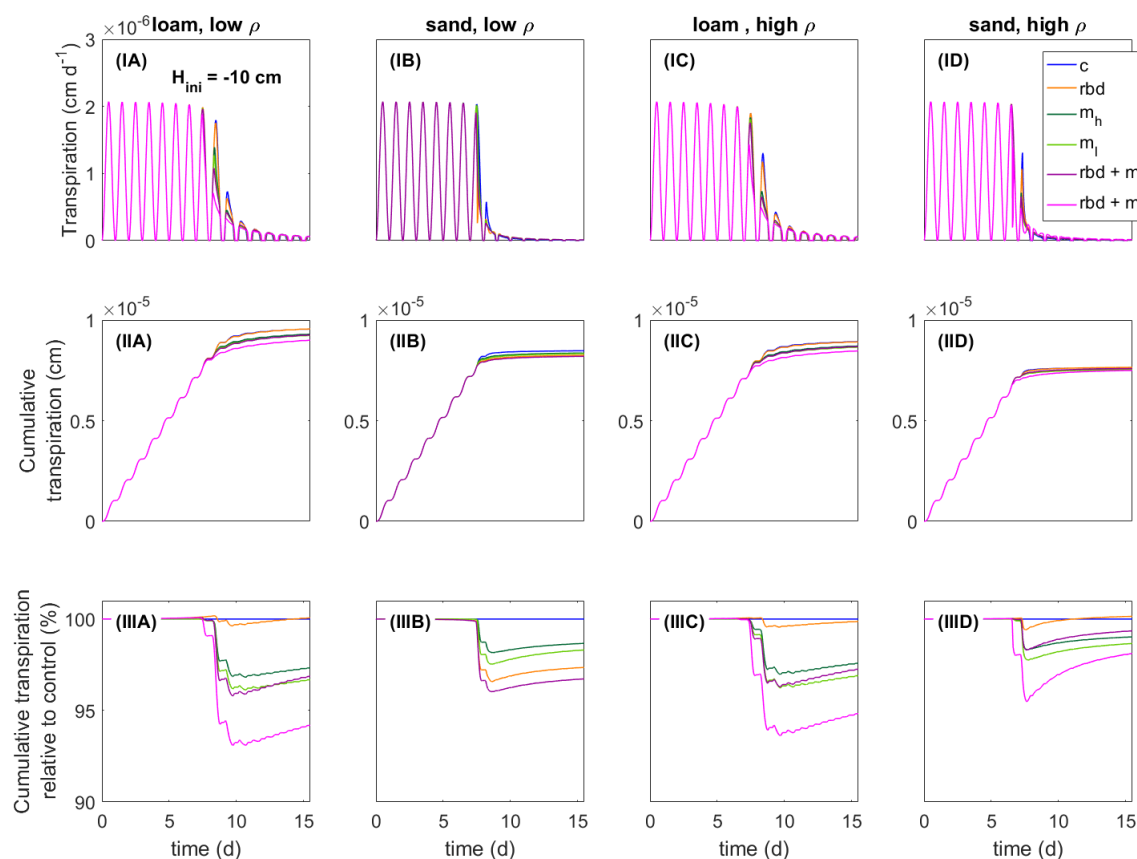
Figure 5.13: Transpiration rates (I), cumulative transpiration rates (II) and cumulative transpiration rate relative to the control scenario (III) for loam and sand as well as for low and high soil bulk density (A, B, C, D) for an initial pressure head of h_{ini} = -10 cm, an overview of the different scenarios is given in table 5.3.

than in the control scenario for the high mucilage concentration (Figure 5.10 (B *mh*, D *mh*)). However, this effect could not compensate for the lower hydraulic conductivity at a greater distance from the root surface, where the mucilage concentration was low and the effect of the viscosity was stronger than the effect of the increased water retention. The decrease in transpiration was stronger for the low than for the high mucilage concentration. This is because at low mucilage concentrations the increase in viscosity is more important than the increase in water retention.

The combination of rhizosphere bulk density and mucilage gradients (scenarios *rbd* + *mh*, *rbd* + *ml*) led to an even earlier onset of water stress respectively an even higher reduction in transpiration rate by 5 to 8 % (Figure 5.13 and 5.14). Interestingly, this decrease was much more pronounced for the low than for the high mucilage concentration. This is because the combination of the rhizosphere bulk density gradient with a low mucilage concentration not only increased the viscosity but also decreased water retention in the rhizosphere, which was not the case with the high mucilage concentration (Figure 5.9 (rbd + mh, rbd + ml) and 5.10 (rbd + mh, rbd + ml)). This resulted in a drastic reduction of the pressure head and the soil hydraulic conductivity at the root-soil boundary.

The impact of gradients in rhizosphere bulk density was stronger when the soil was initially drier. This is caused by differences in the amount of available water, which
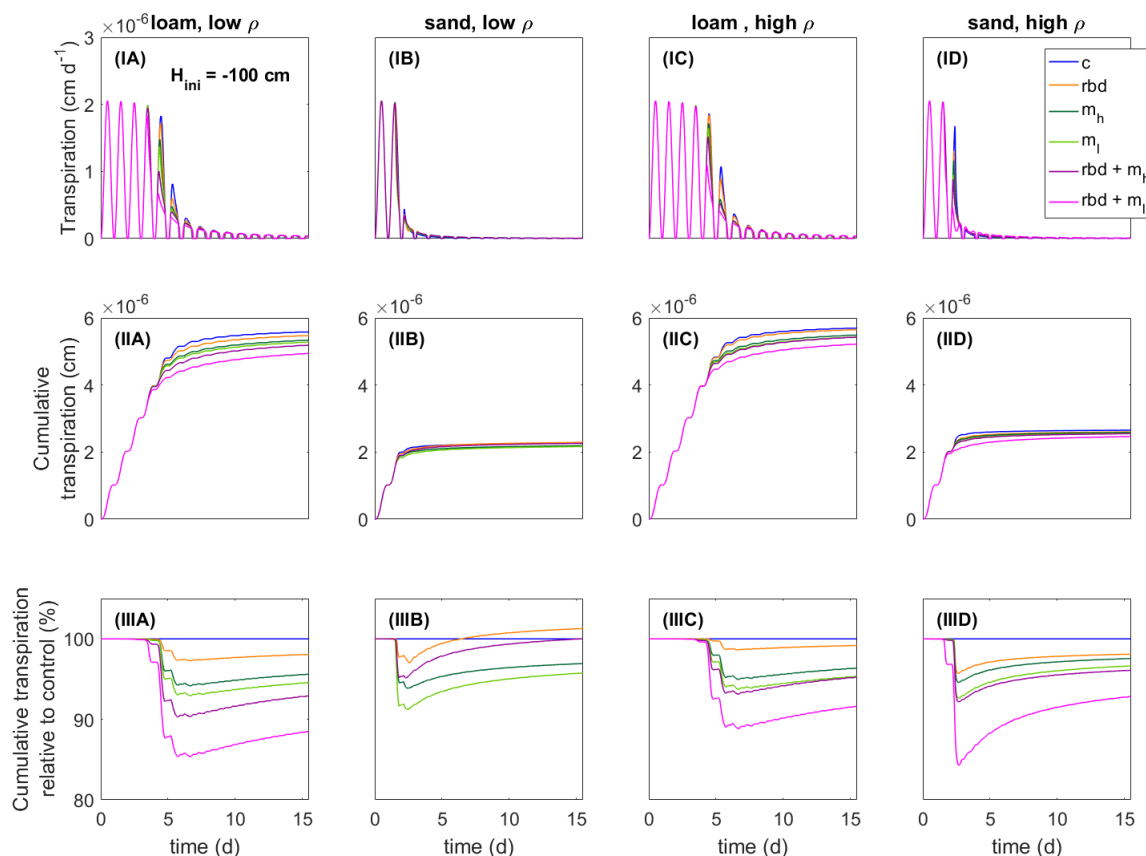
Figure 5.14: Transpiration rates (I), cumulative transpiration rates (II) and cumulative transpiration rate relative to the control scenario (III) for loam and sand as well as for low and high soil bulk density (A, B, C, D) for an initial pressure head of h_{ini} = -100 cm, an overview of the different scenarios is given in table 5.3.

depends on the initial pressure heads. The low rhizosphere bulk density in the immediate vicinity of the root led to an increased amount of available water if the initial pressure head was higher and to a decreased amount of available water if the initial pressure head was lower (Figure 5.13 and 5.14).

The intensity of the effect of rhizosphere bulk density and mucilage gradients was different for the two soil textures and bulk densities. However, there could not be identified a general rule, for which the effect of soil texture or bulk density was greater. It all depended on the initial soil hydraulic conditions and therefore on the soil hydraulic properties of the specific soil.

5.4 Discussions

5.4.1 Gradients in rhizosphere bulk density

The experimentally measured gradients of rhizosphere bulk density extended over a distance of 0.5 to 1 mm from the root surface for the loam and sand, respectively. A typical decrease in rhizosphere bulk density was observed in the immediate vicinity of the root and, in loam, a minor soil compaction was observed farther away from the

root (Figure 5.4). These observations agree well with previous findings (Helliwell et al., 2017, 2019; Koebernick et al., 2019; Lucas et al., 2019). The decrease in rhizosphere bulk density in the immediate vicinity of the root was assumed to originate from an increased number of larger pores. An increased number of larger pores again leads to a reduced retention and conductivity at intermediate to low water potentials, which is in line with experimental findings by Whalley et al. (2005). Radial soil compaction, such as described in many earlier studies (Aravena et al., 2011, 2014; Bruand et al., 1996; Koebernick et al., 2017; Lucas et al., 2019; Vollsnes et al., 2010), was much less significant than soil loosening in our experimental observations. A compaction of the rhizosphere associated with an increase in the number of smaller pores would lead to an increased retention and conductivity at medium to low water potentials, as observed by Aravena et al. (2014).

5.4.2   Gradients in mucilage concentration

We have used values from the literature to predict the distribution of mucilage in the rhizosphere of a maize plant. This was achieved by solving the diffusion-reaction equation. The most important parameters affecting the mucilage concentration in the diffusion-reaction equation are the mucilage deposition rate and the liquid diffusion coefficient of mucilage. According to the range of plausible literature values (Chaboud, 1983; Zickenrott et al., 2016), we used mucilage deposition rates of 12 (low) and 24 (high) μg d^{-1} per root tip. This led to maximum concentrations of mucilage derivatives between 5 and 10 mg g^{-1} dry soil, which is within the range of plausible mucilage concentration values of 0.05 up to 50 mg g^{-1} dry soil specified by Zickenrott et al. (2016). Observed mucilage deposition rates of *Zea mays* are lower than those of other plants such as *Vicia faba* or *Lupinus albus* where values of up to 34 μg d^{-1} per root tip were measured (Zickenrott et al., 2016). Such high mucilage deposition rates would lead to a larger proportion of the root system being affected by mucilage and therefore to a larger impact of mucilage on root water uptake. The gradient in mucilage concentration from the root surface to the bulk soil as well as the extent of the rhizosphere that is affected by mucilage is determined by the liquid diffusion coefficient (Holz, Zarebanadkouki et al., 2018; Zickenrott et al., 2016). However, mucilage diffusion can only be expected if the mucilage is freshly exuded. Dry mucilage has been shown to be firmly bound to soil particles, from where it cannot diffuse freely into the soil (Ahmed et al., 2014; Albalasmeh & Ghezzehei, 2014). We parameterized the liquid diffusion coefficient of mucilage with a value from literature (McCully & Boyer, 1997) and assumed that only fresh mucilage, but not mucilage derivatives can diffuse into the soil. Our simulation model predicted a rhizosphere thickness of approximately 0.6 mm, which corresponds well to the experimental values of Holz, Leue et al. (2018).

5.4.3   Relation between rhizosphere gradients and soil hydraulic parameters

We used the pedotransfer functions by Assouline (2006a, 2006b) and Carman (1997) to relate the changes in rhizosphere bulk density to changes in soil hydraulic parameters. These pedotransfer functions were originally developed based on differently compacted soil samples from the field. Due to a lack of more appropriate functions

(Alaoui et al., 2011), we assumed that these pedotransfer functions are also valid at the rhizosphere scale. Further experimental studies on the effects of changes in pore size distribution on soil hydraulic properties at the rhizosphere scale are needed. In our model, we use the Richards equation to simulate water flow in soil at the continuum scale. The reduced rhizosphere bulk density at the root-soil interface is thereby accounted for by adjusting the van Genuchten parameters according to the pedotransfer functions by Assouline (2006a, 2006b). In reality, it can be expected that the reduced rhizosphere bulk density at the root-soil interface is the result of averaging differences in rhizosphere bulk density on the pore scale, i.e., averaging gaps and the density of unchanged soil aggregates (Carminati et al., 2013). Considering that the loss of root-soil contact not only reduces, but prevents water flow, the unsaturated hydraulic conductivity could be lower than predicted by the pedotransfer functions by Assouline (2006a, 2006b). Carminati et al. (2008) predicted a decrease in unsaturated conductivity due to a loss of contact between soil aggregates by a few orders of magnitude. This would lead to a greater reduction in transpiration due to the gradient of rhizosphere bulk density than predicted by our simulation model. A possibility to take into account a stronger reduction in unsaturated conductivity due to a reduced contact area is the increase of the tortuosity parameter l (Equation 5.11) such as proposed by Schlüter et al. (2012) and Carminati et al. (2008). However, currently there are no pedotransfer functions to parameterize the tortuosity parameter when facing gap formation.

To evaluate the effect of mucilage concentration on the soil water retention curve and further on soil hydraulic parameters, we used the model by Kroener et al. (2014). Qualitatively, the impact of mucilage on soil hydraulic parameters matches well with findings from previous studies such as Carminati et al. (2010) and Carminati und Vetterlein (2012). Quantitatively, however, the effect depends much on the parametrization of the fitting parameters of this model. We chose these fitting parameters using experimental results on the influence of soil texture on the mucilage-related increase in water content at a given water potential from Kroener et al. (2018). However, this experimental information gives rather a plausible range than actual values for the fitting parameters and our parameter choice can be expected to have affected the simulation results.

5.4.4 Challenges of the non-linearity of the parameterization of the mucilage model

Several parameter functions show a huge nonlinearity, e.g., the soil water retention and soil hydraulic conductivity functions of the Mualem-van Genuchten parameterization, the Millington-Quirk model (Equation 5.3) and the models describing how rhizosphere bulk density and mucilage (Equation 5.5 and 5.8) alter hydraulic functions. These non-linearities could lead to convergence problems in the numerical scheme, especially if all feedback mechanisms between mucilage spreading and hydraulic dynamics were considered. Therefore, we had to make a few simplifications in this study, namely: (a) to calculate the spreading of mucilage around a root, we assumed a water content that is constant in space and time; (b) we assumed a stationary radial mucilage distribution throughout the entire simulation period; (c) we neglected hydrodynamic dispersion of mucilage, which is quite reasonable due to the rather slow water fluxes; (d) We assumed superposition of the effects of rhizosphere bulk density and

mucilage concentration on soil hydraulic parameters; this is possibly a simplification, because the effect of mucilage on soil hydraulic properties depends strongly on pore size. Despite these simplifications, the results show very realistic distributions, indicating that this approach overcomes the challenge to be both reasonable and feasible at the same time. This approach to first simulate spreading of mucilage and then the hydraulic dynamics allows to simulate the coupled physical processes and avoids several numerical convergence problems that which were expected due to the highly non-linear parameterization and feedback mechanisms.

5.4.5 The impact of rhizosphere gradients in rhizosphere bulk density and mucilage concentration on water dynamics

We found that the gradients of rhizosphere bulk density and mucilage concentration have a significant influence on the hydraulic properties of the rhizosphere (Figure 5.9 and 5.10). However, their influence on the absolute amount of water taken up by the root is, depending on the initial conditions and the duration of water absorption by the root, rather small (Figure 5.13 (II) and 5.14 (II)). The greatest effect of rhizosphere properties on root water uptake was observed in the scenarios in which gradients of rhizosphere bulk density and mucilage concentration were combined. While the lower rhizosphere bulk density led to a lower water retention, the presence of mucilage led to an increased viscosity. In combination, this significantly reduced the hydraulic conductivity of the soil and consequently resulted in an earlier water stress onset and a stronger reduction in the transpiration rate. However, considering that the limiting factor for root water uptake was not the available water volume but the reduced soil hydraulic conductivity, the process of root water uptake took longer, but the roots eventually took up the same amount of water. The gradients in rhizosphere bulk density and mucilage concentration therefore keep transpiration at a lower level for a longer time, which prevents fast dehydration and can be regarded as beneficial.

The initial soil hydraulic conditions had a strong effect on the scenarios with rhizosphere bulk density gradient. Our measured rhizosphere bulk density gradient led to a higher water retention when the soil was initially wet and to a lower water retention when the soil was drier, at field capacity. Depending on the initial pressure head, the water content in the rhizosphere was therefore either higher or lower than in the surrounding bulk soil at the start of the simulation. During a drying scenario, root water uptake could be maintained longer if the rhizosphere water content was initially higher.

The gradients in rhizosphere bulk density and mucilage concentration may play an important role in the distribution of root water uptake of an entire root system. To study this effect, however, a three-dimensional model of water flow in soil and roots (e.g., as in Mai et al. (2019)) must be coupled with rhizosphere bulk density and mucilage concentration gradients along the root system. Such a model could then also be used to examine the effects of rhizosphere processes on soil water dynamics at a larger scale (e.g., field scale).

According to our simulation results, gradients in rhizosphere bulk density and mucilage concentration lead to an initially lower, but longer lasting root water uptake. A general statement on whether gradients in rhizosphere bulk density or mucilage concentration lead to a higher or lower root water uptake cannot be made, however, as this depends on the characteristics of the gradients, the initial soil hydraulic conditions,

the soil texture, the soil bulk density, the soil hydraulic properties, and, in the case of mucilage, on the model parameterization. Aravena et al. (2014) found that rhizosphere compaction leads to an increase in water flow towards the roots in a very loose soil. In our experiments, however, the predominant effect of the rhizosphere bulk density gradients was not a compaction, but a loosening of the rhizosphere, and our simulations therefore showed reduced water flow to the roots. Using model simulation, Schwartz et al. (2016) observed that the presence of mucilage in a sandy soil led to a delay in the onset of water stress and thus to a longer maintenance of higher transpiration rates. Our model simulations on a loamy and a sandy soil, however, led to contrasting observations, which has several reasons. Schwartz et al. (2016) assumed constant mucilage concentrations in the rhizosphere and did not consider radial gradients. The presence of radial gradients, however, has an enormous effect on soil hydraulic conductivity and consequently influences root water uptake (Figure 5.10, 5.13 and 5.14). At low pressure heads, high mucilage concentrations lead to a larger soil hydraulic conductivity, while low mucilage concentrations lead to a lower soil hydraulic conductivity (Figure 5.10). When radial gradients are considered, the low mucilage concentration at the outer edge of the rhizosphere results in a low soil hydraulic conductivity, which limits water transport to the root. When no radial gradients are considered, the soil hydraulic conductivity of the entire rhizosphere is larger than that of the bulk soil and water transport to the root is promoted. This phenomenon of an earlier reduction in transpiration at low mucilage concentrations was also shown by Carminati, Kroener et al. (2016).

5.5 Conclusion

In this study, we used a mechanistic simulation model to evaluate the impact of gradients in rhizosphere bulk density and mucilage concentration on soil water dynamics. These gradients lead to differences in soil hydraulic properties and consequently to differences in root water uptake. Our simulations showed that the experimentally observed decrease in rhizosphere bulk density in the immediate vicinity of the root leads to an earlier onset of water stress and to lower transpiration rates. The decreasing radial mucilage concentrations increase the viscosity in the rhizosphere, which leads to a decrease in soil hydraulic conductivity. This in turn also leads to an earlier onset of water stress. When both gradients in rhizosphere bulk density and mucilage concentration are considered, root water uptake decreases even faster. However, considering that the limiting factor for root water uptake was not the available water volume but the reduced soil hydraulic conductivity, the process of root water uptake took longer, but the roots eventually took up the same amount of water. Gradients in rhizosphere bulk density and mucilage concentration thus appear as a measure to sustain transpiration at a lower level and to avoid fast dehydration.

Our simulations proved the importance of considering gradients in rhizosphere bulk density and mucilage concentration. Low values of rhizosphere bulk density and mucilage concentration lead to extremely low hydraulic conductivities, which are then the limiting factor for water flow to the roots. However, these lows in rhizosphere bulk density and mucilage concentration occur only in a limited portion of the rhizosphere and therefore cannot be accounted for with mean values of rhizosphere properties.

CHAPTER *6*

BIOPORE RECYCLING

Biopore recycling is the process during which roots ingress into existing biopores instead of creating new ones. Previous studies investigated biopore recycling under rather artificial conditions, e.g., with artificially created vertical macropores, by neglecting the smaller biopore diameter classes or by focusing on high bulk density soil material only. To address these shortcomings, we designed a soil column experiment and characterized the degree of biopore recycling for two soil textures (sand, loam) and two bulk density treatments. We developed a novel method based on the analysis of X-ray CT 3D images which enabled us to characterize the degree of biopore recycling for root-induced biopores down to 60 µm of diameter. The degree of biopore recycling was two orders of magnitude lower than previously reported in the literature (on average 0.0036 cm of roots were found in 1 cm of biopores). Roots were piercing through the biopores rather than growing into them. Visual analysis of the images showed that the propensity of roots to grow into biopores was higher when the angle at which roots and biopores touched was inferior to 45 degrees and when the root diameter was approximately equal or inferior to the biopore diameter. There were no statistical differences for the biopore recycling fraction between the two bulk density treatments in loam. In loam, roots degraded quickly (less than 78 days) and the biopores created were stable over time. In sand, some biopores were still filled with root residues after 216 days and many biopores had collapsed. We conclude that biopore recycling is less likely to occur in sand, as compared to in loam. We further used the model CPlantBox to simulate root system architectures with identical root length density as observed in the experiment but random arrangement with respect to biopores. By comparing the modeling results with the experimental results, we showed that roots had no preference for growing into biopores.

6.1 Introduction

Biopores are voids in soil resulting from the activity of living organisms. For a long time, the investigation of the nature and spatial distribution of biopores was hampered by the opaque and fragile nature of the soil. Although biopores were observed and described as early as in the late 19th century (Hensen, 1892), the methods which would allow a rigorous measure of the abundance and physical properties of biopores only came about around a century later. Such methods include the use of a soil peel method (Smettem & Collis-George, 1985), profile wall method (Han et al., 2015), horizontal minirhizotrons (Wahlström et al., 2021), rhizotrons (Bauke et al., 2017), *in situ* endoscopy (Athmann et al., 2014, 2013; Kautz & Köpke, 2010; Pagenkemper et al., 2015), isotope labelling (Banfield et al., 2017), photography (Nakamoto, 2000) and X-ray computed tomography (CT) (Cheik et al., 2021; Lucas et al., 2019; Pagenkemper et al., 2015; Z. Zhang et al., 2018; Zhou et al., 2021). The development of those methods paved new ways for the study of the ecological relevance of biopores.

In agroecosystems, biopores play a key role for matter fluxes as well as for plant growth (Kautz, 2015). Biopores provide growing roots with a path of reduced mechanical impedance and therefore ease the exploration of the available soil volume (Bengough & Mullins, 1990; Passioura, 2002), especially of deeper soil layers which are usually more compact. This is particularly beneficial in organic farming systems where the nutrient availability in the topsoil is usually scarce because of the absence or the limited input of mineral fertilization (Kautz et al., 2013; Kuhlmann et al., 1989). By allowing roots to reach deeper layers of the soil horizon, biopores also play an important role for the sequestration of carbon in the form of root necromass into the subsoil (Jones et al., 2009). During rainfall events, biopores influence the water budget by allowing a fast macropore flow of water (Dohnal et al., 2009), which in turn contributes to reducing water run-off and soil erosion (Ehlers, 1975; Kautz, 2015; Yunusa & Newton, 2003).

The term "biopore recycling" or "biopore reuse" refers to the process during which roots ingress into existing biopores instead of creating new ones. In agroecosystems, biopore recycling is usually considered to occur in the subsoil as it is the zone where biopores can pertain for decades (Hagedorn & Bundt, 2002). In the topsoil, the presence of biopores is rather short-lived because the soil structure is more dynamic and is usually subjected to tillage. Many physicochemical and biological processes are thought to influence the degree of biopore recycling. Using artificially created vertical pores, Nakamoto (1997) found that the degree of biopore reuse for *Zea mays* L. c.v ´Nagano´ ranged from 14% at 15 cm depth up to 33% at 40 cm depth. Similar values of biopore recycling were also reported by Athmann et al. (2013) and Han et al. (2017). In a subsequent experiment with a porous subsoil (i.e., 60% porosity), Nakamoto (2000) further observed that plant species differ in their propensity to reuse biopores. Wheat roots were more frequently found in biopores than maize roots. Nakamoto (2000) suggested that this was due to the fact that the thinner root tips of wheat were able to change their direction more easily and diverge into biopores.

In the literature, it is still debated controversially as to whether roots are able to "sense" the presence of biopores and grow towards them or whether root growth in biopores is simply the result of roots preferentially elongating in zones of the soil where the mechanical impedance is lower. On the one hand, roots may exhibit chemotropism to-

wards biopores since the concentration of carbon, nitrogen, phosphorus and the microbial activity might be increased in the wall of macropores (Barej et al., 2014; Pankhurst et al., 2002; Vinther et al., 1999). This chemotropism might be induced by the presence of nitrate and glutamate sensors present at the root tip (Filleur et al., 2005). Biopores also offer a rather continuous and higher supply of oxygen as compared to the bulk soil (Gliński & Lipiec, 2018), which is favorable for root growth (Crawford, 1992). On the other hand, biopores may be associated with certain pathogens (Pankhurst et al., 2002; Rasse & Smucker, 1998), which may cause the roots to be rather indifferent to the presence of biopores or avoid them instead of growing towards/into them.

Supporting the argument of preference of roots towards biopores, Stewart et al. (1999) showed that approximately 5 to 15 % more roots were found in and around pre-existing macropores than expected at random, in two black coarsely structured vertisols. With densely packed soil columns (1.78 g cm^{-3}) and artificially created vertical macropores (3.2 mm of diameter), Stirzaker et al. (1996) showed that the number of roots found in macropores was much higher as compared to the calculated probability that a root enters a biopore. Stirzaker et al. (1996) further hypothesized that roots might be able to detect biopores by growing towards the microcracks that are formed ahead of the root tip and that these microcracks may lead to other structurally weak zones such as a biopore. In a rhizotron study with a silty loam subsoil compacted at 1.40 g cm^{-3}, Bauke et al. (2017) observed that more roots grew into macropores than if root growth in macropores was only driven by chance.

Supporting the argument of indifference of roots towards biopores, Dexter (1986) found that there was no evidence that roots were sensing and growing preferentially towards artificially created biopores in a well-aerated system. Nakamoto (1997) came to similar conclusions after comparing the calculated probability of roots entering biopores and the experimentally measured proportion of roots in artificial macropores.

Based on the literature, it seems that the extent to which the roots reuse biopores might be the result of interacting factors such as soil penetration resistance (Stirzaker et al., 1996), soil depth (Nakamoto, 1997), plant species (Nakamoto, 2000; Rasse & Smucker, 1998), biopores geometry and relief (Hirth et al., 2005) and biopores origin (Athmann et al., 2014; Kautz et al., 2014). Our review of the literature revealed some shortcomings of existing studies on biopore recycling. Indeed, some studies investigated the behavior of roots in vertical artificially created macropores (i.e., macropores created by pushing a rod or a wire into the soil) (Bauke et al., 2017; Dresemann et al., 2018; Hirth et al., 2005; Nakamoto, 1997; Stirzaker et al., 1996). Considering the properties of biopores and, in light of the response of roots to their growing environment, root growth in artificially created macropores is likely somewhat unrealistic and not representative of root growth in pores created by living organisms. Other studies used experimental methods and measuring devices which limit the size range of the biopores investigated, e.g., the use of a 3.8 mm in diameter endoscope (Athmann et al., 2013). Such methods inherently introduce a bias towards the investigation of the largest diameter class of biopores (in the range of millimeters in diameter) and might have drawn conclusions disregarding the behavior of roots in the smallest diameter class of biopores (in the range of micrometers in diameter). Finally, other studies focused exclusively on subsoil material (Bauke et al., 2017; Han et al., 2017; Nakamoto, 2000; Wahlström et al., 2021; White & Kirkegaard, 2010), in which biopores stability

is likely increased due to an increased compaction of the subsoil and the presence of $CaCO_3$ as a cementing agent.

In order to address these shortcomings, we designed a soil column experiment and characterized the degree of biopore reuse occurring under controlled conditions in repacked soil columns. We developed a novel method based on the analysis of X-ray CT derived 3D images which enabled us to characterize the degree of biopore reuse for root-induced biopores down to diameters of 60 μm. The method is based on the repeated scanning of soil samples and co-registration of the acquired images after the creation of biopores and their potential reuse. With this method, we investigated the following hypotheses:

- The reuse of biopores is influenced by the soil texture. It is expected to observe different behavior of biopores as a result of different cohesive forces met by the soil particles of varying sizes. We expect that biopores in a coarse textured soil will be more prone to collapsing and that this will affect the degree of biopore recycling. This hypothesis was investigated by analyzing the degree of biopore recycling for a fine textured (i.e., loam) and a coarse textured soil (i.e., sand).

- Keeping all other factors constant, the reuse of biopores is higher in a substrate with higher penetration resistance. Since soil penetration resistance is proportionally correlated to the bulk density of a porous medium (Hernanz et al., 2000), it is expected that the degree of biopore recycling will increase concomitantly with bulk density. This hypothesis was investigated by introducing a factor "soil bulk density" in our analysis.

In addition to addressing these hypotheses, a new approach to study biopore recycling *in silico* was developed. The purely stochastic root growth model CPlantBox (Schnepf et al., 2018) was used to characterize the degree of biopore recycling which could be expected at random. The modeled results of biopore recycling were compared with the experimental results. The newly developed X-ray CT based method and the associated modeling approach enabled to shed light on the circumstances under which roots reuse biopores or not.

6.2 Material and Methods

6.2.1 Soil and plant material

The substrate loam (L) was obtained from the upper 50 cm of a haplic Phaeozem soil profile, dried to 0.1 g g^{-1} gravimetric water content and then sieved down to 1 mm. The substrate sand (S) constitutes a mix of 83% quartz sand (WF 33, Quarzwerke Weferlingen, Germany) and 17% of the sieved loam. Details on chemical and physical properties are provided elsewhere (Vetterlein et al., 2021). The *Zea mays* L. genotype B73 wild-type (WT) was selected for the growth experiments.

6.2.2 Experimental design and set-up

The experiment was designed in three phases. In the first phase, roots were allowed to grow freely in repacked soil columns. After the end of the growth experiment,

subsamples (i.e., ingrowth cores) were taken. The ingrowth cores consisted of plastic cylinders perforated at the sidewall, the top and bottom with a 2 mm diameter drill so that roots could enter from all sides. In the second phase, the ingrowth cores were incubated and stored in conditions which would allow the roots inside the ingrowth cores to degrade. In the third phase, the ingrowth cores containing biopores were buried inside newly packed soil columns. The soil columns of phase 3 were then seeded and roots were allowed to grow in and around the ingrowth cores (containing biopores). The technical aspects associated to each phase of the experiment are described below. Figure 6.1 gives an overview of the experimental design and set-up of the experiment.

Phase 1 - Root growth   Prior to packing the columns, the soil was fertilized in the same fashion as in Lippold, Phalempin et al. (2021) (see table 3.2). After fertilization, the columns (18 cm height, 10 cm inner diameter) were packed by gradually placing the soil in layers of 1.8 cm and gently consolidating each layer. The columns were packed to different bulk densities in order to investigate the effect of soil compaction on biopore recycling. For the low bulk density treatment, four columns per soil texture were packed to 1.26 and 1.5 g cm^{-3} for the loam and the sand, respectively. For the high bulk density treatment, four columns per soil texture were packed to 1.36 and 1.6 g cm^{-3} for the loam and the sand, respectively. The growth experiment was conducted in a climate chamber (Vötsch Industrietechnik GmbH) set to 22°C during the day and 18°C at night with a 12 hours light-period, 350 µM m^{-2} s^{-1} of photosynthetically active radiation and a constant relative humidity at 65%. Soil volumetric water content was tested in trial experiments in order to ensure appropriate soil moisture conditions for plant growth and to avoid water logging in the bottom part of the columns. The retained average volumetric water content values were 22% and 18% for loam and sand, respectively. At this volumetric water content, the penetration resistance for the low bulk density treatment is approximately equal to 0.17 MPa and 0.08 MPa for the loam and the sand, respectively (Figure AF13; Rosskopf et al. (2021)). Before seeding the columns, maize seeds were surface sterilized for 5 min in 10% hydrogen peroxide and then left to soak for 3 hours in a saturated calcium sulfate solution. The seeds were placed at a depth of 1 cm in the soil columns. The soil surface was covered with quartz gravel to reduce evaporation. Harvest was conducted on day 22 after planting. This growth duration corresponded to the BBCH14 plant growth stage (i.e., four leaves unfolded). At the end of the growing period, the plants were cut and left to dry in the oven at 65°C for 3 days in order to determine shoot dry weight. Directly after cutting the shoot, six ingrowth cores per column (3 cm in diameter and height) were extracted with a subsampling device (UGT GmbH) at 5, 10 and 15 cm depth from the soil surface. This sampling procedure yielded a total of 96 ingrowth cores to analyze, which were stored at 4°C in sealed plastic containers prior to X-ray CT scanning.

Phase 2 - Biopore creation   After X-ray CT scanning, the ingrowth cores were stored in an incubator set at a constant temperature of 25°C. The ingrowth cores were kept in plastic bags along with a damp cloth so that moist conditions were maintained. Occasionally, the bags were opened and visually inspected to make sure that no mold was growing inside. The duration of incubation was 195 days. At day 78 and 115, some cores were re-scanned with X-ray CT in order to assess the state of decomposition of the roots and the potential collapsing of biopores.

Phase 3 - Root growth in the presence of biopores   After phase 2, the ingrowth cores were buried in newly packed soil columns. The plant growth conditions and experimental set-up were the same as for phase 1. However, the seeding procedure was modified. For phase 3, the seeds were pre-germinated in small containers in order to make sure that every column would receive a fully germinated seed. Once the seeds were fully germinated, the small containers were buried at the surface of the soil columns. After the growing period, the ingrowth cores were extracted from the column and were stored at 4°C in sealed plastic containers prior to X-ray CT scanning.

6.2.3   X-ray CT scanning

X-ray CT scanning was performed with an industrial µCT scanner (X-TEK XTH 225, Nikon Metrology) having an Elmer-Perkin 1620 detector panel (1750 × 2000 pixels). The scanner was operated at 130 kV and 150 µA. A total of 2500 projections with an exposure time of 708 ms each were acquired during a full rotation of a sample. The obtained images were reconstructed into a 3D tomogram via a filtered back projection algorithm with the CT Pro 3D software (Nikon metrology). The resulting grayscale images had an 8-bit depth and a voxel size of 19 µm. The conversion to 8-bit allowed saving space without losing considerable information. During the 8-bit conversion, the grayscale range was normalized with a percentile stretching method. This method sets the darkest and brightest 0.2% voxels to 0 and 255, respectively, and performs a linear stretching in between.

6.2.4   Root segmentation

Root segmentation was performed with a modified version of the root segmentation algorithm "Rootine v.2" (Phalempin et al., 2021a). Rootine v.2 is a free macro available for the free image analysis software Fiji/ImageJ (Schindelin et al., 2012). In addition to gray value information, Rootine v.2 is based on the shape detection of cylindrical roots. Some of the key steps of Rootine v.2 and modifications of the original version for this study (when applicable) are briefly described below.

After X-ray CT scanning, all images were visually analyzed and samples devoid of roots were not considered for analysis. For the remaining samples, circular region of interests (ROI) were defined. After defining the ROI, the images were subjected to preprocessing steps. First, the images were filtered with a 3D non local means filter (Tristán-Vega et al., 2012) available in the ITK library (McCormick et al., 2014). After filtering, a step of edge enhancement was performed with the "Unsharp Mask" filter available in ImageJ. Then, a background removal step was applied via an "absolute difference transform" whose rationale and technical aspects are described in chapter 2 (Equation 2.2).

Rootine v.2 is tailored for the segmentation of roots in whole column scans where the image resolution is close to the smallest root diameter to segment. For whole column scans, the distribution of root diameters is continuous within a range that is plant species-dependent. For the samples used in this study, the distribution of root diameters is not continuous but rather discrete, considering that roots of different types and orders can be present within a sample and vary substantially amongst all samples in a dataset. To cope with this discreteness, Rootine v.2 was modified in order to perform

Figure 6.1: Overview of the experimental design and set-up.

a "root diameter targeted approach" instead of using a "root diameter incremented approach", as implemented in the original version of Rootine v.2. With the new approach, every image was visually analyzed and the diameter of the roots in the image was measured using the "Measure" tool available in ImageJ. The sigma values of the tubeness filter implemented in ImageJ were then calculated based on the measured root diam-

eters according to the formalizing steps described in chapter 2 (Equation 2.5). The results of the tubeness filter were segmented using the "3D Hysteresis Thresholding" (Ollion et al., 2013) available in ImageJ.

After root segmentation, the obtained images were subjected to post-processing steps. First, a 3D median filter available in ImageJ was applied in order to smoothen the root surface. In the original version of Rootine v.2, small isolated objects are discarded by using a connectivity criterion of the root branches from top to bottom, which is tailor-made for whole column scans. For the samples as used in this study, roots can enter the ROI from all sides. In order to cope with this, Rootine v.2 was modified and the connectivity criterion was replaced by a size exclusion criterion in order to get rid of every object whose size fell under a user-defined threshold. The size exclusion step was performed with the "Size Opening (2D/3D)" plugin available in the "MorphoLibJ" plugin suite (Legland et al., 2016). The size exclusion threshold was set to 4000 voxels.

With the obtained images, several properties of the roots within the ingrowth cores were computed. The root length was calculated after a step of skeletonization with the "Skeletonize (2D/3D)" plugin available in the BoneJ plugin (Doube et al., 2010). The root diameter was computed with the "Local Thickness" plugin available in ImageJ. This plugin relies on the "Maximum Inscribing Sphere" method and assigns to every root voxel a value corresponding to the diameter of the largest sphere which locally fits into the root.

6.2.5   Image registration

The images obtained after phase 1 and phase 3 had different orientation with respect to the source of X-rays in the scanner. In order to cope with this, image registration was necessary to align the images. Non-rigid image registration was carried out with the software Elastix (Klein et al., 2009; Shamonin et al., 2014). Finding landmarks (i.e., points defined on the same locations in the two 3D volumes to register) was facilitated by the use of the plugin "Big Warp" available in ImageJ. The number of landmark pairs per image was adapted to the quality of the registration and ranged from four to nine.

6.2.6   Modeling approach

The root architecture model CPlantBox (Schnepf et al., 2018) was used to simulate three weeks old root systems of *Zea mays* growing within the boundaries of the soil columns used in the experiment. As a baseline parameter set for the root architecture model, the maize root parameters reported by Landl et al. (2021) were used. The baseline parameter set was then optimized so that the average root length density (RLD) obtained with CPlantBox matched the experimentally measured RLD. The root parameters with the greatest impact on the RLD distribution were selected for the optimization. These parameters are the mean elongation rate of basal roots, the distribution of the number of basal roots and the distribution of the inter-branch distances of basal roots and first order laterals. For the optimization procedure, the Broyden–Fletcher–Goldfarb–Shanno algorithm (Fletcher, 2013), which is available in Python 3.8, was used. The evaluation of the match between the modeled RLD and experimental RLD was done for the three ingrowth cores that were taken at depths 5,

10 and 15 cm. The optimization of the root growth parameters was done for phase 1 and phase 3, respectively. After the optimization of the root growth parameters, 20 root system realizations were calculated for each phase. In analogy with the experimental dataset, these 40 root system realizations constitute two datasets of 20 modeled soil columns, i.e., one dataset for the phase 1 of the experiment and one dataset for the phase 3 of the experiment.

In the root architecture model CPlantBox, a root system is represented as connected line segments, in the form of vector data. In order to compare the results of CPlantBox with the experimental results, it was necessary to convert this representation into a raster representation. The Bresenham's line algorithm was used to determine the voxels of a 3D grid needed to form a good approximation of a straight line between two root nodes. This resulted in root systems represented by single-voxel lines. The resolution of the 3D raster grid was set to 60 µm, which was the minimum observed root diameter.

Similarly to the optimization of the RLD, the diameter distribution in the simulated ingrowth cores was optimized so that the difference between the measured and simulated mean diameters was minimal. Note that the maximum allowed diameter was constrained to 900 µm in order to reduce the dilation step to a reasonable amount of time. After the optimization of the root diameter, each root voxel was dilated with a 3D ball-shaped kernel using the multiprocessing package available in Python. This resulted in a 3D rasterized representation of the root systems, in which each root segment was represented by a cylinder of a given diameter.

In the modeling approach, the characterization of biopore recycling within the modeled soil cores was evaluated by considering all possible combinations between the 20 modeled root system realizations of each phase. However, the possible combinations between the three different soil depths were not considered. Practically, this means that a simulated ingrowth core located at 5 cm depth in the simulated root system number 1 of phase 1 was compared with the simulated ingrowth cores located at 5 cm depth of the simulated root systems 1, 2, 3, and so forth up to the 20th simulated root system of phase 3. This yielded a total number of 400 combinations between the cores of phase 1 and the cores of phase 3 for each depth, i.e., 1200 combinations for the whole modeling dataset.

6.2.7   Data analysis and model comparison

Two metrics were used as a proxy for biopore recycling, namely the biopore recycling fraction (BRF) and the normalized number of contact points (NCP). The BRF was characterized by computing the root length found in a given biopore length. The BRF is expressed as a ratio of number of voxels and is therefore dimensionless. The NCP was characterized by counting the occurrence of a root touching a biopore, normalized by the volume of the sample. It is therefore expressed in $[1 \ cm^{-3}]$.

In order to calculate the NCP, the root systems of both phases were combined into one image, making sure that one gray value was assigned to the roots grown during phase 3, one gray value was assigned to biopores and another gray value was assigned to the intersection of roots grown during phase 3 and the biopores. With a single thresholding method, the combined images were segmented in order to isolate the voxels where roots and biopores touched. Then, the number of contact points

was calculated with the "Connected Component Labelling" operation available in the MorphoLibJ plugin library (Legland et al., 2016). Note that, for the experiment dataset, all contact points having a size inferior to ten voxels were considered as artifacts and were therefore excluded from the analysis. Artifacts were occasionally created when a root and a biopore were slightly over-segmented and/or not perfectly registered. In that case, it was sometimes observed that some small artificial contact points were created. This was mostly observed when a root and biopore touching one another were almost parallel. For the simulated dataset, all contact points were considered since there was no artifacts introduced by root over-segmentation or imperfect registration.

In this work, we hypothesize that the difference between the NCP obtained experimentally (NCP_{exp}) and the one obtained with CPlantBox (NCP_{mod}) is a valid metric to characterize the tendency of roots to grow towards, avoid or be indifferent to biopores. To generate the NCP_{mod} dataset, we used the formulation of CPlantBox which does not account for any preferential growth of roots towards, into or away from biopores. With this formulation, the model can be used as a benchmark to determine the number of times that roots and biopores touch at random. Considering this, we assume the following:

$$NCP_{exp} - NCP_{mod} < 0 \; ; \; \text{Roots avoid biopores}$$

$$NCP_{exp} - NCP_{mod} \simeq 0 \; ; \; \text{Roots are indifferent to biopores}$$

$$NCP_{exp} - NCP_{mod} > 0 \; ; \; \text{Roots are attracted to biopores}$$

Of course, the likelihood that roots touch biopores at random is positively correlated to the amount of roots and biopores present. To take this into account, we modeled NCP as a function of biopore length density (BLD) (i.e., the RLD observed during phase 1) and the RLD in phase 3 using tensor product smooths to fit a 2D response surface in the framework of generalized additive models (Wood, 2017). We modeled the raw counts of contact points (prior to normalization by the sample volume) using a negative binomial distribution and included an offset in the model to account for the volume of the soil samples. Treatment (model vs experiment) was added to the model to estimate the difference between the number of contact points expected by the CPlantBox model and the experimental data. The generalized additive model enabled to predict the NCP_{exp} and the NCP_{mod} for all possible combinations of BLD and RLD interpolated between the observed values and constrained within the range of values observed.

6.2.8 Visual analysis of contact points

For some instances where roots and biopores touched, a visual analysis of the contact points was carried out in order to understand the circumstances under which roots were reusing biopores or not. A focus was made on the angle of contact between the roots and the biopores and the diameter of the root and the biopore. In order to measure the contact angle, the two 2D planes at the intersection of the roots and the biopores were found with the help of the plugin "Big Warp" available in ImageJ. Once the two 2D planes were found, the angle of contact was measured with the "Angle measurement tool" available in ImageJ. The evaluation of root and biopore diameter was only qualitative and was made visually.

6.2.9 Statistical analysis

Statistical analyses were carried out to test whether the means of the different treatments significantly differed from one another (i.e., one-way ANOVA). Multiple pairwise-comparisons with Tukey HSD tests enabled to determine whether the mean difference between specific pairs of treatments were statistically significant. Unpaired Wilcoxon tests were performed when analyzing two independent groups having non-normally distributed data. The data analyses were carried out in R Studio 3.5 using the multcomp (Hothorn et al., 2008), car (Fox & Weisberg, 2019), Tydiverse (Wickham et al., 2019), plyr (Wickham, 2011), mgcv (Wood, 2011) and ggplot2 (Wickham, 2009) libraries.

6.3 Results

6.3.1 Plant growth and root growth

The plant and root growth observed for the growth experiments of phase 1 and phase 3 differed substantially. This was reflected in the measurement of shoot dry weight (Figure 6.2a), root length density (Figure 6.2b) and the number of ingrowth cores containing roots (Figure 6.2c). The shoot dry weight was approximately two times lower for phase 3 as compared to phase 1. This difference was even bigger for the root growth as root length density was an order of magnitude lower for phase 3 as compared to phase 1. Due to the different methods used for germination of the seeds, a time-lag of approximately 7 days of growth was observed in phase 3 as compared to phase 1. This is supported by the analysis of the evapotranspiration and the soil volumetric water content measured during the growth experiments (Figure AF14 and AF15). Note that since this study focuses on roots exclusively, this difference of root growth has no consequences on the validity of the biopore recycling results but only affects the range of RLD and BLD investigated. The effect of substrate and bulk density was weaker for the shoot dry weight as compared to the root length density. Despite the fact that differences were not statistically significant, the shoot dry weight and the root length density were systematically lower for the high bulk density treatment as compared to the low bulk density treatment and this was true for both loam and sand.

Since the analysis of BRF and NCP can only be performed when roots of the two growth experiments are present within a given ingrowth core, the number of samples containing roots for the intersection of phase 1 and phase 3 was calculated (Figure 6.2c). For loam, the number of samples containing roots was high and equal to 21 and 20 out of 24 for the low and high bulk density treatment, respectively. For sand, the number of samples containing roots was low and amounted to seven and two out of 24 for the low and high bulk density treatment, respectively. Differences in root growth in loam in comparison to sand have already been observed in a similar growth experiment (see figure 3.2), however, the mechanisms behind this difference are still unknown.

6.3.2 Root degradation

The occasional X-ray CT scans performed at day 78 and 114 after the growth experiment of phase 1 provided insights into the time it took for roots to degrade and
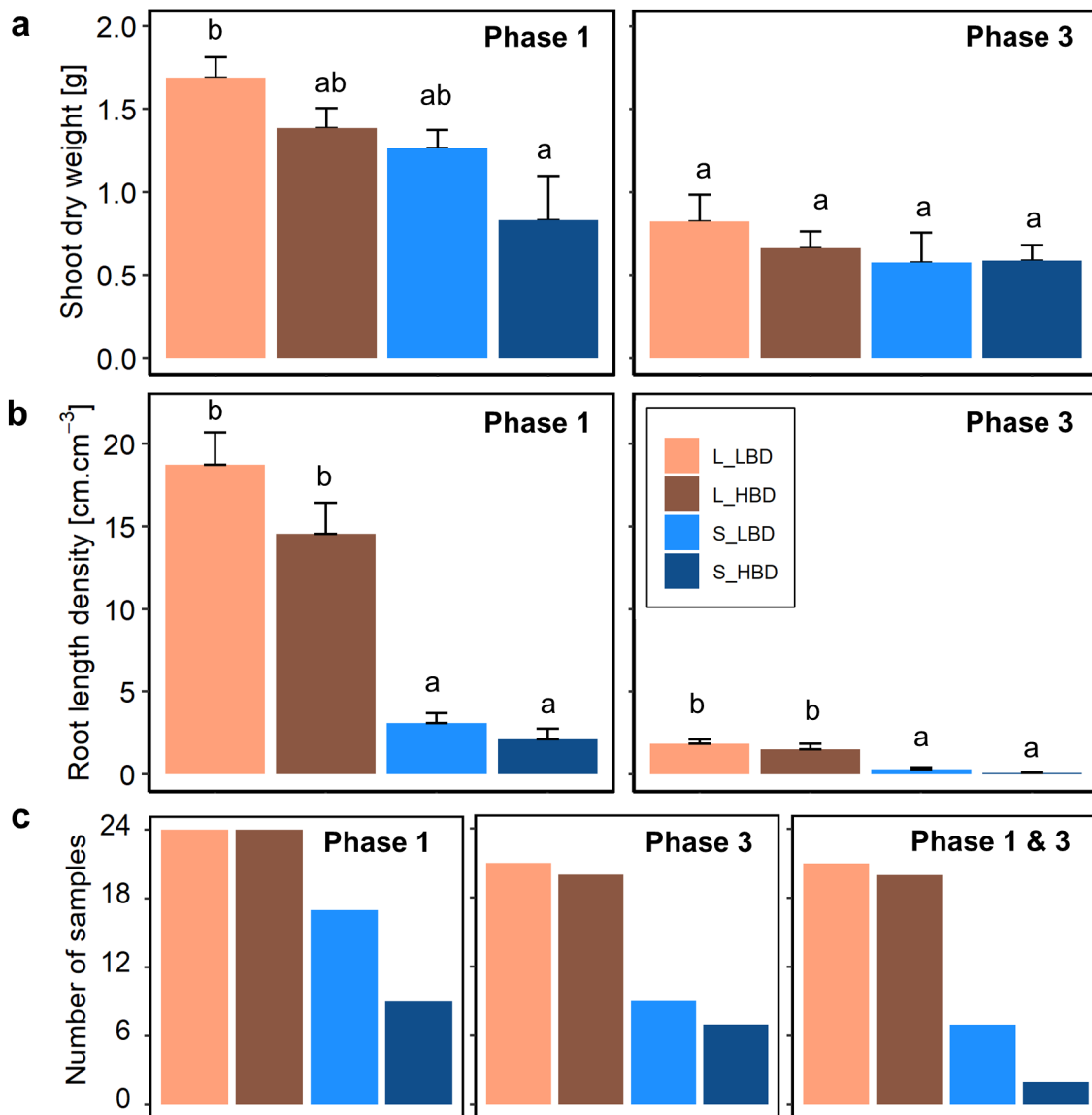
Figure 6.2: Plant growth and root growth measured for the two growth experiments. (a) The shoot dry weight. (b) The root length density. (c) The number of samples containing roots in phase 1, phase 3 and the intersection of phase 1 and 3. The error bars denote the standard error. The letters on top of the error bars denote pairwise-comparison between the mean of the treatments as assessed by a Tukey HSD test with α = 0.05. The legend in subfigure b is also valid for subfigures a and c.

empty biopores to be formed. In loam, it took maximum 78 days for roots to decompose (Figure 6.3a) and leave behind completely empty biopores. For sand, the root degradation was much slower as some roots were only partially shrunken after 115 days of incubation. After the end of the growth experiment of phase 3, i.e., after 216 days after the end of phase 1, some biopores in sand were still partially filled with old root tissues (Figure 6.3b).

The occasional X-ray CT scans also enabled to acquire qualitative information regarding the stability of the biopores in loam and sand. In loam, the biopores were

stable over time and the roots present after the first growth experiment could be very easily and precisely delineated when analyzing the biopores that they left behind after their decomposition (Figure 6.3a). For sand, the arrangement of sand grains was rather fragile and movements of the sand grains in all possible directions (i.e., subsidence and lateral displacement) were frequently observed (Figure 6.3b). When full decomposition of the roots was observed in sand, some biopores subsequently collapsed and/or were partially "refilled" with sand grains in their vicinity (Figure 6.3c).
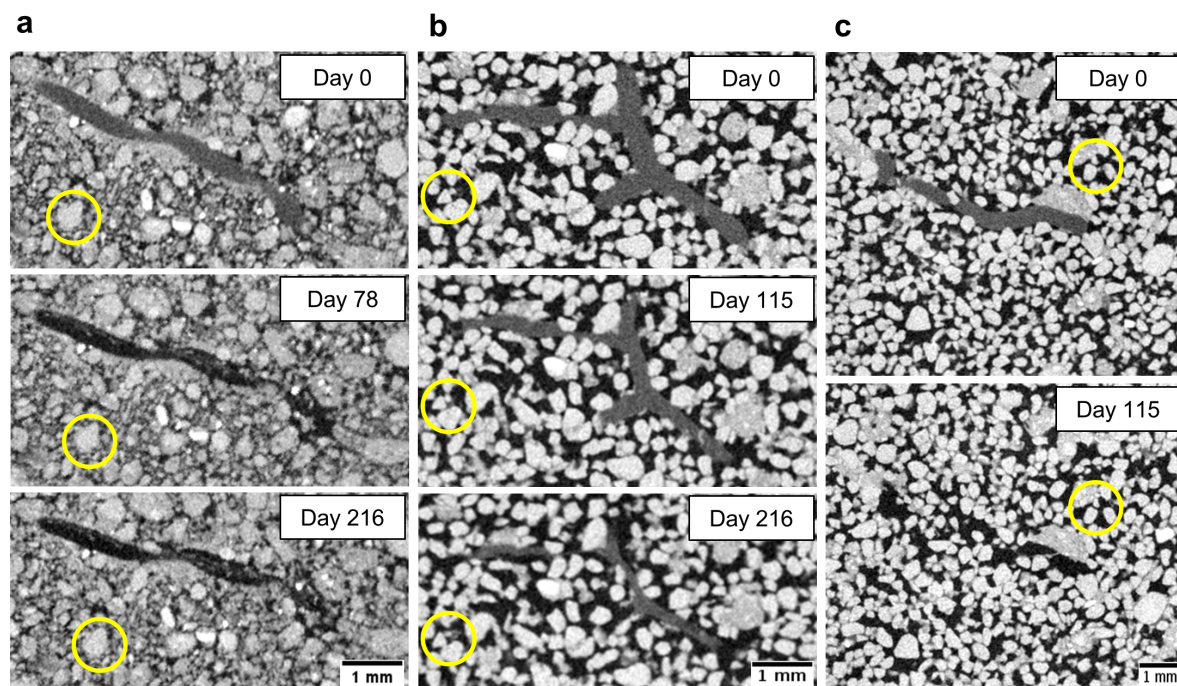
Figure 6.3: Two-dimensional X-ray CT images acquired at different times after the end of the growth experiment of phase 1. For better orientation, the yellow circles indicate grains which are common in the images. In loam, roots degraded quicker than in sand and left behind biopores which were structurally stable over time (subfigure a). In sand, old root tissues were sometimes observed after 216 days of incubation time (subfigure b). When complete root degradation was observed in sand, the biopores were often refilled with sand grains in their vicinity (subfigure c).

6.3.3   Biopore recycling

Before presenting the results of biopore recycling, note that the rest of our analysis will be focusing on the loam treatments. The analysis of the sand treatments was not carried out because the number of samples containing roots in both phase 1 and 3 was not high enough to construct a reliable statistical analysis (Figure 6.2c). Also, the old root tissues created issues when trying to properly segment the roots of phase 3 because they still exhibited a similar gray value as the alive/intact roots of phase 3. On top of that, the fragile structure of the sand created problems when trying to register the images of both phases onto each other. Indeed, finding landmarks on these images proved to be unreliable due to the movement of sand grains (Figure 6.3b).

The calculated BRF values were in the range of 0 to 0.024 and there was no statistical difference between the high and the low bulk density treatments in loam (p-

value = 0.46) (Figure 6.4a). The calculated NCP values were in the range of 0 to 2.8 and there were also no significant differences between the two bulk density treatments (p-value = 0.27) (Figure 6.4b). Since no differences between the high and the low bulk density treatments were found, the two datasets were pooled together for the subsequent analyses. Plotting the relationship between the BRF and the NPC showed a positive correlation between the two variables (R^2 = 0.23), as also supported by the p-value of the linear regression (p-value = $7.21e^{-05}$) (Figure 6.4c).
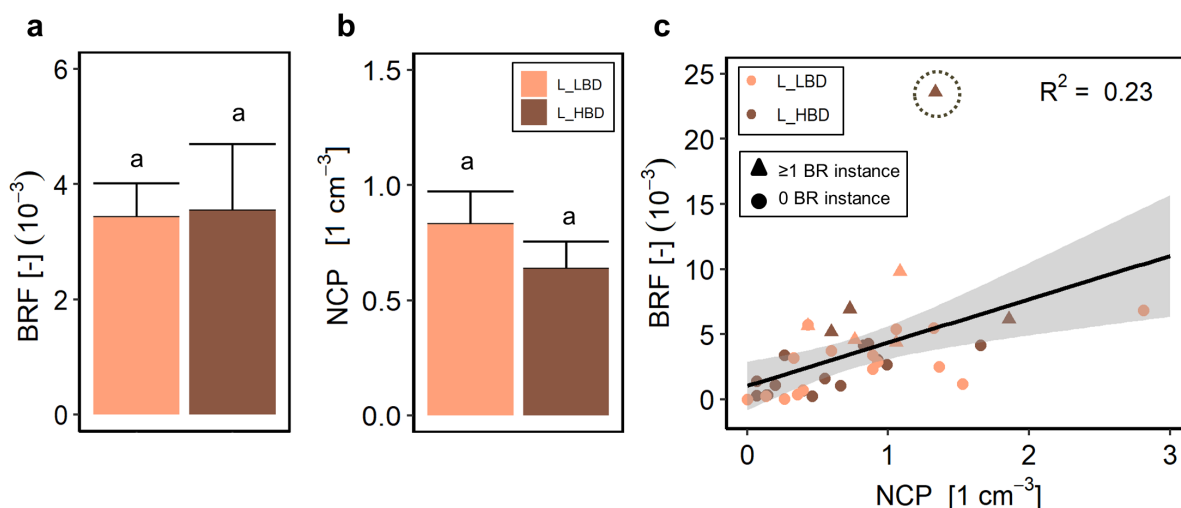
Figure 6.4: The biopore recycling fraction (BRF, subfigure a) and the normalized number of contact points (NCP, subfigure b) for the high and low bulk density treatments in loam. Error bars respresent the standard error of the measurements. The letters indicate the statistical comparison of the two independent treatments according to a Wilcoxon test considering α = 0.05. (c) The relationship between the NCP and BRF calculated for the pooled low and high bulk density treatments in loam. The shaded gray bands represent the 95% confidence interval for predictions from the linear model. The maximum value of BRF (see sample circled with a dashed line) presented the most astonishing biopore recycling of our dataset, in which a root grew into a biopore for a length of 13.1 mm before leaving the field of view. Note that removing this sample from the regression shown in the subfigure c increases the R^2 to 0.35. The triangles denote the samples for which at least one instance of biopore recycling was observed within the sample, whereas the dots denote the samples for which no instance of biopore recycling was observed.

The total number of contact points (not normalized by the volume of the samples) observed for the whole dataset was 438. Out of those contact points, the number of occurrence of a root being deflected and growing into a biopore upon hitting it was only ten. That is, only approximately 2% of the roots grew into a biopore when they had the opportunity to do so. Most contact points were in fact roots piercing through the biopores. Visual examples of a root piercing through a biopore or growing into it are shown in figure 6.5a and 6.5b, respectively.

For those instances for which biopore recycling was observed, we found that the contact angle between the roots and the biopores was inferior to 45 degrees for nine instances out of ten. The average contact angle was 31.8 degrees ($\pm$ 5.7 degrees standard error; n = 10). Interestingly, the diameter of the roots reusing the biopores was approximately equal to the diameter of the biopores for eight instances out of those ten
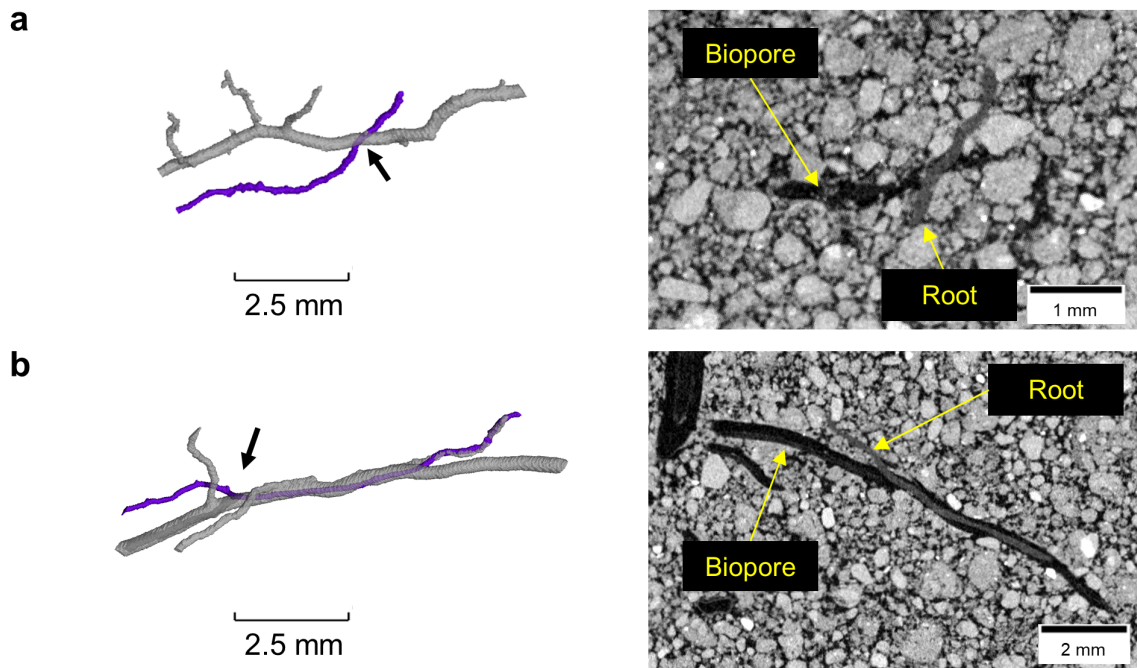
Figure 6.5: Illustration of a root piercing through or a reusing a biopore with the corresponding 2D cross-sectional gray scale. (a) Three-dimensional representation of a root (purple) piercing through a biopore (semi-transparent gray) and its corresponding 2D cross-sectional gray scale image at the point of piercing. (b) Three-dimensional representation of a root (purple) growing into a biopore (semi-transparent gray) and its corresponding 2D cross-sectional gray scale image. The black arrow indicates the point of entry of the root into the biopore. The case of a root piercing through a biopore (subfigure a) was the most commonly observed in our dataset.

contact points. For the two remaining instances of biopores recycling, the diameter of the roots reusing the biopores was smaller than the diameter of the biopores. After entering the biopores, the roots continued their growth for an average distance of 5.8 mm ($\pm$ 1 mm standard error; n = 10) before diverting into the soil again or leaving the ingrowth cores. The greatest length of a root growing inside a biopore was 13.1 mm. This instance had the most astonishing biopore recycling of our dataset. It also corresponded to the highest observed BRF value(i.e., 0.024, see the corresponding sample circled with a dashed line on figure 6.4).

Note that the angle between the roots and the biopores was not an exclusive criterion, i.e., many contact points had a contact angle inferior to 45 degrees but root deflection or biopore reuse was not observed. However, the contact angle between roots and biopores was significantly higher when roots were piercing through the biopores (p-value = $3.4e^{-4}$). For those contact points where roots were just piercing through the biopores, 14 out of 15 contact points had a contact angle superior to 45 degrees. The average contact angle was 63.9 degrees ($\pm$ 6.4 degrees standard error; n = 15). For those 15 piercing points which were visually analyzed, the diameter of the roots and biopores were approximately equal for eight instances. For the seven remaining piercing points, the root diameter was bigger than the diameter of the biopores.

6.3.4   Model comparison

For both the phase 1 and 3, the RLD simulated with CPlantBox matched the experimentally measured RLD profile pretty well, as assessed by the small relative root mean square error (rRMSE = 21% and rRMSE = 31% for phase 1 and phase 3 respectively, see figure AF16). The fit of CPlantBox for the mean root diameter was also good (rRMSE = 14% and rRMSE = 26% for phase 1 and phase 3 respectively, see figure AF16). The fit of the generalized additive model to the experimental and modeled data provided good results, as assessed by a relatively high adjusted R^2 (R^2 = 0.917) and deviance explained (91%).

For both the experimental and modeled data, the predicted NCP for all combinations of BLD and RLD showed an increase from the left bottom corner (low BLD and RLD) to the upper right corner (high BLD and RLD) of the 2D smooth surfaces (Figure 6.6a and 6.6b). This increase was stronger for the modeled dataset, which led to higher predicted NCP values for the model as compared to the experiment. For high BLD and RLD, the NCP values were approximately equal to 6 for the model as opposed to 3 for the experiment. The calculation of the 2D smooth surface of NCP_{exp} – NCP_{mod} illustrate also this difference well (Figure 6.6c). The difference between the modeled and experimental data also shows a strong diagonal gradient from bottom to top. At no point, the calculation of NCP_{exp} – NCP_{mod} yielded positive values. According to the hypothesis related to our methodology, this suggests that roots never showed a preference for growing towards biopores. Keeping the methodological hypothesis in mind, roots rather exhibited indifference towards biopores (i.e., at low BLD and RLD) or avoidance of biopores (i.e., at high BLD and RLD). Yet, this avoidance is rather speculative, as no experimental observations were available for that BLD-RLD range.

6.4   Discussions

6.4.1   Biopore recycling

The degree of biopore recycling observed in our experiment was very low, with a mean value of approximately 0.0036 cm of root found in 1 cm of biopore. Despite the different methods of investigation and the use of different units to characterize biopore reuse, higher values of two orders of magnitude of biopore recycling were previously reported in the literature (Athmann et al., 2013; Han et al., 2017; Nakamoto, 1997, 2000). This difference can be explained by several reasons, namely the mechanical impedance, the oxygen and nutrient status, the origin of the biopores and the inclusion of biopores having a small diameter in our analysis.

The first reason which would explain the small degree of biopore recycling in our experiment is mechanical impedance. Indeed, at the water content investigated in the present experiment, penetration resistance was approximately 0.17 MPa for the low bulk density treatment of loam (Rosskopf et al., 2021). This value is well below the critical value for root elongation of 2 MPa suggested by Bengough et al. (2011). Considering this, there might have been no need for the roots to grow into the available biopores as they could easily explore the available soil volume without restriction to root elongation. Including a treatment with a higher bulk density, and hence higher penetration resistance, did not result in a significantly higher degree of biopore recy-
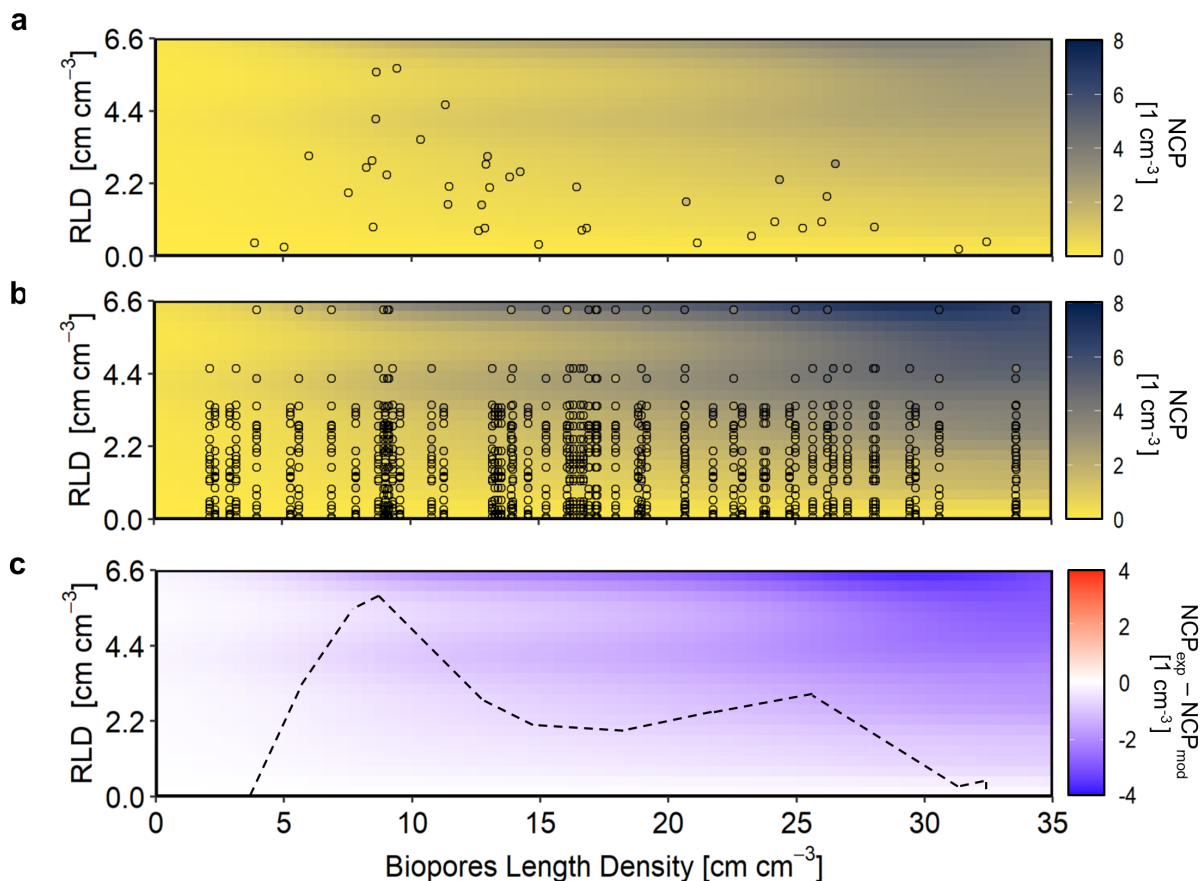
Figure 6.6: Comparison between the modeled and the experimental NCP values. (a) The 2D smooth surface for the experimental dataset, with the experimental data points shown on top of the surface. (b) The 2D smooth surface for the modeling dataset, with the modeling data points shown on top of the surface. For both the experimental and modeling dataset, a positive gradient is observed in the upward diagonal direction, i.e., the higher the BLD and RLD, the more roots touch biopores. (c) The difference of the 2D smooth surface for the modeling dataset and the experiment dataset. According to our methological hypothesis, positive values of this difference indicate a tendency of roots to avoid biopores. The dashed line depicts the BLD and RLD range of values observed in the experimental dataset. Interpreting the values outside of this range is extrapolation.

cling. This is contrary to our original assumption and conflicting with the results of Hirth et al. (2005) who showed that increasing bulk density increased the percentage of root length found in biopores which were inclined with an angle of 40 degrees from the horizontal plane. More extreme compaction of the substrate could have led to more pronounced effects of soil bulk density and to some higher degree of biopore recycling, but might also have reduced drastically root growth and thereby the number of samples which could be analyzed.

A second reason potentially explaining the low degree of biopore recycling is the nutrient and oxygen availability. In this column experiment, the substrate were previously fertilized in order to ensure an adequate plant and root growth. Also, the volumetric water content was kept at an average value of 22% (Figure AF15). This value corresponds to an air-filled fraction of the total pore space of approximately 56%. In the literature, some authors suggest that the reuse of biopores is triggered by the

nutrient and oxygen shortage in the subsoil and the enrichment of the biopores in nutrients and oxygen beneficial to plant and root growth (Athmann et al., 2014; Edwards & Lofty, 1980; Stewart et al., 1999). The reason as to why root growth in biopores was so low in our experiment might be related to the fact that nutrients and oxygen were available in sufficient quantity due to the fertilization and the well-aerated conditions in the soil columns of our experiment.

The nature of the biopores can also provide an explanation for the low degree of biopore recycling in our experiment. In the literature, many studies reported root growth into biopores in field conditions (Athmann et al., 2013; Han et al., 2017, 2015), where the genesis, the history and the usage of the biopores is rarely documented because of the difficulties associated with the determination of these characteristics. Depending on these characteristics, individual biopores can differ widely in their physical conditions (Pagenkemper et al., 2015) and nutrient status (Kautz et al., 2014). Some studies have also investigated biopore recycling under somewhat unrealistic conditions, i.e., by artificially creating vertical holes by pushing a rod or a wire into the soil (Dresemann et al., 2018; Hirth et al., 2005; Nakamoto, 1997; Stirzaker et al., 1996). Under these conditions, the trapping of roots in the biopores is more likely to occur considering the inherent gravitopism that roots exhibit. Articifial pores are also likely to have a greater compaction and a smoother surface at the pore wall, both of which are known to excacerbate root trapping in biopores (Hirth et al., 2005; Stirzaker et al., 1996). Obviously, the comparison of our results with those studies is delicate. Indeed, our study focused exclusively on biopores which extended more laterally than vertically, considering that primary roots were only rarely captured during the extraction of the ingrowth cores. Moreover, the biopores in our experiment were young, induced exclusively by *Zea mays* L. plants and potentially reused exclusively by the roots of *Zea mays* L. plants. This may also have contributed to the low degree of biopore recycling. Indeed, Rasse und Smucker (1998) highlighted the importance of crop succession by showing that biopore recycling of maize after maize was lower than if maize was succeeding alfalfa.

Finally, another potential explanation for the differences between the biopore recycling observed in our study and the values previously reported in the literature is the inclusion of biopores of diameter $\geq$ 60 µm in our analysis. Indeed, previous studies on biopore recycling only focused on a fairly large biopore diameter class (e.g., $\geq$ 400 µm in Nakamoto (2000), $\geq$ 3.8 mm in Athmann et al. (2013), $\approx$ 3.2 mm for Stirzaker et al. (1996) or only biopores visible to the naked eye in Nakamoto (1997)). Excluding the small biopore diameter class from their analysis inherently omits a huge proportion of the existing biopores in soil. Strictly mathematically speaking, calculating "the proportion of roots in biopores" (Nakamoto, 1997, 2000) or "the percentage of biopores with roots" (Athmann et al., 2013) while omitting a large share of biopores results in greatly decreasing the denominator of the fraction, thereby greatly increasing the estimation of biopore recycling. In our study with biopores induced by *Zea mays* L. and a high detection of small roots/biopores (i.e., an image resolution of 19 µm), approximately 97% of the roots/biopores fell into the diameter class $\leq$ 400 µm (Table AT3). By capturing these small biopores, the resulting biopore recycling fraction calculated in our study is inevitably much lower than previously reported in the literature.

Comparing the experimental data and the modeled data allowed drawing conclusions regarding the behavior of roots towards biopores. By doing so, we found that

roots tended to be indifferent to biopores. The reasons as to why roots were indifferent to biopores are currently still unknown. In a very speculative manner, we suggest that this behavior could be explained by the fact that the wall of the biopores in our experiment might have already been depleted in nutrients, as observed by Hendriks et al. (1981), and/or colonized by some pathogens as suggested by Rasse und Smucker (1998). Both of these explanations would support the argument that root growth was favored in regions of the soil column where the nutrient content was higher and the pathogenic pressure lower. Note that our study supports the findings of Dexter (1986) who also found no evidence for the roots sensing and growing preferentially towards the holes in the well-aerated system used in his experiments.

6.4.2   Influence of soil texture

The effect of soil texture on biopore recycling could not be directly investigated as originally intended and stated in the first hypothesis of our work. Due to the low number of samples containing roots in phase 1 and phase 3 and to the technical difficulties related to the processing of those images (segmentation and registration), the analysis of BRF and NPC was not carried out for the sand treatments. However, some qualitative information regarding the nature and stability of biopores in a loam and a sand soil could be gained. In loam, roots completely degraded in a short period of time (less than 78 days of incubation at 25°C under moist conditions) and the biopores that the roots left behind were structurally stable over time. In sand, old root tissues were still found in biopores 216 days after their creation under the same incubation conditions. On some occasions, the biopores in sand were also found to be partially or completely refilled due to the subsidence and lateral displacement of sand grains in the vicinity of the biopores. Considering this, biopore recycling in sandy soils is much less likely to occur as compared to in loamy soils. Note that the lower stability of biopores in sandy in comparison to loamy soils has already been suggested by Schneider und Don (2019).

The influence of soil texture on the decomposition of root tissues has already been observed by other studies (Gijsman et al., 1997; Scott et al., 1996). This difference has been attributed to differences in water and gas regime (Gijsman et al., 1997; Haling, Tighe et al., 2013), both of which are known to alter the microbial activity in soil (Angst et al., 2021; Borowik & Wyszkowska, 2016; Schjønning et al., 2003). Note that, in our study, the fact that root residues were still present in the biopores in sand might also be due to the fact that roots in sand grew bigger in diameter (Figure AF17). Possibly, the decomposition rate of the roots was the same for the loam and the sand, but the decomposition of the roots in sand was not yet complete since more matter had to be decomposed in the same amount of time. Note that the increase in diameter of roots was already reported by Lippold, Phalempin et al. (2021) for the same substrates (see figure AF4 and 3.6), but no explanation for this increase has been found yet.

Soil texture also has an influence on the nature of the biopores themselves, more precisely on the degree of compaction of their walls. Using the same substrate and bulk density treatments as in the present study, Phalempin et al. (2021b) demonstrated that soil texture was a predominant factor which governs the bulk density gradients around roots, and hence, on the level of compaction of the walls of the biopores. For the loam and sand investigated in this experiment, differences in the compaction of the soil in the

vicinity of roots were also observed (Figure 6.3). Indeed, the rhizosphere soil was more compacted in loam as compared to in sand (see also figure 4.3 in chapter 4). These differences may lead to different tendencies of the roots to be "trapped" in biopores, as already suggested by Stirzaker et al. (1996), Stewart et al. (1999) and Nakamoto (2000). In our experiment, we did not observe roots being trapped as most roots were piercing through the biopores and those which diverged into biopores escaped them only after a short distance (on average 5.8 mm).

6.4.3   Limitations and future work

In this paper, we presented a novel methodology for the study of biopore recycling with the help of X-ray CT and *in silico*. Our modeling approach integrated 3D root architecture information and therefore combined much more information in comparison to previous simulation studies, which focused on soil 2D thin sections (Stewart et al., 1999) or on the simple application of probabilistic laws (Nakamoto, 1997; Stirzaker et al., 1996). With this methodology, we further introduced a new metric (i.e., the normalized number of contact points) to characterize the behavior of roots towards biopores. The new approach also allowed determining the effect of the biopore length density and the root length density on the normalized number of contact points. To the best our knowledge, such a modeling effort has not been undertaken before.

One limitation of our approach is related to the range of biopore length density and root length density covered by our analysis. By constraining root growth in a pot, the biopore length density which was created during phase 1 was much higher than the biopore length density which can expected in field conditions. Lucas et al. (2019) showed that root length density was as low as 1.83 cm cm^{-3} after one year of reclamation of a mining area and that biopore length density reached a plateau of 18.79 cm cm^{-3} at $0 - 20$ cm depth after six years of reclamation. In our study, the biopore length density observed was approximately two times higher than the expected biopore length density after reaching equilibrium, which might not be realistic compared to natural conditions. For the root length density observed during phase 3, however, the values observed in our study are well in line with the values which can be expected in the field after one season of growth (Lucas et al., 2019; Phalempin et al., 2021b) (see also figure AF10a).

In our study, we investigated biopore recycling for a crop succession of maize after maize. Future work should orient towards implementing the presented methodology to multi-species succession to find out whether others species behave in a similar manner as compared to the maize-maize succession investigated in this experiment. Finally, the natural continuation of this work is to include the presence of biopores in the initial conditions of the root growth modeling of phase 3. This would enable to explicitly model root growth in biopores as in Landl et al. (2019).

6.5   Conclusion

In this study, we developed a novel methodology to characterize the degree of biopore recycling occurring in repacked soil columns under controlled conditions.

The novel methodology is based on the repeated scanning of soil samples and co-registration of the acquired images after the creation of biopores and their potential reuse. With this methodology, we showed that the degree of biopore recycling in repacked loam columns was low, i.e., on average 0.0036 cm of roots was found in 1 cm of biopore, which was two orders of magnitude lower than the values previously reported in the literature. We attributed this difference to the low mechanical impedance, the good nutrient and aeration status in the repacked soil columns and to the inclusion of biopores of small diameter in our analysis. In our experiment, roots were most prominently piercing through the biopores rather than growing into them. Root growth inside biopores was only anecdotally observed. The effect of bulk density on the biopore recycling fraction and on the normalized number of contact points between roots and biopores was not statistically significant.

The visual analysis of intermittent X-ray CT scans provided insights into the degradation of roots and the behavior of biopores in two soils with contrasted textures. In loam, roots had completely degraded in a short period of time (less than 78 days) and the biopores that the roots left behind were structurally stable over time. In sand, old root tissues were still found in biopores 216 days after their creation. When full root decomposition was observed in sand, many biopores had collapsed due to the weak cohesive forces between the coarse sand grains. Both effects together render biopore recycling in sand unlikely to occur. Visual analysis of the images showed that the propensity of roots to grow into biopores was higher when the angle at which roots and biopores touched was inferior to 45 degrees and when the root diameter was approximately equal to or inferior to the biopore diameter.

In addition to the analysis of the experimental data, we introduced a new methodology which enabled to characterize the behavior of roots towards biopores. This methodology relies on the use of the stochastic root growth model CPlantBox and the comparison with the experimental data. With this new approach, we showed that maize roots were indifferent to maize-induced biopores, in well aerated, fertilized and repacked soil columns.

CHAPTER *7*

SYNTHESIS AND CONCLUSION

7.1 Summary and discussions

The overarching goal of this thesis was to improve the understanding of the interplay between root growth patterns and soil properties. Specifically, several research questions were enunciated in section 1.2 and the answers to those questions were disseminated in the form of chapters throughout this manuscript. To address the research questions, several methods of investigating root growth patterns were employed, most of them relied on the use of X-ray CT and implied different levels of complexity in terms of image processing. This section is an attempt to briefly summarize the methods used and their limitations. It also aims at wrapping up the main findings of this work, to integrate them and to address the overarching objective in a broader context.

In its simplest level of complexity, simple 2D projections of segmented root systems were visually analyzed to assess root growth patterns (Figure AF6). This method can be very effective to detect quickly features and properties of the root system just by eye-balling. It can be used for instance to notice differences in root diameter and/or in root branching angle between different treatments very easily. A more complex visual method include the analysis of X-ray CT timely-registered scans. With such a method, it is possible to observe root growth in time as each root segment is assigned an age (Figure 3.3). This method provides a lot more information than simple 2D projections but requires the registration of the images of each column at all scanning intervals, which is a time-consuming and non-trivial task. Despite the advantages of visual methods, these methods remain qualitative and do not allow rigorous statistical analyses.

To assess root growth patterns quantitatively, root length density as well as the fraction of young roots (i.e., roots younger than the scanning time interval) were also calculated and provided insights into the root growth dynamics in a plant growth column experiment (see chapter 3). In comparison to the visual analysis, these methods present a significant advantage as they allow to perform statistical analyses of differences between treatments. Moreover, the root length density is a typical measure of root growth in soil and it is used commonly in practical books of agronomy as well as scientific literature. Root length density values can therefore be easily compared with the work of others for the same plant species and similar growth conditions.

Additionally, a new method for the quantification of root growth patterns was adopted. This method relies on the computation of root distance maps, as firstly introduced by Schlüter et al. (2018). Root distance maps present several advantages, e.g., they allow the quantification of mean root distance as well as rhizosphere volume fraction (see section 3.3.6). The measure of mean root distance is very correlated with root length density but provides additional information with regard to how roots explore the available soil volume over time. The rhizosphere volume fraction allows to determine the fraction of the soil that is influenced by the roots (i.e., potentially depleted of nutrients or water) assuming a given hypothetical rhizosphere extent. Both the mean root distance and rhizosphere volume fraction can provide valuable information regarding root growth patterns. However, because these measures are still quite new for the community of plant scientists, they present the limitation that it is currently hard to find values in the literature for cross-comparison and it will certainly take some time for the potential of these measures to be widely understood and recognized.

Note that the above methods were applied to soil column experiments for which the image resolution used during scanning with X-ray CT was close to the minimum root diameter to segment. Therefore, they have the limitations that they suffer from the trade-off between the sample size and the image resolution (see section 1.1.3), which affects the quality of root segmentation and root recovery. As was the case in this study, the root recovery was different for the two investigated substrates, i.e., fine roots were not recovered in the loam as well as in the sand. These aspects should always be considered when relying on X-ray CT scanning to perform root growth patterns analysis.

In chapter 4, it was shown that the analysis of bulk density gradients around roots could also be used as an indirect method for the investigation of root growth patterns, more precisely to assess whether roots grow in loose or dense zones of the soil. This method required the scanning of subsamples at a higher resolution. Thanks to the scanning at higher resolution, most roots could be recovered and this analysis was much less impacted by the trade-off between the image resolution and the sample size. However, due to sampling of smaller samples, this method presents the limitation that the spatial context was lost. As a consequence, the analysis could not be performed for targeted root orders but rather for only different diameter classes.

In practice, the investigated methods have different levels of sensitivity and enabled to investigate different (sometimes complementary) root system and/or rhizosphere properties. Applied to the research questions of this thesis, these methods enabled to identify the following effects of soil texture and structure on root system architecture, root traits and/or rhizosphere properties:

1. **Adaptation in root diameter**. This adaptation led to the development of roots having a bigger diameter in a soil with a coarse texture (i.e., sand), in comparison to a soil with a finer texture (i.e., loam) (Figure 3.6, AF4 and AF17). This difference in root diameter in sand was very consistent across the different laboratory and field experiments. This phenomenon has only been anecdotally reported in the literature, e.g., by Anderson et al. (2007). The potential mechanisms behind the influence of soil texture on root diameter are discussed in section 7.2.

2. **Modification of the growth angle of the roots**. In the pot experiment, this modification was expressed by a different tendency of roots to grow towards and along the wall, supposedly where desiccation cracks had formed (see chapter 3). This tendency was higher for loam in comparison to sand, as revealed by the analysis of rhizosphere volume fraction (Figure 3.9) as well as by the visual analysis of 2D projections of young seedlings at 7DAP (Figure AF6). This might be well related to differences in penetration resistance encountered by roots growing in loam as compared to sand. Indeed, at the volumetric water content observed in the column experiment (Figure AF5), the penetration resistance could have been up to four times higher in loam as compared to in sand (Figure AF13). The propensity of maize root systems to become shallower (i.e., in this study, to expand more laterally towards the wall) with increasing penetration resistance was already reported by Colombi et al. (2018). Note that, whether the modification of the growth angle of the roots was caused by an increased penetration resistance in loam remains speculative as the value of penetration resistance for which an effect on root system architecture can be expected has not yet been determined for the loam and sand investigated.

3. **Change in root growth environment**. The differences in the structural nature of the soil in which roots grew were addressed in chapter 4. Specifically, it was shown that, under heterogeneous soil structure conditions, roots preferentially grew in existing pores, in areas of the soil where the packing of particles was loose and the bulk density was lower than the average bulk density (see figure 4.4). The extent to which soil texture and structure affected root growth in structurally heterogeneous soil patches depended on the antecedent structure heterogeneity. Therefore, it was found more pronounced in loam than in sand, considering that the structure in sand was rather homogeneous (Figure 4.2) due to its fairly uniform particle size distribution (Figure 4.7).

4. **Alterations of root growth dynamics**. In the laboratory, these alterations were noticeable on the depth profile of RLD (Figure 3.4) as well as on the fraction of young roots at each scanning time interval (Figure 3.5). In the field, root growth was also impacted by soil texture (see RLD data in figure AF10 or figure 12 in Vetterlein et al. (2021)). Interestingly, the impact of soil texture was inconsistent, e.g., total root length in loam was higher than in sand in the laboratory, but lower in the field experiment. This inconsistency might well be related to differences in availability of water or water distribution in the field and in the laboratory. Indeed, the laboratory experiments were carried out in well-watered conditions whereas drought stress occurred in the field experiment. Plants growing in loam in the field were affected by drought stress earlier than plants growing in sand because they were bigger and therefore required more water to sustain evapotranspiration. It is also possible that plants growing in loam in the field suffered from drought stress earlier than in sand because roots grew in loose areas of the soil and had therefore less contact with the soil aggregates (containing water).

Contrary to the original assumption (see research question 1 in section 1.2), the absence of root hairs had small effects on the investigated root system architecture and root traits. Lack of root hairs resulted in a slight reduction of shoot and root growth. These effects were larger for shoots than for roots, the latter being reflected in a shift in root:shoot ratio towards the roots for rth3 (Figure 3.2c). Growth reduction (shoot and root) was larger for loam than for sand and the differences between genotypes were even more obvious for plant P content (Figure 3.2d). There was no significant difference between the genotypes with respect to phosphorus uptake per unit root surface, albeit there was a tendency for lower uptake for rth3 as compared to WT for loam (Figure 3.2e). Likewise the Ca:P ratio showed higher values for rth3 as compared to WT for loam. However, no difference between genotypes was found for sand (Figure 3.2f). The fact that the root hairs had more effect in loam was attributed to the lower nutrient mobility of the loam substrate (due to its higher number of sorption sites). These observations confirms the previous findings of Haling, Brown et al. (2013); N. Suzuki et al. (2003), i.e, root hairs influence plant and root growth in substrates with low nutrient mobility.

Soil texture and structure did not only affect root growth patterns at the plant scale (cm-dm), but also affected how roots interact with the soil at the scale of individual root segments (μm-mm). This interaction was studied with an imaging workflow, which enabled to assess the changes of soil bulk density as a function of the distance from the roots (see chapter 4). This interaction was also studied via an assessment of the nature and the behavior of biopores in soil (see chapter 6). The effects of root growth on soil structure manifested themselves in the main following aspects:

1. **Reorganization of soil particles**. As a result of their ingression into the soil, roots rearranged soil particles. Due to the imperfect packing of convex particles around the roots (Koebernick et al., 2019), a zone of increased of porosity at a distance <250 μm from the root surface was observed (Figure 4.3 and 4.4). In loam, the effect of root growth on soil structure in the vicinity of roots was dependent on the antecedent soil structure. When the antecedent soil structure was homogeneous and no existing pores were present, the roots created their own pores by plastically deforming the loam aggregates. Under these conditions, a zone of compaction was observed within a distance range of 250 μm and 1 mm from the root surface (Figure 4.3 and 4.4). When the antecedent soil structure was heterogeneous and existing pores were present, roots grew into these pores and the soil within a distance <1 mm from the root surface was looser than the soil farther away (Figure 4.3 and 4.5). In sand, the roots could not deform the rigid sand grains but rather pushed them away. Fine roots (<200 μm in diameter) caused sand grains to align along their axis whereas big roots (>350 μm in diameter) broke the fragile arrangement of grains (Figure 4.6) and pushed them away farther than their own diameter. These experimental observations were used to derive soil hydraulic parameters in the vicinity of roots (see chapter 5). In both loam and sand, roots induced in their vicinity an increase of the saturated volumetric content and hydraulic conductivity as well as of the inverse of the air entry suction. A decrease of the residual volumetric water content was observed (Figure 5.6). These alterations of soil hydraulic properties were mainly attributed to the gap formation at the root soil interface due to the surface wall effect (M. Suzuki

et al., 2008). Note that the effects of root-induced soil compaction and sand grain alignment on the above-mentioned soil hydraulic properties were small.

2. **Creation of a biopore network**. After the degradation of roots in soil, a network of biopores was left behind. In this work, it was observed that the time necessary for biopores to be created depended on the soil texture. Incubated under the same conditions, it took 78 days for biopores to be created in loam, whereas some root residues were still found after 216 days in sand (Figure 6.3b). Also, the behavior and longevity of these biopores differed substantially between the sand and loam (see chapter 6). In loam, the biopores were structurally stable over time whereas it was often observed that some biopores had collapsed in sand. These observations are solid evidence that the influence of roots on soil structure is mostly influenced by soil texture.

Contrary to the original assumption (see research question 2 in section 1.2), the presence of root hairs had no effects on the root-induced alterations in rhizosphere bulk density. This could be explained by two factors, i.e., the root hair length and the age of the plants. In this experiment, the root hairs for the WT were relatively short (0.24 mm), in comparison to the values which can be found in the literature (0.7 mm according to Hendriks et al. (1981)). Shorter root hairs decrease the ability to anchor the growing root tip in soil if an insufficient length of each root hair is secured within the rhizosphere soil pores (Bengough et al., 2016). Also, since the plants investigated in this thesis were relatively old, the role of root hairs for anchorage might have been taken over by the seminal and lateral roots (Bailey et al., 2002).

Compiling the main findings of this thesis, it appears clear that all of the above-mentioned processes are extremely complex and inter-linked and that **there is indeed a strong interplay between root growth patterns and soil properties**. In an attempt to summarize the main findings of this thesis, figure 7.1 illustrates the influence that root growth, soil texture and structure exert on one another.

On top of addressing the research questions suggested by the priority program 2089 in the framework of this thesis, this work has once more demonstrated the numerous applications and benefits of the use of X-ray CT for the study of root-soil inter-actions processes. Indeed, X-ray CT allowed a fast and reliable analysis of hundreds of undisturbed soil samples of different sizes. In conjunction with the use of X-ray CT, this analysis was made possible thanks to the development of a new root segmentation algorithm. The root segmentation algorithm is based on the root segmentation algo-rithm of Gao, Schlüter et al. (2019) Rootine v.1 and has therefore been named Rootine v.2. Rootine v.2 has an increased performance and user-friendliness, as compared to its preceding version and other state of the art root segmentation methods. Thanks to that, Rootine v.2 (or slightly modified versions of it) has also been used extensively by many projects partners within the priority program 2089. It demonstrates a high po-tential for improving high-throughput root phenotyping procedures based on X-ray CT data analysis.
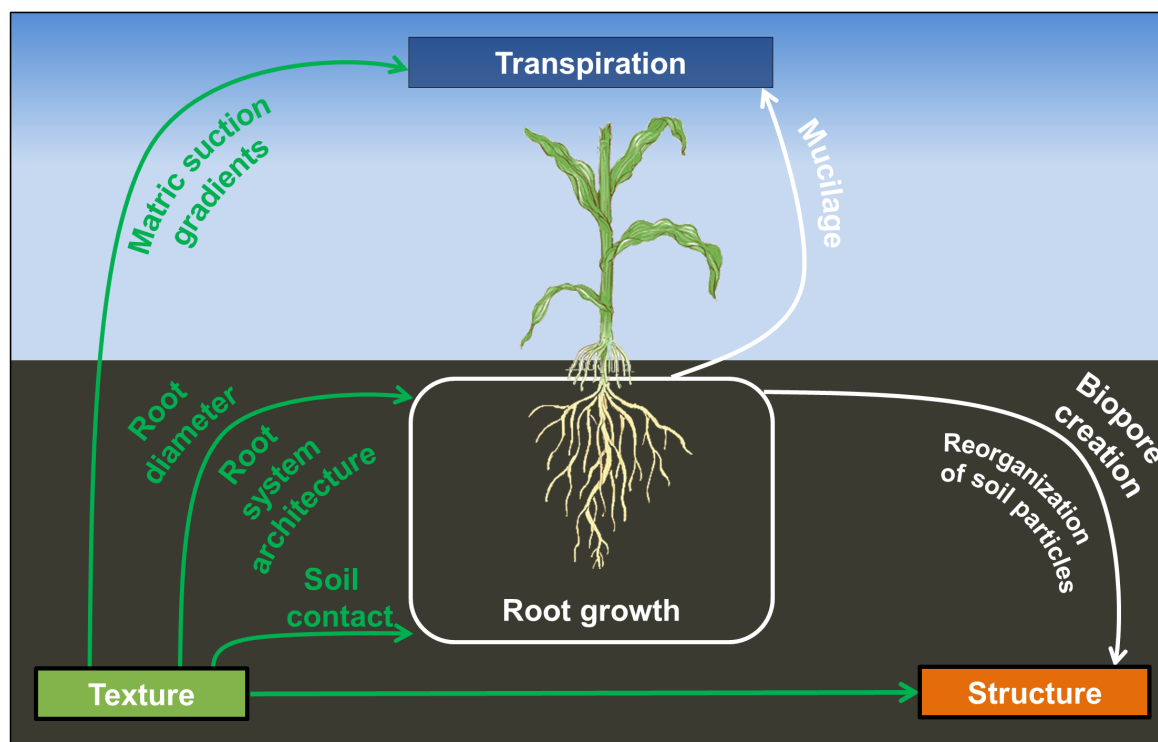
Figure 7.1: Illustrated summary of the main interplay effects of roots and soil properties investigated in this thesis.

7.2   Limitations

Despite the rigorous analysis of the effect of soil texture and the absence of root hairs on root growth patterns and soil structure properties, the work presented in this thesis lacks a certain representativity in comparison to natural conditions. Some of the aspects for which the experiments lacked representativity are described below.

Homogeneity of soil structure: In the laboratory experiments, the soil was sieved down to 1 mm and the columns were packed in a way which minimizes soil structure heterogeneity (i.e., the formation of layers and the presence of packing pores). In the field experiment where the undisturbed cores were extracted (see chapter 4), the procedure for sieving the soil (to < 20 mm) and filling the plots also guaranteed a fairly homogeneous soil structure. By placing the layers in 15 cm depth increments and using a vibrating plate to compact the soil after each layer, the presence of layers or vertical gradients of bulk density in the field were initially absent (see figure 3 in Vetterlein et al. (2021)).

Homogeneity of nutrient distribution: In the laboratory experiments, the soil and the fertilizer were mixed in a tray in order to obtain a very homogeneous distribution of nutrient prior to packing the columns. In the field experiment, the fertilization was applied on the surface of the plots, 50% prior to seeding, and the remaining 50% after the first sampling campaign (BBCH14). Possibly, this surface fertilization induced a

small vertical gradient of nutrients from top to bottom. This vertical gradient was very likely much less steep than what could be expected under natural conditions, where nutrient distribution is the result of many (hundreds of) years of nutrient leaching and/or organic matter accumulation within a soil profile.

Pot constrained growth: A bias was inherently introduced due to the restriction of available soil volume for root growth. This was most certainly true for the column experiments (see chapter 3, 4 and 6). This restriction of soil volume for root growth affected the root system architecture already in the early stages of growth. This can be seen on figure AF6 where the roots were hitting the pot wall and growing along it as early as 7 days after seeding. Constraining root growth in pots also affected the range of root length density values investigated. Indeed, the root length density values observed were up to one order of magnitude higher in the column experiment as compared to the values observed in the field (figure AF10c) or which can be expected in natural conditions (Lucas et al., 2019).

Influence of micro-organisms: In this thesis, the experimental design excluded the study of interactions of roots with the presence of pathogens and/or symbiotic micro-organisms. No incubation of particular micro-organisms were performed, i.e., the presence of micro-organisms in the soil was inherited from the biota of the haplic Phaeozem soil extracted in Schladebach, Germany.

In natural conditions, roots exploring the soil encounter a mixture of soil patches potentially having very different properties in terms of water, nutrient, compaction status and pathogen pressure. In order to thrive in such heterogeneous conditions, plant roots most likely exhibit a much higher degree of root plasticity and tropism mechanisms than the one observed in this work. As a result, other drivers for adaptation in root system architecture, root traits and/or rhizosphere properties might come into play in nature but have been missed in the scope of the experiments carried out in this thesis. Such drivers might be for instance vertical gradients of bulk density (Tracy et al., 2013), scarcity or abundance of water (Rich & Watt, 2013), nutrients (Shahzad & Amtmann, 2017; Yu et al., 2014) or the presence of pathogens (Mattupalli et al., 2019). Note that, in the framework of the SPP 2089 priority program, the need for such homogeneous conditions as studied in the field and in the laboratory experiments is justified because (i) it allows to consider every column/field plot as replicates, (ii) it allows to study the system behavior over time, e.g., to investigate how long does it take for spatial and temporal patterns to develop and (iii) it is a requirement to simplify the system under study before increasing its complexity.

Another possible limitation of this study is related to the expression of pleiotropic effect by the root hair defective rth3 mutant. Pleotropic effects are expressed when knocking out a gene responsible for one trait of interest influences the expression of other phenological traits. During the course of the priority programme, the research work by project partners pointed out that the rth3 mutant does not only show disturbed root hair elongation but also a disturbed cell elongation in the leaves. This induced an increase of the number stomata per unit cell area at roughly the same stomatal conductance. So far it is believed that this stomata density was intrinsic to the rth3 mutant and was not affected by water stress or soil type. The higher stomata density caused

higher transpiration and photosynthesis rates (Ahmed et al., personnal communication). Other pleotropic effects such as a higher exudation rate have been observed for the root hair defective rth3 mutant (Oburger et al., personnal communication). To which extent these pleotropic effects (and possibly others to discover) affected plant and root growth in the experiments is currently under discussion.

7.3   Future work

7.3.1   Improving Rootine v.2

Currently, the biggest weakness of Rootine v.2 is related to the disconnection of fine root segments from the main root system, fine root segments which are later discarded during post-processing. This disconnection is caused by a decrease of gray value intensities after tubeness filtering. This decrease occurs when roots have a fine diameter (i.e., close to the image resolution) and/or when roots are branching out (i.e., at the point of branching, the shape of the roots is not tubular anymore but rather shows a "Y" pattern). In order to cope with this that, the false negatives recovery step was incorporated in Rootine v.2 to recover the disconnected fine root segments. The false negatives recovery step uses a vesselness and size criterion (Figure 2.7). On some occasions, even these two criteria combined could not properly distinguish the segmentation noise from the false negatives. This introduced some noise in the segmentation results and was partly responsible for the root recovery superior to 100 % for the best case scenario. As can be seen on figure 2.8b and 2.8d, the segmentation noise is usually isolated and distant from any roots. It is likely not the results of roots which were disconnected from the main root system, but rather false positives which were incorrectly considered false negatives during the false negatives recovery step. In order to tackle this issue, an additional criterion could be introduced in the recovery step in order to sharpen the evaluation of the false negatives. Such criterion could be a "distance to the closest root" criterion, i.e., a potential false negative would have to be in the vicinity of another root connected to the root system in order to be considered a false negative. The script which would allow to include the "distance to the closest root" criterion is presented in the appendix. The consideration of the "distance to the closest root" criterion should considerably reduce the number of isolated false positives. Future work should include the "distance to the closest root" criterion and evaluate to which extent it reduces segmentation noise and improves the segmentation results.

As already mentioned in section 1.1.3, the development of root segmentation algorithms is an ever growing field. In the recent years, some incredible advances have been made with the development of machine learning methods. Despite the wide applications of such methods in the field of medical image analysis, so far only a few studies have applied machine learning tools for the segmentation of roots from X-ray CT images (Gribbe et al., 2020; Smith et al., 2020; Soltaninejad et al., 2020). The application of machine learning for image segmentation is based on the definition of a limited number of manual annotations on the image to segment in order to train a classifier and segment the remaining data automatically. Such classifier harvests different features of the image such as the gray values as well as the first and second derivatives of the gray values, at once and at different scales and hierarchical levels. Such machine

learning methods can be implemented with softwares such as "Ilastik" (Berg et al., 2019) (available as a standalone application) or the "Trainable Weka Segmentation" tool (Arganda-Carreras et al., 2017) (available in ImageJ). Promising applications of machine learning for root segmentation have already been demonstrated by Soltaninejad et al. (2020). The natural continuation of this work is to assess to which extent can deterministic methods such as Rootine v.2 compete with machine learning methods.

7.3.2   Understanding root radial thickening in sand

One of the most prominent and intriguing result of this thesis is the adaptation of root diameter with respect to soil texture, i.e., the increase of root diameter in sand as compared to loam (see chapter 3). In the literature, it is well documented that an increase of mechanical impedance can induce a radial thickening of roots (Atwell, 1993), as already discussed in section 3.4. However, differences in mechanical impedance are likely not responsible for the differences in root diameter between the two soil texture investigated. Indeed, in this study, penetration resistance was lower in sand than in loam (see figure AF13). Beyond mechanical resistance, two hypotheses could explain the observed differences in root diameter:

- **Concentrations of ethylene were higher in sand as compared to in loam.** This explanation is supported by the recent publications of Pandey et al. (2021) and Vanhees et al. (2021), which provide strong evidence that root thickening is induced by high concentrations of ethylene. These publications consolidates the previous findings of Kays et al. (1974) and Sarquis et al. (1991). The reasons as to why concentrations of ethylene would be higher in sand are still very speculative but could include the presence of local dry patches (drought-induced ethylene), microwounds at the root surface and/or excessive sloughing off of root cells due to the abrasive nature of the sand (wound-induced ethylene) (Yang & Hoffman, 1984).

- **Root-soil contact was lower in sand as compared to loam.** This is supported by a publication of S. Schmidt et al. (2012) who showed that root-soil contact decreases with aggregates size. In order to increase root-soil contact, the roots in sand could have increased their diameter to increase the number of contact points with sand grains. Indeed, in a porous medium with a fairly uniform particle size distribution, an increase in diameter would necessarily mean an increase in number of contact points between roots and soil particles. Maintaining contact with sand grains could be viewed as a strategy to reach the water films (and their associated nutrients) adsorbed at the surface of the sand grains. Considering the role of root hairs in increasing root-soil contact (Haling, Brown et al., 2013), the fact that root diameter in sand for the rth3 genotype was higher than for the WT (see figure 3.6) is supporting this hypothesis.

In order to rule out one explanation or the other, future work should focus on column experiments in which the ethylene concentration in the soil gas phase is measured with in-line gas measuring devices. The second explanation could be revoked by conducting experiments where the particle size distribution of the sand and the loam is modified. This could be achieved by changing the sieving procedure adopted in the

column experiments presented in this thesis. Finally, it would be worth investigating to which extent the differences in root diameter with respect to substrate depend on the plant species.

7.3.3 Understanding the difference of root degradation rates in sand

Another very interesting result which deserves more attention and research is the difference in decomposition rate of roots in sand as compared to loam. This difference was observed within the scope of the biopore recycling experiment (see figure 6.3). As briefly discussed in the section 6.4.2, this difference could be due to an increase of root diameter in sand, which would lead to an increased amount of organic matter to decompose in a given amount of time. Very possibly, this difference could also emerge from different properties of the root tissues themselves (e.g., the relative proportions of soluble, cellulose, hemicellulose, lignin and phenolic compounds). Differences in root decomposition in soil for maize genotypes differing in their phenolic composition have already been reported by Machinet et al. (2011). In subsequent experiments, chemical analysis of root tissues would be required to elucidate whether roots in sand are composed of more recalcitrant compounds than the roots in loam. Such experiments could also include respirometric measurements to measure the rate of organic carbon mineralization for a set of incubated samples and to see to which extent the mineralization rate differs for roots growing in loam or sand.

Appendix for chapter 3
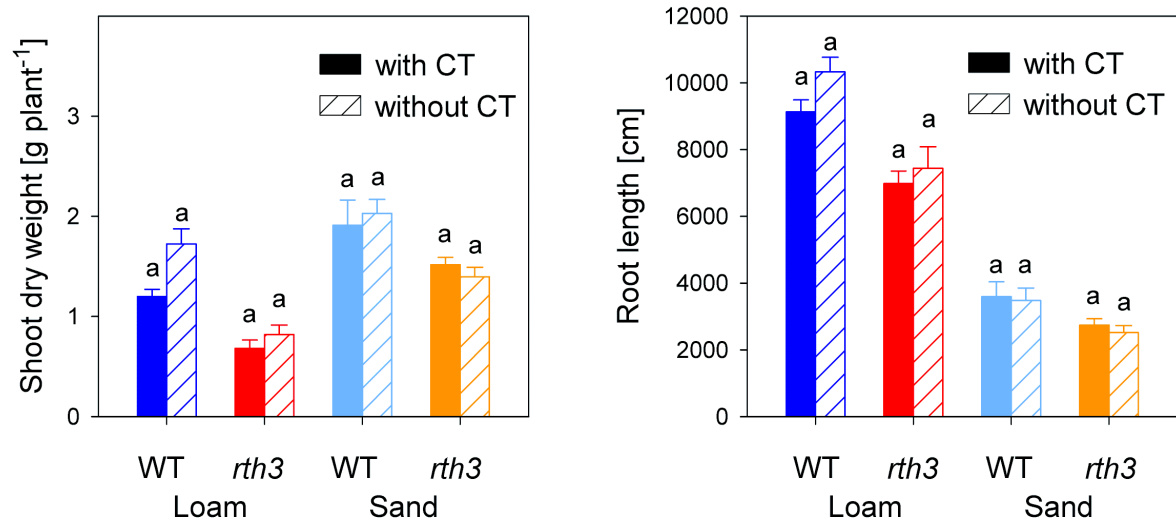
Figure AF1: Impact of X-ray CT scanning on shoot and root growth of two maize genotypes (wild-type - WT, root hair defective mutant rth3 – rth3) in loam (L) and sand (S) 22 days after planting. Plants were either scanned 7, 14 and 21 days after planting or were not exposed to X-ray CT at all. Mean values of six replicates are shown, error bars denote the standard error. Three-factorial ANOVA in conjunction with Tukey's HSD test. Significant differences between treatments are displayed with small letters for p < 0.05.

Figure AF2: Root recovery with destructive sampling (DS) as compared to root recovery with non-invasive X-ray CT scanning and subsequent segmentation of roots with the algorithm Roo-tine v.1. For the correlation only layers WR2 and WR3 were used (Figure 3.1). The circled values from the layer WR2 from treatment L _WT at 21 days after planting were not included in the calculation.

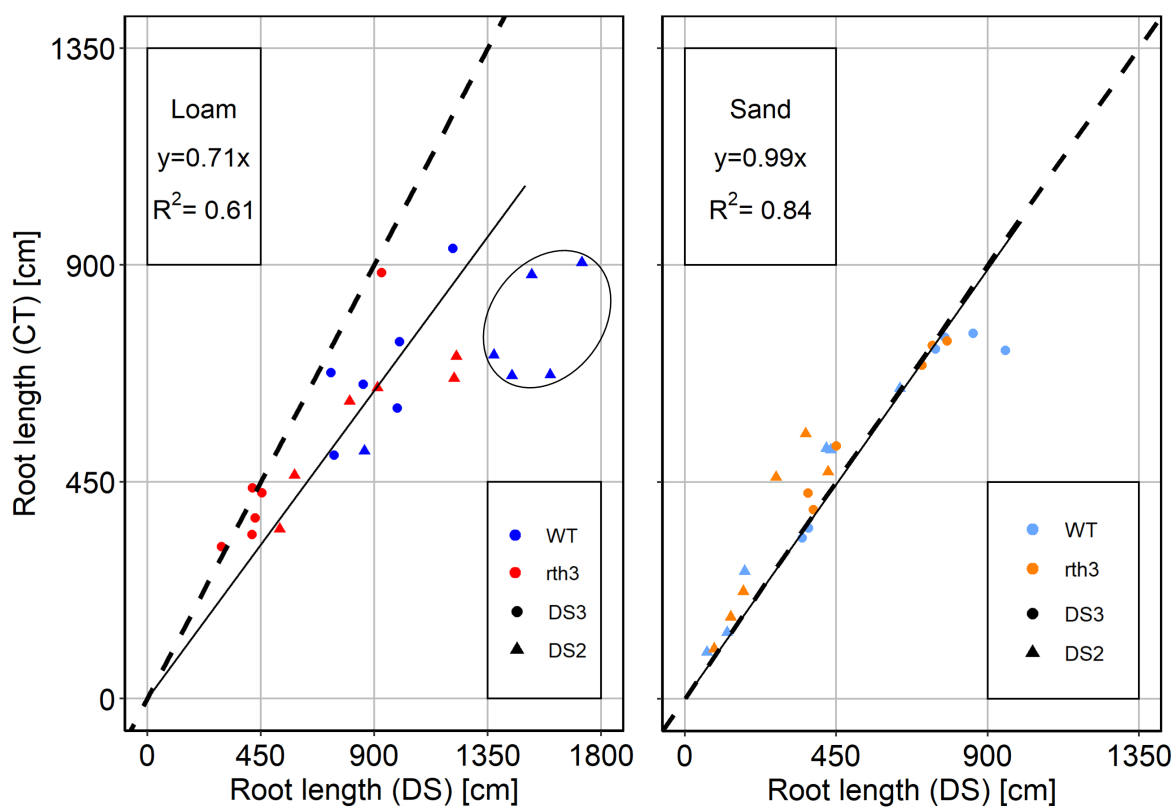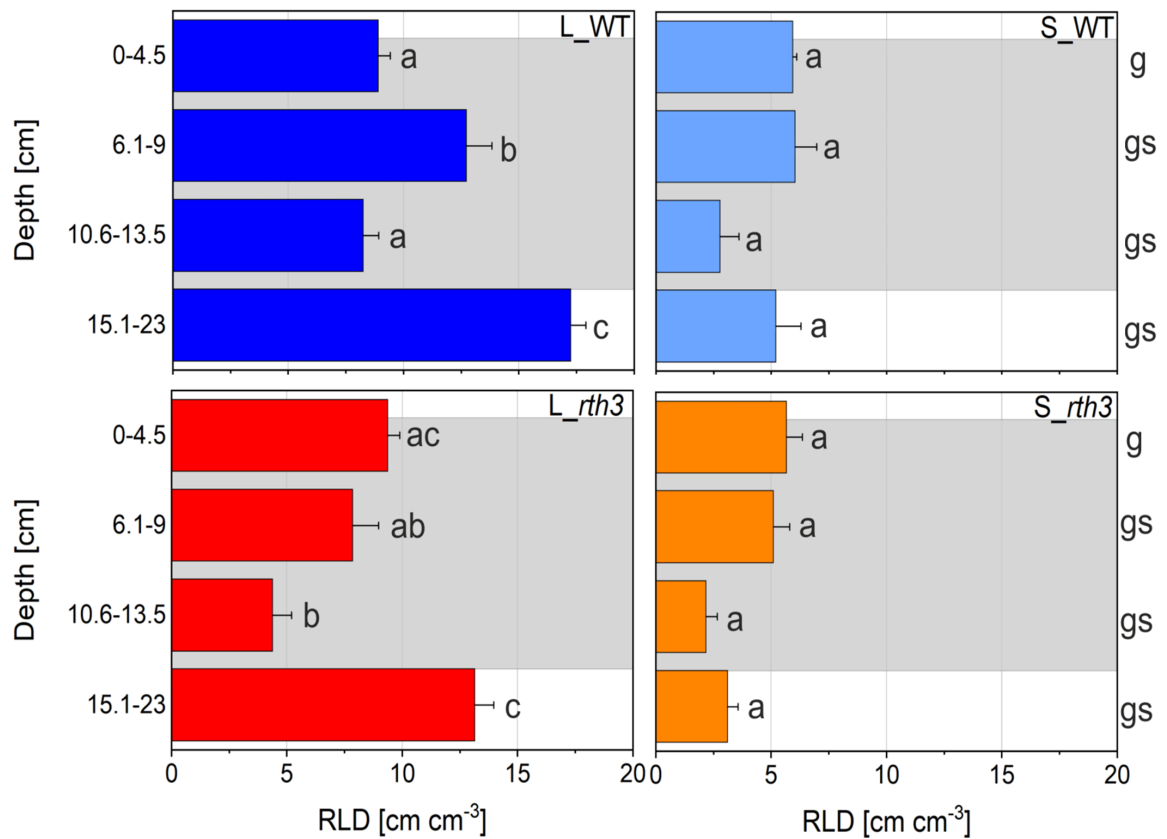*Figure AF3: Change of root length density with depth for 22 days after planting for two maize genotypes (wild-type - WT, root hair defective mutant rth3 – rth3) grown in loam (L) and sand (S). Data are derived from destructive sampling of soil columns in layers; n=6, bars represent standard error. The layers which correspond to the depth analyzed by X-ray CT are shaded in gray. Significant differences between depths within treatments are displayed next to the bars with small letters for p < 0.05. Significant effects of factor between treatments within the same depth is denoted by s for substrate, g for genotype and x for interaction next to the graphs for p < 0.05.*

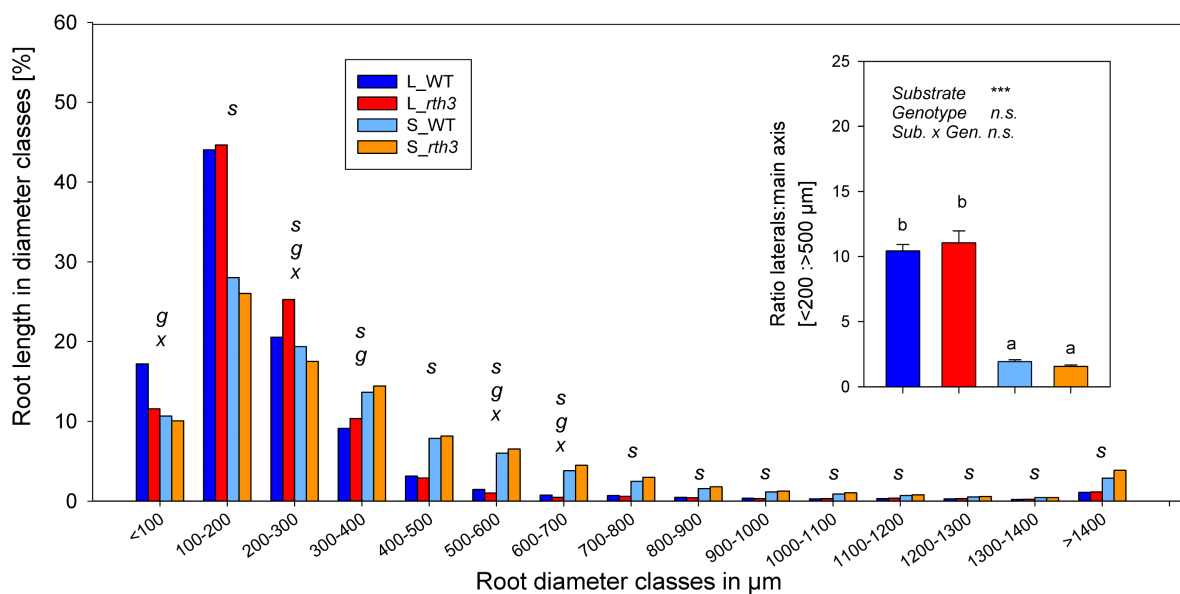*Figure AF4: Root length in different root diameter classes (class width 100 μm) 22 days after planting for two maize genotypes (wild-type - WT, root hair defective mutant rth3 – rth3) grown on either loam (L) or sand (S). Data are derived from WinRHIZO after destructive sampling of soil columns; n=6. Two-factorial ANOVA in conjunction with Tukey's HSD test was conducted for each diameter class. Significant effect of factor is denoted by s for substrate, g for genotype and x for interaction, for p > 0.05 no letter is displayed. The inset shows proportion of laterals roots versus thick axial roots, i.e., assuming that roots diameter classes < 200 μm comprise laterals only; root diameter classes > 500 μm comprise thick axial roots only. Mean values of six replicates are shown, error bars denote the standard error.*
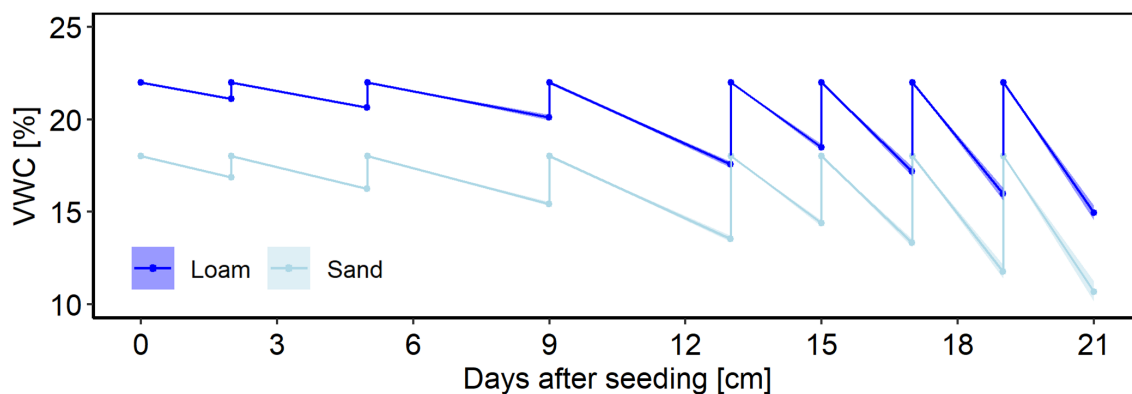
Figure AF5: Soil volumetric content measured during the course of the column experiment presented in chapter 3, for loam (blue) and sand (light blue). The semi transparent ribbon denotes the standard error around the mean (n=18).
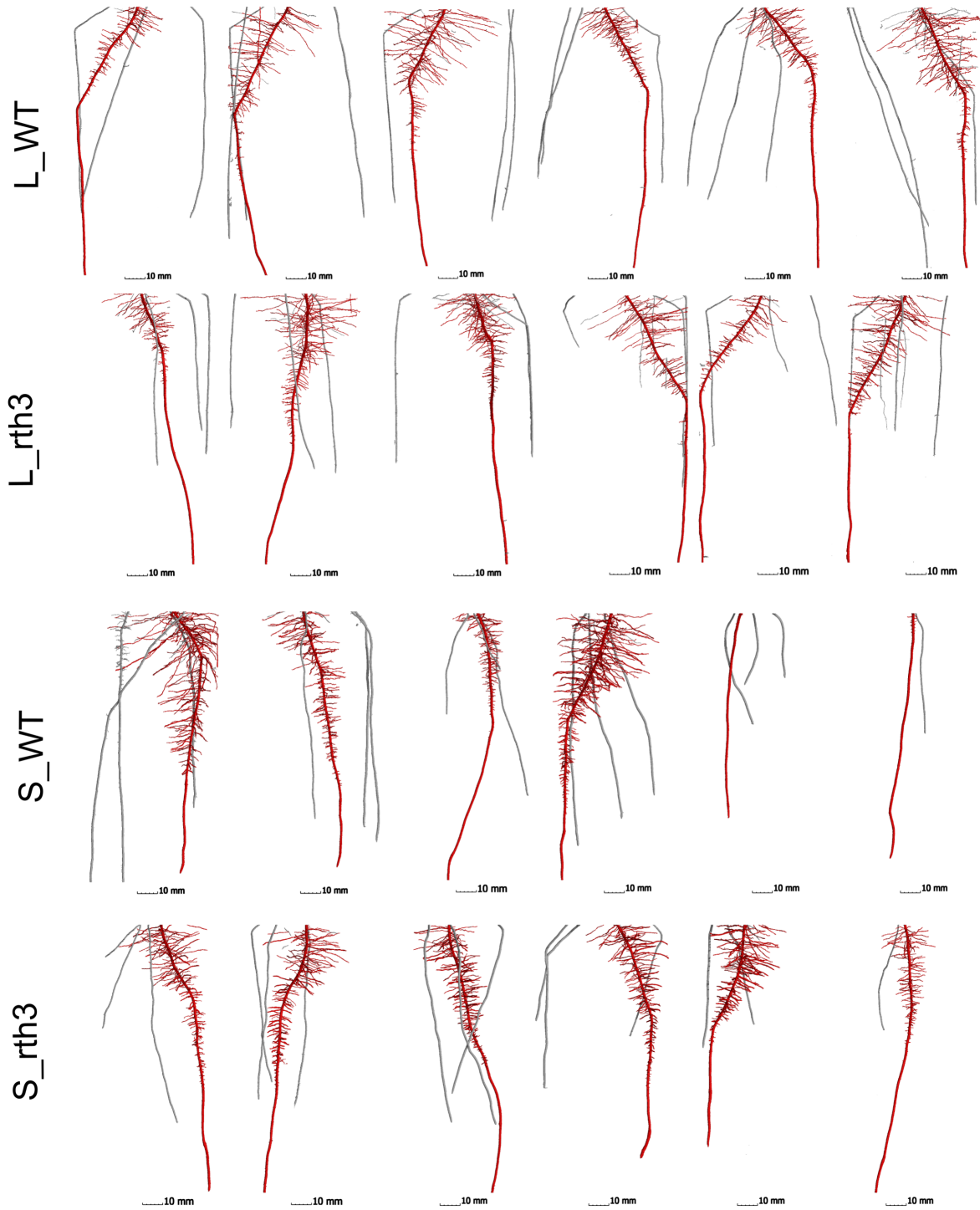
Figure AF6: Three-dimensional rendering of root networks 7 days after planting for all replicates of each treatment. The primary root and all laterals connected to it are depicted in red; seminal roots in gray.
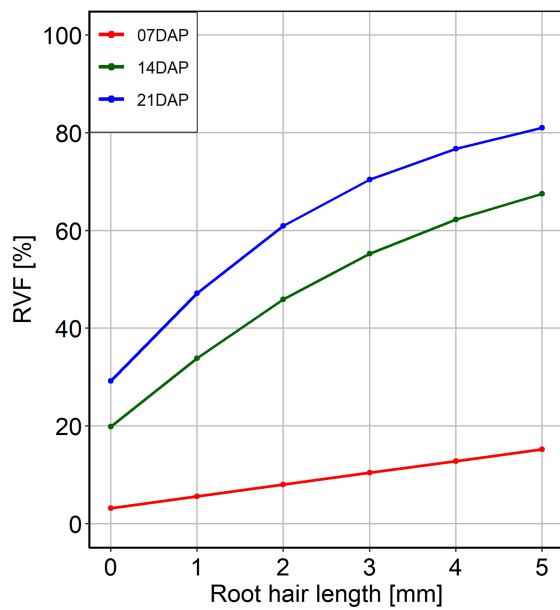
Figure AF7: Change of rhizosphere volume fraction for different root hair length and days after planting. Scenarios were calculated based on root system architecture of the treatment S _WT. Values for root hair length = 0 correspond to extent of P depletion zone of 1.8 mm (see figure 3.9).
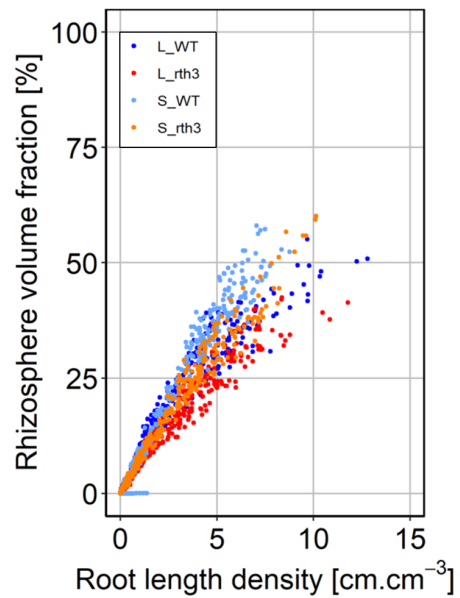
Figure AF8: Relationship between rhizosphere volume fraction and root length density for all time points and treatments across all depths. The different colors indicate the different treatments. Rhizosphere volume fraction is determined assuming a typical rhizosphere extent for P depletion of < 1.8 mm, plus 0.24 mm for hair length in WT.

Table AT1: Impact of substrate (loam, sand) and maize genotype (wild-type - WT, root hair defective mutant rth3 – rth3) on mycorrhizal colonization of roots 22 days after planting; numbers in brackets refer to standard error.

	L_WT	L_rth3	S_WT	S_rth3
Arbuscules [%]	1 (0.5)	3.3 (0.9)	3.5 (1.5)	3.02 (0.6)
Hyphea [%]	9.3	27.3	21.2	26.8
Vesicles [%]	0 (0)	0.5 (0.5)	0 (0)	0 (0)

Table AT2: Share of root length in diameter classes > 0.5 mm for two different bulk densities in loam for root hair defective mutant rth3 and its corresponding wild-type. Results refer to an additional experiment set-up like the experiment conducted in chapter 3 but for loam only and with n=5.

	L_WT		L_rth3	
Bulk density [g cm^{-3}]	1.3	1.45	1.3	1.45
Root length in the diameter classes >500 μm [%]	3	45	7	58

Appendix for chapter 4
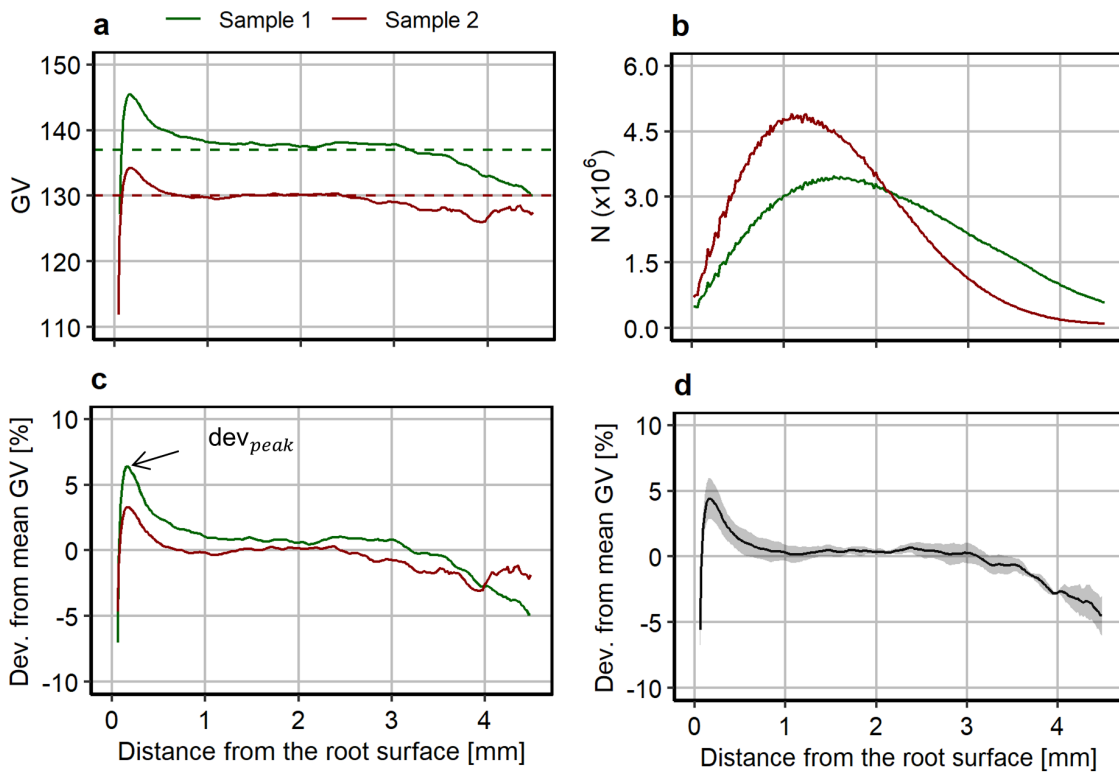
Figure AF9: Example of the output and the data analysis steps for two loam samples scanned at a resolution of 19 μm. Root length density of sample 1 and 2 are equal to 6 and 11 cm cm^{-3}, respectively. (a) Gray value as a function of the distance from the root surface. The two dashed lines indicate GV_{im} and denote a difference in contrast between the two samples. (b) Number of voxels as function of the distance from the root surface. Sample 2 has a higher RLD and shows therefore more voxels in the vicinity of roots. (c) Results obtained after normalizing the data of subfigure a. The normalization step eases the comparison between images with different contrasts. The peak deviation from mean GV (dev$_{peak}$), if present, is used as an indicator for the degree of compaction. (d) The deviation from the mean GV profiles of the two samples is averaged using the number of voxels of the two samples as weighting factors. The transparent ribbon denotes the standard error of the deviation from the mean GV of the two samples.
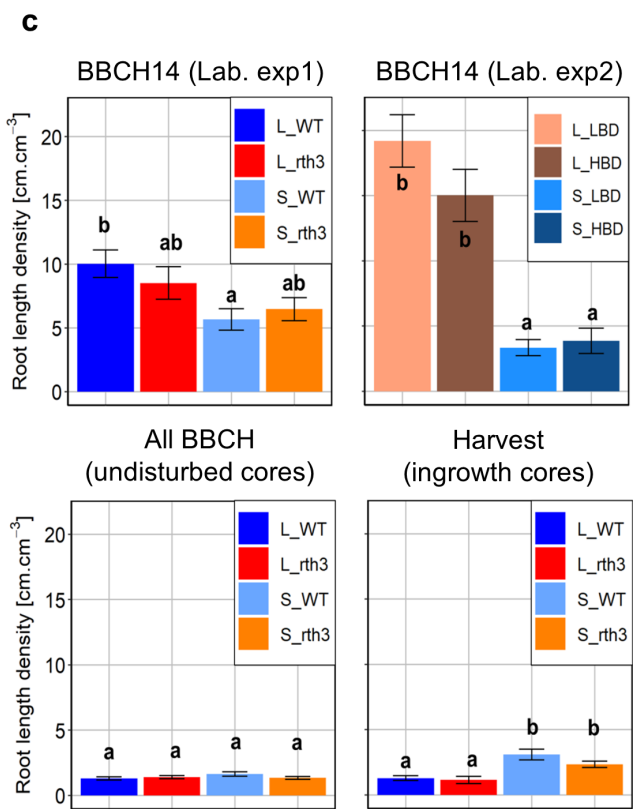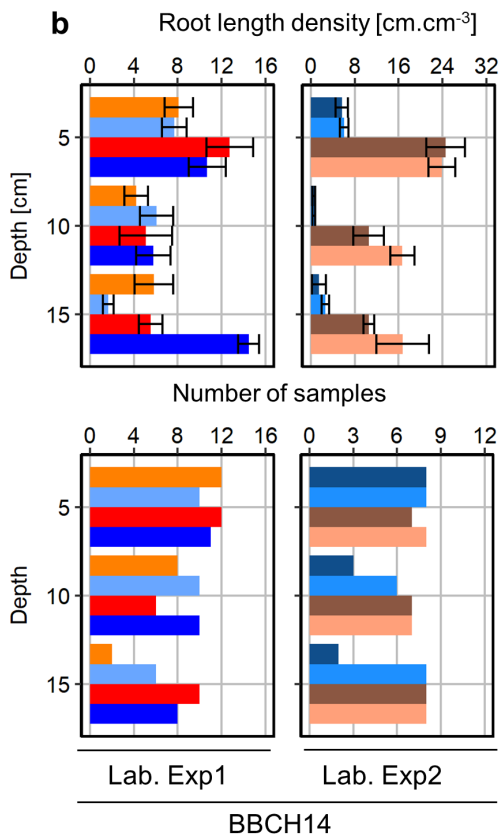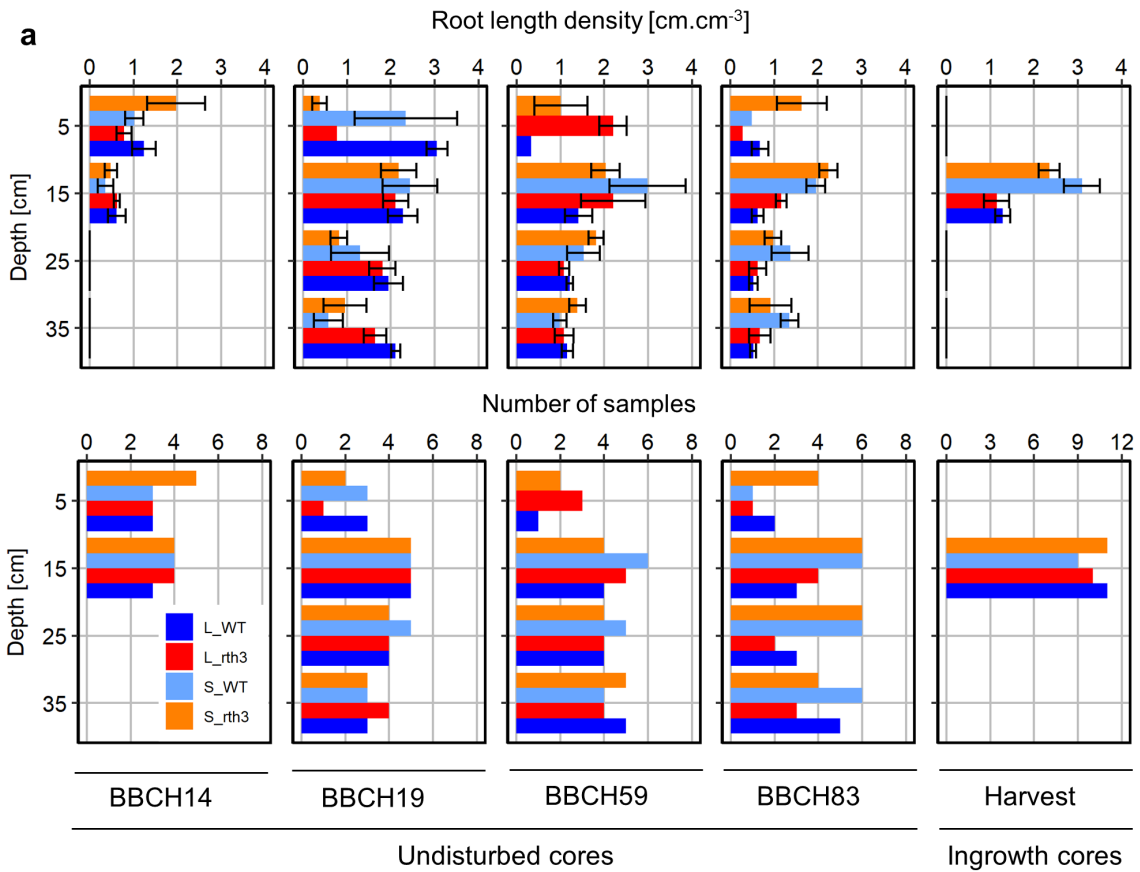
Figure AF10: Root length density (RLD) measured via X-ray CT after skeletonization of the root system. (a) RLD for the field experiments (upper row) and the corresponding number of samples used for the calculation of the RLD (lower row). (b) RLD for the laboratory experiments (upper row) and the corresponding number of samples used for the calculation of the RLD (lower row). (c) RLD results for all experiments averaging across depths (and BBCH stages for the undisturbed cores). The letters "L" and "S" refers to loam and sand respectively whereas the letters "WT" and "rth3" refers to the wild-type and root hair defective mutant. For the laboratory experiment 2, the letters "LBD" and "HBD" refers to the low and high bulk density treatments respectively. The legend of subfigure c is valid for subfigure b. Note that RLD is calculated only for the samples which were used for the analysis of the rhizosphere properties (i.e., for samples containing roots) and should therefore not be taken strictly as an indicator for root and plant growth.
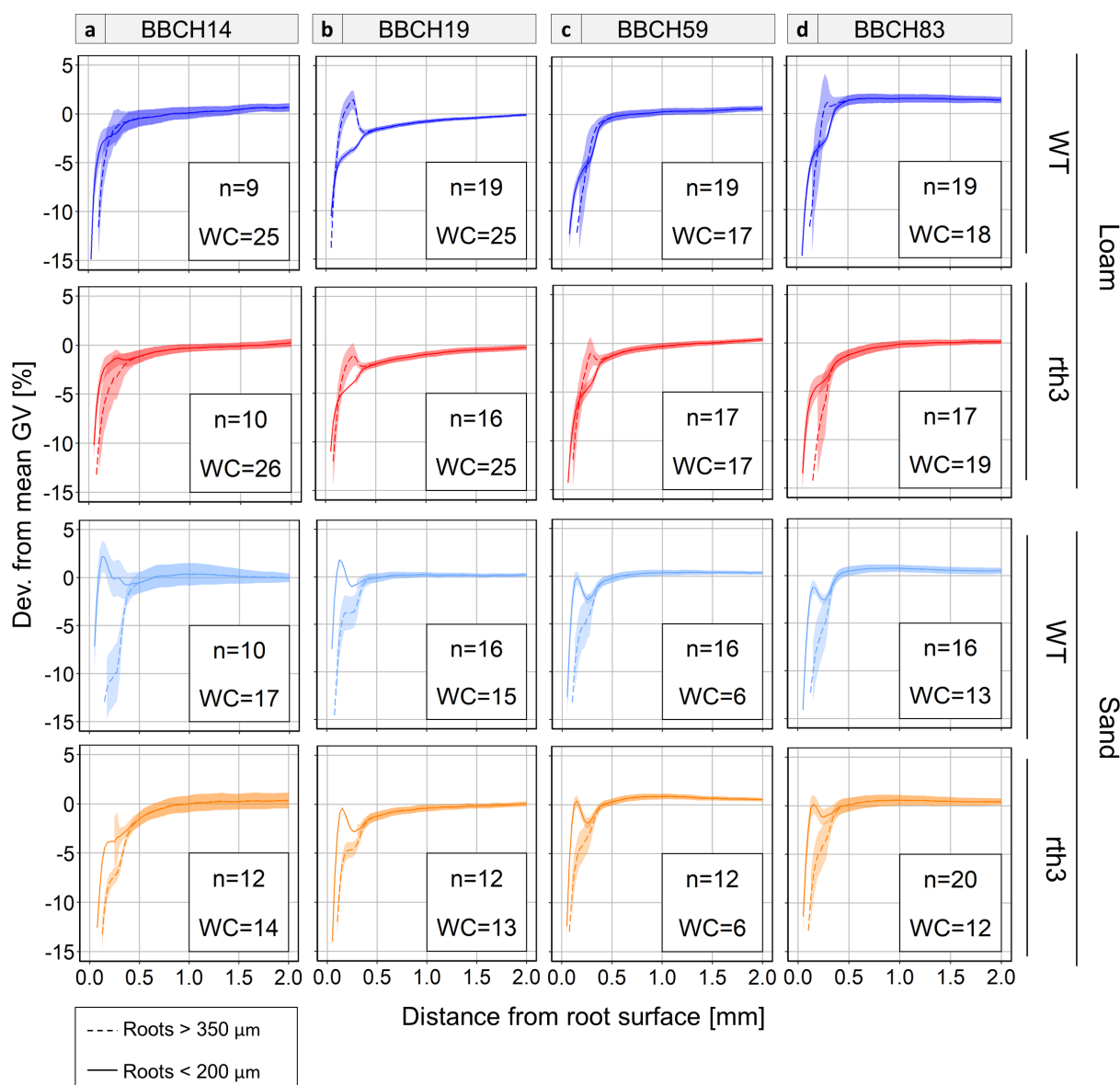
Figure AF11: Deviation from the mean GV as a function from the distance from the root surface for the BBCH stages investigated with the undisturbed cores in the field. Root diameter class < 200 µm is depicted with a solid line whereas the root diameter class > 350 µm is indicated by a dashed line. The semitransparent ribbon denotes the standard error. The mention "n=" refers to the number of samples used for each treatment whereas "WC=" refers to the volumetric water content.
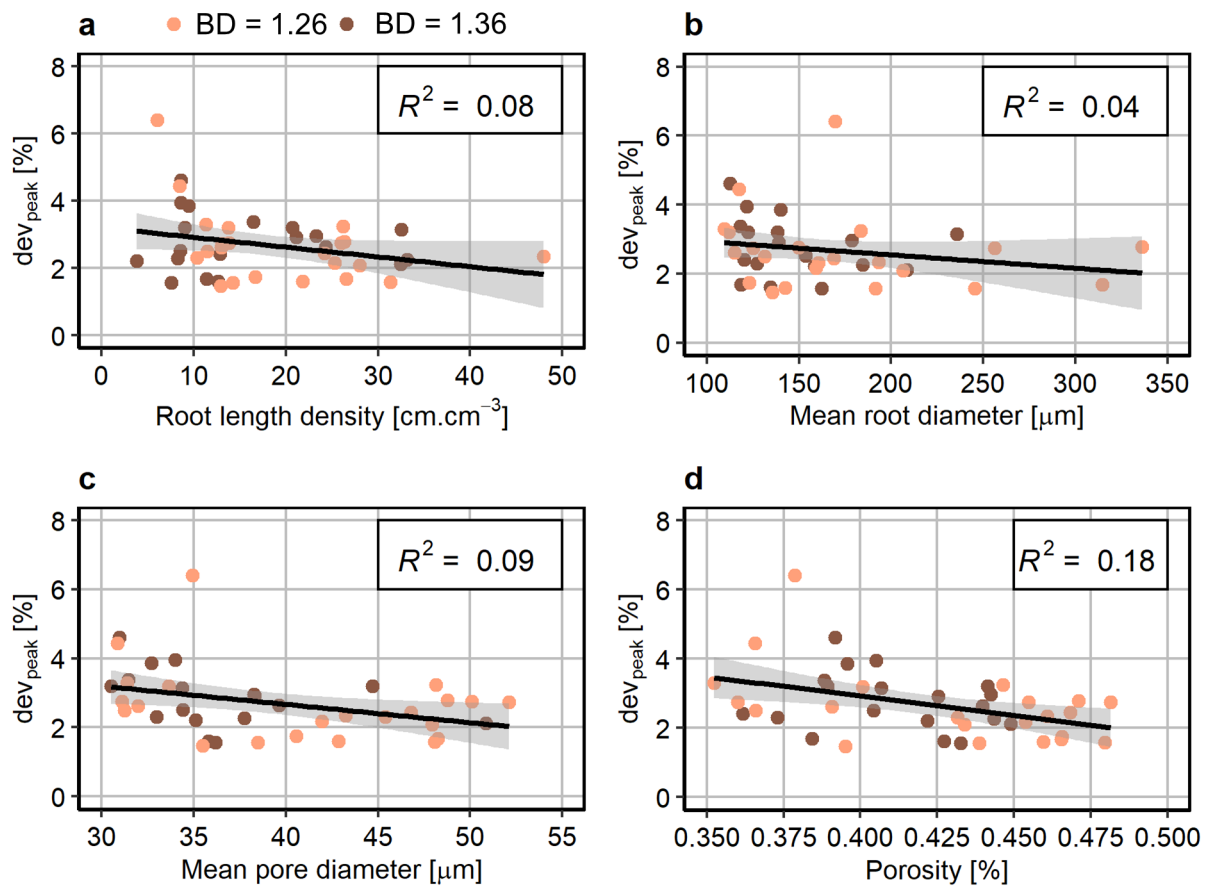
Figure AF12: Peak deviation (dev$_{peak}$) from the mean GV plotted against (a) the RLD and (b) the mean root diameter within a sample and (c) the mean pore diameter and (d) the porosity of the bulk soil. No or only weak correlations were found between these four properties and the root induced compaction in loam for the low and high BD treatments in the second laboratory experiment.

Appendix for chapter 6
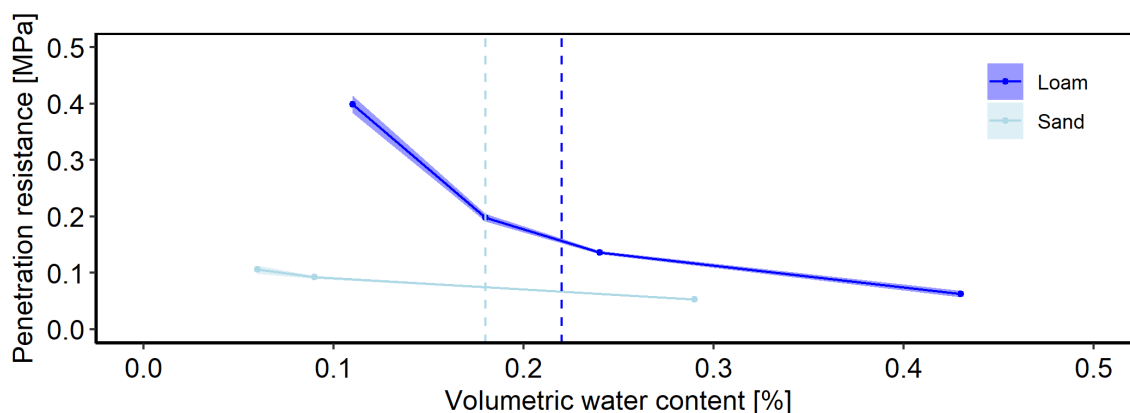
Figure AF13: Penetration resistance as a function of water content for the loam and the sand substrate packed at 1.26 and 1.50 g cm^{-3}, respectively. Data modified from Rosskopf et al. (2021). The vertical dashed lines depicts the average volumetric water content which was maintained during the course of the column experiments, for loam and sand.
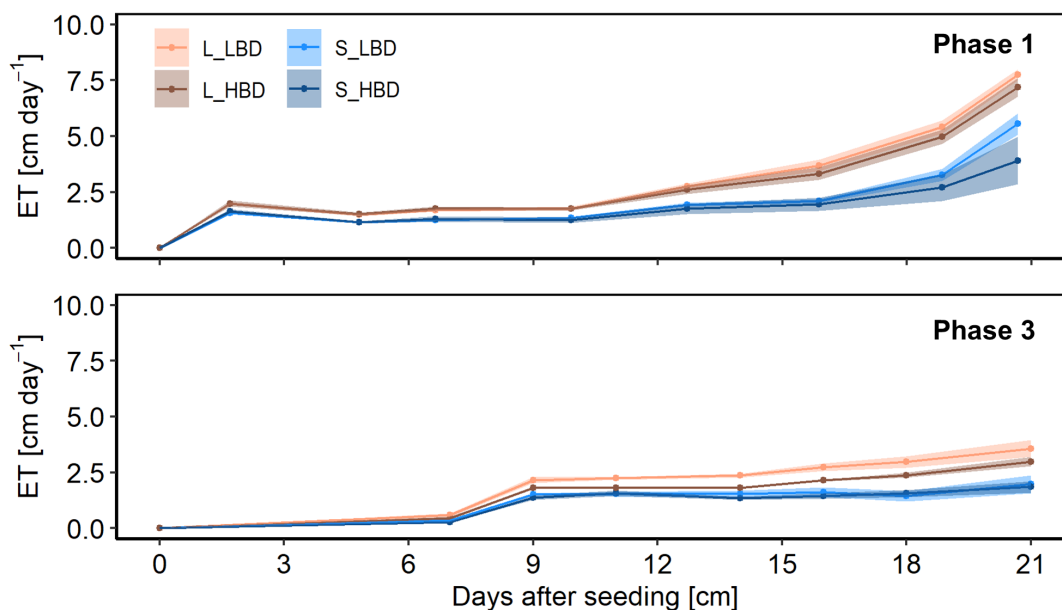
Figure AF14: Evapotranspiration calculated during the growth experiments of phase 1 and phase 3. A time-lag of 7 days of growth was observed between the two phases, likely due to the different methods used for seed germination. The semi transparent ribbons denote the standard error around the mean of the measurements.
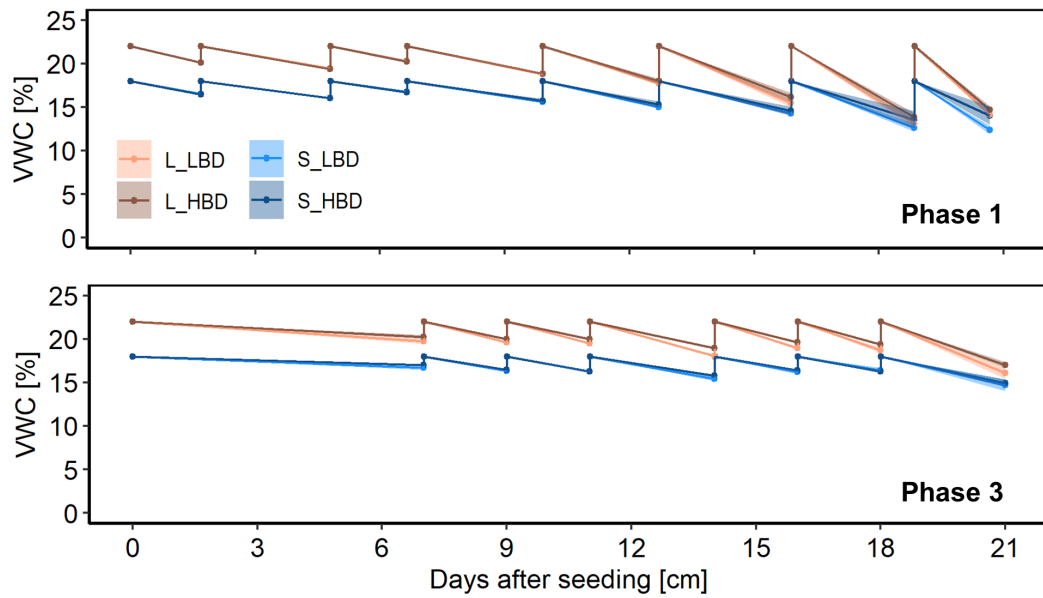
Figure AF15: Soil volumetric water content calculated during the growth experiments of phase 1 and phase 3. A time-lag of 7 days of growth was observed between the two phases, likely due to the different methods used for seed germination. The semi transparent ribbons denote the standard error around the mean of the measurements.
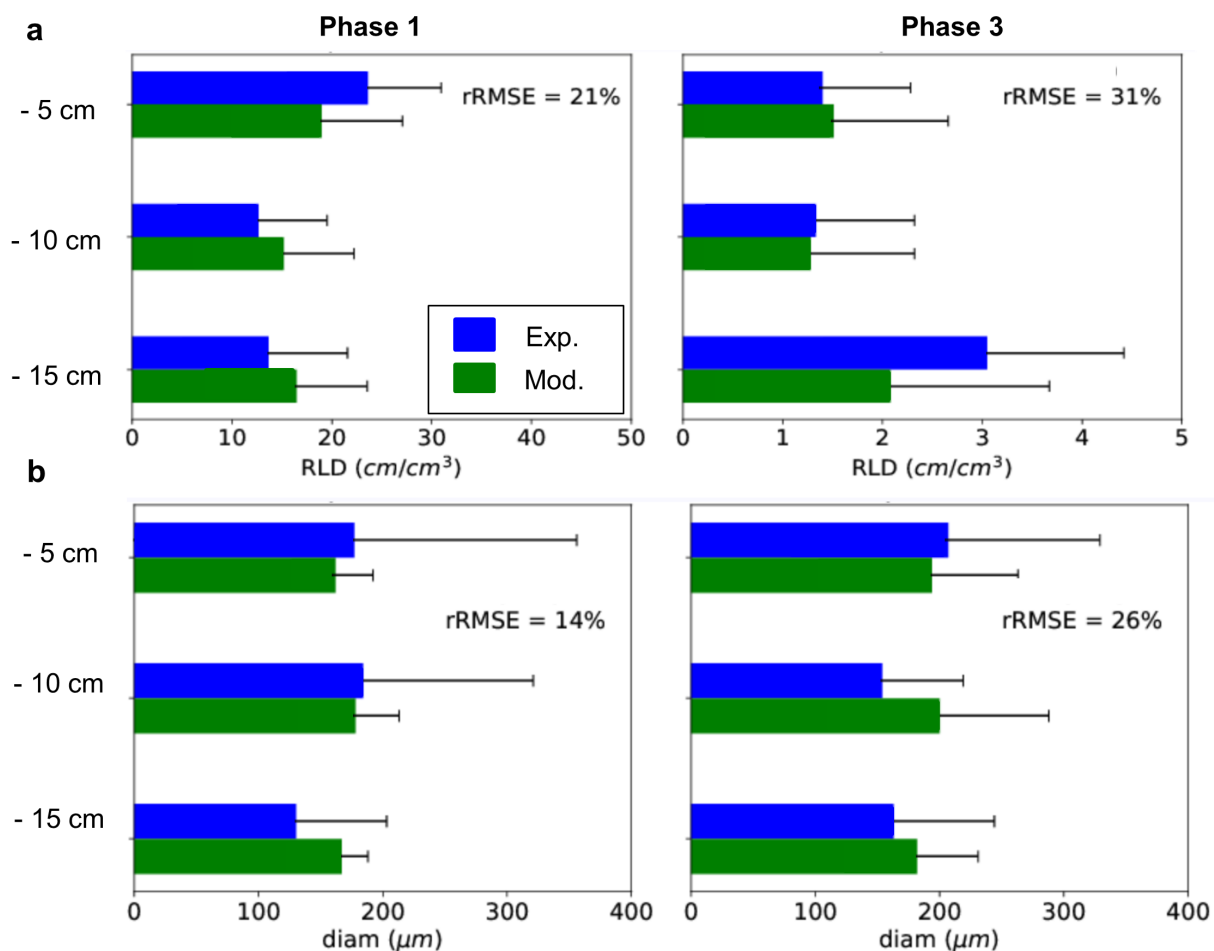
Figure AF16: Comparison between the measured (Meas.) and modeled (Mod.) values for the root length density (subfigure a) and the root diameter (subfigure b) for the cores located at 5, 10 and 15 cm depth. The error bars denote the standard deviation around the mean. The "rRMSE" notation stands for the measurement of the relative root mean square error. A relatively small rRMSE indicates a good fit of the RLD and the root diameter between the modeled data and the experimental measurements.
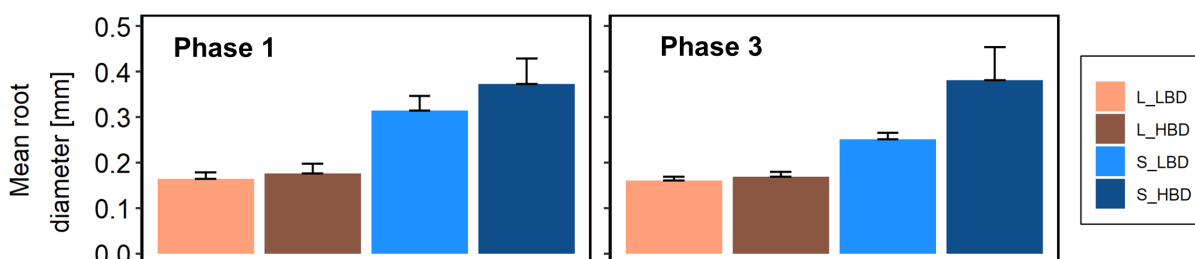
Figure AF17: Mean root diameter calculated for the phase 1 and phase 3. The error bars denote the standard error around the mean. An increase in root diameter was observed for roots growing in sand.

Table AT3: Root diameter classes, their mean diameter, standard deviation and proportion of roots defined with the experimental data set and which served as an input parameter for CPlantBox.

Phase	Diameter class	Diameter range [μm]	Mean diameter [μm]	Standard deviation [μm]	Percent of total root length [%]
	fine	[19:399]	139	66	97.04
1	intermediate	[627:1026]	818	88	1.20
	big	[1235:1634]	1425	94	1.28
	fine	[19:399]	157	76	98.38
3	intermediate	[627:1026]	786	38	0.64
	big	[1235:1634]	1322	21	0.08

Appendix for chapter 7

The necessary operation in order to include a "distance to the closest root" criterion in the false negatives recovery step are the following:

1. Computing the euclidian distance transform on the connected root system image;

2. Assigning a label to each unconnected object;

3. Creating a RGB composite image containing the root distance maps of the connected root system (channel R), the labels of each unconnected object (channel G) and the mask (channel B);

4. For each slice of the RGB image, initiating a loop on the X-Y voxels and retrieving the minimum distance to the closest connected root of each unconnected object which is contained within the mask;

5. Adding the minimum distance information in the "Results" table generated by the "Analyze Regions 3D" function and including the minimum distance information in the "if" condition which evaluates whether the unconnected objects fulfill the defined criteria.

Note that including these steps requires the computation of the EDT of the connected root system and that this would likely add about 30 minutes of processing time of the original Rootine v.2. The following lines of code show how can those steps be directly integrated into the current version of Rootine v.2.

```
// Compute EDT on connected roots
selectWindow("Connected_roots");
run("Exact Euclidean Distance Transform (3D)");
run("Conversions...", " ");
run("8-bit");
rename("Connected_roots_EDT");

// Compute label on unconnected_roots
selectWindow("Unconnected_roots");
run("Connected Components Labeling", "connectivity=6 type=float");
rename("Unconnected_label");

// Create RGB images
run("Merge Channels...", "c1=Connected_roots_EDT c2=Unconnected_label c3=Unconnected_label c3=mask keep ignore");
rename("RGB");

// Compute minimum distance from any roots for each unconnected object
selectWindow("Unconnected_label");
Stack.getStatistics(voxelCount, mean, min, nr_unconnected_object, stdDev);
selectWindow("RGB");
getDimensions(width, height, channels, slices, frames);
distance_min=newArray(nr_unconnected_object+1);

for(i=0;i<distance_min.length;i++)
{
        distance_min[i]=256;
}
for (z = 1; z <= slices; z++) {
                setSlice(z);
        // Loop through all the rows of pixels
        for (y = 0; y < height; y++) {
        // Loop through all the columns of pixels
                for (x = 0; x < width; x++) {
                // Extract the pixel value at coordinate (x, y)
                        v = getPixel(x, y);
                EDT = (v>>16)&0xff;   // extract red byte (bits 23-17)
                unconnected_object_label = (v>>8)&0xff; // extract green byte (bits 15-8)
                mask_val = v&0xff;      // extract blue byte (bits 7-0)

                if (mask_val!=0 && unconnected_object_label !=0){
                        if(EDT < distance_min[unconnected_object_label])
                        {
                                distance_min[unconnected_object_label]= EDT;
                        }
                }
                }
```

```
    }
  }

// Compute vesselness and size criteria, create results table and tag the unconnected objects which fulfills the user defined criteria
selectWindow("Unconnected_label");
run("Analyze Regions 3D", "equivalent_ellipsoid ellipsoid_elongations surface_area_method=[Crofton (13 dirs.)] euler_connectivity=C26");
Table.rename("Unconnected_label-morpho", "Results");
for(i=0;i<nResults;i++)
{
    Rb=getResult("Elli.R3",i)/sqrt(getResult("Elli.R2",i)*getResult("Elli.R1",i));
    Ra=getResult("Elli.R2",i)/getResult("Elli.R1",i);
    setResult("Vesselness", i, exp(-Rb*Rb)*exp(-Ra*Ra));
    setResult("Distance_min", i, distance_min[i+1]);
    flag=0;
    if(getResult("Vesselness", i)> t_v && getResult("Elli.R1", i)> t_s && getResult("Distance_min", i) < t_d)
    {
        flag=255;
    }
    setResult("Flag", i, flag);
}

run("Assign Measure to Label", "results="+"Results"+" column="+"Flag"+" min=0 max=255");
run("Conversions...", "scale");
run("8-bit");
rename("false_negatives");
imageCalculator("Max create stack", "connected_roots","false_negatives"); // The false negatives are added to the connected roots.
rename("root_system");
```

BIBLIOGRAPHY

Ahkami, A. H., Allen White, R., Handakumbura, P. P. & Jansson, C. (2017). Rhizosphere engineering: Enhancing sustainable plant ecosystem productivity. *Rhizosphere*, *3*, 233-243. doi: 10.1016/j.rhisph.2017.04.012

Ahmed, M. A., Kroener, E., Holz, M., Zarebanadkouki, M. & Carminati, A. (2014). Mucilage exudation facilitates root water uptake in dry soils. *Functional Plant Biology*, *41* (11), 1129-1137. doi: 10.1071/FP13330

Ahmed, M. A., Zarebanadkouki, M., Ahmadi, K., Kroener, E., Kostka, S., Kaestner, A. & Carminati, A. (2018). Engineering rhizosphere hydraulics: Pathways to improve plant adaptation to drought. *Vadose Zone Journal*, *17* (1), 160090. doi: 10.2136/vzj2016.09.0090

Alaoui, A., Lipiec, J. & Gerke, H. (2011). A review of the changes in the soil pore system due to soil deformation: A hydrodynamic perspective. *Soil and Tillage Research*, *115-116*, 1-15. doi: 10.1016/j.still.2011.06.002

Albalasmeh, A. A. & Ghezzehei, T. A. (2014). Interplay between soil drying and root exudation in rhizosheath development. *Plant Soil*, *374* (1), 739-751. doi: 10.1007/s11104-013-1910-y

Anderson, T., Starmer, W. & Thorne, M. (2007). Bimodal root diameter distributions in serengeti grasses exhibit plasticity in response to defoliation and soil texture: implications for nitrogen uptake. *Functional Ecology*, 50–60.

Angst, G., Pokorný, J., Mueller, C. W., Prater, I., Preusser, S., Kandeler, E., . . . Angst, r. (2021). Soil texture affects the coupling of litter decomposition and soil organic matter formation. *Soil Biology and Biochemistry*, *159*, 108302. doi: 10.1016/j.soilbio.2021.108302

Aravena, J. E., Berli, M., Ghezzehei, T. A. & Tyler, S. W. (2011). Effects of root-induced compaction on rhizosphere hydraulic properties-x-ray microtomography imaging and numerical simulations. *Environ Sci Technol*, *45* (2), 425-431. doi: 10.1021/es102566j

Aravena, J. E., Berli, M., Ruiz, S., Suárez, F., Ghezzehei, T. A. & Tyler, S. W. (2014). Quantifying coupled deformation and water flow in the rhizosphere using x-ray microtomography and numerical simulations. *Plant Soil*, *376* (1-2), 95-110. doi: 10.1007/s11104-013-1946-z

Arganda-Carreras, I., Kaynig, V., Rueden, C., Eliceiri, K. W., Schindelin, J., Cardona, A. & Sebastian Seung, H. (2017). Trainable Weka Segmentation: a machine

learning tool for microscopy pixel classification. *Bioinformatics*, *33* (15), 2424-2426. doi: 10.1093/bioinformatics/btx180

Assouline, S. (2006a). Modeling the relationship between soil bulk density and the hydraulic conductivity function. *Vadose Zone Journal*, *5* (2), 697-705. doi: 10.2136/vzj2005.0084

Assouline, S. (2006b). Modeling the relationship between soil bulk density and the water retention curve. *Vadose Zone Journal*, *5* (2), 554-563. doi: 10.2136/vzj2005.0083

Athmann, M., Kautz, T., Huang, N. & Köpke, U. (2014). Biopore characterization with in situ endoscopy: Influence of earthworms on carbon and nitrogen contents. *Building Organic Bridges*, *2*, 415-418. doi: 10.3220/REP_20_1_2014

Athmann, M., Kautz, T., Pude, R. & Köpke, U. (2013). Root growth in biopores—evaluation with in situ endoscopy. *Plant Soil*, *371* (1), 179-190. doi: 10.1007/s11104-013-1673-5

Atwell, B. (1993). Response of roots to mechanical impedance. *Environmental and Experimental Botany*, *33* (1), 27–40. doi: 10.1016/0098-8472(93)90053-I

Bailey, P. H., Currey, J. & Fitter, A. (2002). The role of root system architecture and root hairs in promoting anchorage against uprooting forces in allium cepa and root mutants of arabidopsis thaliana. *Journal of Experimental Botany*, *53* (367), 333-340. doi: 10.1093/jexbot/53.367.333

Baluška, F., Brailsford, R. W., Hauskrecht, M., Jackson, M. B. & Barlow, P. W. (1993). Cellular dimorphism in the maize root cortex: Involvement of microtubules, ethylene and gibberellin in the differentiation of cellular behaviour in postmitotic growth zones. *Botanica Acta*, *106* (5), 394-403. doi: 10.1111/j.1438-8677.1993.tb00766.x

Banfield, C. C., Zarebanadkouki, M., Kopka, B. & Kuzyakov, Y. (2017). Labelling plants in the chernobyl way: A new 137cs and 14c foliar application approach to investigate rhizodeposition and biopore reuse. *Plant Soil*, *417* (1), 301-315. doi: 10.1007/s11104-017-3260-7

Barej, J. A. M., Pätzold, S., Perkons, U. & Amelung, W. (2014). Phosphorus fractions in bulk subsoil and its biopore systems. *European Journal of Soil Science*, *65* (4), 553-561. doi: 10.1111/ejss.12124

Barley, K. S. S. (1954). Effects of root growth and decay on the permeability of a synthetic sandy loam. *Soil Science*, *78* (3), 205-210.

Bates, D., Mächler, M., Bolker, B. & Walker, S. (2015). Fitting linear mixed-effects models using lme4. *Journal of Statistical Software*, *67* (1), 1–48. doi: 10.18637/jss.v067.i01

Bates, T. & Lynch, J. P. (1996). Stimulation of root hair elongation in arabidopsis thaliana by low phosphorus availability. *Plant, Cell & Environment*, *19* (5), 529-538. doi: 10.1111/j.1365-3040.1996.tb00386.x

Bates, T. & Lynch, J. P. (2001). Root hairs confer a competitive advantage under low phosphorus availability. *Plant Soil*, *236* (2), 243-250. doi: 10.1023/A:1012791706800

Bauke, S. L., Landl, M., Koch, M., Hofmann, D., Nagel, K. A., Siebers, N., ... Amelung, W. (2017). Macropore effects on phosphorus acquisition by wheat roots – a rhizotron study. *Plant Soil*, *416* (1), 67-82. doi: 10.1007/s11104-017-3194-0

Beck, E., Fußeder, A. & Kraus, M. (1989). The maize root system in situ: Evaluation of structure and capability of utilization of phytate and inorganic soil phosphates. *Zeitschrift für Pflanzenernährung und Bodenkunde*, *152* (2), 159-167. doi: 10.1002/jpln.19891520205

Bengough, A. G., Bransby, M. F., Hans, J., McKenna, S. J., Roberts, T. J. & Valentine, T. A. (2006). Root responses to soil physical conditions; growth dynamics from field to cell. *Journal of Experimental Botany*, *57* (2), 437-447. doi: 10.1093/jxb/erj003

Bengough, A. G., Loades, K. & McKenzie, B. M. (2016). Root hairs aid soil penetration by anchoring the root surface to pore walls. *Journal of Experimental Botany*, *67* (4), 1071-1078. doi: 10.1093/jxb/erv560

Bengough, A. G., McKenzie, B., Hallett, P. & Valentine, T. (2011). Root elongation, water stress, and mechanical impedance: a review of limiting stresses and beneficial root tip traits. *Journal of Experimental Botany*, *62* (1), 59–68. doi: 10.1093/jxb/erq350

Bengough, A. G. & Mullins, C. E. (1990). Mechanical impedance to root growth: a review of experimental techniques and root growth responses. *Journal of Soil Science*, *41* (3), 341-358. doi: 10.1111/j.1365-2389.1990.tb00070.x

Berg, S., Kutra, D., Kroeger, T., Straehle, C. N., Kausler, B. X., Haubold, C., . . . Kreshuk, A. (2019, September). ilastik: interactive machine learning for (bio)image analysis. *Nature Methods*. doi: 10.1038/s41592-019-0582-9

Bergmann, W. (1986). *Farbatlas ernährungsstörungen bei kulturpflanzen: visuelle und analytische diagnose*. Spektrum Akademischer Verlag.

Biot, E., Crowell, E., Hofte, H., Maurin, Y., Vernhettes, S. & Andrey, P. (2008). A new filter for spot extraction in n-dimensional biological imaging. In *2008 5th ieee international symposium on biomedical imaging: From nano to macro* (S. 975-978). IEEE. doi: 10.1109/ISBI.2008.4541161

Blaser, S. R., Koebernick, N., Spott, O., Thiel, E. & Vetterlein, D. (2020). Dynamics of localised nitrogen supply and relevance for root growth of vicia faba ("fuego") and hordeum vulgare ("marthe") in soil. *Sci Rep*, *10* (1), 1-16. doi: 10.1038/s41598-020-72140-1

Blaser, S. R., Schlüter, S. & Vetterlein, D. (2018). How much is too much? influence of x-ray dose on root growth of faba bean (vicia faba) and barley (hordeum vulgare). *PloS one*, *13* (3), e0193669. doi: 10.1371/journal.pone.01936690

Bleiholder, H., Weber, E., Lancashire, P., Feller, C., Buhr, L., Hess, M., . . . Klose, R. (2001). Growth stages of mono-and dicotyledonous plants, bbch monograph. *Federal Biological Research Centre for Agriculture and Forestry, Berlin/Braunschweig, Germany*, *158*.

Borowik, A. & Wyszkowska, J. (2016). Soil moisture as a factor affecting the microbiological and biochemical activity of soil. *Plant, Soil and Environment*, *62* (6), 250-255. doi: 10.17221/158/2016-PSE

Bravin, M., Tentscher, P., Rose, J. & Hinsinger, P. (2009). Rhizosphere ph gradient controls copper availability in a strongly acidic soil. *Environmental Science & Technology*, *43* (15), 5686–5691. doi: 10.1021/es900055k

Bresler, E. (1973). Simultaneous transport of solutes and water under transient unsaturated flow conditions. *Water Resources Research*, *9* (4), 975-986. doi: 10.1029/WR009i004p00975

Bruand, A., Cousin, I., Nicoullaud, B., Duval, O. & Begon, J. C. (1996). Backscattered electron scanning images of soil porosity for analyzing soil compaction around roots. *Soil Science Society of America Journal*, *60* (3), 895-901. doi: 10.2136/sssaj1996.03615995006000030031x

Burr-Hersey, J. E., Ritz, K., Bengough, G. A. & Mooney, S. J. (2020). Reorganisation of rhizosphere soil pore structure by wild plant species in compacted soils. *Journal of Experimental Botany*, *71* (19), 6107-6115. doi: 10.1093/jxb/eraa323

Cai, G., Vanderborght, J., Couvreur, V., Mboh, C. M. & Vereecken, H. (2018). Parameterization of root water uptake models considering dynamic root distributions and water uptake compensation. *Vadose Zone Journal*, *17* (1), 160125. doi: 10.2136/vzj2016.12.0125

Canny, J. (1986). A computational approach to edge detection. *IEEE Transactions on pattern analysis and machine intelligence*, 679-698. doi: 10.1109/TPAMI.1986.4767851

Carman, P. (1997). Fluid flow through granular beds. *Chemical Engineering Research and Design*, *75*, S32-S48. doi: 10.1016/S0263-8762(97)80003-2

Carminati, A. (2013). Rhizosphere wettability decreases with root age: a problem or a strategy to increase water uptake of young roots? *Frontiers in Plant Science*, *4* (298). doi: 10.3389/fpls.2013.00298

Carminati, A., Kaestner, A., Lehmann, P. & Flühler, H. (2008). Unsaturated water flow across soil aggregate contacts. *Advances in Water Resources*, *31* (9), 1221-1232. doi: 10.1016/j.advwatres.2008.01.008

Carminati, A., Kroener, E., Ahmed, M. A., Zarebanadkouki, M., Holz, M. & Ghezzehei, T. (2016). Water for carbon, carbon for water. *Vadose Zone Journal*, *15* (2), vzj2015.04.0060. doi: 10.2136/vzj2015.04.0060

Carminati, A., Moradi, A. B., Vetterlein, D., Vontobel, P., Lehmann, E., Weller, U., ... Oswald, S. E. (2010). Dynamics of soil water content in the rhizosphere. *Plant Soil*, *332* (1), 163-176. doi: 10.1007/s11104-010-0283-8

Carminati, A., Passioura, J. B., Zarebanadkouki, M., Ahmed, M. A., Ryan, P. R., Watt, M. & Delhaize, E. (2017). Root hairs enable high transpiration rates in drying soils. *New Phytologist*, *216* (3), 771-781. doi: 10.1111/nph.14715

Carminati, A. & Vetterlein, D. (2012). Plasticity of rhizosphere hydraulic properties as a key for efficient utilization of scarce resources. *Annals of Botany*, *112* (2), 277-290. doi: 10.1093/aob/mcs262

Carminati, A., Vetterlein, D., Koebernick, N., Blaser, S., Weller, U. & Vogel, H.-J. (2013). Do roots mind the gap? *Plant Soil*, *367* (1), 651-661. doi: 10.1007/s11104-012-1496-9

Carminati, A., Vetterlein, D., Weller, U., Vogel, H.-J. & Oswald, S. E. (2009). When roots lose contact. *Vadose Zone Journal*, *8* (3), 805-809. doi: 10.2136/vzj2008.0147

Carminati, A., Zarebanadkouki, M., Kroener, E., Ahmed, M. A. & Holz, M. (2016). Biophysical rhizosphere processes affecting root water uptake. *Annals of Botany*, *118* (4), 561-571. doi: 10.1093/aob/mcw113

Chaboud, A. (1983). Isolation, purification and chemical composition of maize root cap slime. *Plant Soil*, *73* (3), 395-402. doi: 10.1007/BF02184316

Cheik, S., Jouquet, P., Maeght, J.-L., Capowiez, Y., Tran, T. & Bottinelli, N. (2021). X-ray tomography analysis of soil biopores structure under wetting and drying

cycles. *European Journal of Soil Science*, *72* (5), 2128-2132. doi: 10.1111/e-jss.13119

Chou, H., Wu, L., Zeng, L. & Chang, A. (2012). Evaluation of solute diffusion tortuosity factor models for variously saturated soils. *Water Resources Research*, *48* (10). doi: 10.1029/2011WR011653

Clark, L., Whalley, W. & Barraclough, P. (2003). How do roots penetrate strong soil? In *Roots: The dynamic interface between plants and the earth* (S. 93–104). Springer. doi: 10.1007/978-94-017-2923-9_10

Cnudde, V. & Boone, M. (2013). High-resolution x-ray computed tomography in geosciences: A review of the current technology and applications. *Earth-Science Reviews*, *123*, 1-17. doi: 10.1016/j.earscirev.2013.04.003

Colombi, T., Torres, L. C., Walter, A. & Keller, T. (2018). Feedbacks between soil penetration resistance, root architecture and water uptake limit water accessibility and crop growth – a vicious circle. *Science of The Total Environment*, *626*, 1026-1035. doi: 10.1016/j.scitotenv.2018.01.129

Colombi, T. & Walter, A. (2016). Root responses of triticale and soybean to soil compaction in the field are reproducible under controlled conditions. *Functional Plant Biology*, *43* (2), 114-128. doi: 10.1071/FP15194

Correa, J., Postma, J. A., Watt, M. & Wojciechowski, T. (2019). Soil compaction and the architectural plasticity of root systems. *Journal of Experimental Botany*, *70* (21), 6019-6034. doi: 10.1093/jxb/erz383

Crawford, R. M. M. (1992). Oxygen availability as an ecological limit to plant distribution. In M. Begon & A. H. Fitter (Hrsg.), *Advances in ecological research* (Bd. 23, S. 93-185). Academic Press. doi: 10.1016/S0065-2504(08)60147-6

Daly, K. R., Mooney, S. J., Bennett, M. J., Crout, N. M., Roose, T. & Tracy, S. (2015). Assessing the influence of the rhizosphere on soil hydraulic properties using x-ray computed tomography and numerical modelling. *Journal of Experimental Botany*, *66* (8), 2305-2314. doi: 10.1093/jxb/eru509

de Dorlodot, S., Forster, B., Pagès, L., Price, A., Tuberosa, R. & Draye, X. (2007). Root system architecture: opportunities and constraints for genetic improvement of crops. *Trends in Plant Science*, *12* (10), 474-481. doi: 10.1016/j.tplants.2007.08.012

Dexter, A. R. (1986). Model experiments on the behaviour of roots at the interface between a tilled seed-bed and a compacted sub-soil. *Plant Soil*, *95* (1), 149-161. doi: 10.1007/BF02378860

Dexter, A. R. (1987). Compression of soil around roots. *Plant Soil*, *97* (3), 401-406. doi: 10.1007/BF02383230

Dodd, I. C. & Diatloff, E. (2016). Enhanced root growth of the brb (bald root barley) mutant in drying soil allows similar shoot physiological responses to soil water deficit as wild-type plants. *Functional Plant Biology*, *43* (2), 199-206.

Dohnal, M., Dušek, J., Vogel, T., Císlerová, M., Lichner, u. & Štekauerová, V. (2009). Ponded infiltration into soil with biopores — field experiment and modeling. *Biologia*, *64* (3), 580-584. doi: 10.2478/s11756-009-0078-7

Douarre, C., Schielein, R., Frindel, C., Gerth, S. & Rousseau, D. (2018). Transfer learning from synthetic data applied to soil–root segmentation in x-ray tomography images. *Journal of Imaging*, *4* (5), 65. doi: 10.3390/jimaging4050065

Doube, M., Kłosowski, M. M., Arganda-Carreras, I., Cordelières, F. P., Dougherty, R. P., Jackson, J. S., ... Shefelbine, S. J. (2010). Bonej: free and extensible bone image analysis in imagej. *Bone*, *47* (6), 1076-1079. doi: 10.1016/j.bone.2010.08.023

Doussan, C., Pagès, L. & Pierret, A. (2003). Soil exploration and resource acquisition by plant roots: an architectural and modelling point of view. *Agronomie*, *23* (5-6), 419-431. doi: 10.1051/agro:2003027

Dresemann, T., Athmann, M., Heringer, L. & Kautz, T. (2018). Effects of continuous vertical soil pores on root and shoot growth of winter wheat: a microcosm study. *Agricultural Sciences*, *9* (6), 750-764. doi: 10.4236/as.2018.96053

Dreyer, J. & Edelmann, H. G. (2018). Root cap-mediated evaluation of soil resistance towards graviresponding roots of maize (zea mays l.) and the relevance of ethylene. *Annals of Botany*, *122* (5), 791-800. doi: 10.1093/aob/mcx209

Edwards, C. A. & Lofty, J. R. (1980). Effects of earthworm inoculation upon the root growth of direct drilled cereals. *Journal of Applied Ecology*, *17* (3), 533-543. doi: 10.2307/2402635

Ehlers, W. (1975). Observations on earthworn channels and infiltration on tilled and untilled loess soil. *Soil Science*, *119* (3). doi: 10.1097/00010694-197503000-00010

Fåhraeus, G. (1957). The infection of clover root hairs by nodule bacteria studied by a simple glass slide technique. *Microbiology*, *16* (2), 374-381. doi: 10.1099/00221287-16-2-374

Filleur, S., Walch-Liu, P., Gan, Y. & Forde, B. G. (2005). Nitrate and glutamate sensing by plant roots. *Biochemical Society Transactions*, *33* (1), 283-286. doi: 10.1042/BST0330283

Fischer, W. R., Flessa, H. & Schaller, G. (1989). ph values and redox potentials in microsites of the rhizosphere. *Journal of Plant Nutrition and Soil Science*, *152*, 191-195. doi: 10.1002/JPLN.19891520209

Flavel, R. J., Guppy, C. N., Rabbi, S. M. & Young, I. M. (2017). An image processing and analysis tool for identifying and analysing complex plant root systems in 3d soil using non-destructive analysis: Root1. *PloS one*, *12* (5), e0176433. doi: 10.1371/journal.pone.0176433

Flavel, R. J., Guppy, C. N., Tighe, M., Watt, M., McNeill, A. & Young, I. M. (2012, 01). Non-destructive quantification of cereal roots in soil using high-resolution x-ray tomography. *Journal of Experimental Botany*, *63* (7), 2503-2511. doi: 10.1093/jxb/err421

Fletcher, R. (2013). *Practical methods of optimization*. John Wiley & Sons.

Fox, J. & Weisberg, S. (2019). *An R companion to applied regression* (Third Aufl.). Thousand Oaks CA: Sage.

Frangi, A. F., Niessen, W. J., Vincken, K. L. & Viergever, M. A. (1998). Multiscale vessel enhancement filtering. In W. M. Wells, A. Colchester & S. Delp (Hrsg.), *Medical image computing and computer-assisted intervention — miccai'98* (S. 130–137). Berlin, Heidelberg: Springer Berlin Heidelberg. doi: 10.1007/BFb0056195

Fransen, B., de Kroon, H. & Berendse, F. (1998). Root morphological plasticity and nutrient acquisition of perennial grass species from habitats of different nutrient availability. *Oecologia*, *115* (3), 351–358. doi: 10.1007/s004420050527

Gahoonia, T. S. & Nielsen, N. E. (1991). A method to study rhizosphere processes in thin soil layers of different proximity to roots. *Plant Soil*, *135* (1), 143–146. doi: 10.1007/BF00014787

Ganther, M., Vetterlein, D., Heintz-Buschart, A. & Tarkka, M. T. (2021). Transcriptome sequencing analysis of maize roots reveals the effects of substrate and root hair formation in a spatial context. *Plant Soil*. doi: 10.1007/s11104-021-04921-0

Ganther, M., Yim, B., Ibrahim, Z., Bienert, M. D., Lippold, E., Maccario, L., . . . Tarkka, M. T. (2020). Compatibility of x-ray computed tomography with plant gene expression, rhizosphere bacterial communities and enzyme activities. *Journal of Experimental Botany*, *71* (18), 5603-5614. doi: 10.1093/jxb/eraa262

Gao, W., Blaser, S. R. G. A., Schlüter, S., Shen, J. & Vetterlein, D. (2019). Effect of localised phosphorus application on root growth and soil nutrient dynamics in situ – comparison of maize (zea mays) and faba bean (vicia faba) at the seedling stage. *Plant Soil*, *441* (1), 469-483. doi: 10.1007/s11104-019-04138-2

Gao, W., Schlüter, S., Blaser, S. R., Shen, J. & Vetterlein, D. (2019). A shape-based method for automatic and rapid segmentation of roots in soil from x-ray computed tomography images: Rootine. *Plant Soil*, *441* (1-2), 643-655. doi: 10.1007/s11104-019-04053-6

Gardner, W. R. (1960). Dynamic aspect of water availibility to plants. *Soil Science*, *89* (2), 63-73.

Gerth, S., Claußen, J., Eggert, A., Wörlein, N., Waininger, M., Wittenberg, T. & Uhlmann, N. (2021). Semiautomated 3d root segmentation and evaluation based on x-ray ct imagery. *Plant Phenomics*, *2021*, 8747930. doi: 10.34133/2021/8747930

Ghezzehei, T. A. & Albalasmeh, A. A. (2015). Spatial distribution of rhizodeposits provides built-in water potential gradient in the rhizosphere. *Ecological Modelling*, *298*, 53-63. doi: 10.1016/j.ecolmodel.2014.10.028

Gijsman, A. J., Alarcón, H. F. & Thomas, R. J. (1997). Root decomposition in tropical grasses and legumes, as affected by soil texture and season. *Soil Biology and Biochemistry*, *29* (9), 1443-1450. doi: 10.1016/S0038-0717(97)00039-4

Gliński, J. & Lipiec, J. (2018). *Soil physical conditions and plant roots*. CRC press. doi: 10.1201/9781351076708

Gregory, P. J. (2008). *Plant roots: growth, activity and interactions with the soil*. John Wiley & Sons.

Ågren, G. I. & Weih, M. (2012). Plant stoichiometry at different scales: element concentration patterns reflect environment more than genotype. *New Phytologist*, *194* (4), 944-952. doi: 10.1111/j.1469-8137.2012.04114.x

Gribbe, S., Blume-Werry, G. & Couwenberg, J. (2020). Digital, three-dimensional visualization of root systems in peat. *Soil Systems*, *4* (1). Zugriff auf `https://www.mdpi.com/2571-8789/4/1/13` doi: 10.3390/soilsystems4010013

Grierson, C., Nielsen, E., Ketelaarc, T. & Schiefelbein, J. (2014). Root hairs. *The Arabidopsis Book/American Society of Plant Biologists*, *12*. doi: 10.1199/tab.0172

Guo, Z., Sun, Z., Zhang, N., Ding, M. & Cao, X. (2017). Radial porosity peak at the centerline of packed beds with small tube to particle diameter ratios. *Powder Technology*, *319*, 445-451. doi: 10.1016/j.powtec.2017.06.061

Hagedorn, F. & Bundt, M. (2002). The age of preferential flow paths. *Geoderma*, *108* (1), 119-132. doi: 10.1016/S0016-7061(02)00129-5

Haling, R. E., Brown, L. K., Bengough, A. G., Valentine, T. A., White, P. J., Young, I. M. & George, T. S. (2014). Root hair length and rhizosheath mass depend on soil porosity, strength and water content in barley genotypes. *Planta*, *239* (3), 643–651. doi: 10.1007/s00425-013-2002-1

Haling, R. E., Brown, L. K., Bengough, A. G., Young, I. M., Hallett, P. D., White, P. J. & George, T. S. (2013). Root hairs improve root penetration, root–soil contact, and phosphorus acquisition in soils of different strength. *Journal of Experimental Botany*, *64* (12), 3711-3721. doi: 10.1093/jxb/ert200

Haling, R. E., Tighe, M. K., Flavel, R. J. & Young, I. M. (2013). Application of x-ray computed tomography to quantify fresh root decomposition in situ. *Plant Soil*, *372* (1), 619–627. doi: 10.1007/s11104-013-1777-y

Han, E., Kautz, T., Huang, N. & Köpke, U. (2017). Dynamics of plant nutrient uptake as affected by biopore-associated root growth in arable subsoil. *Plant Soil*, *415* (1), 145-160. doi: 10.1007/s11104-016-3150-4

Han, E., Kautz, T., Perkons, U., Uteau, D., Peth, S., Huang, N., . . . Köpke, U. (2015). Root growth dynamics inside and outside of soil biopores as affected by crop sequence determined with the profile wall method. *Biology and Fertility of Soils*, *51* (7), 847-856. doi: 10.1007/s00374-015-1032-1

Hartman, S. (2020). Trapped in the rhizosheath: Root-bacterial interactions modulate ethylene signaling. *Plant Physiology*, *183* (2), 443-444. doi: 10.1104/pp.20.00379

Hartmann, A., Rothballer, M. & Schmid, M. (2008). Lorenz hiltner, a pioneer in rhizosphere microbial ecology and soil bacteriology research. *Plant Soil*, *312* (1), 7–14. doi: 10.1007/s11104-007-9514-z

Haupenthal, A., Brax, M., Bentz, J., Jungkunst, H. F., Schützenmeister, K. & Kroener, E. (2021). Plants control soil gas exchanges possibly via mucilage. *Journal of Plant Nutrition and Soil Science*, *184* (3), 320-328. doi: 10.1002/jpln.202000496

Helliwell, J. R., Sturrock, C. J., Mairhofer, S., Craigon, J., Ashton, R., Miller, A., . . . Mooney, S. J. (2017). The emergent rhizosphere: imaging the development of the porous architecture at the root-soil interface. *Sci Rep*, *7*. doi: 10.1038/s41598-017-14904-w

Helliwell, J. R., Sturrock, C. J., Miller, A. J., Whalley, W. R. & Mooney, S. J. (2019). The role of plant species and soil condition in the structural development of the rhizosphere. *Plant, Cell & Environment*, *42* (6), 1974-1986. doi: 10.1111/pce.13529

Hendriks, L., Claassen, N. & Jungk, A. (1981). Phosphate-depletion at the soil-root interface and the phosphate-uptake of maize and rape. *Zeitschrift Fur Pflanzenernahrung Und Bodenkunde*, *144* (5), 486-499. doi: 10.1002/jpln.19811440507

Hensen, V. (1892). Die wurzeln in den tieferen bodenschichten. *Jahrbuch der Deutschen Landwirtschafts-Gesellschaft*, *7*, 84-96.

Hernanz, J. L., Peixoto, H., Cerisola, C. & Sánchez-Girón, V. (2000). An empirical model to predict soil bulk density profiles in field conditions using penetration resistance, moisture content and soil depth. *Journal of Terramechanics*, *37* (4), 167-184. doi: 10.1016/S0022-4898(99)00020-8

Hinsinger, P., Bengough, A. G., Vetterlein, D. & Young, I. M. (2009). Rhizosphere: biophysics, biogeochemistry and ecological relevance. *Plant Soil*, *321* (1-2), 117-152. doi: 10.1007/s11104-008-9885-9

Hirth, J. R., McKenzie, B. M. & Tisdall, J. M. (2005). Ability of seedling roots of lolium perenne l. to penetrate soil from artificial biopores is modified by soil bulk density, biopore angle and biopore relief. *Plant Soil*, *272* (1), 327-336. doi: 10.1007/s11104-004-5764-1

Hochholdinger, F., Wen, T., Zimmermann, R., Chimot-Marolle, P., Da Costa e Silva, O., Bruce, W., ... Schnable, P. S. (2008). The maize (zea mays l.) roothairless3 gene encodes a putative gpi-anchored, monocot-specific, cobra-like protein that significantly affects grain yield. *The Plant Journal*, *54* (5), 888-898. doi: 10.1111/j.1365-313X.2008.03459.x

Hodge, A. (2004). The plastic plant: root responses to heterogeneous supplies of nutrients. *New Phytologist*, *162* (1), 9-24. doi: 10.1111/j.1469-8137.2004.01015.x

Hodge, A. (2006). Plastic plants and patchy soils. *Journal of Experimental Botany*, *57* (2), 401-411. doi: 10.1093/jxb/eri280

Hoffmann, C. & Jungk, A. (1995). Growth and phosphorus supply of sugar beet as affected by soil compaction and water tension. *Plant Soil*, *176* (1), 15–25. doi: 10.1007/BF00017671

Holz, M., Leue, M., Ahmed, M. A., Benard, P., Gerke, H. H. & Carminati, A. (2018). Spatial distribution of mucilage in the rhizosphere measured with infrared spectroscopy. *Frontiers in Environmental Science*, *6* (87). doi: 10.3389/fenvs.2018.00087

Holz, M., Zarebanadkouki, M., Kaestner, A., Kuzyakov, Y. & Carminati, A. (2018). Rhizodeposition under drought is controlled by root growth rate and rhizosphere water content. *Plant Soil*, *423* (1), 429-442. doi: 10.1007/s11104-017-3522-4

Hothorn, T., Bretz, F. & Westfall, P. (2008). Simultaneous inference in general parametric models. *Biometrical Journal*, *50* (3), 346–363. doi: 10.1002/bimj.200810425

Iijima, M., Sako, Y. & Rao, T. (2003). A new approach for the quantification of root-cap mucilage exudation in the soil. In *Roots: The dynamic interface between plants and the earth* (S. 399-407). Springer. doi: 10.1007/978-94-017-2923-9_38

Jasechko, S., Sharp, Z. D., Gibson, J. J., Birks, S. J., Yi, Y. & Fawcett, P. J. (2013). Terrestrial water fluxes dominated by transpiration. *Nature*, *496* (7445), 347-350. doi: 10.1038/nature11983

Jawahar, C., Biswas, P. K. & Ray, A. (1997). Investigations on fuzzy thresholding based on fuzzy clustering. *Pattern Recognition*, *30* (10), 1605-1613. doi: 10.1016/S0031-3203(97)00004-6

Jobbágy, E. G. & Jackson, R. B. (2004). The uplift of soil nutrients by plants: Biogeochemical consequences across scales. *Ecology*, *85* (9), 2380-2389. doi: 10.1890/03-0245

Jones, D. L., Nguyen, C. & Finlay, R. D. (2009). Carbon flow in the rhizosphere: carbon trading at the soil–root interface. *Plant Soil*, *321* (1), 5-33. doi: 10.1007/s11104-009-9925-0

Jungk, A. (2001). Root hairs and the acquisition of plant nutrients from soil. *Journal of Plant Nutrition and Soil Science*, *164* (2), 121-129. doi: 10.1002/1522-2624(200104)164:2<121::AID-JPLN121>3.0.CO;2-6

Kandeler, E., Marschner, P., Tscherko, D., Gahoonia, T. S. & Nielsen, N. E. (2002). Microbial community composition and functional diversity in the rhizosphere of maize. *Plant Soil*, *238* (2), 301–312. doi: 10.1023/A:1014479220689

Kautz, T. (2015). Research on subsoil biopores and their functions in organically managed soils: A review. *Renewable Agriculture and Food Systems*, *30* (4), 318-327. doi: 10.1017/S1742170513000549

Kautz, T., Amelung, W., Ewert, F., Gaiser, T., Horn, R., Jahn, R., . . . Köpke, U. (2013). Nutrient acquisition from arable subsoils in temperate climates: A review. *Soil Biology and Biochemistry*, *57*, 1003-1022. doi: 10.1016/j.soilbio.2012.09.014

Kautz, T., Athmann, M. & Köpke, U. (2014). Growth of barley (hordeum vulgare l.) roots in biopores with differing carbon and nitrogen contents. *Building Organic Bridges*, *2*, 391-394. doi: 10.3220/REP_20_1_2014

Kautz, T. & Köpke, U. (2010). In situ endoscopy: New insights to root growth in biopores. *Plant Biosystems - An International Journal Dealing with all Aspects of Plant Biology*, *144* (2), 440-442. doi: 10.1080/11263501003726185

Kays, S., Nicklow, C. & Simons, D. (1974). Ethylene in relation to the response of roots to physical impedance. *Plant Soil*, *40* (3), 565–571. doi: 10.1104/pp.96.4.1171

Kim, T. K. & Silk, W. K. (1999). A mathematical model for ph patterns in the rhizospheres of growth zones. *Plant, Cell & Environment*, *22* (12), 1527-1538. doi: 10.1046/j.1365-3040.1999.00512.x

Kirby, J. & Bengough, A. (2002). Influence of soil strength on root growth: experiments and analysis using a critical-state model. *European Journal of Soil Science*, *53* (1), 119-127. doi: 10.1046/j.1365-2389.2002.00429.x

Klamer, F., Vogel, F., Li, X., Bremer, H., Neumann, G., Neuhäuser, B., . . . Ludewig, U. (2019). Estimating the importance of maize root hairs in low phosphorus conditions and under drought. *Annals of Botany*, *124* (6), 961-968. doi: 10.1093/aob/mcz011

Klein, S., Staring, M., Murphy, K., Viergever, M. A. & Pluim, J. P. (2009). Elastix: a toolbox for intensity-based medical image registration. *IEEE transactions on medical imaging*, *29* (1), 196–205. doi: 10.1109/TMI.2009.2035616

Koebernick, N., Daly, K. R., Keyes, S. D., Bengough, A. G., Brown, L. K., Cooper, L. J., . . . Raffan, A. (2019). Imaging microstructure of the barley rhizosphere: particle packing and root hair influences. *New Phytologist*, *221* (4), 1878-1889. doi: 10.1111/nph.15516

Koebernick, N., Daly, K. R., Keyes, S. D., George, T. S., Brown, L. K., Raffan, A., . . . Sinclair, I. (2017). High-resolution synchrotron imaging shows that root hairs influence rhizosphere soil structure formation. *New Phytologist*, *216* (1), 124-135. doi: 10.1111/nph.14705

Koebernick, N., Schlüter, S., Blaser, S. R. & Vetterlein, D. (2018). Root-soil contact dynamics of vicia faba in sand. *Plant Soil*, *431* (1), 417-431. doi: 10.1007/s11104-018-3769-4

Koebernick, N., Weller, U., Huber, K., Schlüter, S., Vogel, H.-J., Jahn, R., . . . Vetterlein, D. (2014). In situ visualization and quantification of three-dimensional root system architecture and growth using x-ray computed tomography. *Vadose Zone Journal*, *13* (8), 1-10. doi: 10.2136/vzj2014.03.0024

Kroener, E., Holz, M., Zarebanadkouki, M., Ahmed, M. & Carminati, A. (2018). Effects of mucilage on rhizosphere hydraulic functions depend on soil particle size. *Vadose Zone Journal*, *17* (1), 170056. doi: 10.2136/vzj2017.03.0056

Kroener, E., Zarebanadkouki, M., Bittelli, M. & Carminati, A. (2016). Simulation of root water uptake under consideration of nonequilibrium dynamics in the rhizosphere. *Water Resources Research*, *52* (8), 5755-5770. doi: 10.1002/2015WR018579

Kroener, E., Zarebanadkouki, M., Kaestner, A. & Carminati, A. (2014). Nonequilibrium water dynamics in the rhizosphere: How mucilage affects water flow in soils. *Water Resources Research*, *50* (8), 6479-6495. doi: 10.1002/2013WR014756

Kuhlmann, H., Barraclough, P. B. & Weir, A. H. (1989). Utilization of mineral nitrogen in the subsoil by winter wheat. *Zeitschrift für Pflanzenernährung und Bodenkunde*, *152* (3), 291-295. doi: 10.1002/jpln.19891520305

Kuka, K., Illerhaus, B., Fox, C. A. & Joschko, M. (2013). X-ray computed microtomography for the study of the soil–root relationship in grassland soils. *Vadose Zone Journal*, *12* (4), 1-10. doi: 10.2136/vzj2013.01.0014

Kumar, A., Shahbaz, M., Koirala, M., Blagodatskaya, E., Seidel, S. J., Kuzyakov, Y. & Pausch, J. (2019). Root trait plasticity and plant nutrient acquisition in phosphorus limited soil. *Journal of Plant Nutrition and Soil Science*, *182* (6), 945-952. doi: 10.1002/jpln.201900322

Landl, M., Phalempin, M., Schlüter, S., Vetterlein, D., Vanderborght, J., Kroener, E. & Schnepf, A. (2021). Modeling the impact of rhizosphere bulk density and mucilage gradients on root water uptake. *Frontiers in Agronomy*, *3* (6). doi: 10.3389/fagro.2021.622367

Landl, M., Schnepf, A., Uteau, D., Peth, S., Athmann, M., Kautz, T., . . . Vanderborght, J. (2019). Modeling the impact of biopores on root growth and root water uptake. *Vadose Zone Journal*, *18* (1), 180196. doi: 10.2136/vzj2018.11.0196

Legland, D., Arganda-Carreras, I. & Andrey, P. (2016). Morpholibj: integrated library and plugins for mathematical morphology with imagej. *Bioinformatics*, *32* (22), 3532-3534. doi: 10.1093/bioinformatics/btw413

Leij, F. J., Ghezzehei, T. A. & Or, D. (2002). Analytical models for soil pore-size distribution after tillage. *Soil Science Society of America Journal*, *66* (4), 1104-1114. doi: 10.2136/sssaj2002.1104

Li, T., Lin, G., Zhang, X., Chen, Y., Zhang, S. & Chen, B. (2014). Relative importance of an arbuscular mycorrhizal fungus (rhizophagus intraradices) and root hairs in plant drought tolerance. *Mycorrhiza*, *24* (8), 595-602. doi: 10.1007/s00572-014-0578-3

Lippold, E., Kleinau, P., Blaser, S. R. G. A., Schlüter, S., Phalempin, M. & Vetterlein, D. (2021). In soil measurement of radiation dose caused by x-ray computed tomography. *Journal of Plant Nutrition and Soil Science*, *184* (3), 343-345. doi: 10.1002/jpln.202000276

Lippold, E., Phalempin, M., Schlüter, S. & Vetterlein, D. (2021). Does the lack of root hairs alter root system architecture of zea mays? *Plant Soil*. doi: 10.1007/s11104-021-05084-8

Logsdon, S. & Reneau, R. (1988). Influence of storage methods on corn root length measurements. *Plant Soil*, *111* (1), 155-157. doi: 10.1007/BF02182051

Lombardi, M., De Gara, L. & Loreto, F. (2021). Determinants of root system architecture for future-ready, stress-resilient crops. *Physiologia Plantarum*, *172* (4), 2090-2097. doi: 10.1111/ppl.13439

Lucas, M., Schlüter, S., Vogel, H.-J. & Vetterlein, D. (2019). Roots compact the surrounding soil depending on the structures they encounter. *Sci Rep*, *9* (1), 1-13. doi: 10.1038/s41598-019-52665-w

Lynch, J. P. (2011). Root phenes for enhanced soil exploration and phosphorus acquisition: Tools for future crops. *Plant Physiology*, *156* (3), 1041-1049. doi: 10.1104/pp.111.175414

Lynch, J. P., Ho, M. D. & phosphorus, L. (2005). Rhizoeconomics: Carbon costs of phosphorus acquisition. *Plant Soil*, *269* (1), 45-56. doi: 10.1007/s11104-004-1096-4

Ma, B., He, S.-J., Duan, K.-X., Yin, C.-C., Chen, H., Yang, C., ... Zhang, J.-S. (2013). Identification of rice ethylene-response mutants and characterization of mhz7/osein2 in distinct ethylene response and yield trait regulation. *Molecular Plant*, *6* (6), 1830-1848. doi: 10.1093/mp/sst087

Ma, R., Cai, C., Li, Z., Wang, J., Xiao, T., Peng, G. & Yang, W. (2015). Evaluation of soil aggregate microstructure and stability under wetting and drying cycles in two ultisols using synchrotron-based x-ray micro-computed tomography. *Soil and Tillage Research*, *149*, 1-11. doi: 10.1016/j.still.2014.12.016.

Ma, Z., Bielenberg, D. G., Brown, K. M. & Lynch, J. P. (2001). Regulation of root hair density by phosphorus availability in arabidopsis thaliana. *Plant, Cell & Environment*, *24* (4), 459-467. doi: 10.1046/j.1365-3040.2001.00695.x

Machinet, G. E., Bertrand, I., Barrière, Y., Chabbert, B. & Recous, S. (2011). Impact of plant cell wall network on biodegradation in soil: Role of lignin composition and phenolic acids in roots from 16 maize genotypes. *Soil Biology and Biochemistry*, *43* (7), 1544-1552. doi: 10.1016/j.soilbio.2011.04.002

Maenhout, P., Sleutel, S., Xu, H., Van Hoorebeke, L., Cnudde, V. & De Neve, S. (2019). Semi-automated segmentation and visualization of complex undisturbed root systems with x-ray microct. *Soil and Tillage Research*, *192*, 59-65. doi: 10.1016/j.still.2019.04.025

Mai, T. H., Schnepf, A., Vereecken, H. & Vanderborght, J. (2019). Continuum multi-scale model of root water and nutrient uptake from soil with explicit consideration of the 3d root architecture and the rhizosphere gradients. *Plant Soil*, *439* (1), 273-292. doi: 10.1007/s11104-018-3890-4

Mairhofer, S., Zappala, S., Tracy, S. R., Sturrock, C., Bennett, M., Mooney, S. J. & Pridmore, T. (2012). Rootrak: Automated recovery of three-dimensional plant root architecture in soil from x-ray microcomputed tomography images using visual tracking. *Plant Physiology*, *158* (2), 561–569. doi: 10.1104/pp.111.186221

Marin, M., Feeney, D. S., Brown, L. K., Naveed, M., Ruiz, S., Koebernick, N., ... George, T. S. (2020). Significance of root hairs for plant performance under contrasting field conditions and water deficit. *Annals of Botany*. doi: 10.1093/aob/mcaa181

Mary, B., Fresneau, C., Morel, J. L. & Mariotti, A. (1993). C and n cycling during decomposition of root mucilage, roots and glucose in soil. *Soil Biology and Biochemistry*, *25* (8), 1005-1014. doi: 10.1016/0038-0717(93)90147-4

Materechera, S. A., Dexter, A. R. & Alston, A. M. (1991). Penetration of very strong soils by seedling roots of different plant species. *Plant Soil*, *135* (1), 31-41. doi: 10.1007/BF00014776

Mattupalli, C., Seethepalli, A., York, L. M. & Young, C. A. (2019). Digital imaging to evaluate root system architectural changes associated with soil biotic factors. *Phytobiomes Journal*, *3* (2), 102-111. doi: 10.1094/PBIOMES-12-18-0062-R

McCormick, M. M., Liu, X., Ibanez, L., Jomier, J. & Marion, C. (2014). Itk: enabling reproducible research and open science. *Frontiers in Neuroinformatics*, *8*, 13. doi: 10.3389/fninf.2014.00013

McCully, M. E. & Boyer, J. S. (1997). The expansion of maize root-cap mucilage during hydration. 3. changes in water potential and water content. *Physiologia Plantarum*, *99* (1), 169-177. doi: 10.1111/j.1399-3054.1997.tb03445.x

McGonigle, T. P., Miller, M. H., Evans, D. G., Fairchild, G. L. & Swan, J. A. (1990). A new method which gives an objective measure of colonization of roots by vesicular—arbuscular mycorrhizal fungi. *New Phytologist*, *115* (3), 495-501. doi: 10.1111/j.1469-8137.1990.tb00476.x

Mees, F., Swennen, R., Van Geet, M. & Jacobs, P. (2003). Applications of x-ray computed tomography in the geosciences. *Geological Society, London, Special Publications*, *215* (1), 1–6. doi: 10.1144/GSL.SP.2003.215.01.01

Menon, M., Jia, X., Lair, G., Faraj, P. & Blaud, A. (2015). Analysing the impact of compaction of soil aggregates using x-ray microtomography and water flow simulations. *Soil and Tillage Research*, *150*, 147-157. doi: 10.1016/j.still.2015.02.004

Meunier, F., Zarebanadkouki, M., Ahmed, M. A., Carminati, A., Couvreur, V. & Javaux, M. (2018). Hydraulic conductivity of soil-grown lupine and maize unbranched roots and maize root-shoot junctions. *Journal of Plant Physiology*, *227*, 31-44. doi: 10.1016/j.jplph.2017.12.019

Millington, R. & Quirk, J. (1961). Permeability of porous solids. *Transactions of the Faraday Society*, *57*, 1200-1207.

Moldrup, P., Olesen, T., Schjønning, P., Yamaguchi, T. & Rolston, D. E. (2000). Predicting the gas diffusion coefficient in undisturbed soil from soil water characteristics. *Soil Science Society of America Journal*, *64* (1), 94-100. doi: 10.2136/sssaj2000.64194x

Mollier, A. & Pellerin, S. (1999). Maize root system growth and development as influenced by phosphorus deficiency. *Journal of Experimental Botany*, *50* (333), 487-497. doi: 10.1093/jxb/50.333.487

Mooney, S. J., Pridmore, T. P., Helliwell, J. & Bennett, M. J. (2012). Developing x-ray computed tomography to non-invasively image 3-d root systems architecture in soil. *Plant Soil*, *352* (1-2), 1-22. doi: 10.1007/s11104-011-1039-9

Moradi, A. B., Carminati, A., Vetterlein, D., Vontobel, P., Lehmann, E., Weller, U., . . . Oswald, S. E. (2011). Three-dimensional visualization and quantification of water content in the rhizosphere. *New Phytologist*, *192* (3), 653-663. doi: 10.1111/j.1469-8137.2011.03826.x

Moreno-Espíndola, I. P., Rivera-Becerril, F., de Jesús Ferrara-Guerrero, M. & De León-González, F. (2007). Role of root-hairs and hyphae in adhesion of sand particles. *Soil Biology and Biochemistry*, *39* (10), 2520-2526. doi: 10.1016/j.soilbio.2007.04.021.

Morris, E. C., Griffiths, M., Golebiowska, A., Mairhofer, S., Burr-Hersey, J., Goh, T., . . . Bennett, M. J. (2017). Shaping 3d root system architecture. *Current Biology*, *27* (17), R919-R930. doi: 10.1016/j.cub.2017.06.043

Mualem, Y. (1976). A new model for predicting the hydraulic conductivity of unsaturated porous media. *Water Resources Research*, *12* (3), 513-522. doi: 10.1029/WR012i003p00513

Mueller, G. E. (2010). Radial porosity in packed beds of spheres. *Powder Technology*, *203* (3), 626-633. doi: j.powtec.2010.07.007

Nakamoto, T. (1997). The distribution of maize roots as influenced by artificial vertical macropores. *Japanese Journal of Crop Science*, *66* (2), 331-332. doi: 10.1626/jcs.66.331

Nakamoto, T. (2000). The distribution of wheat and maize roots as influenced by biopores in a subsoil of the kanto loam type. *Plant Production Science*, *3* (2), 140-144. doi: 10.1626/pps.3.140

Nelder, J. A. & Mead, R. (1965). A simplex method for function minimization. *The Computer Journal*, *7* (4), 308-313. doi: 10.1093/comjnl/7.4.308

Nguyen, C., Froux, F., Recous, S., Morvan, T. & Robin, C. (2008). Net n immobilisation during the biodegradation of mucilage in soil as affected by repeated mineral and organic fertilisation. *Nutrient Cycling in Agroecosystems*, *80* (1), 39-47. doi: 10.1007/s10705-007-9119-1

Nye, P. (1981). Changes of ph across the rhizosphere induced by roots. *Plant Soil*, *61* (1), 7–26. doi: 10.1007/BF02277359

Ollion, J., Cochennec, J., Loll, F., Escudé, C. & Boudier, T. (2013). Tango: a generic tool for high-throughput 3d image analysis for studying nuclear organization. *Bioinformatics*, *29* (14), 1840-1841. doi: 10.1093/bioinformatics/btt276

Or, D. & Ghezzehei, T. A. (2002). Modeling post-tillage soil structural dynamics: a review. *Soil and Tillage Research*, *64* (1), 41-59. doi: 10.1016/S0167-1987(01)00256-2

Or, D., Leij, F. J., Snyder, V. & Ghezzehei, T. A. (2000). Stochastic model for post-tillage soil pore space evolution. *Water Resources Research*, *36* (7), 1641-1652. doi: 10.1029/2000WR900092

Or, D., Phutane, S. & Dechesne, A. (2007). Extracellular polymeric substances affecting pore-scale hydrologic conditions for bacterial activity in unsaturated soils. *Vadose Zone Journal*, *6* (2), 298-305. doi: 10.2136/vzj2006.0080

Otsu, N. (1979). A threshold selection method from gray-level histograms. *IEEE transactions on systems, man, and cybernetics*, *9* (1), 62-66.

Pagenkemper, S. K., Athmann, M., Uteau, D., Kautz, T., Peth, S. & Horn, R. (2015). The effect of earthworm activity on soil bioporosity – investigated with x-ray computed tomography and endoscopy. *Soil and Tillage Research*, *146*, 79-88. doi: 10.1016/j.still.2014.05.007

Pandey, B. K., Huang, G., Bhosale, R., Hartman, S., Sturrock, C. J., Jose, L., . . . Bennett, M. J. (2021). Plant roots sense soil compaction through restricted ethylene diffusion. *Science*, *371* (6526), 276–280. doi: 10.1126/science.abf3013

Pankhurst, C. E., Pierret, A., Hawke, B. G. & Kirby, J. M. (2002). Microbiological and chemical properties of soil associated with macropores at different depths in a red-duplex soil in nsw australia. *Plant Soil*, *238* (1), 11-20. doi: 10.1023/A:1014289632453

Papendick, R. I. & Campbell, G. S. (1981). Theory and measurement of water potential. In *Water potential relations in soil microbiology* (S. 1-22). doi: 10.2136/sssaspecpub9.c1

Partridge, G. P., Lehman, D. M. & Huebner, R. S. (1999). Modeling the reduction of vapor phase emissions from surface soils due to soil matrix effects: Porosity/tortuosity concepts. *Journal of the Air & Waste Management Association*, *49* (4), 412-423. doi: 10.1080/10473289.1999.10463812

Passioura, J. (2002). Soil conditions and plant growth. *Plant, Cell & Environment*, *25* (2), 311–318. doi: 10.1046/j.0016-8025.2001.00802.x

Pertassek, T., Peters, A. & Durner, W. (2015). *Hyprop-fit software user's manual, v. 3.0.*

Pfeifer, J., Kirchgessner, N., Colombi, T. & Walter, A. (2015). Rapid phenotyping of crop root systems in undisturbed field soils using x-ray computed tomography. *Plant Methods*, *11* (1), 41. doi: 10.1186/s13007-015-0084-4

Phalempin, M., Lippold, E., Vetterlein, D. & Schlüter, S. (2021a). An improved method for the segmentation of roots from x-ray computed tomography 3d images: Rootine v. 2. *Plant Methods*, *17* (1), 1-19. doi: 10.1186/s13007-021-00735-4

Phalempin, M., Lippold, E., Vetterlein, D. & Schlüter, S. (2021b). Soil texture and structure heterogeneity predominantly governs bulk density gradients around roots. *Vadose Zone Journal*, e20147. doi: 10.1002/vzj2.20147

Pierret, A., Doussan, C., Capowiez, Y., Bastardie, F. & Pagès, L. (2007). Root functional architecture: A framework for modeling the interplay between roots and soil. *Vadose Zone Journal*, *6* (2), 269-281. doi: 10.2136/vzj2006.0067

Pla, C., Cuezva, S., Martinez-Martinez, J., Fernandez-Cortes, A., Garcia-Anton, E., Fusi, N., . . . Sanchez-Moral, S. (2017). Role of soil pore structure in water infiltration and co2 exchange between the atmosphere and underground air in the vadose zone: A combined laboratory and field approach. *CATENA*, *149*, 402-416. doi: 10.1016/j.catena.2016.10.018.

R Core Team. (2017). R: A language and environment for statistical computing [Software-Handbuch]. Vienna, Austria. Zugriff auf `https://www.R-project.org/`

Rasse, D. P. & Smucker, A. J. M. (1998). Root recolonization of previous root channels in corn and alfalfa rotations. *Plant Soil*, *204* (2), 203-212. doi: 10.1023/A:1004343122448

Razavi, B. S., Zarebanadkouki, M., Blagodatskaya, E. & Kuzyakov, Y. (2016). Rhizosphere shape of lentil and maize: Spatial distribution of enzyme activities. *Soil Biology and Biochemistry*, *96*, 229-237. doi: 10.1016/j.soilbio.2016.02.020

Reimann, J., Vicente, J., Brun, E., Ferrero, C., Gan, Y. & Rack, A. (2017). X-ray tomography investigations of mono-sized sphere packing structures in cylindrical containers. *Powder Technology*, *318*, 471-483. doi: 10.1016/j.powtec.2017.05.033

Rüger, L., Feng, K., Dumack, K., Freudenthal, J., Chen, Y., Sun, R., . . . Bonkowski, M. (2021). Assembly patterns of the rhizosphere microbiome along the longitudinal root axis of maize (zea mays l.). *Frontiers in Microbiology*, *12*, 237. doi: 10.3389/fmicb.2021.614501

Rich, S. M. & Watt, M. (2013, 02). Soil conditions and cereal root system architecture: review and considerations for linking Darwin and Weaver. *Journal of Experimental Botany*, *64* (5), 1193-1208. doi: 10.1093/jxb/ert043

Richardson, A. E., Hocking, P. J., Simpson, R. J. & George, T. S. (2009). Plant mechanisms to optimise access to soil phosphorus. *Crop and Pasture Science*, *60* (2), 124-143. doi: 10.1071/CP07125

Rosskopf, U., Uteau, D. & Peth, S. (2021). Effects of mucilage concentration at different water contents on mechanical stability and elasticity in a loamy and a sandy soil. *European Journal of Soil Science.* doi: 10.1111/ejss.13189

Rudolph-Mohr, N., Tötzke, C., Kardjilov, N. & Oswald, S. E. (2017). Mapping water, oxygen, and ph dynamics in the rhizosphere of young maize roots. *Journal of Plant Nutrition and Soil Science*, *180* (3), 336-346. doi: 10.1002/jpln.201600120

Rugova, A., Puschenreiter, M., Koellensperger, G. & Hann, S. (2017). Elucidating rhizosphere processes by mass spectrometry–a review. *Analytica Chimica Acta*, *956*, 1-13. doi: 10.1016/j.aca.2016.12.044

Ryan, P. R., Dessaux, Y., Thomashow, L. S. & Weller, D. M. (2009). Rhizosphere engineering and management for sustainable agriculture. *Plant Soil*, *321* (1), 363–383. doi: 10.1007/s11104-009-0001-6

Sarquis, J. I., Jordan, W. R. & Morgan, P. W. (1991). Ethylene evolution from maize (zea mays l.) seedling roots and shoots in response to mechanical impedance. *Plant Physiology*, *96* (4), 1171–1177. doi: 10.1104/pp.96.4.1171

Schindelin, J., Arganda-Carreras, I., Frise, E., Kaynig, V., Longair, M., Pietzsch, T., . . . Schmid, B. (2012). Fiji: an open-source platform for biological-image analysis. *Nat Methods*, *9* (7), 676-682. doi: 10.1038/nmeth.2019

Schjønning, P., Thomsen, I. K., Moldrup, P. & Christensen, B. T. (2003). Linking soil microbial activity to water- and air-phase contents and diffusivities. *Soil Science Society of America Journal*, *67* (1), 156-165. doi: 10.2136/sssaj2003.1560

Schlüter, S., Blaser, S. R. G. A., Weber, M., Schmidt, V. & Vetterlein, D. (2018). Quantification of root growth patterns from the soil perspective via root distance models. *Frontiers in Plant Science*, *9* (1084). doi: 10.3389/fpls.2018.01084

Schlüter, S., Sheppard, A., Brown, K. & Wildenschild, D. (2014). Image processing of multiphase images obtained via x-ray microtomography: a review. *Water Resources Research*, *50*, 3615-3639. doi: 10.1002/2014WR015256

Schlüter, S., Vogel, H.-J., Ippisch, O., Bastian, P., Roth, K., Schelle, H., . . . Vanderborght, J. (2012). Virtual soils: Assessment of the effects of soil structure on the hydraulic behavior of cultivated soils. *Vadose Zone Journal*, *11* (4), vzj2011.0174. doi: 10.2136/vzj2011.0174

Schlüter, S., Weller, U. & Vogel, H.-J. (2010). Segmentation of x-ray microtomography images of soil using gradient masks. *Computers and Geosciences*, *36* (10), 1246-1251. doi: 10.1016/j.cageo.2010.02.007

Schmidt, J. E. & Gaudin, A. C. M. (2017). Toward an integrated root ideotype for irrigated systems. *Trends in Plant Science*, *22* (5), 433-443. doi: 10.1016/j.tplants.2017.02.001

Schmidt, S., Bengough, A. G., Gregory, P. J., Grinev, D. V. & Otten, W. (2012). Estimating root-soil contact from 3d x-ray microtomographs. *European Journal of Soil Science*, *63* (6), 776–786. doi: 10.1111/j.1365-2389.2012.01487.x

Schneider, F. & Don, A. (2019). Root-restricting layers in german agricultural soils. part ii: Adaptation and melioration strategies. *Plant Soil*, *442* (1), 419-432. doi: 10.1007/s11104-019-04186-8

Schnepf, A., Leitner, D., Landl, M., Lobet, G., Mai, T. H., Morandage, S., . . . Vereecken, H. (2018). Crootbox: a structural–functional modelling framework for root systems. *Annals of Botany*, *121* (5), 1033-1053. doi: 10.1093/aob/mcx221

Schulz, H., Postma, J. A., van Dusschoten, D., Scharr, H. & Behnke, S. (2013). Plant root system analysis from mri images. In *Computer vision, imaging and computer graphics. theory and application* (S. 411-425). Springer. doi: 10.1007/978-3-642-38241-3_28

Schwartz, N., Carminati, A. & Javaux, M. (2016). The impact of mucilage on root water uptake—a numerical study. *Water Resources Research*, *52* (1), 264-277. doi: 10.1002/2015WR018150

Scott, N. A., Cole, C. V., Elliott, E. T. & Huffman, S. A. (1996). Soil textural control on decomposition and soil organic matter dynamics. *Soil Science Society of America Journal*, *60* (4), 1102–1109. doi: 10.2136/sssaj1996.03615995006000040020x

Searle, S. R., Speed, F. M. & Milliken, G. A. (1980). Population marginal means in the linear model: An alternative to least squares means. *The American Statistician*, *34* (4), 216-221. doi: 10.1080/00031305.1980.10483031

Shahzad, Z. & Amtmann, A. (2017). Food for thought: how nutrients regulate root system architecture. *Current Opinion in Plant Biology*, *39*, 80-87. doi: 10.1016/j.pbi.2017.06.008

Shamonin, D. P., Bron, E. E., Lelieveldt, B. P., Smits, M., Klein, S. & Staring, M. (2014). Fast parallel image registration on cpu and gpu for diagnostic classification of alzheimer's disease. *Frontiers in Neuroinformatics*, *7*, 50. doi: 10.3389/fninf.2013.00050

Sheppard, A. P., Sok, R. M. & Averdunk, H. (2004). Techniques for image enhancement and segmentation of tomographic images of porous materials. *Physica A: Statistical mechanics and its applications*, *339* (1-2), 145-151. doi: 10.1016/j.physa.2004.03.057

Smettem, K. R. J. & Collis-George, N. (1985). Statistical characterization of soil biopores using a soil peel method. *Geoderma*, *36* (1), 27-36. doi: 10.1016/0016-7061(85)90061-8

Smith, A. G., Petersen, J., Selvan, R. & Rasmussen, C. R. (2020). Segmentation of roots in soil with u-net. *Plant Methods*, *16* (1), 1–15. doi: 10.1186/s13007-020-0563-0

Soltaninejad, M., Sturrock, C. J., Griffiths, M., Pridmore, T. P. & Pound, M. P. (2020). Three dimensional root ct segmentation using multi-resolution encoder-decoder networks. *IEEE Transactions on Image Processing*, *29*, 6667-6679. doi: 10.1109/TIP.2020.2992893

Stange, C. F. & Horn, R. (2005). Modeling the soil water retention curve for conditions of variable porosity. *Vadose Zone Journal*, *4* (3), 602-613. doi: 10.2136/vzj2004.0150

Stewart, J. B., Moran, C. J. & Wood, J. T. (1999). Macropore sheath: quantification of plant root and soil macropore association. *Plant Soil*, *211* (1), 59-67. doi: 10.1023/A:1004405422847

Stirzaker, R., Passioura, J. & Wilms, Y. (1996). Soil structure and plant growth: impact of bulk density and biopores. *Plant Soil*, *185* (1), 151-162. doi: 10.1007/BF02257571

Stolzy, L. & Barley, K. (1968). Mechanical resistance encountered by roots entering compact soils. *Soil Science*, *105* (5), 297-301.

Suzuki, M., Shinmura, T., Iimura, K. & Hirota, M. (2008). Study of the wall effect on particle packing structure using x-ray micro computed tomography. *Advanced Powder Technology*, *19* (2), 183-195. doi: 10.1163/156855208X293817.

Suzuki, N., Taketa, S. & Ichii, M. (2003). Morphological and physiological characteristics of a root-hairless mutant in rice (oryza sativa l.). In *Roots: The dynamic interface between plants and the earth* (S. 9-17). Springer.

Tabb, A., Duncan, K. E. & Topp, C. N. (2018). Segmenting root systems in x-ray computed tomography images using level sets. In *2018 ieee winter conference on applications of computer vision (wacv)* (S. 586-595). doi: 10.1109/WACV.2018.00070

Teramoto, S., Takayasu, S., Kitomi, Y., Arai-Sanoh, Y., Tanabata, T. & Uga, Y. (2020). High-throughput three-dimensional visualization of root system architecture of rice using x-ray computed tomography. *Plant Methods*, *16*, 1-14. doi: 10.1186/s13007-020-00612-6

Tinevez, J.-Y. (2018). *The tubeness filter: enhance filamentous structures of a specified thickness [https://github.com/imagej/imagej-ops/pull/527]*. (Accessed on 18.10.2020)

Tracy, S. R., Black, C. R., Roberts, J. A. & Mooney, S. J. (2013). Exploring the interacting effect of soil texture and bulk density on root system development in tomato (solanum lycopersicum l.). *Environmental and Experimental Botany*, *91*, 38-47. doi: 0.1016/j.envexpbot.2013.03.003

Tracy, S. R., Black, C. R., Roberts, J. A., Sturrock, C., Mairhofer, S., Craigon, J. & Mooney, S. A. o. B. (2012). Quantifying the impact of soil compaction on root system architecture in tomato (solanum lycopersicum) by x-ray micro-computed tomography. *Annals of Botany*, *110* (2), 511-519. doi: 10.1093/aob/mcs031

Tristán-Vega, A., García-Pérez, V., Aja-Fernández, S. & Westin, C.-F. (2012). Efficient and robust nonlocal means denoising of mr data based on salient features matching. *Computer Methods and Programs in Biomedicine*, *105* (2), 131-144. doi: 10.1016/j.cmpb.2011.07.014.

Uga, Y. (2021). Challenges to design-oriented breeding of root system architecture adapted to climate change. *Breeding science*, *71* (1), 3–12. doi: 10.1270/jsbbs.20118

van Genuchten, M. T. (1980). A closed-form equation for predicting the hydraulic conductivity of unsaturated soils. *Soil Science Society of America Journal*, *44* (5), 892-898. doi: 10.2136/sssaj1980.03615995004400050002x

Vanhees, D. J., Schneider, H. M., Sidhu, J. S., Loades, K. W., Bengough, A. G., Bennett, M. J., ... Lynch, J. P. (2021). Soil penetration by maize roots is negatively related to ethylene-induced thickening. *Plant, Cell & Environment*, *n/a* (n/a). doi: 10.1111/pce.14175

van Veelen, A., Koebernick, N., Scotson, C. S., McKay-Fletcher, D., Huthwelker, T., Borca, C. N., ... Roose, T. (2020). Root-induced soil deformation influences fe, s and p: rhizosphere chemistry investigated using synchrotron xrf and xanes. *New Phytologist*, *225* (4), 1476-1490. doi: 10.1111/nph.16242

van Veelen, A., Tourell, M. C., Koebernick, N., Pileio, G. & Roose, T. (2018). Correlative visualization of root mucilage degradation using x-ray ct and mri. *Frontiers in Environmental Science*, *6* (32). doi: 10.3389/fenvs.2018.00032

172

Vetterlein, D., Carminati, A., Kögel-Knabner, I., Bienert, G. P., Smalla, K., Oburger, E., ... Schlüter, S. (2020). Rhizosphere spatiotemporal organization–a key to rhizosphere functions. *Front. Agron*, *2* (8). doi: 10.3389/fagro.2020.00008

Vetterlein, D. & Doussan, C. (2016). Root age distribution: how does it matter in plant processes? a focus on water uptake. *Plant Soil*, *407* (1), 145-160. doi: 10.1007/s11104-016-2849-6

Vetterlein, D., Lippold, E., Schreiter, S., Phalempin, M., Fahrenkampf, T., Hochholdinger, F., ... Schlüter, S. (2021). Experimental platforms for the investigation of spatiotemporal patterns in the rhizosphere—laboratory and field scale. *Journal of Plant Nutrition and Soil Science*, *184* (1), 35-50. doi: 10.1002/jpln.202000079

Vetterlein, D. & Tarkka, M. (2018). Seeds with low phosphorus content: not so bad after all? *Journal of Experimental Botany*, *69* (21), 4993-4996. doi: 10.1093/jxb/ery313

Vierheilig, H., Coughlan Andrew, P., Wyss, U. & Piché, Y. (1998). Ink and vinegar, a simple staining technique for arbuscular-mycorrhizal fungi. *Applied and Environmental Microbiology*, *64* (12), 5004-5007. doi: 10.1128/AEM.64.12.5004-5007.1998

Vinther, F. P., Eiland, F., Lind, A. M. & Elsgaard, L. (1999). Microbial biomass and numbers of denitrifiers related to macropore channels in agricultural and forest soils. *Soil Biology and Biochemistry*, *31* (4), 603-611. doi: 10.1016/S0038-0717(98)00165-5

Vollsnes, A., Futsaether, C. & Bengough, A. (2010). Quantifying rhizosphere particle movement around mutant maize roots using time-lapse imaging and particle image velocimetry. *European Journal of Soil Science*, *61* (6), 926-939. doi: 10.1111/j.1365-2389.2010.01297.x

Wahlström, E. M., Kristensen, H. L., Thomsen, I. K., Labouriau, R., Pulido-Moncada, M., Nielsen, J. A. & Munkholm, L. J. (2021). Subsoil compaction effect on spatiotemporal root growth, reuse of biopores and crop yield of spring barley. *European Journal of Agronomy*, *123*, 126225. doi: 10.1016/j.eja.2020.126225

Wang, T., Rostamza, M., Song, Z., Wang, L., McNickle, G., Iyer-Pascuzzi, A. S., ... Jin, J. (2019). Segroot: a high throuput segmentation method for root image analysis. *Computers and Electronics in Agriculture*, *162*, 845–854. doi: 10.1016/j.compag.2019.05.017

Wang, Y. & Lambers, H. (2020). Root-released organic anions in response to low phosphorus availability: recent progress, challenges and future perspectives. *Plant Soil*, *447* (1), 135-156. doi: 10.1007/s11104-019-03972-8

Watt, M., Silk, W. K. & Passioura, J. B. (2006). Rates of root and organism growth, soil conditions, and temporal and spatial development of the rhizosphere. *Annals of Botany*, *97* (5), 839-855. doi: 10.1093/aob/mcl028

Weber, N., Herrmann, I., Hochholdinger, F., Ludewig, U. & Neumann, G. (2018). Pgpr-induced growth stimulation and nutrient acquisition in maize: do root hairs matter? *Scientia Agriculturae Bohemica*, *49* (3), 164-172. doi: 10.2478/sab-2018-0022

Wen, T.-J. & Schnable, P. S. (1994). Analyses of mutants of three genes that influence root hair development in zea mays (gramineae) suggest that root hairs are

dispensable. *American Journal of Botany*, *81* (7), 833-842. doi: 10.1002/j.1537-2197.1994.tb15564.x

Wen, Z., Li, H., Shen, Q., Tang, X., Xiong, C., Li, H., . . . Shen, J. (2019). Tradeoffs among root morphology, exudation and mycorrhizal symbioses for phosphorus-acquisition strategies of 16 crop species. *New Phytologist*, *223* (2), 882-895. doi: 10.1111/nph.15833

Whalley, W. R., Riseley, B., Leeds-Harrison, P. B., Bird, N. R., Leech, P. K. & Adderley, W. P. (2005). Structural differences between bulk and rhizosphere soil. *European Journal of Soil Science*, *56* (3), 353-360. doi: 10.1111/j.1365-2389.2004.00670.x

White, R. G. & Kirkegaard, J. A. (2010). The distribution and abundance of wheat roots in a dense, structured subsoil–implications for water uptake. *Plant, Cell & Environment*, *33* (2), 133-148. doi: 10.1111/j.1365-3040.2009.02059.x

Wickham, H. (2009). *ggplot2: Elegant graphics for data analysis*. Springer-Verlag New York.

Wickham, H. (2011). The split-apply-combine strategy for data analysis. *Journal of Statistical Software*, *40* (1), 1-29. doi: 10.18637/jss.v040.i01

Wickham, H., Averick, M., Bryan, J., Chang, W., McGowan, L. D., François, R., . . . others (2019). Welcome to the tidyverse. *Journal of open source software*, *4* (43), 1686. doi: 10.21105/joss.01686

Wood, S. N. (2011). Fast stable restricted maximum likelihood and marginal likelihood estimation of semiparametric generalized linear models. *Journal of the Royal Statistical Society: Series B (Statistical Methodology)*, *73* (1), 3-36. doi: 10.1111/j.1467-9868.2010.00749.x

Wood, S. N. (2017). *Generalized additive models: an introduction with r* [Book]. CRC press.

Wu, W., Ma, B. & Whalen, J. K. (2018). Chapter three - enhancing rapeseed tolerance to heat and drought stresses in a changing climate: Perspectives for stress adaptation from root system architecture. In (Bd. 151, S. 87-157). Academic Press. doi: 10.1016/bs.agron.2018.05.002

Xiong, P., Zhang, Z., Hallett, P. D. & Peng, X. (2020). Variable responses of maize root architecture in elite cultivars due to soil compaction and moisture. *Plant Soil*, 1-13. doi: 10.1007/s11104-020-04673-3

Yang, S. F. & Hoffman, N. E. (1984). Ethylene biosynthesis and its regulation in higher plants. *Annual review of plant physiology*, *35* (1), 155–189.

Yoshida, S. & Hallett, P. (2008). Impact of hydraulic suction history on crack growth mechanics in soil. *Water Resources Research*, *44* (5). doi: 10.1029/2007WR006055

Yu, P., White, P. J., Hochholdinger, F. & Li, C. (2014). Phenotypic plasticity of the maize root system in response to heterogeneous nitrogen availability. *Planta*, *240* (4), 667–678. doi: 10.1007/s00425-014-2150-y

Yunusa, I. A. M. & Newton, P. J. (2003). Plants for amelioration of subsoil constraints and hydrological control: the primer-plant concept. *Plant Soil*, *257* (2), 261-281. doi: 10.1023/A:1027381329549

Zhang, Y., Du, H., Xu, F., Ding, Y., Gui, Y., Zhang, J. & Xu, W. (2020). Root-bacteria associations boost rhizosheath formation in moderately dry soil through ethylene responses. *Plant Physiology*, *183* (2), 780-792. doi: 10.1104/pp.19.01020

Zhang, Z., Liu, K., Zhou, H., Lin, H., Li, D. & Peng, X. (2018). Three dimensional characteristics of biopores and non-biopores in the subsoil respond differently to land use and fertilization. *Plant Soil*, *428* (1), 453-467. doi: 10.1007/s11104-018-3689-3

Zhou, H., Whalley, W. R., Hawkesford, M. J., Ashton, R. W., Atkinson, B., Atkinson, J. A., ... Mooney, S. J. (2021). The interaction between wheat roots and soil pores in structured field soil. *Journal of Experimental Botany*, *72* (2), 747-756. doi: 10.1093/jxb/eraa475

Zickenrott, I.-M., Woche, S. K., Bachmann, J., Ahmed, M. A. & Vetterlein, D. (2016). An efficient method for the collection of root mucilage from different plant species—a case study on the effect of mucilage on soil water repellency. *Journal of Plant Nutrition and Soil Science*, *179* (2), 294-302. doi: 10.1002/jpln.201500511

LIST OF PUBLICATIONS

1. Lippold, E., **Phalempin, M.**, Schlüter, S., & Vetterlein, D. (2021). Does the lack of root hairs alter root system architecture of Zea mays?. *Plant Soil*, 1-20. doi : 10.1007/s11104-021-05084-8

2. Schnepf, A., Carminati, A., Ahmed, M. A., Ani, M., Benard, P., Bentz, J., Bonkowski, M., Brax, M., Diehl, D., Duddek, P., Kröner, E., Javaux, M., Landl, M., Lehndorff, E., Lippold, E., Lieu, A., Mueller, C. W., Oburger, E., Otten, W., Portell, X., **Phalempin, M.**, Prechtel, A., Schulz, R., Vanderborght, J., & Vetterlein, D. (2021). Linking rhizosphere processes across scales: Opinion. *bioRxiv*. doi : 10.1101/2021.07.08.451655

3. **Phalempin, M.**, Lippold, E., Vetterlein, D., & Schlüter, S. (2021). Soil texture and structure heterogeneity predominantly governs bulk density gradients around roots. *Vadose Zone Journal*, 1-17. doi : 10.1002/vzj2.20147

4. **Phalempin, M.**, Lippold, E., Vetterlein, D., & Schlüter, S. (2021). An improved method for the segmentation of roots from X-ray computed tomography 3D images: Rootine v. 2. *Plant Methods*, 17(1), 1-19. doi : 10.1186/s13007-021-00735-4

5. Lippold, E., Kleinau, P., Blaser, S. R., Schlüter, S., **Phalempin, M.**, & Vetterlein, D. (2021). In soil measurement of radiation dose caused by X-ray computed tomography. *J. Plant Nutr. Soil Sci.*, 184(3), 343-345. doi : 10.1002/jpln.202000276

6. Landl, M., **Phalempin, M.**, Schlüter, S., Vetterlein, D., Vanderborght, J., Kroener, E., & Schnepf, A. (2021). Modeling the Impact of Rhizosphere Bulk Density and Mucilage Gradients on Root Water Uptake. *Front. Agron*, 3, 6. doi : 10.3389/fagro.2021.622367

7. Vetterlein, D., Lippold, E., Schreiter, S., **Phalempin, M.**, Fahrenkampf, T., Hochholdinger, F., Marcon, C., Tarkka, M., Oburger, E., Ahmed, Javaux, M. & Schlüter, S. (2021). Experimental platforms for the investigation of spatiotemporal patterns in the rhizosphere—laboratory and field scale. *J. Plant Nutr. Soil Sci.*, 184(1), 35-50. doi : 10.1002/jpln.202000079

CURRICULUM VITAE

see next page.

Maxime Phalempin

maxime.phalempin@ufz.de
Born in Namur (BE) on the 26.05.1991

Experience

Doctoral Candidate, Umweltforschhungzentrum, Halle(Saale) (GER)　　　2018 - 2021
Supervised by Steffen Schlueter and Doris Vetterlein, funded by DFG.

- Development of image processing methods to analyze root system architecture and soil physical properties from X-ray CT data images.
- Organization and participation in undisturbed cores sampling campaigns and soil physical properties measurements in the field.
- Independent and rigorous conduction of laboratory experiments entailing the scanning of soil samples with X-ray CT.

Research Assistant, Earth and Life Institute, Louvain-la-Neuve (BE)　　　2016 - 2018
Supervised by Marnik Vanclooster and Patrick Gerin, funded by FNRS.

- Site selection, sampling and equipment (TDR probes, tensiometers, soil solution samplers) of large undisturbed soil cores.
- Collection, analysis and associated modelling of hydrological data collected on large undisturbed soil cores.
- Collection and biochemical analysis of septic tank effluent and associated leachates.
- Development of a mathematical tool to design septic tank effluent drain field.

Education

PhD. Geological Sciences, MLU Halle-Wittenberg, Halle(Saale) (GER)	2018 -
MSc. Environmental Engineering, Université Catholique de Louvain (BE)	2014 - 2016
Pre-MSc. Environmental Engineering, Université Catholique de Louvain (BE)	2013 - 2014
BSc. Agronomy and Horticultural Sciences, ISIa-Gembloux (BE)	2010 - 2013
Language Exchange Program, EF International School in Santa Barbara (USA)	2010 - 2010
Language Exchange Program, EF International School in Antwerp (BE)	2009 - 2010
High School, College Notre Dame de la Paix a Erpent (BE)	2003 - 2009

_____　　　　_____

Date　　　　　　　　　　　　　　　　**Signature**

ACKNOWLEDGMENTS

I owe an enormous debt of gratitude to my family. Carine and Marc have a special contribution to this thesis. Despite your shallow understanding of what I do, you, as parents, have trusted me from the start and have given me everything I needed to succeed: love, education and financial support. This will never be forgotten. Georges, "papy", I dedicate this work to you. You have always been so proud of me and encouraged me to study and educate myself further, I wish you could still be there to read what certainly constitutes the apogee of my work as a member of the academic world. Lastly, I cannot thank enough my friends in Halle for changing this PhD experience into an extraordinary life experience, rich in encounters, love and travels. Amine, James, Alessandro, Lama, Farina, Linda... Citing all of them would drastically increase the size of this paragraph. I wish the ones that I did not mention can forgive me. Of all the experiences that I have had during my stay in Germany, meeting you, Antonia, was certainly the most intense one. Thank you that you were there with me during this time.

Eidesstattliche Erklärung / *Declaration under Oath*

Ich erkläre an Eides statt, dass ich die Arbeit selbstständig und ohne fremde Hilfe verfasst, keine anderen als die von mir angegebenen Quellen und Hilfsmittel benutzt und die den benutzten Werken wörtlich oder inhaltlich entnommenen Stellen als solche kenntlich gemacht habe.
I declare under penalty of perjury that this thesis is my own work entirely and has been written without any help from other people. I used only the sources mentioned and included all the citations correctly both in word or content.

_____   _____
Datum / Date   Unterschrift des Antragstellers / *Signature of the applicant*